Fraunhofer IWES

FRAUNHOFER INSTITUTE FOR WIND ENERGY SYSTEMS IWES

Wojciech Popko

Impact of Sea Ice Loads on Global Dynamics of Offshore Wind Turbines

FRAUNHOFER VERLAG

Fraunhofer Institute for
Wind Energy Systems IWES

Wojciech Popko

Impact of Sea Ice Loads on Global Dynamics of Offshore Wind Turbines

FRAUNHOFER VERLAG

Contact:
Fraunhofer Institute for
Wind Energy Systems
Am Seedeich 45
27572 Bremerhaven
Telefon +49 (0)471 14290-100
E-Mail info@iwes.fraunhofer.de
URL www.iwes.fraunhofer.de

Cover image: © iStock.com/T.W. van Urk "Dutch offshore wind turbines in a frozen sea"

Bibliographic information of the German National Library:
The German National Library has listed this publication in its Deutsche Nationalbibliografie; detailed bibliographic data is available on the internet at www.dnb.de.

ISBN 978-3-8396-1684-0

D 89

Zugl.: Hannover, TIB, Diss., 2020

Print and finishing:
Fraunhofer Verlag, Mediendienstleistungen

The book was printed with chlorine- and acid-free paper.

Nobelstrasse 12
70569 Stuttgart
Germany
verlag@fraunhofer.de
www.verlag.fraunhofer.de

is a constituent entity of the Fraunhofer-Gesellschaft, and as such has no separate legal status.

Fraunhofer-Gesellschaft zur Förderung
der angewandten Forschung e.V.
Hansastrasse 27 c
80686 München
Germany
www.fraunhofer.de

institut für windenergiesysteme

Leibniz Universität Hannover

Impact of Sea Ice Loads on Global Dynamics of Offshore Wind Turbines

Von der Fakultät für Bauingenieurwesen und Geodäsie
der Gottfried Wilhelm Leibniz Universität Hannover
zur Erlangung des Grades

Doktor der Ingenieurwissenschaften
– Dr.-Ing. –

genehmigte Dissertation von

M.Sc. Wojciech Popko
geboren am 26.07.1985 in Białystok, Polen

2020

Referent:	**Prof. Dr.-Ing. Andreas Reuter** Gottfried Wilhelm Leibniz Universität Hannover Institut für Windenergiesysteme
Korreferent:	**Prof. Dr. Michael Muskulus** Norwegian University of Science and Technology Department of Civil and Environmental Engineering
Kommissionsmitglied:	**Prof. Dr.-Ing. Peter Schaumann** Gottfried Wilhelm Leibniz Universität Hannover Institut für Stahlbau
Vorsitz:	**Prof. Dr.-Ing. Dominik Schillinger** Gottfried Wilhelm Leibniz Universität Hannover Institut für Baumechanik und Numerische Mechanik

Tag der Promotion: 18. September 2020

Eigenständigkeitserklärung

Hiermit erkläre ich, dass ich die vorliegende Dissertation mit dem Titel

Impact of Sea Ice Loads on Global Dynamics of Offshore Wind Turbines

ohne unzulässige Hilfe Dritter und ohne Benutzung anderer als der angegebenen Hilfsmittel angefertigt habe. Die aus fremden Quellen direkt oder indirekt übernommenen Gedanken sind als solche kenntlich gemacht.

Insbesondere habe ich nicht die Hilfe einer kommerziellen Beratung in Anspruch genommen. Dritte haben von mir weder unmittelbar noch mittelbar geldwerte Leistungen für Tätigkeiten erhalten, die im Zusammenhang mit dem Inhalt der vorgelegten Arbeit stehen.

Die Dissertation wurde bisher weder im Inland noch im Ausland in gleicher oder ähnlicher Form eingereicht und ist als Ganzes auch noch nicht veröffentlicht.

Ich bin damit einverstanden, dass die Dissertation zum Zwecke der Überprüfung der Einhaltung allgemein geltender wissenschaftlicher Standards genutzt wird. Dies gilt insbesondere auch unter Verwendung elektronischer Datenverarbeitungsprogramme.

Die Regeln der geltenden Promotionsordnung der Fakultät für Bauingenieurwesen und Geodäsie der Gottfried Wilhelm Leibniz Universität Hannover sind mir bekannt und wurden eingehalten. Mit einer Prüfung nach den Bestimmungen der Promotionsordnung bin ich einverstanden.

Bremerhaven, den 8. Juni 2020,

M.Sc. Wojciech Popko

Executive Summary

Support structures for offshore wind turbines (OWTs) are designed and certified site-specific based on the calculated load effects. These load effects originate from static, cyclic, stochastic, and transient loads from the met-ocean environment and rotating components of the wind turbine. The met-ocean environment of the Baltic Sea accounts for variable wind and marine conditions. Sea ice is part of marine conditions — which among others — should be included in the design process of OWT support structures.

The load analysis and design of OWTs, including its components, rely on the time-domain based, coupled aero-hydro-servo-elastic simulation tools. Only this approach can provide an accurate prediction of the OWT dynamic response, as discussed in Chapter 2. Dynamic interaction between an OWT and external loads — including ice loads — cannot be disregarded as it may result in considerable loss of accuracy. A proper understanding of sea ice impact on the global dynamics of OWTs — involving the fully-integrated simulation approach — is necessary within the offshore wind research community, industry, and certification authorities. So far, they all had to rely on the ice experts, whose methods for ice loads calculation were not fully transparent and not always compatible with the design and certification methodologies for OWTs.

The main contributions of this work to the state-of-the-art are summarized as follows:

- A simple phenomenological ice model from Määttänen — which was already available in Modelica® Library for Wind Turbines (MoLWiT), the in-house aero-hydro-servo-elastic tool from Fraunhofer IWES — has been validated against ice tank tests. It has been shown that with careful calibration, satisfactory results can be achieved.
- An advanced phenomenological ice model from Hendrikse has been fully integrated into an aero-hydro-servo-elastic simulation tool for the first time.
- The implementation of the Hendrikse ice model in MoLWiT has been cross-verified against its original source code, which simulation capabilities have been extended to accommodate modally reduced mDOF structures. The extended source code of the ice model has also been coupled with a newly developed FEM code for modeling mDOF structures.
- The newly developed FEM code for modeling mDOF structures is publicly available within this dissertation. The code can be coupled by other researchers with the publicly available version of the Hendrikse ice model (for sDOF structures) upon the extension of its simulation capabilities to multi-mode structures.
- The fully-integrated implementation of the Hendrikse ice model in MoLWiT has been used for advanced studies of ice-OWT interaction in Chapter 5. The analysis has been performed at three distinct design situations — idling below the cut-in wind speed, power production below the rated wind speed, and power production above the rated wind speed. Each design

situation has been simulated with multiple ice velocities covering three main ice-structure interaction modes — intermittent ice crushing, frequency lock-in, and continuous brittle crushing. The impact of ice on the OWT dynamics has been investigated in terms of short-term damage-equivalent loads (DELs) and power spectral densities (PSDs). It has been shown that:

- The most severe fatigue load effects are always caused by intermittent ice crushing, regardless of whether the OWT is idling or operating.
- The highest increase of fatigue load effects occurs when the OWT is idling and there is an ice action on its support structure, when compared to the corresponding reference design situation where ice loads are not present. However, in terms of the absolute values, DELs at idling are usually smaller than those obtained at power production.
- During the OWT operation, the increase of short-term DELs is not that severe as for the idling case, as the increased aerodynamic damping can effectively mitigate load effects resulting from the ice load action at mean sea level (MSL). Nevertheless, this increase is still noticeable: the increase of around 74% is observed at the intermittent ice crushing mode, around 30% at the frequency lock-in mode, and around 5% for the continuous brittle crushing mode — when compared to the corresponding reference design situations without ice loads.

• The work-energy flow between ice and the structure during different operational regions of an OWT has been analyzed for the first time according to the author's best knowledge.

• The sensitivity analysis of eigenmodes contribution to short-term DELs has been performed. It has been shown that the 1st eigenmode always has a significant contribution to DELs. The impact of the 2nd eigenmode on DELs is also very considerable, though it might have mitigating effect at certain design situations. The 3rd and the 4th eigenmodes have less impact on DELs than the first two eigenmodes. Nevertheless, their presence is important from the perspective of the OWT global dynamics. Those modes are often coupled with blade flapwise modes.

• A set of indicative ice properties for the southern Baltic Sea has been estimated. These properties can be directly used as an input to the Hendrikse ice model.

A set of recommendations are given for the load analysts who are dealing with simulations of ice loads on OWTs. Also, research ideas are suggested for future work in the context of ice-OWT interaction.

Keywords: Offshore wind turbine, OWT dynamics, ice-structure interaction

Zusammenfassung

Tragstrukturen für Offshore-Windenergieanlagen (OWEA) werden auf Basis der berechneten Lasteffekte standortspezifisch entworfen und zertifiziert. Diese Lasteffekte entstehen durch statische, zyklische, stochastische und transiente Lasten aus der meteorologischen und ozeanografischen (Met-Ocean) Umgebung und rotierenden Komponenten der Windenergieanlage.

Die Met-Ocean-Umgebung der Ostsee ist für unterschiedliche Wind- und Meeresbedingungen verantwortlich. Meereis ist Teil der Meeresbedingungen, welche unter anderem in den Entwurfsprozess von OWEA-Tragstrukturen einbezogen werden sollten. Die Lastanalyse und das Design von OWEA einschließlich ihrer Komponenten basieren auf Simulationsergebnissen im Zeitbereich, welche mittels aero-servo-hydro-elastischen Simulationswerkzeugen gewonnen werden. Nur dieser Ansatz kann eine genaue Vorhersage des dynamischen Verhaltens einer OWEA liefern, wie in Kapitel 2 erläutert. Die dynamische Interaktion zwischen einer OWEA und äußeren Lasten – einschließlich von Eislasten – kann nicht außer Acht gelassen werden, da dies zu einem erheblichen Genauigkeitsverlust führen kann. Ein angemessenes Verständnis der Auswirkungen von Meereis auf die Gesamtanlagendynamik von OWEA – unter Einbeziehung des vollständig integrierten Simulationsansatzes – ist innerhalb der Offshore-Windforschungsgemeinschaft, Industrie und Zertifizierungsstellen erforderlich. Bisher musste man sich auf die Eisexperten verlassen, deren Methoden zur Berechnung der Eislasten nicht vollständig transparent und nicht immer kompatibel mit den Entwurfs- und Zertifizierungsmethoden für OWEA waren.

Die wichtigsten Beiträge dieser Arbeit zum Stand der Wissenschaft sind wie folgt zusammengefasst:

- Ein einfaches phänomenologisches Eismodell von Määttänen, das bereits in der Modelica® Library for Wind Turbines (MoLWiT), dem hauseigenen aero-servo-hydro-elastisches Simulationswerkzeug von Fraunhofer IWES, verfügbar war, wurde gegen Eistank-Tests validiert. Es wurde gezeigt, dass durch sorgfältige Kalibrierung zufriedenstellende Ergebnisse erzielt werden können.
- Ein fortschrittliches phänomenologisches Eismodell von Hendrikse wurde erstmals vollständig in ein aero-servo-hydro-elastisches Simulationswerkzeug integriert.
- Die Implementierung des Hendrikse-Eismodells in MoLWiT wurde mit dem originalen Quellcode verglichen. Simulationsfunktionen wurden erweitert, um modal reduzierte mDOF-Strukturen zu berücksichtigen. Der erweiterte Quellcode des Eismodells wurde auch mit einem neu entwickelten FEM-Code zur Modellierung von mDOF-Strukturen gekoppelt.
- Der neu entwickelte FEM-Code zur Modellierung von mDOF-Strukturen ist innerhalb dieser Dissertation öffentlich verfügbar. Der Code kann von anderen Forschern mit der öffentlich verfügbaren Version des Hendrikse-Eismodells (für sDOF-Strukturen) gekoppelt werden, um Simulationen mit Multi-Mode-Strukturen durchführen zu können.

- Die vollständig integrierte Implementierung des Hendrikse-Eismodells in MoLWiT wurde in Kapitel 5 für fortgeschrittene Studien zur Eis-OWEA-Interaktion verwendet. Die Analyse wurde unter drei unterschiedlichen Entwurfsszenarien durchgeführt – Leerlauf unterhalb der Einschaltwindgeschwindigkeit, Produktionsbetrieb unterhalb der Nennwindgeschwindigkeit und Produktionsbetrieb oberhalb der Nennwindgeschwindigkeit. Jedes Entwurfszenario wurde mit mehreren Eisgeschwindigkeiten simuliert, die drei Haupteisstrukturen-Interaktionsmodi abdecken – intermittierendes Eiszerkleinern, Frequenzsperre und kontinuierliches Sprödzerkleinern. Der Einfluss von Eis auf die OWEA-Dynamik wurde im Hinblick auf schadensäquivalente Lasten (DELs) und Leistungsspektraldichten (PSDs) untersucht. Hierbei wurde Folgendes festgestellt:
  - Die schwerwiegendsten Ermüdungsbelastungseffekte werden immer durch intermittierendes Eiszerkleinern verursacht, unabhängig davon, ob die OWEA im Leerlauf oder in Betrieb ist.
  - Die höchste Zunahme von Ermüdungslasten tritt auf, wenn sich die OWEA im Leerlauf befindet und eine Eiswirkung auf ihre Tragstruktur auftritt, verglichen mit dem entsprechenden Referenzentwurfsszenario, in dem keine Eislasten vorhanden sind. In Bezug auf die absoluten Werte sind die DELs im Leerlauf normalerweise kleiner als diejenigen, die sich beim Produktionsbetrieb einstellen.
  - Während des OWEA-Betriebs ist der Anstieg der kurzzeitigen DELs nicht so massiv wie im Leerlauf, da die erhöhte aerodynamische Dämpfung der Anlage die Lasteffekte, die sich aus der Eislastwirkung auf dem mittleren Meeresspiegel (MSL) ergeben, wirksam abschwächen kann. Trotzdem ist dieser Anstieg feststellbar: Ein Anstieg von etwa 74% im intermittierenden Eiszerkleinerungsmodus, etwa 30% im Frequenzsperrmodus und etwa 5% im kontinuierlichen Sprödzerkleinerungsmodus wird beobachtet – im Vergleich zu entsprechenden Referenzentwurfsszenarien ohne Eislasten.
- Der Energiefluss zwischen Eis und Struktur in verschiedenen Betriebsbereichen einer OWEA wurde analysiert.
- Die Sensitivitätsanalyse des Eigenmodenbeitrags zu kurzzeitigen DELs wurde durchgeführt. Es wurde gezeigt, dass die 1. Eigenmode immer einen signifikanten Beitrag zu DELs leistet. Der Einfluss der 2. Eigenmode auf DELs ist ebenfalls sehr beträchtlich, obwohl er in bestimmten Entwurfsszenarien eine mildernde Wirkung haben kann. Die 3. und die 4. Eigenmode haben weniger Einfluss auf DELs als die ersten beiden Eigenmoden. Dennoch ist ihre Präsenz aus Sicht der Gesamtanlagendynamik von OWEA wichtig. Diese Moden sind häufig mit Blattmoden in Schalgrichtung gekoppelt.
- Eine Reihe von indikativen Eiseigenschaften für die südliche Ostsee wurde geschätzt. Diese Eigenschaften können direkt als Eingabe für das Hendrikse-Eismodell verwendet werden.

Eine Reihe von Empfehlungen wird für die Lastanalysten gegeben, die sich mit Simulationen von Eislasten auf OWEA befassen. Außerdem werden Forschungsideen für zukünftige Arbeiten im Kontext der Eis-OWEA-Interaktion vorgeschlagen.

Schlüsselwörter: Offshore-Windenergieanlagen, Dynamik von OWEA, Eis-Struktur-Interaktion

Acknowledgments

I would like to thank Prof. Dr. Michael Muskulus from the Norwegian University of Science and Technology (NTNU) for his constant support, countless technical discussions, and multiple ideas for this research. His tremendous help is highly appreciated. Michael has been an exceptional mentor — I am grateful for the opportunity to work with him.

Prof. Dr.-Ing. Andreas Reuter is acknowledged for supporting this dissertation and for the financial support from the budget of Fraunhofer Institute for Wind Energy Systems IWES.

All colleagues from IWES should be acknowledged for many engineering-related discussions and great working atmosphere. I would like to thank especially PD Dr.-Ing. Adrian Gambier, Dipl.-Ing. Philipp Thomas, and Dr.-Ing. Fabian Vorpahl. Adrian helped me to structure my dissertation and provided valuable comments on its content. Philipp is acknowledged for his help with Modelica® Library for Wind Turbines (MoLWiT). Fabian should be recognized for his great support during my first years at IWES. At that time, Fabian was my boss and mentor. He shared with me a lot of knowledge concerning the global dynamics of wind turbines and load analysis. He also gave me the possibility to work in various international research communities.

I would like to thank multiple people from the "ice community", who provided crucial inputs to my work. First of all, Dr. Hayo Hendrikse from the Delft University of Technology should be acknowledged for sharing the source code of his sea ice model, which I could use for my dissertation. Dipl.-Ing. Gesa Ziemer, Dipl.-Ing. Karl-Ulrich Evers, and Dipl.-Ing. Peter Jochmann from the Hamburg Ship Model Basin (HSVA) are acknowledged for sharing the ice tank test results and the full-scale measurements, which I used for the validation of numerical models for ice-structure interaction. Last but not least, M.Sc. Vilho Jussila and Dr. Jaakko Heinonen from the VTT Technical Research Centre of Finland are acknowledged for multiple discussions concerning ice-structure interaction.

Many thanks to Dr.-Ing. Björn Schümann from Ramboll for sharing a conceptual design of the support structure and proofreading of this dissertation.

Prof. Knut Vilhelm Høyland is acknowledged for helping me to organize my research stay at NTNU and involving me in teaching activities in two M.Sc. level courses at the Department of Civil and Transport Engineering.

I would like to thank Dr. Tu Ying and Prof. Cheng Zhengshun for their hospitality and friendship during my research stay at NTNU in Trondheim. I should also thank all colleagues from the NTNU "basement" for a welcoming and delightful atmosphere during the dark Norwegian winter of 2016/2017.

I should acknowledge my two former Master's students — M.Sc. Sofia Georgiadou and M.Sc. Wang Chao — who helped me a lot by setting up multiple simulations in MoLWiT.

The results presented in this dissertation are part of widespread research realized in the framework of two research projects — BReaking the ICE (BRICE) (funding code FKZ 0325297A/B) and Sea ice Loads on Offshore Wind Turbines (SeaLOWT) (funding code FKZ 0324022A/B/C) — which were funded by the Federal Ministry for Economic Affairs and Energy (BMWi) on the basis of a decision by the German Bundestag.

Contents

List of Figures

List of Tables

List of Symbols

Latin symbols

Symbol	Unit	Description
A_{ref}	m^2	Reference loading area in the Määttänen-Blenkarn model
A	m^2	Member cross-sectional area, loading area
C_{R}	$\text{N}\,\text{m}^{-2}$	Ice strength in the ISO equation
$[\boldsymbol{C}]$	–	Global viscous damping matrix
D	m	Diameter
E_{k}	J	Kinetic energy
E_{p}	J	Potential energy
E_{t}	J	Total mechanical energy
E	$\text{N}\,\text{m}^{-2}$	Young's modulus
$F_{2v\text{db}}$	N	Mean value of the global ice load at $2v_{\text{db}}$ (from the measurements of ice action on the rigid structure)
F_{brittle}	N	Mean brittle crushing ice load at v_{brittle} (from the measurements of ice action on the rigid structure)
F_{d}	N	Viscous damping force
F_{ice}	N	Ice force
F_{max}	N	Maximum ice load at the ductile-to-brittle transition at v_{db} (from the measurements of ice action on the rigid structure)
F_{slip}	N	Slip force of the sliding element in the Hendrikse ice model
$\{\boldsymbol{F}\}$	N	Force vector
Fr	–	Froude number
F	N	Force
G	$\text{N}\,\text{m}^{-2}$	Shear modulus
$\{\boldsymbol{I}\}$	–	Influence vector representing the displacements of masses resulting from static application of unit ground displacements and rotations in the direction of the corresponding translational or rotational DOF
I_{xx}	m^4	Second moment of area with respect to the x-axis

Symbol	Unit	Description
I_{xy}	$\mathrm{kg\,m^2}$	Product moment of inertia with respect to the x- and y-axis
I_{xz}	$\mathrm{kg\,m^2}$	Product moment of inertia with respect to the x- and z-axis
I_x	$\mathrm{kg\,m^2}$	Moment of inertia with respect to the x-axis
I_{yy}	$\mathrm{m^4}$	Second moment of area with respect to the y-axis
I_{yz}	$\mathrm{kg\,m^2}$	Product moment of inertia with respect to the y- and z-axis
I_y	$\mathrm{kg\,m^2}$	Moment of inertia with respect to the y-axis
I_{zz}	$\mathrm{m^4}$	Second moment of area with respect to the z-axis
I_z	$\mathrm{kg\,m^2}$	Moment of inertia with respect to the z-axis
$[\boldsymbol{K}_\mathrm{f}]$	–	Foundation stiffness matrix
$[\boldsymbol{K}]$	–	Global stiffness matrix
L	m	Member length
$[\boldsymbol{M}_\mathrm{f}]$	–	Foundation mass matrix
$[\boldsymbol{M}]$	–	Global mass matrix
$[\boldsymbol{M}_\mathrm{p}]$	–	Point mass and inertia matrix
N_dof	–	Number of degrees of freedom
N_el	–	Number of elements
N_m	–	Number of eigenmodes
N_n	–	Number of nodes
N_st	–	Number of ice stripes in the Hendrikse ice model
P_ice	$\mathrm{N\,m^{-2}}$	Ice pressure
R	m	Radius
$[\boldsymbol{T}]$	–	Transformation matrix
T	s	Period of oscillation
$U(a,b)$	–	Uniform distribution with equal probability in the range from a to b
V_hub	$\mathrm{m\,s^{-1}}$	Mean wind speed at hub height
V	$\mathrm{m\,s^{-1}}$	Wind speed
W_d	J	Energy loss per cycle
W_ice	J	Work done by ice on the structure
c_c	$\mathrm{kg\,s^{-1}}$	Damping coefficient for creep in the Hendrikse ice model
$[\boldsymbol{c}]$	–	Generalized modal damping matrix
c_ref	–	Fraction of critical deformation of the ice stripe (element) until which the ice behaves elastically
$c_\mathrm{v\text{-}p}$	$\mathrm{kg\,s^{-1}}$	Damping coefficient of the viscoplastic element in the Hendrikse ice model

Symbol	**Unit**	**Description**
c	$\mathrm{kg\,s^{-1}}$	Damping coefficient
f_{AR}	–	Empirical term for calculation of the global ice pressure
f_{d}	Hz	Damped natural frequency
f_{n}	Hz	Undamped natural frequency (eigenfrequency)
f_{peak}	Hz	Frequency in the spectrum of the global ice load, which contains the major part of the energy at v_{brittle} and above
$\{\boldsymbol{f}_{\mathrm{ice}}\}$	–	Modal ice load vector
g	$\mathrm{m\,s^{-2}}$	Gravitational acceleration
h_{ice}	m	Thickness of ice
h_{ref}	m	Reference ice thickness of 1 m in the ISO equation
j	–	Eigenmode number
k_1	–	Shape factor for the shape of structure in the Korzhawin equation
k_2	–	Indentation factor in the Korzhawin equation
k_3	–	Contact factor between ice and structure in the Korzhawin equation
$[\boldsymbol{k}_{\mathrm{e}}]$	–	Element elastic stiffness matrix
k_{emp}	–	Unitless empirical factor in the Iowa formula
k_{ice}	$\mathrm{N\,m^{-1}}$	Stiffness of ice
$[\boldsymbol{k}]$	–	Generalized modal stiffness matrix
$k_{\mathrm{v\text{-}p}}$	$\mathrm{N\,m^{-1}}$	Stiffness of the viscoplastic element in the Hendrikse ice model
k	$\mathrm{N\,m^{-1}}$	Stiffness
l_{ice}	m	Characteristic failure length of ice in the Matlock model
$[\boldsymbol{m}_{\mathrm{e}}]$	–	Element mass matrix
$[\boldsymbol{m}]$	–	Generalized modal mass matrix
m	kg	Mass
p_{G}	$\mathrm{N\,m^{-2}}$	Global average ice pressure
$\{\boldsymbol{r}\}$	–	Modal coordinates vector
t_{peak}	s	Time of peak load at v_{db} for a rigid structure
t	s	Time
u_1	m	Displacement component along the x-axis at node 1 of beam element
u_2	m	Displacement component along the x-axis at node 2 of beam element
u_{ice1}	m	Displacement of the front part of the individual ice stripe
$\dot{u}_{\mathrm{ice2}}$	$\mathrm{m\,s^{-1}}$	Velocity in the middle part of the individual ice stripe
u_{ice2}	m	Displacement in the middle part of the individual ice stripe
$\dot{u}_{\mathrm{ice3}}$	$\mathrm{m\,s^{-1}}$	Velocity at the back part of the individual ice stripe

Symbol	Unit	Description
u_{ice3}	m	Displacement of the back part of the individual ice stripe
$\ddot{u}_{\text{ice}}$	$\mathrm{m\,s^{-2}}$	Acceleration of the ice cover
$\dot{u}_{\text{ice}}$	$\mathrm{m\,s^{-1}}$	Velocity of the ice cover
u_{ice}	m	Displacement of the ice cover
u_{init}	m	Offset of the individual ice stripe upon its failure with respect to the structure equilibrium position
v_1	m	Displacement component along the y-axis at node 1 of beam element
v_2	m	Displacement component along the y-axis at node 2 of beam element
v_{brittle}	$\mathrm{m\,s^{-1}}$	Transition velocity to continuous brittle crushing (from the measurements of ice action on the rigid structure)
v_{db}	$\mathrm{m\,s^{-1}}$	Transition velocity between ductile and brittle failure of ice (from the measurements of ice action on the rigid structure)
w_1	m	Displacement component along the z-axis at node 1 of beam element
w_2	m	Displacement component along the z-axis at node 2 of beam element
x	–	Axis in the Cartesian coordinate system
x_{m}	m	Offset of the point mass from the node along the x-axis
$\ddot{x}_{\text{s}}$	$\mathrm{m\,s^{-2}}$	Acceleration of the structure at ice level
$\dot{x}_{\text{s}}$	$\mathrm{m\,s^{-1}}$	Velocity of the structure at ice level
x_{s}	m	Displacement of the structure at ice level
y	–	Axis in the Cartesian coordinate system
y_{m}	m	Offset of the point mass from the node along the y-axis
z	–	Axis in the Cartesian coordinate system
z_{m}	m	Offset of the point mass from the node along the z-axis

Greek symbols

Symbol	Unit	Description
Θ_{x_1}	rad	Rotation component around the x-axis at node 1 of beam element
Θ_{x_2}	rad	Rotation component around the x-axis at node 2 of beam element
Θ_{y_1}	rad	Rotation component around the y-axis at node 1 of beam element
Θ_{y_2}	rad	Rotation component around the y-axis at node 2 of beam element
Θ_{z_1}	rad	Rotation component around the z-axis at node 1 of beam element
Θ_{z_2}	rad	Rotation component around the z-axis at node 2 of beam element
α_{NWP}	–	Power law exponent of wind shear for normal wind profile

Symbol	Unit	Description
α	–	Mass proportional Rayleigh damping coefficient
β	–	Stiffness proportional Rayleigh damping coefficient
δ_{crit}	m	Critical deformation of a single ice stripe in the Hendrikse ice model
δ_{jk}	–	Kronecker delta
δ	m	Deformation
$\dot{\varepsilon}$	s^{-1}	Strain rate
ε	–	Strain
λ	–	Geometric scale factor
ω	–	Eigenfrequency, eigenvalue
$\{\boldsymbol{\phi}\}$	–	Mode shape vector
$[\boldsymbol{\phi}]$	–	Matrix with mode shape vectors arranged in columns
ψ	–	Unifying dimensionless parameter
ρ	$\mathrm{kg\,m^{-3}}$	Density
σ_{c}	$\mathrm{N\,m^{-2}}$	Crushing strength of sea ice
$\dot{\sigma}$	$\mathrm{N\,m^{-2}\,s^{-1}}$	Stress rate
σ_{ice}	N	Standard deviation of brittle crushing force of ice at v_{brittle} and above
σ_{lat}	$\mathrm{m\,s^{-1}}$	Standard deviation of lateral wind component
σ_{long}	$\mathrm{m\,s^{-1}}$	Standard deviation of longitudinal wind component
σ_{ref}	$\mathrm{N\,m^{-2}}$	Reference crushing strength of ice
σ_{vert}	$\mathrm{m\,s^{-1}}$	Standard deviation of vertical wind component
σ	$\mathrm{N\,m^{-2}}$	Stress
ζ	–	Damping ratio

Indices and special characters

Symbol	Description
$_{\text{fs}}$	Subscript indicating the full-scale value
$_{\text{ms}}$	Subscript indicating the model-scale value
$\ddot{\ }$	Second derivative with respect to time
$\dot{\ }$	First derivative with respect to time
$[\ \ ]$	Rectangular or square matrix
$[\ \ ]^{\mathrm{T}}$	Transpose of a matrix
$\{\ \ \}^{\mathrm{T}}$	Transpose of a vector

Symbol	Description
$\{ \}$	Column vector

List of Acronyms

3D	three-dimensional
API	American Petroleum Institute
ASCE	American Society of Civil Engineers
Ashes	Aero-servo-hydro-elastic simulation
ASME	American Society of Mechanical Engineers
BEM	blade element momentum
BHawC	Bonus Horizontal axis wind turbine Code
BMWi	Bundesministerium für Wirtschaft und Energie (in English: Federal Ministry for Economic Affairs and Energy)
BRICE	BReaking the ICE
BSH	Bundesamts für Seeschifffahrt und Hydrographie (in English: Federal Maritime and Hydrographic Agency)
CFD	computational fluid dynamics
CMS	component mode synthesis
CRREL	Cold Regions Research and Engineering Laboratory
CSV	comma-separated value
DB	ductile-to-brittle
DEL	damage-equivalent load
DEM	discrete element method
DIIV	Deciphering Ice Induced Vibrations
DIN	Deutsches Institut für Normung (in English: German Institute for Standardization)
DKE	Deutsche Kommission Elektrotechnik Elektronik Informationstechnik im DIN und VDE (in English: German Commission for Electrical, Electronic & Information Technologies of DIN and VDE)
DLC	design load case

DLL	dynamic-link library
DNV	Det Norske Veritas
DOF	degree of freedom
DONG	Dansk Olie og Naturgas (in English: Danish Oil and Natural Gas)
DSM	direct stiffness method
Dymola	Dynamic modeling laboratory
EU	European Union
FAST	Fatigue, Aerodynamics, Structures, and Turbulence
FATICE	FATigue damage from dynamic ICE action
FE	finite element
FEA	finite element analysis
FEM	finite element method
FKZ	Förderkennzeichen
FVW	free vortex wake
GAST	General Aerodynamic and Structural prediction Tool
GDW	generalized dynamic wake
GE	General Electric
GL	Germanischer Lloyd
HAWC2	Horizontal Axis Wind turbine simulation Code 2nd generation
HSVA	Hamburgische Schiffbau-Versuchsanstalt (in English: Hamburg Ship Model Basin)
IE	ice expert
IEA	International Energy Agency
IEC	International Electrotechnical Commission
IFFT	inverse fast Fourier transform
IRS	improved reduction system
ISO	International Organization for Standardization
ISOPE	International Society of Offshore and Polar Engineers
IVOS	Ice-induced Vibrations of Offshore Structures
IWES	Fraunhofer Institute for Wind Energy Systems IWES
JONSWAP	JOint North Sea WAve Project
LC	load case
LOLEIF	Validation of Low Level Ice Forces on Coastal Structures

LSODAR	Livermore Solver for Ordinary Differential equations, with Automatic method switching for stiff and nonstiff problems, and with Root-finding
MBS	multibody simulation
mDOF	multiple degrees of freedom
MoLWiT	Modelica® Library for Wind Turbines
MSL	mean sea level
N/A	not available
NREL	National Renewable Energy Laboratory
NTNU	Norwegian University of Science and Technology
OC3	Offshore Code Comparison, Collaboration
OC4	Offshore Code Comparison, Collaboration, Continuation
OC5	Offshore Code Comparison, Collaboration, Continuation, with Correlation
OC6	Offshore Code Comparison, Collaboration, Continuation, with Correlation, and unCertainty
ODE	ordinary differential equation
OWT	offshore wind turbine
PDF	probability density function
PF	potential flow
PID	proportional-integral-derivative
PISA	PIle Soil Analysis
PSD	power spectral density
PSSII	Procedure for Soil-Structure-Ice-Interaction
R&D	research and development
RIL	Suomen Rakennusinsinöörien Liitto (in English: Finnish Association of Civil Engineers)
RNA	rotor-nacelle assembly
ROSAP	Ramboll Offshore Structural Analysis Package
RP	recommended practice
RVE	representative volume element
SAMCoT	Sustainable Arctic Marine and Coastal Technology
SD	substructure designer
sDOF	single degree of freedom
SeaLOWT	Sea ice Loads on Offshore Wind Turbines
SiWEC	Simulation of Wind Energy Converters

SNiP	Stroitel'nye Normy i Pravila
	(in English: Construction Codes and Regulations)
SPH	smoothed particle hydrodynamics
STRICE	Measurements on Structures in Ice
TÜV	Technischer Überwachungsverein
	(in English: Technical Inspection Association)
TP	transition piece
TS	technical specification
TUHH	Technische Universität Hamburg
	(in English: Hamburg University of Technology)
UD	user-defined
UNIS	University Centre in Svalbard
VANILLA	Variation of contact Area model for Numerical Ice Load Level Analyses
VDE	Verband Deutscher Elektrotechniker
	(in English: German Electrical Engineering Association)
VSN	Vedomstvennye Stroitel'nye Normy
	(in English: Industrial Construction Standards)
VTS	Vestas Turbine Simulator
VTT	Teknologian tutkimuskeskus VTT
	(in English: VTT Technical Research Centre of Finland)
WADAM	Wave Analysis by Diffraction and Morison
WAMIT	WaveAnalysisMIT
WTM	wind turbine manufacturer

Chapter 1

Introduction

1.1 Background and research motivation

Offshore wind energy is one of the most promising and rapidly developing technologies in the field of renewable energy in Europe and worldwide (Ohlenforst et al., 2019). There is a high potential for deployment of OWTs in north, cold climate regions. In northern Europe, the Baltic Sea is particularly interesting for installation of OWTs mainly due to the excellent wind conditions[1], relatively shallow waters, and low penetration of wind energy sector in this region. The estimated techno-economic resource potential[2] for offshore wind deployment is around 200 GW according to the Baltic Sea Region Energy Co-operation (2012, p. 22) report.

Twenty offshore wind farms are operating in the Baltic Sea as of June 2020 — nine of them belong to Denmark, five to Germany, four to Sweden, and two to Finland. Figure 1.1 shows their locations and names. The total power output of these wind farms is around 2 GW. The expected output of the offshore wind power installed in the Baltic Sea is estimated to around 9 GW by 2030, which is more than four times the current value, as reported by Nghiem and Pineda (2017, p. 29). Other Baltic region countries are also actively developing offshore wind projects. The rapid development of the Polish offshore wind is expected in the upcoming years, with at least 2.5 GW of installed power by 2030. Estonia, Latvia, and Lithuania are also considering offshore wind in their energy supply portfolio.

Support structures for OWTs are designed and certified site-specific based on the calculated load effects. These load effects originate from static, cyclic, stochastic, and transient loads from the met-ocean environment and rotating components of the wind turbine. The met-ocean environment of the Baltic Sea accounts for variable wind and marine conditions. Sea ice is part of marine conditions, which among others, should be included in the design process of OWTs support structures (IEC, 2019b).

[1] Excellent wind conditions when compared to the vast majority of onshore locations. However, when compared to the North Sea, the wind conditions in the Baltic Sea are actually worse (Geyer et al., 2015).

[2] The techno-economic potential accounts for aspects, such as grid infrastructure availability, met-ocean conditions, seabed conditions, spatial constraints, and site accessibility.

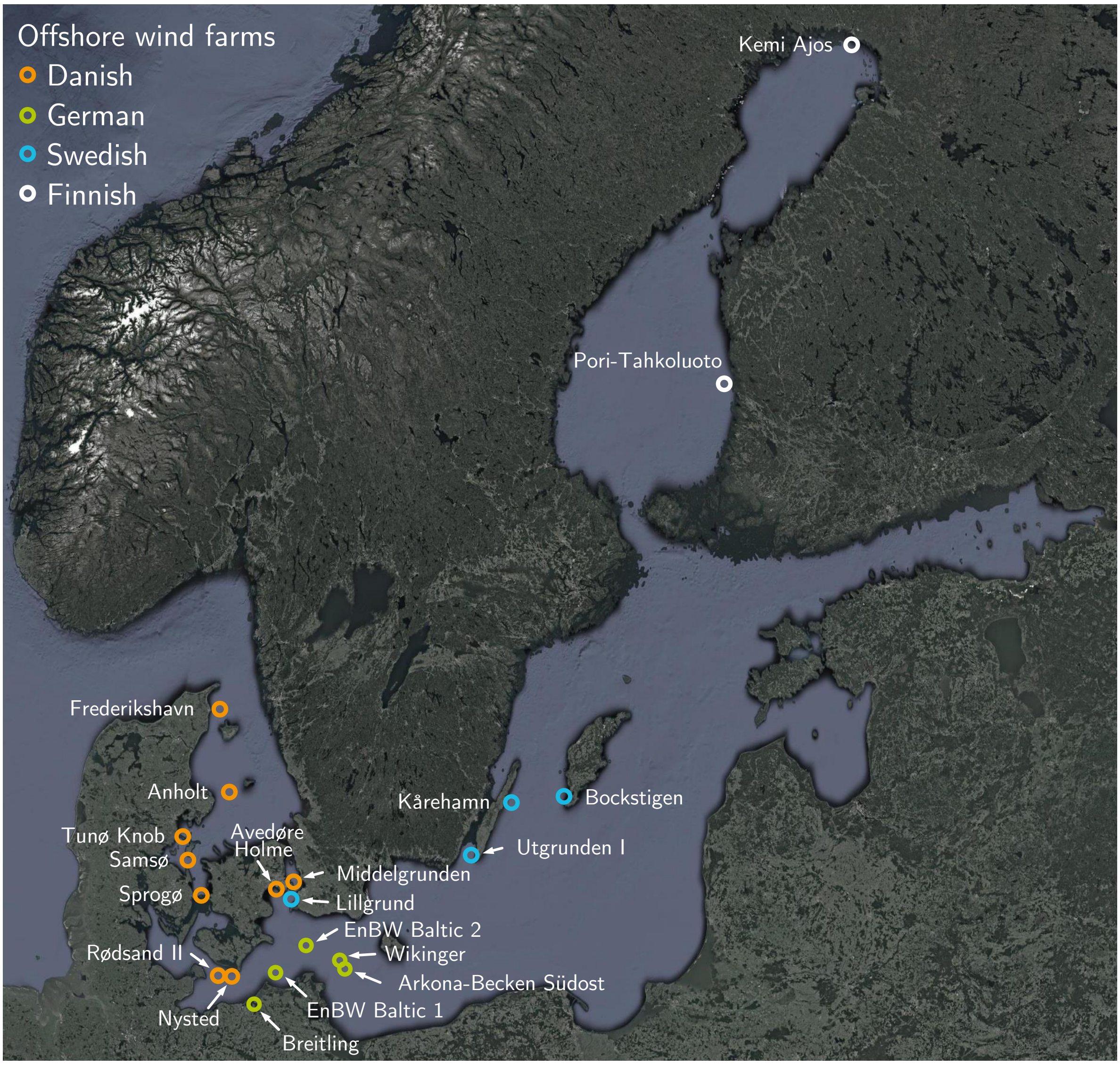

Figure 1.1: Operating offshore wind farms in the Baltic Sea as of June 2020—the majority of them is located less than 10 km from the shore. Danish offshore wind farms marked with orange circles, German with green, Swedish with blue, and Finnish with white. Figure adapted from Google Earth (2020a).

Development of the majority of the wind farms in the Baltic Sea requires consideration of sea ice. Due to its relatively high probability of occurrence, sea ice may affect fatigue and ultimate loads of OWTs. The extent of sea ice dramatically varies depending on the latitude and season severity. During heavy winters the coastal area of the entire Baltic Sea may be covered by different sea ice formations such as landfast ice[3] and ice floes[4], whereas in mild winters mostly the Gulf of Bothnia

[3]Sea ice that is attached to the coastline.
[4]Flat pieces of floating ice with dimensions of 20 m up to more than 10 km across.

is affected. Figure 1.2 shows the probability of sea ice occurrence in the southern Baltic Sea, where the majority of the offshore wind farms are located and will also be built in the future.

The sea ice probability reaches 30% in the Danish straits — Kattegat, Øresund, Great Belt, and Little Belt — which means that sea ice might be present there roughly every third year. The German coastal zone may be affected by sea ice every three to nine years, depending on the distance from the coast[5]. Similar probabilities are observed at the southern coast of Sweden at the Arkona Basin and the Bornholm Basin. The Polish coastline has the lowest probability of sea ice occurrence, which varies between three to more than ten years, at the sites in the Eastern Gotland Basin located between 20 km and 70 km from the shore. At those sites, the majority of the Polish offshore wind farms will be built.

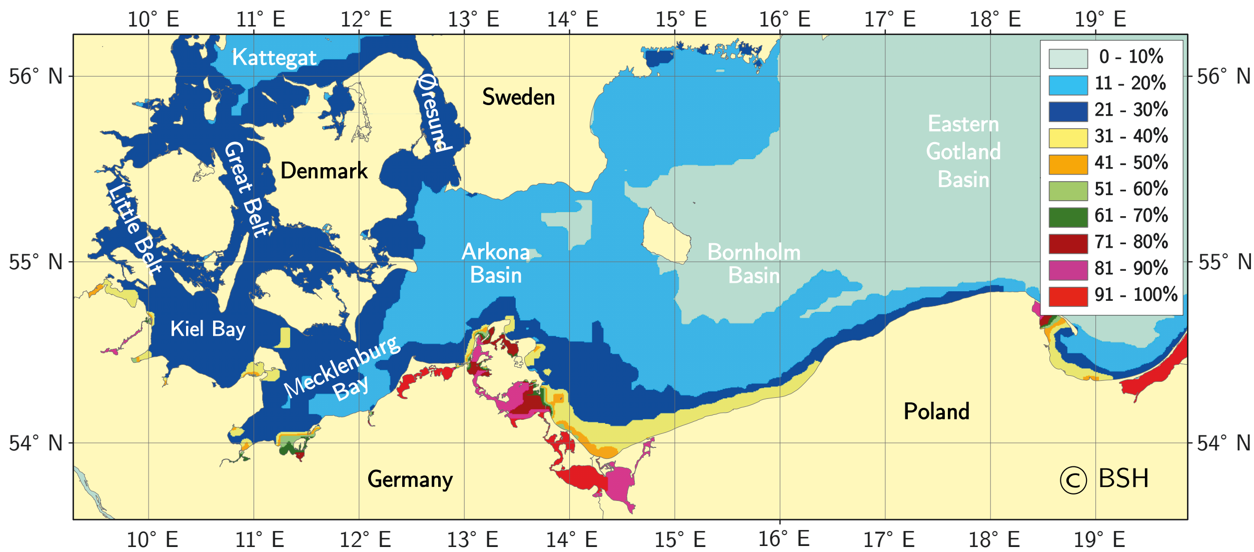

Figure 1.2: Probability of sea ice occurrence in the southern Baltic Sea between 1961 and 2010. Each degree of latitude on the map is around 111 km apart. Figure adapted from Schmelzer et al. (2012, p. 8) with permission from BSH.

Sea ice is an important, but still not well-examined, source of loading for all offshore structures. A complicated ice mechanics influenced by a plethora of factors brings a severe uncertainty in the assessment of sea ice loads imposed on OWT support structures. Nowadays, such uncertainty is mitigated by a conservative design approach. However, overestimated safety factors yield to not cost-effective designs of support structures. Additionally, methods for sea ice load analysis proposed in standards and guidelines are not always suitable to the unique characteristic of highly dynamic OWTs (cf. Section 2.4). For example, a dynamic sea ice action on the support structure may induce vibration of an entire OWT, including its machinery and blades; and therefore increase their fatigue loading. Also, relatively vague guidance and recommendations from the certification

[5]A detailed study of different sea ice formations and their occurrence probabilities at the German coastline was performed by the Hamburg Ship Model Basin (HSVA) within the BReaking the ICE (BRICE) project. More information on this topic can be found in Popko et al. (2015, pp. 20–47).

bodies, who are often not specialized in the sea ice topic, do not help for confident evaluation of sea ice load effects on OWTs.

Due to global warming, the reduction of the sea ice extent in the Baltic Sea will proceed in the 21st century[6], which is indicated by multiple simulation models (Haapala et al., 2001; Luomaranta et al., 2014; Höglund et al., 2017). Nevertheless, sea ice will not disappear entirely — it will instead become thinner and more mobile — and therefore will still be considered as an important source of loading for offshore structures, including OWTs. Furthermore, the offshore sites, where sea ice was too thick for the OWT deployment in the past, may become economically feasible for OWTs in the future once the ice cover becomes thinner.

There is a dire need in the industry for a more confident evaluation of sea ice loads imposed on OWT support structures and further optimization of these structures. However, all these cannot be performed with OWT simulation tools that are currently available as they do not account for the coupling between sea ice and the OWT. Several advanced sea ice models have been developed in recent years. The applicability of these models to OWT has to be evaluated. Some of these models need to be coupled with OWT simulation tools. Their accuracy has to be verified and validated.

The following points summarize research motivation for this dissertation:

- The installed wind power in the Baltic Sea will increase more than four times from 2020 to 2030. This means that many new OWTs will have to be designed and erected in this region.
- Support structures of OWTs are certified site-specific, which requires consideration of local met-ocean conditions — including sea ice — in their design process.
- Sea ice may affect fatigue and ultimate loads of OWTs due to its relatively high probability of occurrence in the coastal areas of the Baltic Sea where offshore wind farms are built.
- Current standards, guidelines, and certification bodies provide vague recommendations on how to address the influence of sea ice loads on the global OWT dynamics.
- Impact of sea ice loads on the OWT dynamics is not well studied.

1.2 Research objectives and methodology

A proper understanding of sea ice impact on the global dynamics of OWTs is necessary within the offshore wind research community, industry, and certification authorities. So far, they all had to rely on the ice experts, whose methods for ice loads calculation were not fully transparent and not always compatible with the design and certification methodologies for OWTs.

[6] A comprehensive assessment of climate change within the Baltic Sea can be found in a book authored by The BACC II Author Team (2015).

This dissertation extends the current knowledge by including new aspects that were not covered before. The main goals reached in this work are:

- To investigate simple approaches for sea ice-structure interaction and to check whether they might be suitable for OWT analysis.
  - To validate uncoupled simulation of ice loading (superposition) against the full-scale measurements.
  - To validate a simple phenomenological ice model from Määttänen (1998) coupled with a single degree of freedom (sDOF) structure in Modelica® Library for Wind Turbines (MoLWiT)[7] against ice tank experiments from HSVA.
- To fully integrate the Hendrikse and Metrikine (2015, 2016) ice model in MoLWiT.
- To cross-verify coupling of this ice model by extending the simulation capabilities of its source code to multimodal multiple degrees of freedom (mDOF) structures and comparing the simulation results with the results from fully-integrated simulations in MoLWiT.
- To set up an OWT numerical model with a support structure that is used in the most recent, commercial projects where Ramboll Wind is involved. This also accounts for the real met-ocean condition data.
- To analyze the impact of sea ice loads on the global dynamics of OWTs. Such impact is barely studied and known. This includes a detailed investigation of ice-OWT interaction at three distinct design situations (idling, power production below the rated wind speed, and power production above the rated wind speed) and multiple ice velocities, corresponding to different ice-structure interaction regions.

1.2.1 Research limitations

Unfortunately, there has been neither full-scale nor scale test data of the operating OWT under the sea ice excitation available for the investigation. Määttänen and Vähätaini (2013) performed some measurements of structural strains induced by sea ice loading on a monopile support structure with a concrete block atop. This structure was supposed to mimic an idling OWT. However, these measurements are not available in the public domain, and they do not give any picture concerning the dynamics of an operating OWT where coupling between the rotor and aerodynamic damping plays an important role in the mitigation of load effects.

[7] MoLWiT (formerly called OneWind and OnWind) is the aero-hydro-servo-elastic tool for OWT simulation developed at IWES (Strobel et al., 2011, 2012; Wihlfahrt et al., 2015). The overview of its simulation capabilities is available in Table 2.1. MoLWiT is based on the Modelica® language, which is a non-proprietary, object-oriented, equation based language for modeling complex physical systems (Modelica Association, 2017). MoLWiT utilizes Dymola® as a simulation environment. Dymola® is a commercial modeling and simulation environment developed by Dassault Systèmes. For this work Dymola® 2020 was used.

However, the basic principles of structural dynamics, also applicable to OWT support structures, can be studied based on the measurements from the Norströmsgrund lighthouse. Its dynamic behavior and ice loading time histories are well documented and were available within the BRICE project. Therefore, the Norströmsgrund lighthouse was used as a full-scale reference structure in Chapter 3.

Influence of sea ice loads on the OWT dynamics could only be analyzed by simulations in Chapter 5. Validation of a coupled simulation of an OWT with sea ice against full-scale measurements is not possible as measurements of ice forces on OWT support structures do not exist. Furthermore, significant measurement uncertainties would make such validation extremely challenging.

1.3 Contribution of dissertation to state-of-the-art

The main contributions of this dissertation can be summarized as follows:

- A simple phenomenological Määttänen (1998) ice model implemented in an aero-hydro-servo-elastic tool has been validated against ice tank tests showing that with careful calibration satisfactory results can be achieved.
- An advanced phenomenological ice model from Hendrikse and Metrikine (2015, 2016) has been fully integrated into an aero-hydro-servo-elastic simulation tool for the first time.
- The implementation of the Hendrikse ice model in MoLWiT has been cross-verified against its original source code, which simulation capabilities have been extended by the author to accommodate modally reduced mDOF structures. The extended source code of ice model has been coupled by the author with his newly developed FEM code for modeling mDOF structures.
- The newly developed finite element method (FEM) code for modeling mDOF structures is publicly available within this dissertation and can be easily coupled by other researchers with the publicly available version of the Hendrikse ice model source code (Hendrikse, 2019).
- The results of fully-integrated simulations of ice-OWT in MoLWiT show that the most severe fatigue loads occur during the intermittent crushing of ice, not during the frequency lock-in events as it has been stipulated over the years.
- The work-energy flow between ice and the structure during different operational regions of an OWT has been analyzed for the first time. It has been shown that depending on the ice velocity different eigenmodes can become dominant source of vibration.
- The contribution of different structural eigenmodes to short-term DELs at different ice-structure interaction regions has been investigated.

1.4 Dissertation outline

The dissertation has been organized in the following form:

The already presented **Chapter 1** describes the background and research motivation for this dissertation. The development plans for the new offshore wind farms in the Baltic Sea are discussed. It is also explained why sea ice is an important, but still not well-examined source of loading for OWTs in the Baltic Sea. Research objectives, methodology, and limitations of this dissertation are described. Also, the dissertation outline is delineated.

This is followed by **Chapter 2**, which provides an overview of the state-of-the-art. The principle of the coupled simulation and its importance in the design of OWTs is explained. An overview of modern aero-hydro-servo-elastic simulation tools for OWTs and their simulation capabilities is given. The mid-fidelity engineering models utilized in those tools are reviewed in Section 2.1. The current industrial approach in addressing sea ice loads in dynamic analysis of OWTs is presented in Section 2.2. Also, the drawbacks and limitations of this approach are explained. Section 2.3 defines ice-structure interaction modes, which are important for the dynamic analysis of OWTs. Furthermore, an overview of the standards for certification of OWTs with a focus on their provisions for sea ice loads is presented in Section 2.4. Some of the existing sea ice models are listed in Section 2.5. Their applicability for analysis of OWTs is discussed. The overview of multiple research projects focused on ice-structure interaction from the past ten years is provided in Section 2.6.

Chapter 3 presents the validation results of ice-structure interaction simulations against the full-scale measurements and scaled ice tank tests. Section 3.1 compares dynamic response of the full-scale Norströmsgrund lighthouse and its numerical implementation in Abaqus. The lighthouse dynamic response is analyzed based on the measurements from accelerometers located at two distinct heights. These measurements are correlated with ice loading measurements from the load panels installed at the mean sea level (MSL). The eigenfrequencies of the numerical model are tuned to correspond with the structural response of the full-scale lighthouse. Afterward, predefined time histories of the measured ice loading are directly applied to the numerical model at the areas where load panels are installed in the full-scale structure. Section 3.2 describes a validation procedure of the Määttänen-Blenkarn phenomenological ice model for ice-structure interaction against scaled ice tank tests. The tests were performed by HSVA, where a simplified scaled model of the Norströmsgrund lighthouse was built. A numerical representation of the HSVA structure is implemented in MoLWiT — an in-house aero-hydro-servo-elastic simulation tool for OWTs. A complicated geometry of the structure is represented in the numerical model by an sDOF oscillator consisting of a rigid beam, a spring, and a damper. This implementation is validated with a set of load cases of increasing complexity. The original representation of the Määttänen-Blenkarn ice model could not be directly used for the validation against ice tank tests, where ice properties were scaled. The reason is that the relationship between stress and stress rate in the original representation of the ice model was derived from the full-scale measurements. A new relationship between stress and stress rate for scaled ice has to be established. After calibrating the ice model, the results of HSVA experiments are compared against results of the numerical simulations performed in the framework of this dissertation.

Chapter 4 describes the implementation of the state-of-the-art phenomenological ice model from Hendrikse and Metrikine (2015, 2016) in the in-house simulation tool MoLWiT and verification of this implementation against the source code in MATLAB®. The verification is divided into two phases. In the first phase, the ice interaction with a simple sDOF oscillator is analyzed in Section 4.1. In the second phase, the MATLAB® source code of the Hendrikse ice model is extended to cope with support structures consisting of mDOF, as described in Section 4.3. The extended source code is used in Section 4.4 for the cross-verification of the simulation results from MoLWiT, where a full-scale monopile support structure designed by Ramboll is modeled. Furthermore, the ice properties that were utilized in the original ice model are derived from the scaled ice tests. It is necessary to retune those properties for the full-scale application in the southern Baltic Sea, which is done in Section 4.2.

Chapter 5 shows results of the fully-integrated simulation of OWT with the Hendrikse ice model implemented in MoLWiT. Section 5.1 presents the advantages of the fully-integrated simulation of the ice-OWT interaction and compares this approach with the coupled simulation where the ice model is encapsulated in the external dynamic-link library (DLL). In Section 5.2, multiple load cases (LCs) are defined for the analysis of ice impact on the global dynamics of the OWT. The analysis is performed at three distinct design situations — idling below the cut-in wind speed, power production below and above the rated wind speed. At each design situation, the influence of multiple ice velocities on the OWT dynamics is investigated. The simulated range of ice velocities covers three main ice-structure interaction modes — intermittent ice crushing, frequency lock-in, and continuous brittle crushing — which are defined in Section 2.3. Section 5.3 quantifies the impact of ice on the global dynamics of the OWT. The quantification is done in terms of DELs and power spectral densities (PSDs). Section 5.4 presents the results of the work-energy principle. The work-energy transfer between ice and the OWT is analyzed at several design situations, such as idling and power production at different wind speeds. Finally, in Section 5.5, a contribution of different eigenmodes to DELs is investigated at different ice-structure interaction regions by switching off the contribution of a certain eigenmode to the system displacement at MSL but still preserving its contribution to the system stiffness.

Finally, in **Chapter 6** conclusions of this research, recommendations for load analysts, and recommendations for future work are presented.

Chapter 2

State-of-the-art

In this chapter, the state-of-the-art in OWT modeling and simulation is presented. The chapter is divided into seven sections. Section 2.1 explains the principle of the coupled simulation and its importance in the design process of OWTs. It provides an overview of modern, coupled simulation tools for OWTs. The mid-fidelity, engineering-level models utilized in those tools are presented, their simulation capabilities and limitations are briefly discussed. Section 2.2 describes a current industrial approach in addressing sea ice loads in dynamic analysis of OWTs. Drawbacks and limitations of this approach are explained. Section 2.3 defines ice-structure interaction modes, which are important for the dynamic analysis of OWTs. Section 2.4 presents an overview of the standards for certification of OWTs with focus on their provisions for sea ice loads. Section 2.5 gives an overview of sea ice models of different complexity. The drawbacks of these models and their potential applicability to dynamic analysis of OWTs are discussed. Section 2.6 presents an overview of recent, applied research projects, which are focused on the ice-structure interaction. The content of some of these projects is also relevant for dynamic analysis of OWTs. Section 2.7 summarizes the state-of-the-art chapter.

2.1 Coupled simulation tools for offshore wind turbines

The analysis of OWTs relies on time-domain based, coupled aero-hydro-servo-elastic simulation tools.[8] These coupled tools account for the interaction of various environmental conditions and the structural assembly of the OWT, including its control system, as shown in Figure 2.1. This includes various models describing aerodynamics (aero), hydrodynamics (hydro), control systems (servo), and structural dynamics of a wind turbine and its support structure (elastic). The integrated approach is required by certification standards.[9] Only this approach can provide an accurate prediction of the OWT dynamic response and the extreme and fatigue load effects. Dynamic interaction between an OWT and external loads should not be disregarded as it may

[8] Different naming nomenclature is used across the literature. The following names are often used interchangeably: aero-hydro-servo-elastic simulation tools, aero-elastic tools, coupled simulation tools, OWT simulation tools, integrated design tools.

[9] See IEC (2019b, p. 21) and DNV GL (2016, p. 51).

result in a considerable loss of accuracy. For example, the aerodynamic damping resulting from an aeroelastic interaction of the spinning rotor and wind can significantly reduce hydrodynamic load effects on a monopile support structure. This phenomenon can only be captured correctly in the coupled analysis, as shown by Kühn (2001, p. 127). Also, the interaction between different OWT components can only be reproduced correctly in the coupled simulation environment — for example, local vibrations of jacket braces, which can be induced by higher harmonics of the spinning rotor, as shown by Böker (2010); Kjetså and Saaghus (2010); Schafhirt et al. (2014); Popko et al. (2013); Popko, Georgiadou, et al. (2016).

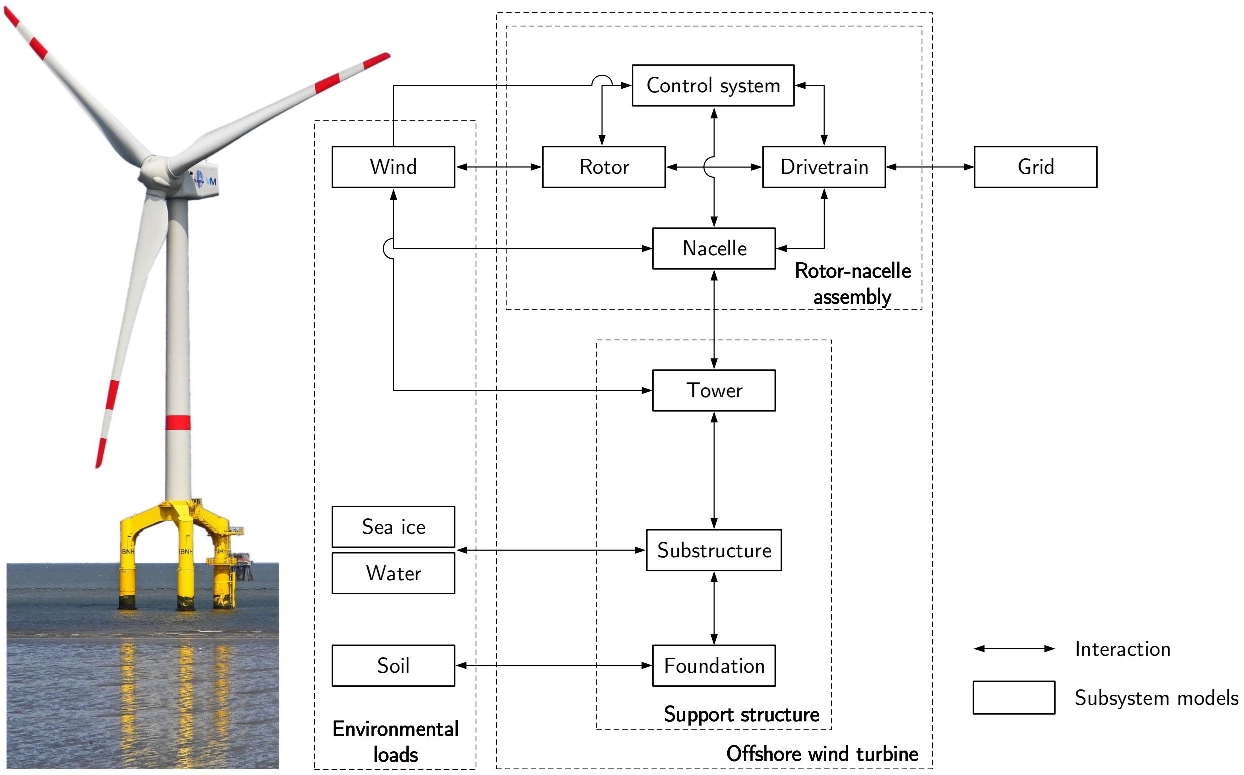

Figure 2.1: Generic scheme of the aero-hydro-servo-elastic tool for coupled simulation of bottom-fixed OWTs. Interactions of different subsystems are indicated with arrows. On the left side modified picture of OWT from Westendarp (2016).

The design process of an OWT requires prediction of multiple fatigue and ultimate loading scenarios, which an OWT may encounter during its lifetime. These loading scenarios are conveniently represented in terms of the design load cases (DLCs), which account for different combinations of met-ocean loads and operating states of the wind turbine[10]. A typical load envelope accounts for thousands of individual load cases resulting in a high simulation effort.

[10]A typical set of DLCs for full-load envelope simulation can be found in e.g., IEC (2019b, pp. 45–61) or DNV GL (2016, pp. 66–68).

For this reason, computationally efficient though sufficiently accurate[11] engineering-level models are necessary. They are often based on mid-fidelity empirical[12], semi-empirical[13], phenomenological[14], and analytical[15] models. High-fidelity[16] models, for example, those used in conjunction with the computational fluid dynamics (CFD) method, are too complex and computationally demanding for simulation of the full-load envelope, which an OWT may encounter during its lifetime. However, these high-fidelity models are often used for detailed analysis of wake effects, vortex-induced vibrations, optimization of blade design, etc. The high-fidelity models are also used to enable a better understanding of insufficiencies of the mid-fidelity, engineering-level models in specific application areas — for example, the applicability of engineering-level hydrodynamic models for predicting the nonlinear hydrodynamic loading.

Table 2.1 shows an overview of the simulation capabilities of some of the modern, mid-fidelity aero-hydro-servo-elastic tools. The table is focused on the capabilities that are commonly used for simulation of the bottom-fixed OWTs. Aspects important for floating OWTs are not discussed herein. Therefore, this overview is not fully comprehensive and should rather be considered as informative. It should be pointed out that different tools can use different formulations of mathematical theories and various numerical approaches for the implementation of those theories. Such differences are not discriminated herein.

2.1.1 Development paths, verification and validation needs

The aero-hydro-servo-elastic tools have been developed with different historical inheritances and focus. Five main branches of their development can be distinguished according to Vorpahl and Popko (2014), although the boundaries between these branches might often be ambiguous and permeate each other.

Tools with onshore wind origin (e.g., Bladed, FAST, Flex5, HAWC2)
: These are the well-established simulation tools, which derive from the aeronautic know-how. Many of them have been extended to address the offshore environment, including offshore bottom-fixed and floating support structures. Some of these simulation tools offer a streamlined process for the full-load envelope calculation. They have been utilized by multiple

[11] In this context, "sufficiently accurate" means that the global dynamics of an OWT and external loading conditions are reproduced to such extent that the simulated load effects (including safety factors) are adequate for a reliable design of an OWT according to certification standards, e.g., IEC (2019b).

[12] Empirical models are based on experimental results and they are not supported by fundamental scientific laws.

[13] Semi-empirical models combine measurements and theoretical principles, which are based on fundamental scientific laws.

[14] Phenomenological models are mathematical descriptions of empirical relationships, which are to some extent consistent with theory, but not derived from it.

[15] Analytical models rely on fundamental laws of physics, such as conservation of mass and energy, Newton's laws of motion, Newton's law of universal gravitation.

[16] The high-fidelity term refers to more complex models, usually represented with a larger number of differential equations. Those models may account for more precise representation of nonlinearities, reduced approximations, and some special effects.

Table 2.1: Overview of simulation capabilities of some of the modern aero-hydro-servo-elastic tools. Only capabilities that are commonly used in simulation of bottom-fixed OWTs are listed.

Tool (Developer)	Structural	Aerodynamics	Hydrodynamics	Soil-Foundation	Control
3DFloat (Institute for Energy Technology)	**Structural dynamics:** BEM **Beam model:** Support Structure: Euler-Bernoulli; Blade: airfoil elements with offsets between shear, aerodynamic, and mass centers and elastic axis **Damping model:** Stiffness and mass proportional Rayleigh	**Basic aerodynamics:** BEM with corrections (Glauert correction, Prandtl tip and root losses, skew inflow) **Dynamic wake model:** Øye **Dynamic stall model:** N/A **Wind field grid format:** Rectangular	**Regular linear wave model:** Airy^{str} **Regular nonlinear wave model:** Stream **Irregular wave spectrum:** JONSWAP/PM, EU **Hydro model:** ME, ME + MF, 1st order PF (Interface to WAMIT, WADAM, NEMOH)	Clamped at seabed; Linear springs; Nonlinear lateral p-y curves; Linear stiffness, mass, and damping matrices; DLL	DLL, UD
Ashes (Simis AS)	**Structural dynamics:** FEM **Beam model:** Euler-Bernoulli **Damping model:** Stiffness proportional Rayleigh	**Basic aerodynamics:** BEM with corrections (Glauert correction, Prandtl tip and root losses, skew inflow) **Dynamic wake model:** Øye **Dynamic stall model:** Øye **Wind field grid format:** Rectangular	**Regular linear wave model:** Airy^{str} **Regular nonlinear wave model:** N/A **Irregular wave spectrum:** JONSWAP/PM, UD **Hydro model:** ME, ME + MF	Clamped at seabed; Apparent fixity; Linear translational and rotational springs; Nonlinear lateral p-y curves	DLL, UD
Bladed V4.9 (DNV GL)	**Structural dynamics:** MBS + flexible modally reduced bodies **Beam model:** Timoshenko, superelement for support structure **Damping model:** Modal damping	**Basic aerodynamics:** BEM with corrections (Glauert correction, Prandtl tip and root losses, skew inflow), GDW **Dynamic wake model:** Øye, Pitt-Peters **Dynamic stall model:** Beddoes-Leishman, Øye **Wind field grid format:** Rectangular	**Regular linear wave model:** Airy^{str} **Regular nonlinear wave model:** Stream **Irregular wave spectrum:** JONSWAP/PM, UD **Hydro model:** ME, ME + MF, 1st and 2nd order PF	Clamped at seabed; Apparent fixity; Linear translational and rotational springs; Nonlinear lateral p-y curves; Linear stiffness, mass, and damping matrices	DLL, UD
DeepLines Wind V5R4 (Principia)	**Structural dynamics:** FEM **Beam model:** Mindlin-Reissner **Damping model:** Stiffness proportional Rayleigh	**Basic aerodynamics:** BEM with corrections (Glauert correction, Prandtl tip and root losses, skew inflow, relaxation of induction factors) **Dynamic wake model:** Øye **Dynamic stall model:** Øye, Risø **Wind field grid format:** Rectangular	**Regular linear wave model:** Airy^{str} **Regular nonlinear wave model:** Stream **Irregular wave spectrum:** JONSWAP/PM, Ochi-Hubble, UD **Hydro model:** ME, 1st order PF	Clamped at seabed; Apparent fixity; Nonlinear lateral p-y and axial t-z curves	DLL, UD
DIEGO (Electricité de France – Recherche et Développement)	**Structural dynamics:** FEM **Beam model:** Euler-Bernoulli **Damping model:** Stiffness and mass proportional Rayleigh	**Basic aerodynamics:** BEM with corrections (Glauert correction, Prandtl tip and root losses), GDW **Dynamic wake model:** Pitt-Peters **Dynamic stall model:** Beddoes-Leishman, Risø **Wind field grid format:** Rectangular	**Regular linear wave model:** Airy^{str} **Regular nonlinear wave model:** Stokes **Irregular wave spectrum:** JONSWAP/PM, Ochi-Hubble **Hydro model:** ME, ME + MF, PF (Interface to NEMOH)	Clamped at seabed; Apparent fixity; Linear stiffness, mass, and damping matrices	DLL
Flex5-Poseidon (Stig Øye, Leibniz University Hannover, University of Stuttgart – Stuttgart Wind Energy)	**Structural dynamics:** FEM/Modal **Beam model:** Euler-Bernoulli (Poseidon) **Damping model:** Modal damping (Flex5), stiffness and mass proportional Rayleigh damping (Poseidon)	**Basic aerodynamics:** BEM with corrections (Glauert correction, Prandtl tip and root losses, skew inflow), GDW **Dynamic wake model:** Øye **Dynamic stall model:** Øye **Wind field grid format:** Polar	**Regular linear wave model:** Airy^{str} **Regular nonlinear wave model:** Stream **Irregular wave spectrum:** JONSWAP/PM, UD **Hydro model:** ME, Interface to WaveLoads	Clamped at seabed; Apparent fixity	DLL, UD
FloaWDyn (Polytechnic University of Catalonia)	**Structural dynamics:** FEM (co-rotational formulation) **Beam model:** Euler-Bernoulli **Damping model:** Support structure: stiffness and mass proportional Rayleigh	**Basic aerodynamics:** (AeroDyn) BEM with corrections (Glauert correction, Prandtl tip and root losses), GDW **Dynamic wake model:** Peters-He **Dynamic stall model:** Beddoes-Leishman **Wind field grid format:** Single point wind at hub height	**Regular linear wave model:** Airy^{str} **Regular nonlinear wave model:** Stokes **Irregular wave spectrum:** JONSWAP/PM **Hydro model:** ME	Clamped at seabed; Apparent fixity; Linear springs; Nonlinear lateral p-y curves	DLL, UD
HAWC2 (Technical University of Denmark – Department of Wind Energy)	**Structural dynamics:** MBS/FEM **Beam model:** Timoshenko, anisotropic beam for blades **Damping model:** Support structure and blades: stiffness and mass proportional Rayleigh	**Basic aerodynamics:** BEM with corrections (Madsen-Larsen correction for shear and dynamic inflow, Glauert-Coleman skew inflow), GDW **Dynamic wake model:** Øye **Dynamic stall model:** Øye, Beddoes-Leishman **Wind field grid format:** Rectangular	**Regular linear wave model:** Airy^{str} **Regular nonlinear wave model:** Stream **Irregular wave spectrum:** JONSWAP/PM, UD **Hydro model:** ME, 1st order PF, 2nd order PF (coupling with WAMIT)	Clamped at seabed; Apparent fixity; Nonlinear lateral p-y, axial t-z, and rotation θ-τ curves	DLL, SM

Airy^{str} – linear Airy wave theory with Wheeler stretching
BEM – blade element momentum
DLL – dynamic-link library
FEM – finite element method
FVW – free vortex wake (various formulations)
GDW – generalized dynamic wake (various formulations)
JONSWAP – deep-water wave spectrum
MBS – multibody simulation
ME – semi-empirical Morison's equation
MF – MacCamy-Fuchs linear diffraction theory
N/A – not available
PF – potential flow using panel method (various formulations)
PM – Pierson-Moskowitz spectrum
SM – interface to MATLAB® and Simulink®
Stokes – nonlinear Stokes wave
Stream – Dean's Stream function
UD – user-defined
WAMIT – WaveAnalysisMIT
WADAM – Wave Analysis by Diffraction and Morison

Table 2.1: (Continuation) Overview of simulation capabilities of some of the modern aero-hydro-servo-elastic tools. Only capabilities that are commonly used in simulation of bottom-fixed OWTs are listed.

Tool (Developer)	Structural	Aerodynamics	Hydrodynamics	Soil-Foundation	Control
hGAST (National Technical University of Athens)	**Structural dynamics:** MBS + FEM **Beam model:** Timoshenko + Superelement **Damping model:** Modal damping	**Basic aerodynamics:** BEM with corrections (Glauert correction, Prandtl tip and root losses, skew inflow, relaxation of induction factors), FVW **Dynamic wake model:** Øye, Pitt-Peters, Peters-He **Dynamic stall model:** Beddoes-Leishman, Tran-Petot **Wind field grid format:** Rectangular, polar	**Regular linear wave model:** N/A **Regular nonlinear wave model:** Stream **Irregular wave spectrum:** JONSWAP/PM **Hydro model:** ME, 1st and 2nd order PF	Clamped at seabed; Linear springs; Linear stiffness, mass, and damping matrices	DLL
NK-UTWind (ClassNK, University of Tokyo)	**Structural dynamics:** Support structure: FEM; Turbine: modeled in FAST v8 **Beam model:** Euler-Bernoulli **Damping model:** Support structure: stiffness proportional Rayleigh; Turbine: modal damping (in FAST v8)	**Basic aerodynamics:** BEM with corrections (Glauert correction, Prandtl tip and root losses), GDW **Dynamic wake model:** Pitt-Peters **Dynamic stall model:** Beddoes-Leishman **Wind field grid format:** Rectangular	**Regular linear wave model:** Airy^{str} **Regular nonlinear wave model:** N/A **Irregular wave spectrum:** JONSWAP/PM **Hydro model:** ME, PF (under development)	Nonlinear stiffness curves	DLL
MoLWiT (Fraunhofer Institute for Wind Energy Systems IWES)	**Structural dynamics:** Support structure: FEM; Blades: MBS + modal reduced bodies **Beam model:** Timoshenko, anisotropic beam **Damping model:** Stiffness and mass proportional Rayleigh, modal damping	**Basic aerodynamics:** BEM with corrections (Glauert correction, Prandtl tip and root losses, skew inflow, relaxation of induction factors), GDW **Dynamic wake model:** Øye **Dynamic stall model:** Øye, Beddoes-Leishman **Wind field grid format:** Rectangular	**Regular linear wave model:** Airy^{str} **Regular nonlinear wave model:** Stokes **Irregular wave spectrum:** JONSWAP/PM, UD **Hydro model:** ME, ME + MF	Clamped at seabed; Apparent fixity; Linear stiffness, mass, and damping matrices	DLL, SM
OpenFAST v2.1.0, FAST v8 (National Renewable Energy Laboratory)	**Structural dynamics:** Support structure: FEM + Craig-Bampton; Turbine: FEM preprocessor + Modal/MBS; Blades: Modal reduced **Beam model:** Substructure and blades: Timoshenko; Turbine: Euler-Bernoulli **Damping model:** Modal damping	**Basic aerodynamics:** BEM with corrections (Glauert correction, Prandtl tip and root losses), GDW **Dynamic wake model:** Pitt-Peters **Dynamic stall model:** Beddoes-Leishman **Wind field grid format:** Rectangular	**Regular linear wave model:** Airy^{str} **Regular nonlinear wave model:** Stokes **Irregular wave spectrum:** JONSWAP/PM, UD **Hydro models:** ME, 1st and 2nd order PF	Clamped at seabed; Apparent fixity; Linear springs; Nonlinear springs; Linear stiffness and damping matrices	DLL, UD, SM
SAMCEF Wind Turbines 18.0 (Siemens Industry Software)	**Structural dynamics:** FEM/MBS/Modal (Craig-Bampton) **Beam model:** Timoshenko **Damping model:** Support structure: stiffness proportional Rayleigh; Blades: modal damping	**Basic aerodynamics:** BEM with corrections (Glauert correction, Prandtl tip and root losses, skew inflow, relaxation of induction factors), GDW **Dynamic wake model:** Øye **Dynamic stall model:** Beddoes-Leishman **Wind field grid format:** Rectangular, polar	**Regular linear wave model:** Airy^{str} **Regular nonlinear wave model:** Stokes, Stream **Irregular wave spectrum:** JONSWAP/PM, UD **Hydro model:** ME, ME + MF	Clamped at seabed; Apparent fixity; Linear springs; Nonlinear lateral p-y, axial t-z, and rotation θ-τ curves; Linear stiffness, mass, and damping matrices; Nonlinear stiffness and damping matrices	DLL, UD, SM
SIMA (Norwegian University of Science and Technology)	**Structural dynamics:** FEM **Beam model:** Euler-Bernoulli with shear correction **Damping model:** Stiffness and mass proportional Rayleigh	**Basic aerodynamics:** BEM with corrections (Glauert correction, Prandtl tip and root losses, skew inflow correction) **Dynamic wake model:** Øye **Dynamic stall model:** Øye **Wind field grid format:** Rectangular	**Regular linear wave model:** Airy^{str} **Regular nonlinear wave model:** Stokes **Irregular wave spectrum:** JONSWAP/PM, Ochi-Hubble **Hydro model:** ME, ME + MF, 1st and 2nd order PF	Clamped at seabed; Apparent fixity; Linear springs at seabed; Nonlinear lateral p-y curves; Macro element	DLL, UD
Simpack (Dassault Systèmes, University of Stuttgart – Stuttgart Wind Energy)	**Structural dynamics:** MBS, linear/nonlinear modal reduced FEM **Beam model:** Euler-Bernoulli, Timoshenko, nonlinear beams, superelement approach **Damping model:** Modal damping, stiffness and mass proportional Rayleigh	**Basic aerodynamics:** (AeroDyn) BEM with corrections (Glauert correction, Prandtl tip and root losses), GDW; (ECN AeroModule) FVW **Dynamic wake model:** Pitt-Peters **Dynamic stall model:** Beddoes-Leishman, Snel **Wind field grid format:** Rectangular, polar	**Regular linear wave model:** Airy^{str} **Regular nonlinear wave model:** N/A **Irregular wave spectrum:** JONSWAP/PM **Hydro model:** ME, ME + MF, PF	Clamped at seabed; Apparent fixity; Linear springs; Nonlinear lateral p-y, axial t-z, and rotation θ-τ curves; Linear stiffness, mass, and damping matrices; UD	DLL, UD, SM
SiWEC (University of Rostock – Chair of Wind Energy Technology, Windrad Engineering GmbH)	**Structural dynamics:** MBS, modal reduced **Beam model:** Euler-Bernoulli, superelement approach **Damping model:** Modal damping	**Basic aerodynamics:** BEM with corrections (Glauert correction, Prandtl tip loss, skew inflow correction, relaxation of induction factors) **Dynamic wake model:** Øye **Dynamic stall model:** Øye, Beddoes-Leishman **Wind field grid format:** Polar	**Regular linear wave model:** Airy^{str} **Regular nonlinear wave model:** Stream function **Irregular wave spectrum:** JONSWAP/PM **Hydro model:** ME, ME + MF	Clamped at seabed; Apparent fixity; Linear stiffness, mass, and damping matrices	DLL, UD

Airy^{str} – linear Airy wave theory with Wheeler stretching
BEM – blade element momentum
DLL – dynamic-link library
FEM – finite element method
FVW – free vortex wake (various formulations)
GDW – generalized dynamic wake (various formulations)
JONSWAP – deep-water wave spectrum
MBS – multibody simulation
ME – semi-empirical Morison's equation
MF – MacCamy-Fuchs linear diffraction theory
N/A – not available
PF – potential flow using panel method (various formulations)
PM – Pierson-Moskowitz spectrum
SM – interface to MATLAB® and Simulink®
Stokes – nonlinear Stokes wave
Stream – Dean's Stream function
UD – user-defined
WAMIT – WaveAnalysisMIT
WADAM – Wave Analysis by Diffraction and Morison

industrial players in many commercial projects. Flex5 has been used by e.g., Suzlon, Senvion (formerly REpower), Nordex, Vestas[17], and Ørsted (formerly DONG Energy); Bladed has been used by e.g., DNV GL, China General Certification Center, Guodian United Power Technology, TÜV Nord, and Saipem; HAWC2 has been used by e.g., Aerodyn, Enercon, Siemens Gamesa Renewable Energy, and Vestas. FAST has been used by e.g., American Bureau of Shipping, Principle Power, Goldwind, and TÜV Nord. FAST is also a popular tool among universities and research institutes due to its open-source code and the modularized framework, which allows for relatively easy coupling with other tools.

Tools with offshore oil and gas origin (e.g., DeepLines Wind, FloaWDyn)
They contain advanced models for hydrodynamics and are extended to accommodate a wind turbine structural model, aeroelastic interaction, and the control system. However, in some cases (e.g., FloaWDyn) the rotor-nacelle assembly (RNA) and aerodynamic models are simplified compared to those, which are implemented in the simulation tools with the onshore origin.

Tools with offshore wind origin (e.g., Ashes, 3DFloat)
They are developed specifically for the analysis of bottom-fixed and floating OWTs. They have similar capabilities as the well-established onshore wind tools and also quite sophisticated hydrodynamic capabilities. It is a relatively fresh branch of tools. They do not have a proven track record in many commercial projects.

General-purpose multibody tools (e.g., SAMCEF Wind Turbines, Simpack)
These simulation tools are adapted to specific simulation needs of OWTs. They offer a possibility for detailed modeling of structural components, such as drivetrain, pitch system, yaw drive, etc. Multibody simulation tools are getting more popular within the large industrial players in recent years. SAMCEF Wind Turbines has been utilized by e.g., GE Renewable Energy (after merging with ALSTOM), Envision Energy, and Siemens Gamesa Renewable Energy; Simpack has been used by e.g., Senvion, Suzlon, and Vestas.

Combination of two different tools (e.g., Bladed-Sesam, Flex5-Poseidon, Flex5-ASAS, FAST-OrcaFlex, FAST-MicroSAS, FAST-NK-UTWind, HAWC2-WAMIT)
The simulation tools of the onshore wind origin that are combined with specialized tools for hydrodynamic analysis or detailed structural analysis. Usually, one tool is open-source and the other one is a proprietary, closed code. Their full integration or co-simulation might not always be possible. Therefore, different workaround methods have to be used, such as superposition (Böker, 2010; Seidel & Kelma, 2012), semi-integrated (Böker, 2010; Seidel et al., 2004) or sequential approach (Böker, 2010; Seidel et al., 2005). This may lead to a limited exchange of information between the tools; and therefore attention is required in the interpretation of the results.

The development of aero-hydro-servo-elastic tools is driven by new OWT concepts (e.g., different types of floating OWTs), new design concepts for OWT subsystems (e.g., very long and flexible

[17] Vestas Turbine Simulator (VTS) is based on Flex5.

blades, direct drives, large diameter monopiles), and environmental challenges at the deployment sites (e.g., sea ice, ice accretion on blades, tsunamis). All these require relevant numerical models, which can adequately represent OWT dynamics and load effects. Correct representation of structural dynamics and load effects is important for the design and certification of OWTs. For these reasons, tools must be continuously verified and validated. Verification is performed by code-to-code comparison, whereas validation is performed by comparing simulated results to measured physical system response data.

In recent years, a gap in the simulation capabilities between aero-hydro-servo-elastic tools of different origins is becoming smaller thanks to international efforts in their verification and validation. The vast majority of the OWT simulation tools, which are used in the industry and the research environment, have been verified and validated in the set of subsequent OCX projects[18] — Offshore Code Comparison, Collaboration (OC3), Continuation (OC4), with Correlation (OC5), and unCertainty (OC6). The projects have helped to identify small and large errors in tools and modeling practices and to identify the limitations of some of the tools. The results of these projects are published in several conference and journal papers, e.g., Vorpahl et al. (2009, 2014); Popko, Vorpahl, et al. (2012); Popko et al. (2014); Popko, Huhn, et al. (2018); Popko et al. (2019); Robertson et al. (2014, 2015, 2016, 2017).

There are also many validation and verification activities performed by individual tool developers, apart from the OCX projects. Multiple conference and journal publications summarizing such activities for specific simulation tools can be found in the public domain.

2.1.2 Aerodynamics

This section presents the most popular empirical, semi-empirical, and analytical aerodynamic models that are used in many OWT simulation tools (see Table 2.1). A comprehensive overview of multiple aerodynamic models used for simulation of wind turbines can be found in M. O. L. Hansen et al. (2006); M. O. L. Hansen and Madsen (2011). Examples of implementations of different models are presented in e.g., Moriarty and Hansen (2005); M. O. L. Hansen (2015).

Modeling of deterministic and stochastic wind fields

A wind field can be modeled as deterministic or stochastic. Deterministic wind fields can include constant wind profile, wind gust, wind direction change, and wind shear — their equations are rather simple and are not discussed herein. They are presented in the IEC standard (IEC, 2019a).

Three methods for stochastic wind field generation are commonly used in the OWT simulation tools — the von Kármán method developed by von Kármán (1948), the Sandia method developed by Veers (1988) using the Kaimal spectrum (Kaimal et al., 1972), and the Mann method developed

[18] Operated under the International Energy Agency (IEA), Wind Tasks 23 and 30.

by Mann (1994, 1998). In these methods, the stochastic processes are first defined in the frequency domain and then transferred to the time domain by the inverse fast Fourier transform (IFFT). The random process in the time domain follows the Gaussian distribution governed by the central limit theorem, where the arithmetic mean has a normal distribution. It should be noted that this is only the approximated representation of the real wind field, which has not been reflected in the statistics of measured atmospheric turbulence.

The first evidence of the non-Gaussian distribution of atmospheric turbulence was revealed in the 1960s within several aerospace research programs, where statistical properties of atmospheric turbulence were measured and analyzed by Frenkiel and Klebanoff (1967) and Reeves (1969). Similar observations were made during analysis of the met-mast measurements in the 1990s and 2000s by e.g., Højstrup et al. (1999); Nielsen et al. (2004); Mücke et al. (2012).

There is no consensus in the research community on too what extent the non-Gaussian distribution of turbulence might impact OWT load effects. On the one hand, some researchers reported an increase of diverse OWT load effects when using different models of non-Gaussian wind fields instead of the models based on the Gaussian distribution (Nielsen et al., 2000; Gontier et al., 2007; Mücke et al., 2011). On the other hand, Berg et al. (2016) and Popko, Wächter, and Thomas (2016) observed that non-Gaussian wind fields do not alter OWT load effects. Note that all these researchers used different simulation tools, turbine models, and different methods for the generation of Gaussian and non-Gaussian wind fields. Therefore, a direct comparison of their results is not possible. The recent edition of the IEC standard (IEC, 2019a) suggests the Kaimal spectrum or the Mann method for the generation of stochastic wind fields.

The vast majority of the OWT simulation tools can utilize wind files generated by a standalone, stochastic inflow turbulence tool — TurbSim (Kelley & Jonkman, 2007). Some of them also have built-in wind generators (e.g., Bladed, Flex5, HAWC2, MoLWiT).

Aerodynamic modeling

Basic aerodynamics can be modeled with the classical blade element momentum (BEM) theory developed by Glauert (1935). The theory is based on the following assumptions and limitations: (1) The flow is incompressible, homogeneous, steady, and axisymmetric; (2) There is an infinite number of blades; (3) The thrust is uniform over the rotor area; (4) Wake rotation and expansion are not considered; and (5) Static pressures upstream and downstream the rotor are equal to the undisturbed static pressure. To overcome some of these limitations BEM is often extended with various empirical and semi-empirical correction models for tip and hub losses, dynamic stall, dynamic wake, and skewed wake. The extended BEM theory is habitually implemented in all simulation tools for OWTs, as shown in Table 2.1.

The free vortex wake (FVW) theory, also known as the acceleration potential method, is a more advanced approach towards modeling of the pressure distribution over a rotor plane than the classical BEM theory. It was initially developed for the helicopter industry by Peters and He (1991) and later on adapted for wind turbines. The advantage of generalized dynamic wake (GDW) over BEM is that it inherently accounts for tip losses, dynamic wake, and skewed wake effects. Different formulations of GDW are implemented in many OWT simulation tools, but these differences are not discriminated here (see Table 2.1).

Another engineering-level model, which is used in some of the OWT simulation tools (e.g., hGAST, Simpack) is based on the FVW theory that accounts for the potential, inviscid, irrotational flow, and skewed wake effects. It determines the induced velocity field by calculating vorticity distribution in the wake. FVW is more computationally expensive than BEM or GDW though it is still faster than CFD. More information about different FVW formulations can be found in e.g., Hauptmann et al. (2014); Branlard (2017).

Tip and root losses

Prandtl (1923) introduced an empirical correction factor, which addresses the phenomenon of the loss of lift force near the blade tip resulting from the induced velocities associated with a finite number of blades. A similar correction is also applied at the blade root in the vast majority of OWT simulation tools (see Table 2.1). A more advanced, analytical formulation of the tip loss was proposed by Branlard and Gaunaa (2014) based on the vortex method. However, it has not yet been broadly adapted in different aero-elastic tools.

Skewed inflow correction

Wind turbines usually operate with a yaw misalignment between the rotor and the incoming wind resulting in an azimuthal variation of induced velocities during blade revolution. The blade that is in the upstream of the wake would experience higher wind loads, than the blade that is in the downstream of the wake. This phenomenon is not accounted for in the classical BEM formulation, which describes only the axisymmetric flow. An empirical model for the skewed inflow correction is suggested by Øye (1992) and is based on the work of Glauert (1926). It is implemented in many OWT simulation tools, as listed in the third column of Table 2.1.

Dynamic stall

A dynamic stall can be described as a nonlinear, transient aerodynamic effect that occurs when the angle of attack of the airfoil is rapidly changed due to turbulent wind flow, wind gust, blade passage in the tower shadow, etc. In most cases, the flow separation starts at the trailing edge of the blade and propagates upstream when the angle of attack is increased. The rapid change of the angle of attack may increase the lift force for a short time. This effect is not modeled in BEM, where aerodynamic forces are iteratively calculated based on the lookup tables for steady lift, drag, and moment coefficients represented as a function of angle of attack. There are several, semi-empirical dynamic stall models commonly used in the OWT simulation tools in conjunction with the BEM theory, e.g., Tran and Petot (1980); Leishman and Beddoes (1989); Øye (1990); Snel (1997). A comprehensive overview of different dynamic stall models can be found in the dissertation of Modarres (2016).

Dynamic wake

The change in the rotor load, caused by changes in turbine operating conditions, affects the induced flow field. However, this does not happen instantaneously, but with a certain time lag as observed in full-scale measurements by Øye (1991). To address this phenomenon, diverse semi-empirical dynamic wake models are commonly used in conjunction with the BEM theory, e.g., Pitt and Peters (1980); Øye (1991); Peters and He (1991).

2.1.3 Hydrodynamics

Regular linear and nonlinear waves

Regular waves can be modeled with multiple linear and nonlinear wave theories. Only those theories, which are commonly implemented in the OWT simulation tools are briefly discussed in this section. The applicability of different linear and nonlinear wave theories as a function of normalized wave height and water depth was presented by Le Méhauté (1976) and it is broadly reproduced across the literature.

Regular waves are usually modeled with the linear wave theory developed by Airy (1845), which assumes the inviscid, incompressible, and irrotational flow. The Airy theory is only valid for nonbreaking waves, which amplitudes are much smaller than the wavelength. It predicts a symmetric wave shape where the wave crests and troughs are of the same size. It is commonly extended with the Wheeler stretching (Wheeler, 1969) to account for wave kinematics — velocity and acceleration of fluid particles — above the MSL. The Airy theory with the Wheeler stretching is implemented in the vast majority of the OWT simulation tools, as listed in the fourth column of Table 2.1.

Regular nonlinear waves are often modeled with wave theories of multiple orders — Stokes wave theory (Stokes, 1847) or the Stream function wave theory developed by Dean (1965). The order of the wave theory is a measure of wave nonlinearity. Nonlinear wave theories are more accurate than the linear wave theory when the wave height is a significant proportion of the mean water depth. Furthermore, higher-order nonlinear wave theories are important in capturing the higher-order components of the hydrodynamic force, which are important in predicting the extreme loads on the structure as observed by Robertson et al. (2016). Both nonlinear wave theories are commonly utilized in many OWT simulation tools (see Table 2.1).

Irregular waves

Irregular waves can be modeled based on different spectra models, which describe an empirical relationship defining the distribution of energy with frequency within waves. Pierson and Moskowitz (1964) introduced spectrum for a fully-developed sea state, where the wave growth is not limited by the fetch[19]. Its more universal form was proposed by Hasselmann et al. (1973) within the JOint North Sea WAve Project (JONSWAP) by including an extra peak enhancement factor in the equation of the original PM spectrum. The JONSWAP spectrum accounts for a developing sea state in fetch-limited conditions and shallow waters. Other spectra models — e.g., Bretschneider (1959); Ochi and Hubble (1976) — can also be used though they are not commonly implemented in the majority of the OWT simulation tools. Many tools also offer the possibility for user-defined irregular waves based on the linear Airy theory. These irregular waves can be defined as a superposition of many individual wavelets described by corresponding wave numbers, frequencies, random phases, and amplitudes that correspond to the required spectrum. The fourth column of Table 2.1 lists irregular wave spectra models available for each OWT simulation tool.

Hydrodynamic loads

Hydrodynamic loads on the OWT support structure are usually modeled with the semi-empirical Morison equation (Morison et al., 1950), which is the sum of two inline force components — an inertia and drag force. The Morison equation is often extended with the approximation[20] of the MacCamy and Fuchs (1954) linear diffraction theory to account for diffraction effects, which become important when the wavelength is comparable with the dimensions of the structure[21]. For example, this is often the case for extra-large monopiles with diameters reaching up to 10 m at the seabed.

Some OWT simulation tools can also utilize the 1st and the 2nd order potential flow (PF) theory using a panel method approach for the calculation of hydrodynamic loads (see Table 2.1). PF is computationally more expensive than the Morison equation though it is still more efficient than CFD. The PF theory is used when modeling bottom-fixed or floating support structures with bulky members and complicated geometries — dominated by diffraction effects — where the Morison equation is not able to accurately predict the hydrodynamic loading. In the context of the rapid development of floating OWTs, many developers are nowadays implementing PF in their OWT simulation tools or coupling those tools with other specialized programs for analyzing wave interactions with offshore structures — e.g., the coupling of FAST and OrcaFlex (Masciola et al., 2011) or the coupling of HAWC2 and WAMIT (Borg et al., 2016).

There is a number of other complex models for the diffraction phenomenon around offshore structures, which are not discussed herein. They are computationally expensive; and therefore not commonly used for the time domain analysis of the full-load envelope in the OWT simulation tools.

[19] Fetch is defined by IEC (2019b, p. 12) as "distance over which the wind blows constantly over the sea with approximately constant wind speed and direction".

[20] The originally proposed MacCamy-Fuchs theory is only applicable to the frequency domain analysis.

[21] This is considered when the ratio of wave length and the structure diameter is smaller than five. More information about the relative importance of viscous effects and potential flow effects like diffraction and radiation is presented in Faltinsen (1993).

2.1.4 Structural dynamics

The majority of tools relies on linear Euler-Bernoulli and Timoshenko beam elements for the representation of various structural components, as shown in Table 2.1.

The Euler-Bernoulli theory (classical beam theory) was developed in the mid of the 18th century and is still commonly used in many engineering applications. Its main assumptions are that: (1) The beam cross-section does not deform under transverse and axial loads; and (2) The beam cross-section is planar and normal to the deformed beam axis. Timoshenko (1921) extended the classical beam theory by introducing rotatory inertia and shear deformation. He assumed that the distribution of the transverse shear strain is constant along the beam and requires a shear correction factor, which depends on the cross-sectional shape of the beam. Due to this assumption, the Timoshenko model delivers more realistic results for beams with a low aspect ratio (thick and short), than the Euler-Bernoulli beam theory. The importance of the shear effect; and therefore the superiority of the Timoshenko beam theory for specific OWT applications was proved by Nichols et al. (2009).

Both classical beam models are derived by assuming isotropic material properties. Those models cannot reproduce the nonlinear behavior of very long and slender blades made out of anisotropic composite materials. For this reason, some of the tools (e.g., HAWC2, MoLWiT) may also use various formulations of the anisotropic beam, e.g., Kim et al. (2013). A number of tools can handle a superelement representation of the OWT support structure based on different reduction techniques developed by e.g., Guyan (1965); Craig and Bampton (1968); Paz (1984, 1989); O'Callahan (1989); Suarez and Singh (1992). Also, a hybrid representation of complicated OWT support structures consisting of beam elements and superelements can be used. For example, such an approach was adopted by Tu and Vorpahl (2014) and further investigated by Popko, Georgiadou, et al. (2016). They modeled legs and braces of the jacket substructure with beam elements and its joints with superelements for a more accurate representation of stiffness properties of those joints.

Structural dynamics of OWTs is usually modeled with the multibody simulation (MBS) approach with rigid or elastic bodies, the FEM, flexible modal reduced bodies or any combination of these for arbitrary subsystems of the OWT, as listed in Table 2.1.

Viscous damping of different OWT subsystems may be realized with modal damping or stiffness and mass proportional Rayleigh damping (Rayleigh, 1877).

2.1.5 Soil-foundation models

Soil-foundation interaction has a considerable effect on the dynamics of OWTs. It should be noted that many soil-foundation models rely on linear and nonlinear springs. Damping and mass properties of the soil are less significant than the stiffness properties for determining the dynamic response of the structure. Besides that, the soil damping is difficult to measure — only by advanced laboratory testing, e.g., via resonant column tests (Drnevich, 1978) — and its neglect is often a conservative approach. Soil mass could have more effect on the modal frequencies of the structure, but the movement of the soil would be small compared to the rest of the structure. Therefore, this effect would be minimal.

There are several approaches for modeling soil-foundation interaction, which are commonly used in the OWT simulation tools (see Table 2.1). They are listed according to increasing complexity:

- Rigid foundation where a support structure is clamped directly at the seabed. It is the simplest method, which disregards the influence of soil properties on the OWT dynamics.
- An apparent fixity method, which utilizes a fictitious beam that extends from the seabed to a clamped point below the seabed that mimics the flexibility of the pile penetrating the soil.
- Linear translation and rotational springs applied at the seabed or distributed along the soil depth.
- Nonlinear springs in terms of lateral p-y curves (e.g., Reese et al., 1974), axial t-z curves (e.g., Coyle & Reese, 1966), and rotation τ-θ curves applied at the seabed or distributed along the soil depth. Furthermore, the springs at the pile tip for axial tip resistance (Q-w curves) and base shear (s-y curves) can also be included. They are defined in terms of lookup tables between the foundation displacement and the reaction load from the foundation. Additionally, distributed shaft moment curves (along the soil depth) and base moment curves were introduced in the framework of the PIle Soil Analysis (PISA) projects (Byrne et al., 2019), dealing with pile-soil interaction for large diameter monopiles.
- Linear stiffness, damping, and mass matrices applied at the seabed or distributed along the soil depth. Each matrix consists of three translational and three rotational DOFs.
- Macro element developed by Page et al. (2018); Page, Norén-Cosgriff, et al. (2019); Page, Grimstad, et al. (2019), which accounts for hysteretic damping and nonlinear foundation stiffness at the seabed. The model was validated against large-scale pile tests in clay. The macro element is implemented and validated in multiple OWT simulation tools within the OC6 project.

2.1.6 Control

A controller is an important part of every wind turbine, which assures its autonomous and safe operation. The main focus of the controller is to maximize the energy production and to minimize the structural load effects. Control of wind turbines in industry is frequently based on the proportional-integral-derivative (PID) approach.

The vast majority of the OWT simulation tools can utilize external controllers provided in terms of the DLL, as listed in Table 2.1. Some tools provide built-in control functionality (e.g., Ashes, Bladed, FAST, SAMCEF Wind Turbines). There is also a possibility to interface MATLAB® and Simulink® for controller development and tuning (e.g., HAWC2, MoLWiT, OpenFAST, SAMCEF Wind Turbines).

A comprehensive description of modern controllers and their features can be found in e.g. Bossanyi (2000); Bossanyi and Witcher (2009); Laks et al. (2009); M. H. Hansen and Henriksen (2013). Methods for tuning of wind turbine controllers are described in e.g., Tibaldi et al. (2014, 2015); Lio (2017); Behera and Gambier (2018).

2.2 Industrial approach in addressing sea ice loads

Assessment of sea ice loads and their load effects on all offshore structures is a difficult task due to the unpredictable nature of sea ice influenced by a plethora of factors, such as the temperature, salinity, porosity, grain size, and loading rate, as discussed by Timco and Weeks (2010). A case study on the prediction of sea ice loads was performed by Timco and Croasdale (2006) in a paper titled: "How well we can predict ice loads?". A number of leading specialists with industrial and academic background were asked to calculate sea ice loads on diverse structures based on their experience and knowledge. The experts were allowed to use standards, full-scale data, analytical, and numerical methods for loads estimations. Some of their results for relatively simple interaction scenarios are shown in Figure 2.2, where experts' names are anonymized with numbers.

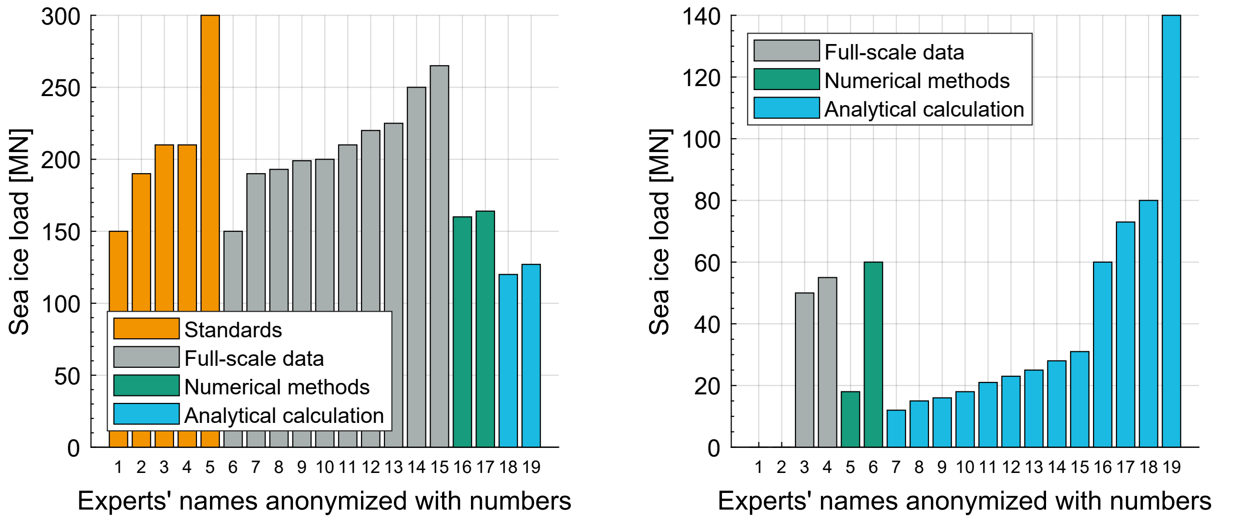

(a) A level ice sheet interacting with a rigid, vertical structure.

(b) A level ice sheet interacting with a rigid, conical-shaped structure.

Figure 2.2: Predictions of sea ice loads for different interaction scenarios. The results are grouped depending on the analysis method and sorted in ascending order. Figures generated based on the data from Timco and Croasdale (2006, p. 170).

The differences between the biggest outliers are in the range of around 150% and 1060% depending on the interaction type and the structure, as shown in Figure 2.2a (expert no. 18 vs. 5) and Figure 2.2b (expert no. 7 vs. 19), respectively. Not only the differences between the biggest outliers are large, but also the standard deviations of subsequent loads are considerable, regardless of the calculation method that was chosen.

Due to such high uncertainties in the prediction of sea ice loads, gravity base substructures with downbending cones of the Nysted offshore wind farm[22] were designed with partial safety factors between 2.0 and 2.5, as reported by Gravesen et al. (2002). By contrast, IEC (2019a, p. 54) suggests normal and abnormal partial safety factors for unfavorable loads of 1.35 and 1.1, respectively. Furthermore, Frandsen et al. (2001) and Gravesen et al. (2005) recommend a superposition of all environmental loads, including sea ice loads in the calculation of the full-load envelope. However, such an approach is no longer considered as the stat-of-the-art method for the OWT load analysis (Kühn, 2001; Vorpahl et al., 2013).

On the other hand, a fully coupled simulation of sea ice loads and OWT is not always possible due to several reasons: (1) So far there has been no OWT simulation tool with fully-integrated state-of-the-art ice models; (2) Many of the existing sea ice load models cannot be easily coupled or directly integrated with OWT simulation tools; (3) Wind turbine manufacturers do not always share their turbine data and control system with substructure designers and external ice experts; and (4) Many commercial ice experts are not willing to share their tools and detailed knowledge with substructure designers and wind turbine manufacturers. Therefore, a sequential approach, involving a chain of different tools is often used, where only a limited data set is exchanged between different parties. A scheme of the sequential approach, which is used by industry in addressing sea ice loads in the design process of OWT substructures is shown in Figure 2.3.

The advantage of the sequential approach is that confidential information concerning the detailed design of wind turbine and the substructure are not shared with another party. On the other hand, this approach may result in inaccurate dynamic representation of the entire system and load effects. There are several reasons for that: (1) The impact of wind loads during the ice-structure interaction is not considered due to the uncoupled nature of this simulation; and (2) Many information has to be exchanged between multiple experts, who might not have a global and in-depth overview of the entire process. Therefore, a lot of experience and expertise has to be involved to obtain adequate results.

The sequential approach can be divided into the following steps:

Step 1. Preliminary design of the substructure and foundation

A preliminary design of the substructure is drafted by the substructure designer (SD) based on the design basis. The design basis contains information about the site-specific met-ocean and soil conditions, such as soil properties, water depth, waves, sea currents, wind, wind-wave misalignment, sea ice, etc. It also includes a general turbine specification, such as tower height and mass, the hub height, the RNA mass, the center of gravity, moments of inertia, the maximum thrust force of a wind turbine, and the allowable frequency range.

[22] Nysted, also known as Rødsand I, is a Danish offshore wind farm commissioned in 2003. It consists of 72 wind turbines of the total capacity of 166 MW. Its location is shown in Figure 1.1.

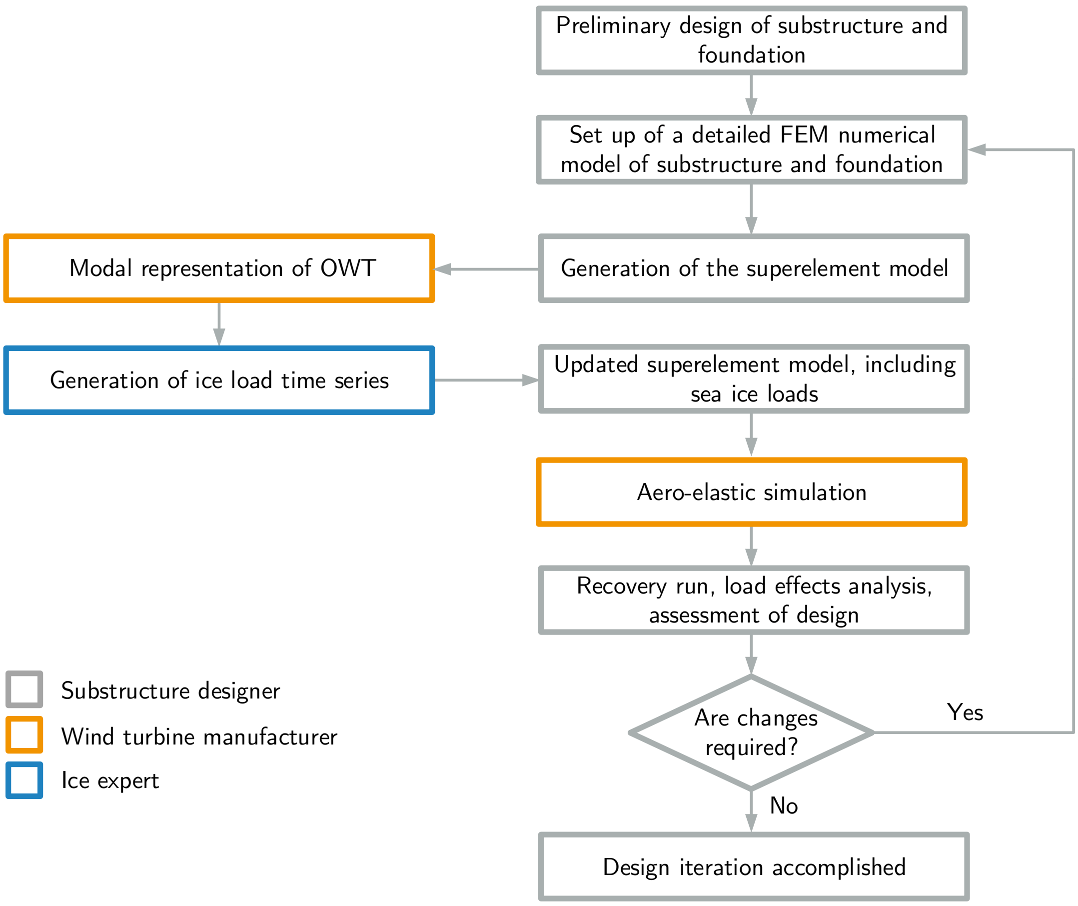

Figure 2.3: Scheme of the sequential approach used in industry for addressing sea ice loads in the design process of the substructure and foundation for OWT.

Step 2. Definition of the FEM numerical model

The preliminary design is followed by a definition of geometrical and structural properties of the substructure and foundation. Based on those properties, the SD sets up a detailed FEM model of the substructure, foundation, and soil-foundation interaction.

Step 3. Generation of the superelement model

The SD creates a superelement[23] model of the substructure and foundation, including contributions from the soil-foundation interaction.[24] The principal steps involved in creation of the superelement are described by e.g., Belyi (1993); Cook et al. (2001). The component

[23]The superelement term refers to a collection of multiple finite element (FEs), which are grouped together and considered as an individual element for the sake of computational efficiency.

[24]This is one possibility for including the substructure and foundation in the load iteration process. It is also possible that the WTM models the substructure and the foundation, including the soil-pile interaction, based on the inputs from the SD. A selected approach depends on the preference of the WTM and the modeling capabilities of its software.

mode synthesis (CMS) method[25] developed by Craig and Bampton (1968) is the most commonly used in the context of structural dynamics[26]. In CMS, a large number of DOFs is represented by constrained modes and component modes. Constrained modes describe static deflections resulting from the application of a unit displacement to an attachment DOF while other DOFs are constrained. Component modes are the vibration modes calculated with all attachments DOFs fixed. These modes are used in conjunction with mass and stiffness matrices, which are then reduced based on the Ritz vector transformation. The superelement model, provided by the SD, consists of reduced mass and stiffness matrices. It has two external nodes — the first one at the substructure-tower interface, and the second one at the point of ice action. A damping matrix for the superelement is usually derived based on the Rayleigh damping approach[27] involving a linear combination of the reduced stiffness and mass matrices.

Step 4. Modal representation of the OWT

The wind turbine manufacturer (WTM) attaches the superelement model at the bottom of the tower, which supports the RNA. Subsequently, the WTM calculates mode shapes of the entire OWT consisting of the RNA, tower, and the superelement model of the substructure and foundation, including contributions from the soil-foundation interaction. The modal representation consisting of modal deflections at the point of ice action, modal frequencies, and modal damping is prepared for the external ice expert (IE). It has to be emphasized that the modal damping includes contributions from the structural damping, soil, hydro loads, aerodynamic damping, and passive or active tower dampers (if those are present).

Step 5. Ice loads simulation

The external IE evaluates the site-specific ice parameters and includes the provided modal representation in the ice simulation tool. Relevant ice-structure interaction modes are analyzed (see Section 2.3). Note that the impact of wind loads during the ice-structure interaction is not considered due to the uncoupled nature of this simulation. The IE sends back the time series of ice load to the SD.

Step 6. Incorporation of ice load time series into superelement

The SD applies the time series of ice load from the IE into the superelement model at the interface node. The SD performs a spatial convergence check to verify correctness of the superelement model with the ice loads. A new superelement model with incorporated ice loads is provided to the WTM.

Step 7. Aero-elastic simulation

The new superelement model with sea ice loads (from Step 6.) is attached to the tower

[25] CMS is also referred in the literature as modal synthesis or dynamic substructuring.

[26] There are multiple reduction techniques, which can be used for reducing a number of DOFs in the system. Among the most popular ones are the Guyan static condensation (Guyan, 1965), CMS (e.g., Hurty, 1965; Craig & Bampton, 1968; Suarez & Singh, 1992), Dynamic Condensation (Paz, 1984, 1989), and the improved reduction system (IRS) method (O'Callahan, 1989). De Klerk et al. (2008) presented a comprehensive overview and applicability of different reduction techniques.

[27] See Eqs. 3.3, 3.4, and 3.5 in Section 3.1.4 for the definition of the Rayleigh damping.

with RNA. The aero-elastic simulation of the entire OWT is run by the WTM. The reaction forces and moments at the interface node between the tower bottom and the superelement are extracted and provided to the SD. Also, the structural deformations from the interface node are extracted for further compliance checks between the models of the SD and WTM.

Step 8. Recovery run and design update
The assessment of the substructure and foundation design is performed by a recovery run (force-controlled) simulation in the time domain. The SD applies simultaneously both the interface reaction time series from the WTM and the time series of ice load from the IE. The load effects for the substructure and foundation design are determined. If any changes in the design are required, the iteration procedure is repeated.

2.3 Ice-structure interaction modes

The ice failure modes can be classified into five main groups after ISO (2019, p. 190): creep[28], crushing[29], bending[30], buckling[31], and splitting[32]. The mode, in which ice fails, depends on multiple factors such as ice type[33], ice properties[34], limiting mechanism[35], and interaction geometry[36].

This work is focused on the sea ice cover interacting with a vertical structure — an OWT supported by a monopile — which is a typically encountered arrangement in the southern Baltic Sea. The

[28] Creep occurs at very low indentation rates — usually up to around $5 \times 10^{-4}\,\mathrm{s}^{-1}$ — and does not cause dynamic excitation to the structure. A detailed overview of ice creep can be found in e.g., Schulson and Duval (2009).

[29] Crushing is a compressive failure process, where ice fails under the compressive stresses related to a collision with a vertical structure. Depending on the indentation velocity, it can cause severe dynamic excitation of compliant structures.

[30] Bending is a dominant failure type for ice interacting with icebreaker ships, slopped, and conical offshore structures. A mechanism of ice bending failure is well described in e.g., Cammaert and Muggeridge (1988).

[31] Buckling is related to the elastic instability of the ice cover under a compressive horizontal load. From an engineering point of view, buckling of ice does not impose significant forces on a structure — the crushing failure usually dominates as the flexural strength of ice is much lower than the crushing strength. Buckling is often followed by circumferential cracks around cylindrical structures. More information about buckling of ice can be found in e.g., Sanderson (1988).

[32] Splitting may occur when the ice floe splits into two or more fragments. Ice floe splitting is considered as a limit stress mechanism.

[33] For example, level ice, rafted ice, ice floes, icebergs. See Sanderson (1988, pp. 5–29) and Cammaert and Muggeridge (1988, pp. 55–65) for a detailed description of different ice types. The most commonly encountered ice types in the southern Baltic Sea are described in Popko et al. (2015, pp. 21–25).

[34] The main parameters, which affect the mechanical behavior of ice are temperature, porosity, grain size, and loading rate. A detailed overview of the physical and mechanical properties of sea ice is presented by Timco and Weeks (2010).

[35] Limit stress, energy, and force. For more details see ISO (2019, pp. 36, 193) or Cammaert and Muggeridge (1988, pp. 208–212).

[36] Offshore structures can be classified, based on their geometry, as wide, narrow, vertical, conical, slopped, multilegged.

most common ice failure mode for this arrangement is crushing[37], which is also the most interesting from the perspective of OWT global dynamics and system excitation.

During the ice crushing different ice-structure interaction modes may arise. The concept of different ice-structure interaction modes was originally proposed by Sodhi (1991) and is applicable to the interaction setup analyzed in this work. The full-scale measurements and model tests showed that depending on the ice velocity and the stiffness of the structure, different modes of interaction can occur. The following main modes, which are also important for the dynamic analysis of OWTs interacting with a sea ice cover, can be distinguished:

Intermittent ice crushing

Intermittent ice crushing may arise if a flexible structure is exposed to ice load at a relatively low ice velocity. A saw-tooth like shape of both the structural displacement at the ice level and the global ice load can be observed in this mode, as shown in Figure 2.4. The ice-structure interaction at intermittent ice crushing can be divided into two phases — loading and unloading, respectively. During the loading phase, the structure is being pushed by the approaching ice with approximately the same velocity. Once the critical ductile load is reached the ice breaks rapidly and the structure springs back. In this short moment, the elastic energy of the structure is converted into kinetic energy and dissipated by the structural damping, and also by ice crushing at the very beginning of the next loading phase. One of the most famous intermittent crushing events was recorded at the Molikpaq Platform located in the Beaufort Sea. The analysis of those measurements was presented by Jefferies and Wright (1988).

Frequency lock-in

Frequency lock-in usually occurs at intermediate ice velocities and at a frequency close to one of the natural frequencies of the structure. During frequency lock-in, the structural displacement and velocity at the ice level have a sinusoidal-like shape, as shown in Figure 2.4. The full-scale measurements of the Norströmsgrund lighthouse in the Baltic Sea indicated that the ice-induced vibrations may occur when the ice velocity is in the range of $0.03\,\mathrm{m\,s^{-1}}$ to $0.12\,\mathrm{m\,s^{-1}}$ (Kärnä et al., 2003). Certainly, this range differs depending on the natural frequencies of the structure and ice properties. The frequency lock-in is often identified when the structural velocity at the ice level is in the range of 1 to 1.5 of the ice cover velocity, as observed by e.g., Toyama et al. (1983); Kärnä and Muhonen (1990); Timco et al. (1992); Huang et al. (2007). A method to identify the structural mode, which might be prone to frequency lock-in was proposed by Palmer et al. (2010) based on the results from several full- and scale-tests for vertical structures. They introduced an unifying dimensionless parameter, ψ, to check whether the given structural mode may experience frequency lock-in vibration. The parameter relates the ice velocity, ice thickness, and the natural frequency of the structure. The lock-in vibrations might occur when ψ is between 0.01 and 0.40.

[37] The crushing failure mode can often be combined with ice buckling resulting in a mixed failure mode. The buckling failure can limit the global load on the structure. The mixed failure may occur in the case of relatively thin ice and a relatively high aspect ratio between the structure width and the ice thickness. In this work, the mixed crushing failure is not analyzed.

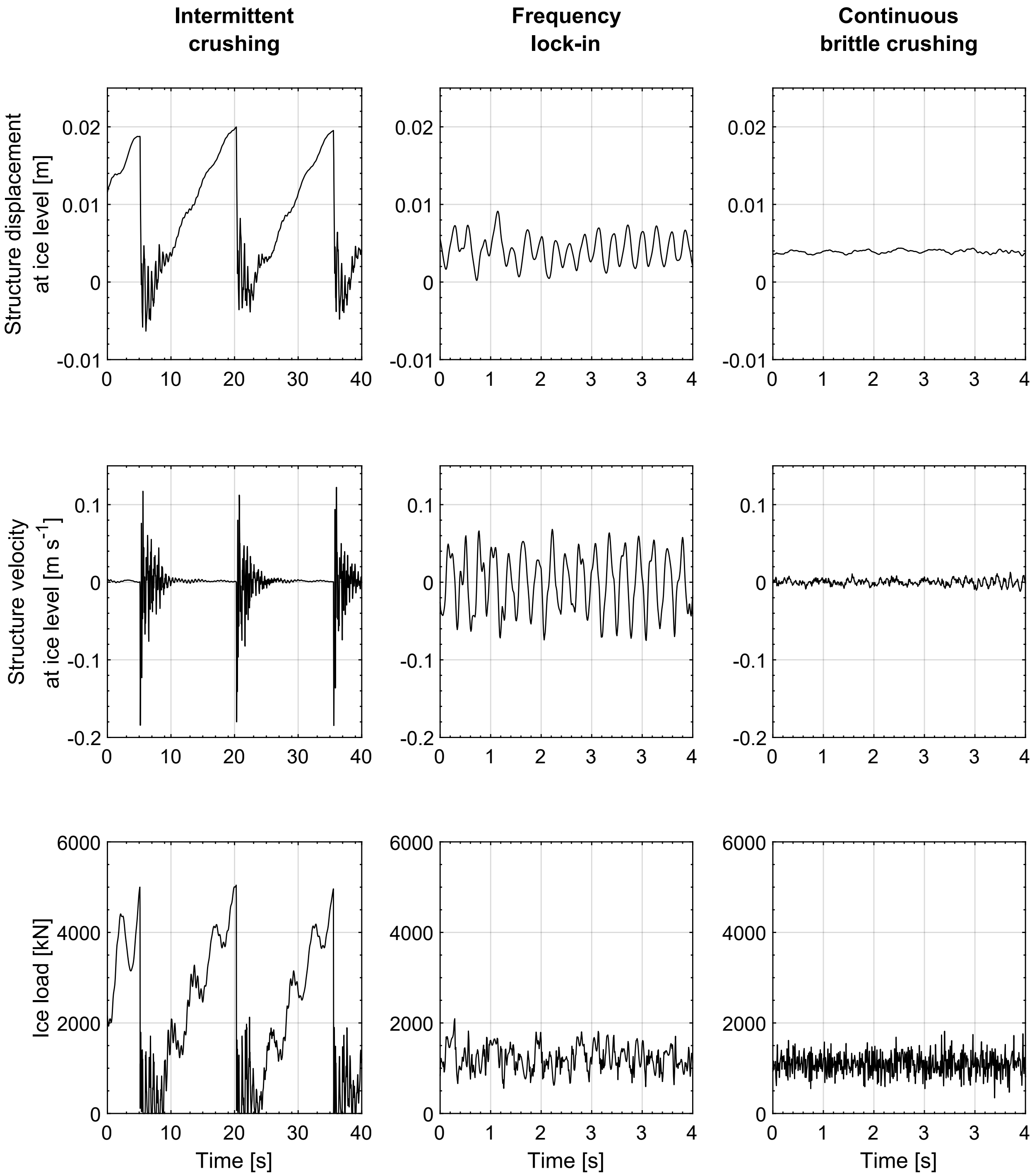

Figure 2.4: Visualization of structural displacements, structural velocities, and ice loads at three distinct ice-structure interaction modes — intermittent crushing, frequency lock-in, and continuous brittle crushing — for a flexible OWT model consisting of a monopile support structure and the RNA. All figures were generated using the Hendrikse ice model implemented in MoLWiT (see Chapter 5).

This was also observed in the validation results presented in Section 3.2. It should be emphasized that the classification criteria for the frequency lock-in provide only approximated results as they are often based on a single mode response, as shown by Seidel and Hendrikse (2018). Furthermore, there is no robust criterion that would explicitly define the frequency lock-in effect. Therefore, for this work, the frequency lock-in region is defined when all of the following criteria are fulfilled: (1) The structural displacement and velocity at the ice level have a sinusoidal-like shape; (2) The ice velocity in the far-field and the structural velocity at the ice level are of the same order of magnitude; and (3) The spectrum of the ice load contains energy peaks only at the frequencies corresponding to the global structural eigenmodes.

Continuous brittle crushing

Continuous brittle crushing occurs at higher ice velocities. The structure response is quasi-static and is characterized by very small amplitudes of displacement and velocity (stiffness forces tend to dominate over inertial forces), as shown in Figure 2.4. The ice load is random — there is no distinct frequency peak in its spectrum.

2.4 Overview of standards and their provision for ice loads

An overview of standards with focus on their provisions for ice loads is presented in this section. Popko, Heinonen, et al. (2012) published a detailed comparison of standards in terms of dominant sea ice loads for OWT support structures in the Baltic Sea — some paragraphs from this publication are also used within this section[38]. Steenfelt (2016) presented an overview of ice loads in several standards with emphasis on their applicability to different offshore structures in the southern Baltic Sea. Also, Kellner et al. (2017) did a review of OWT standards with focus on the empirical formulas for calculation of ice loads and their comparison with the measurements from the Norströmsgrund lighthouse located in the Gulf of Bothnia, in the northern part of the Baltic Sea.

New revisions of IEC[39], DNV GL[40], and ISO[41] standards have been recently published[42]. Therefore, a brief reassessment of the most up-to-date documents is of interest. A comparison of standards

[38] This is in conformity with §2 Promotionsleistungen of the *Promotionsordnung der Fakultät für Bauingenieurwesen und Geodäsie der Gottfried Wilhelm Leibniz Universität Hannover* from September 30, 2019. Also, the explicit written permission to reuse full or parts of this publication in the dissertation was granted by the International Society of Offshore and Polar Engineers (ISOPE) on August 30, 2019.

[39] IEC 61400-3-1 ed.1 was published in 2019. It replaced IEC 61400-3 ed.1 from 2009.

[40] DNVGL-ST-0437 was published in 2016. It replaced the GL *Guideline for the Certification of Offshore Wind Turbines* from 2012 in terms of definitions of loads and site conditions for wind turbines.

[41] ISO 19906 ed.2 was published in 2019. It replaced ISO 19906 ed.1 from 2010.

[42] The IEC and ISO approach to documents revision is that the technical specification (TS) documents are obligatory checked after three years for their technical validity. Ordinary IEC and ISO standards (without the TS suffix) have a prescribed stability date, which is a period over which a standard remains unchanged. It is usually 3 to 12 years.

is essential for better understanding of current industrial approach in accounting for sea ice loads in the OWT analysis.

The IEC 61400-3-1 (IEC, 2019b) and DNVGL-ST-0437 (DNV GL, 2016) standards are specifically dedicated to OWTs. They address load effects on OWT support structures by taking into account the coupled interaction of all environmental loads and the entire OWT assembly. On the other hand, the ISO 19906 ed.2 standard (ISO, 2019) is developed as a general offshore design guidance for oil and gas industry. Some of the ice load scenarios described in ISO are also applicable to OWT support structures. Table 2.2 summarizes contributions from different standards.

Table 2.2: Comparison of sea ice load provisions in different standards, which are applicable to OWTs located in the Baltic Sea and other subarctic regions.

	IEC 61400-3-1	**DNVGL-ST-0437**	**ISO 19906 ed.2**
Dynamic ice-structure interaction modes, as defined in Section 2.3	+ (additional ref. to ISO 19906 ed.1)	- (additional ref. to ISO 19906 ed.1)	+
Static pressure loads due to thermal expansion of ice	++ (additional ref. to ISO 19906 ed.1)	–	++
Static loads due to adfreeze of ice	++	–	+
Buckling of ice	++	–	++
Static loads from ice ridges	+ (additional ref. to ISO 19906 ed.1)	+ (additional ref. to ISO 19906 ed.1)	++
Static ice loads on conical structures	+ (additional ref. to ISO 19906 ed.1)	–	++
Integrated set of DLCs accounting for operational states of an OWT	++	+	–

–	no provision or insufficient provision
+	satisfactory provision
++	good provision
+++	very good provision

Dynamic ice-structure interaction modes

Moving ice can induce severe structural vibration while interacting with an OWT. The excitation of an entire OWT model and vibration of blades were reported in numerical simulations of Hetmanczyk et al. (2011) and Heinonen et al. (2011). Full-scale measurements show that depending on the ice velocity and the stiffness of the structure, different modes of interaction can occur (see Section 2.3).

Three main modes of ice-structure interaction are covered in ISO 19906 ed.2. For intermittent crushing, ISO 19906 ed.2 suggests an idealized time history of ice loading, which can be applied on the support structure. However, in this approach the ice-structure coupling is disregarded, which is not mentioned explicitly in the standard. ISO suggests a formula for analysis of vulnerability of different structural eigenmodes to frequency lock-in. It also suggests a simple, predefined forcing function for analysis of dynamic response to frequency lock-in. ISO 19906 ed.2 does not comment on the lack of ice-structure coupling when applying a predefined forcing function when analyzing frequency lock-in — as in case of the intermittent crushing mode. Continuous brittle crushing is briefly mentioned in the standard. ISO 19906 ed.2 states that both ice load and the structural response are random. The ice load can be described by power spectral density functions. However, there are no formulas or any further guidance provided. Both DNVGL-ST-0437 and IEC 61400-3-1 refer to the first edition of ISO 19906 (ISO, 2010) with respect to dynamic ice load analysis. Additionally, an important remark concerning the lack of coupling between ice and structure when applying a predefined loading time series, was made in IEC (2019b, p. 126) by the author of this dissertation[43]: "In case of a direct application of a pre-defined ice load time history on the numerical model of an offshore wind turbine, the important coupling between the relative movement of structure and ice is neglected. In many cases ice can create substantial damping to the system, by which the dynamic response of the structure is affected. Such effects cannot be properly modelled when a pre-defined time series of loading is applied on the structure. Therefore, the obtained results might not always be reliable, and great care in their interpretation is required".

To sum up — the contribution of IEC 61400-3-1 and ISO 19906 ed.2 with respect to dynamic ice-structure interaction is assessed as satisfactory. The main reason is that both standards do not explicitly require for the coupled analysis of ice-structure interaction. DNVGL-ST-0437 contribution is assessed as insufficient, as it only mentions the ice-structure interaction modes, but does not provide any methods for their analysis (see Table 2.2).

Static pressure loads due to thermal expansion of ice

Thermal expansion of ice may lead to horizontal pressure loading on a structure. Sea ice can expand and contract depending mainly on the cyclic fluctuation of the air temperature. The thermal expansion is usually important for ice thickness less than 0.5 m, as only slower cyclic fluctuation of temperature (more than two weeks period) can propagate deeper through ice. The horizontal pressure due to the sea ice thermal expansion is a potentially important load for an OWT in the Baltic Sea, where a landfast ice zone of thin ice is annually present. IEC 61400-3-1 and ISO 19906 ed.2 state that the horizontal pressure loading is of importance in low salinity environments like fresh water lakes or brackish seas. For example, the salinity of the Baltic Sea is relatively low due to the large amount of freshwater coming from land, the shallowness of the basin, and a low level of water exchange between the Baltic Sea and the Atlantic Ocean.

To sum up — the contribution of IEC 61400-3-1 and ISO 19906 ed.2 with respect to static pressure loads due to thermal expansion of ice is assessed as good; DNVGL-ST-0437 does not explicitly account for thermal expansion of ice (see Table 2.2).

Static loads due to adfreeze of ice

Sea ice can freeze to the structure forming an ice bustle. Accumulation of ice is related to the super-cooling effect of the structure, where heat conductivity of the material is

[43]The author was involved in revision of Annex D *Recommendations for design of offshore wind turbine support structures with respect to ice loads* of IEC 61400-3-1 (IEC, 2019b).

higher than heat conductivity of water, as described by Løset and Marchenko (2009). The vertical span of the ice bustle is determined by tidal changes. High adhesion between ice and the structure prevents the bustle from separation from the structure and makes its further growth possible. Its thickness can reach several meters under favorable conditions. The ice bustle formed on the structure creates additional vertical load and can increase the magnitude of horizontal loads. Vertical loads result from changes of the water level, whereas horizontal loads are the result of the lateral movement of ice. Vertical adfreeze loads are particularly important for light structures, where an uplift of the structure during water level fluctuations may occur, as stated in ISO 19906 ed.2. Gravity based structures are much heavier and stronger, therefore they can resist the adfreeze loads. IEC 61400-3-1 is the only standard providing formulas for vertical adfreeze loads, including shear and bending failure of the ice bustle. Shear failure can be considered as the mitigation factor, if it occurs before the bending failure.

To sum up — the contribution of IEC 61400-3-1 is assessed as good; ISO 19906 ed.2 contribution is assessed as satisfactory, DNVGL-ST-0437 does not explicitly account for adfreeze loads (see Table 2.2).

Buckling of ice

Ice buckling may happen when the ice sheet is thin and acts against relatively wide structures. The ice buckling failure is associated with the elastic instability of the ice cover under a compressive horizontal load. From an engineering point of view, buckling of ice does not impose significant forces on a structure (the crushing failure usually dominates). Furthermore, buckling can be considered as a factor, which limits the driving environmental forces — a thin ice cover may break due to buckling before colliding with an OWT. Both IEC 61400-3-1 and ISO 19906 ed.2 mention ice buckling among the ice loads. However, buckling is not classified as the governing load and no formulas are provided for its calculation.

To sum up — the contribution of IEC 61400-3-1 and ISO 19906 ed.2 with respect to ice buckling is assessed as good; DNVGL-ST-0437 does not explicitly account for ice buckling (see Table 2.2).

Static loads from ice ridges

Ice covers can deform and interact with each other creating ice ridges, which are especially common in the northern Baltic Sea. A ridge is formed under compressive and shear processes and can be described as porous features that consists of ice, water, air and snow. An ice ridge can impose significant loads on offshore structures.

The mechanical and physical properties of ice ridges are not well examined due to the scarce measurement data. This leads to high uncertainties in prediction of ice ridge loads; and therefore conservative assumptions in calculation of these loads. The common approach is to divide an ice ridge into three separated layers: a keel, a consolidated layer and a sail. The consolidated layer of an ice ridge imposes the highest load on a structure, as observed in IEC 61400-3-1 and ISO 19906 ed.2. Both IEC 61400-3-1 and DNVGL-ST-0437 refer to ISO 19906 ed.1 for calculation of ice ridge loads. ISO 19906 ed.2 account for loads generated by the consolidated layer and the keel. Additionally, statistical data regarding the dimensions of ice ridges in the Baltic Sea are presented in ISO 19906 ed.2.

To sum up — the contribution of ISO 19906 ed.2 with respect to ice ridges is assessed as good; IEC 61400-3-1 and DNVGL-ST-0437 contributions are assessed as satisfactory (see Table 2.2).

Static ice loads on conical structures

Ice cover interacting with a conical structure tends to fail in the flexural failure mode, rather than in the crushing mode. Ice loads imposed on sloping structures are lower compared to those observed at vertical ones. The estimation of these loads is of importance for OWTs, where conical elements may be used for mitigation of ice loads. Depending on the geometry of the conical structure, the ice sheet can be broken downwards or upwards. There are several analytical models describing the ice sheet failure, which are accounted in the standards: (1) The Ralston method (Ralston, 1977) based on the plastic limit analysis; (2) The Croasdale method (Croasdale & Cammaert, 1994) based on the elastic bending of a beam supported on an elastic foundation; and (3) The plastic method for cones. IEC 61400-3-1 suggests the Ralston method, which does not account for the ice rubble formation from the broken ice debris. ISO 19906 ed.2. suggests the Croasdale method, which also accounts for the ice rubble formation. Additionally, ISO 19906 ed.2 proposes the plastic method for conical structures based on the flexural failure of ice cover and ride up loads of ice pieces.

To sum up — the contribution of ISO 19906 ed.2 is assessed as good due to the versatility of the suggested analytical methods. The contribution of IEC 61400-3-1 is assessed as satisfactory, as it only accounts for the Ralston method. DNVGL-ST-0437 does not explicitly account for ice loads on conical structures (see Table 2.2).

Integrated set of DLCs accounting for operational states of an OWT

ISO 19906 ed.2 only mentions that fatigue loads on offshore structures result from the cumulative effect of wave, wind, and ice loading. However, an interaction between these loads and a structure is not covered. DNVGL-ST-0437 suggests five DLCs for analysis of the drifting sea ice colliding with the OWT during idling and power production. IEC 61400-3-1 provides the most comprehensive set of clearly classified DLCs, which combine wind and sea ice loads. This includes DLCs accounting for the drifting sea ice colliding with the OWT, and DLCs with adfreeze ice loads and ice thermal expansion loads.

To sum up — IEC 61400-3-1 provision is assessed as good; DNVGL-ST-0437 as satisfactory; ISO 19906 ed.2 does not account for the integrated set of DLCs (see Table 2.2).

2.4.1 Other standards and guidelines

A brief account is also given to other standards and guidelines. Some of those documents are intended to be substituted by ISO 19906 eds.1/2 or revised to reference ISO 19906 eds.1/2 with respect to ice loads.

The GL *Guideline for the Construction of Fixed Offshore Installations in Ice Infested Waters* (GL, 2005) describes procedures for estimation of sea ice properties and ice loads on offshore structures. However, the methods presented herein are considered to deliver only approximated results that may not be reliable. This is explicitly stated in GL (2005, p. 1-1): "In no case may any one of the methods provided herein be taken as reliable, valid method for design load calculation".

API RP 2N is one of the oldest and the most worldwide recognized standards for offshore structures, from which many other standards had derived before the first edition of ISO 19906 was published in 2010. The API most recent, 3rd edition (API, 2015) is harmonized with the obsolete ISO (2010) standard.

The Danish document *Recommendation for Technical Approval of Offshore Wind Turbines* (Frandsen et al., 2001) includes information concerning the technical requirements for approval of OWTs. It refers to the obsolete 2nd edition of API RP 2N from 1995 for analysis of ice loads. This obsolete standard does not account for dynamic ice loads and lock-in vibration — such loads are accounted for in the 3rd edition of API (2015).

The Finnish *RIL 144-2002 Guideline for the loading of structures* (RIL, 2002), includes sea ice load cases that might be applicable to OWT support structures. However, most of the suggested ice load models are outdated in terms of their state-of-the-art level, as observed by Määttänen (2006, p. 2).

The BSH 7005 standard (BSH, 2015) for minimum requirements concerning the constructive design of offshore structures within the Exclusive Economic Zone refers to already obsolete IEC 61400-3 ed.1 concerning the assessment of sea ice loads on OWTs.

Russian oil and gas standards SNiP-2.06.04-82* (SNiP, 2018) and VSN 41.88 (VSN, 1988) contain some methods for analytical calculation of ice loads on vertical structures, including multi-leg platforms. These documents are limited in their sea ice loads provisions, as only two types of ice features are accounted for: level ice and ice ridge, respectively. Both SNiP and VSN do not account for dynamic ice loads, such as ice-induced vibrations, which are important for OWTs.

2.5 Sea ice models and their applicability to OWTs

Reliable numerical ice models to simulate ice-structure interaction do not exist. The reason for the lack of an adequate numerical ice model is that the basic behavior of ice is difficult to model adequately, e.g., its viscoelastic behavior, creep, and damage. The prediction of different ice failures under various loading rates at temperatures around its melting point is challenging, as the local ice failure includes transitions between different phases. The most popular ice models of different complexity are briefly presented in this section.

2.5.1 Static formulas

Most of the static formulas for calculation of sea ice loads were developed between the 1940s and 1970s for piers and bridge columns (Korzhavin, 1971; Hirayama et al., 1974). These formulas are based on scaled tests and contain many empirical factors. The proper choice of these factors is often challenging. Timco et al. (1999, p. 98) showed that: "It is possible to use the equation to get almost any value, depending upon the choice of the coefficients". A more robust approach was presented in the ISO (2010, p. 169) standard, which introduced a new formula based on full-scale measurements in the Baltic Sea. The static formulas might be used for a rough estimation of ice load levels. Nevertheless, none of these formulas can be used for an accurate prediction of dynamic load effects on the OWTs, where transient events and dynamic amplifications play an important role. The most popular static formulas are shortly discussed in this subsection.

Korzhavin equation

Korzhavin (1971) introduced the following equation for estimation of the global force on vertical structures:

$$F_{\text{ice}} = k_1\, k_2\, k_3\, h_{\text{ice}}\, D\, \sigma_{\text{c}} \tag{2.1}$$

where k_1 is the unitless shape factor; k_2 is the unitless indentation factor; k_3 is the unitless contact factor; h_{ice} is the ice thickness; D is the diameter or width of the structure; and σ_{c} is the crushing strength of ice.

Eq. 2.1 seems to be quite straightforward. However, the proper choice of values for its empirical coefficients is challenging, as observed by Sanderson (1988, p. 186). Different standards recommend slightly different values based on own assumptions. The interpretation of individual coefficients in terms of their functional dependence on factors like aspect ratio and strain rate is difficult. This may lead to high discrepancies in load calculation. Furthermore, Eq. 2.1 should only be used when $D/h_{\text{ice}} < 6$, as observed in GL (2005, p. 2-3). This constraint would almost never be fulfilled in case of OWTs located in the southern Baltic Sea, where the mean thickness of the sea ice is in the range of 0.1 m to 0.3 m (cf. Section 4.2.2) and a diameter of a typical monopile support structure varies between 4 m and 8 m at MSL.

Iowa equation

The Iowa formula (Eq. 2.2) was introduced by Hirayama et al. (1974) based on small scale tests. Its relevance to full-scale structures was proved by Wessels and Jochmann (1991) after tuning of the empirical factor, k_{emp}.

$$F_{\text{ice}} = k_{\text{emp}}\, D^{0.5}\, h_{\text{ice}}^{1.1}\, \sigma_{\text{c}} \tag{2.2}$$

where k_{emp} is the unitless empirical factor for interaction characteristics; h_{ice} is the ice thickness; D is the diameter or width of the structure; and σ_{c} is the crushing strength of ice.

ISO equation

The first edition of the ISO 19906 standard (ISO, 2010) introduced a formula based on full-scale measurements in the Baltic Sea, which can provide a confident upper bound of sea ice loads. The formula was slightly modified in the second edition of the standard (ISO, 2019, p. 199) by including the empirical term f_{AR}, and it reads as follows:

$$F_{\mathrm{ice}} = p_{\mathrm{G}} h_{\mathrm{ice}} D = \left[C_{\mathrm{R}} \left(\frac{h_{\mathrm{ice}}}{h_{\mathrm{ref}}} \right)^{n} \left(\frac{D}{h_{\mathrm{ice}}} \right)^{m} + f_{\mathrm{AR}} \right] h_{\mathrm{ice}} D \tag{2.3}$$

where p_{G} is the global average ice pressure; h_{ref} is the reference thickness of 1 m; h_{ice} is the ice thickness; D is the diameter or width of the structure; C_{R} is the sea ice strength; and n, m are the unitless empirical exponents to account for the size effect in this particular equation; and f_{AR} is the empirical term, which can be disregarded when $D/h_{\mathrm{ice}} > 5$ — this is usually the case for OWT monopiles in the southern Baltic Sea.

2.5.2 Phenomenological coupled models

Five phenomenological models for ice-structure interaction are presented in this section. Underlying assumptions behind each model and drawbacks are discussed. A comparison of some of these models can also be found in Muhonen (1996) and Kärnä et al. (2013).

Matlock model

Matlock et al. (1969) introduced one of the first models for ice-structure interaction. It assumes that the structure responds in its fundamental eigenmode. Therefore, only an sDOF system can be considered, which is far away from a realistic OWT model that is a complex mDOF system. In Matlock's model, mechanical properties of ice are simplified to a linear elastic-brittle material. The ice cover is represented by a set of equally spaced cantilevered beams that fail subsequently resulting in the forcing function with a constant frequency, as shown in Figure 2.5. The equal spacing between the subsequent beams is defined as a characteristic failure length of ice, l_{ice}. The characteristic failure length of ice defines the failure frequency for a prescribed constant velocity of the ice cover, $\dot{u}_{\mathrm{ice}}$. When this failure frequency is comparable to the natural frequency of the structure resonance may occur. The subsequent ice failures are assumed to be independent, which is far from reality.

The elastic deformation of the individual ice beam upon its contact with the structure is described by the following equation:

$$\delta = (u_{\mathrm{ice}} - x_{\mathrm{s}}) - (N_i - 1) l_{\mathrm{ice}} \tag{2.4}$$

where u_{ice} is the displacement of the entire ice cover; x_{s} is the displacement of the structure; N is the number of the subsequent ice beams, i; and l_{ice} is the characteristic failure length of ice.

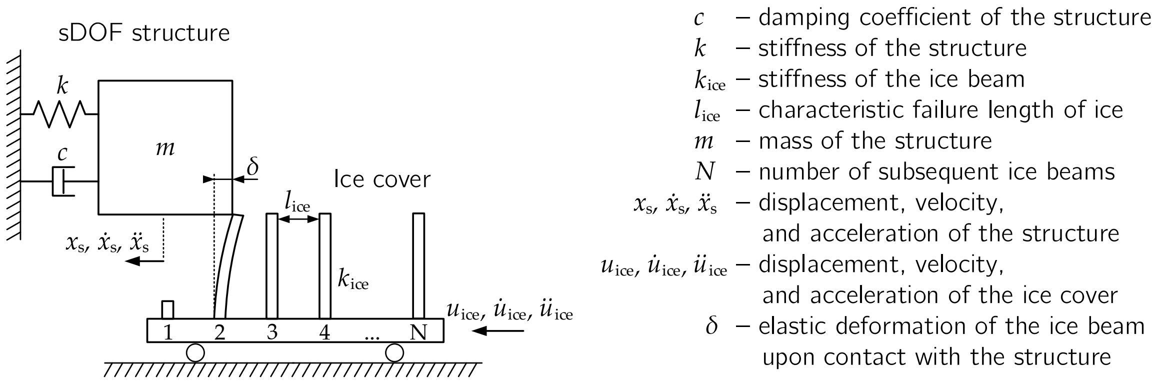

Figure 2.5: Scheme of Matlock's model where the ice cover is divided into a number of equally spaced elastic beams, which would fail subsequently upon their contact with the structure.

The following equation describes the ice-structure interaction in Matlock's model:

$$m\ddot{x}_\mathrm{s} + c\dot{x}_\mathrm{s} + kx_\mathrm{s} = \begin{cases} 0 & \text{if } \delta \leq 0 \text{ or } \delta = 1 \\ k_\mathrm{ice}\delta & \text{if } 0 < \delta < 1 \end{cases} \tag{2.5}$$

where x_s, $\dot{x}_\mathrm{s}$, $\ddot{x}_\mathrm{s}$ are displacement, velocity, and acceleration of the structure; m is the mass of the structure; c is the damping coefficient of the structure; k is the stiffness of the structure; k_ice is the stiffness of the ice beam; and δ is the elastic deformation of the ice beam, as defined in Eq. 2.4.

Matlock's model is only able to reproduce the saw-tooth like response of the structure in the intermittent crushing mode (see Figure 2.4). The quasi-static vibrations of the structure in the brittle crushing mode cannot be reproduced correctly due the periodicity of the ice loading in Matlock's model. According to multiple measurements, the global ice load in the brittle crushing region is random (there is no periodicity). Also creep deformation of ice cannot be modeled. Creep is related to the ductile failure and occurs at very low indentation velocities. Furthermore, the model fails in predicting load levels as observed by Daley and Riska (1994, p. 15). This is a significant drawback in the analysis of the load effects for OWTs, where a proper assessment of load levels is crucial for calculation of the ultimate loads in the design process of any OWT.

In recent years, there were several attempts to modify and to extend Matlock's model in order to overcome its limitations (e.g., Withalm & Hoffmann, 2010; McQueen & Srinil, 2016; Y. Zhang et al., 2016; Y. Zhang & Yu, 2018).

Sodhi model

Sodhi (1994) developed the ice-structure interaction model based on the result of a scale tests campaign described in his previous work (Sodhi, 1988). Its scheme is shown in Figure 2.6.

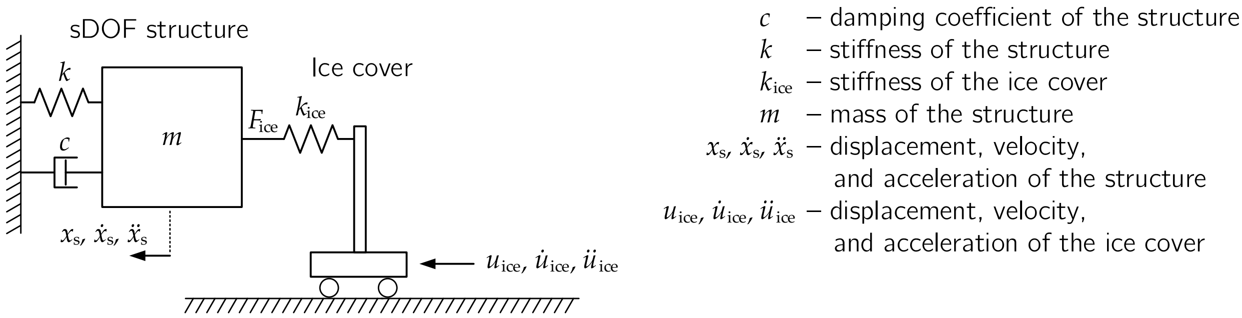

Figure 2.6: Scheme of Sodhi's model for ice-structure interaction.

The model is only able to predict the intermittent crushing and frequency lock-in modes (see Figure 2.4). It assumes ice interaction with an sDOF structure. Likewise Matlock's model, the Sodhi model is based on the concept of a characteristic failure length. Each loading cycle is divided into three phases — loading, extrusion, and separation. However, only the loading phase accounts for the ice-structure interaction by relating structure and ice velocities:

$$F_{\text{ice}}(t) = k_{\text{ice}}\left[(\dot{u}_{\text{ice}}t - u_{\text{ice}}) - x_{\text{s}}\right] \tag{2.6}$$

where F_{ice} is the ice force during the loading phase; x_{s} is the structural displacement; t is time; $\dot{u}_{\text{ice}}$ is the constant velocity of the ice under the assumption that the inertia of the ice cover is high; k_{ice} is the stiffness of the ice; and u_{ice} is the displacement of ice cover.

The loading phase is interrupted once the critical ice force is reached:

$$F_{\text{ice}} = p_{\text{G}} D h_{\text{ice}} \tag{2.7}$$

where p_{G} is the crushing pressure of ice; D is the structure diameter; and h_{ice} is the ice cover thickness.

During the extrusion phase, the ice force exerted on the structure is considered constant. Note that this phase does not account for the dynamic influence of ice on the structure. The negligence of this phenomenon at the ice-structure interface may affect the dynamic response of the structure. The separation phase starts once the sign of the structure velocity is changed.

Määttänen-Blenkarn model

The Määttänen-Blenkarn model is a phenomenological, self-excited, ice-induced vibration model for vertical structures. It was introduced by Määttänen (1998) based on the full-scale measurements of Blenkarn (1970). The model accounts for a nonlinear relation between the stress and the stress rate in the ice cover, as shown in Figure 2.7. According to Määttänen, ice-induced vibrations in the frequency lock-in mode are related to the so-called negative damping effect. This effect is associated with the negative gradient in the relation between the global ice load (stress) and the stress rate (loading velocity) — see the declining red slope in the intermittent crushing and frequency lock-in regions in Figure 2.7.

The negative gradient was observed in a number of measurements from Cook Inlet, where frequency lock-in vibrations occurred (Peyton, 1966; Blenkarn, 1970). However, there are also measurements from the southern Baltic Sea, where such vibrations occurred, but the negative gradient was not observed (Schwarz, 1971). Therefore, the assumption that the negative damping effect is responsible for the frequency lock-in vibrations is not fully correct as it does not really capture physics of the phenomenon, as pointed out by Hendrikse (2017, p. 48).

The stress in the Määttänen-Blenkarn model is described as a function of the stress rate by the following polynomial:

$$\sigma_{\mathrm{c}} = (2.00 + 7.80\dot{\sigma} - 18.57\dot{\sigma}^2 + 13.00\dot{\sigma}^3 + 2.91\dot{\sigma}^4)\sqrt{\frac{A_{\mathrm{ref}}}{A}} \tag{2.8}$$

where $\dot{\sigma}$ is the stress rate, as calculated in Eq. 2.9; A_{ref} is the reference loading area; and A is the loading area. The equation is valid for $\dot{\sigma}$ in the range from 0 MPa s^{-1} to 1.3 MPa s^{-1}. In the continuous brittle crushing region σ_{c} is assumed to be constant.

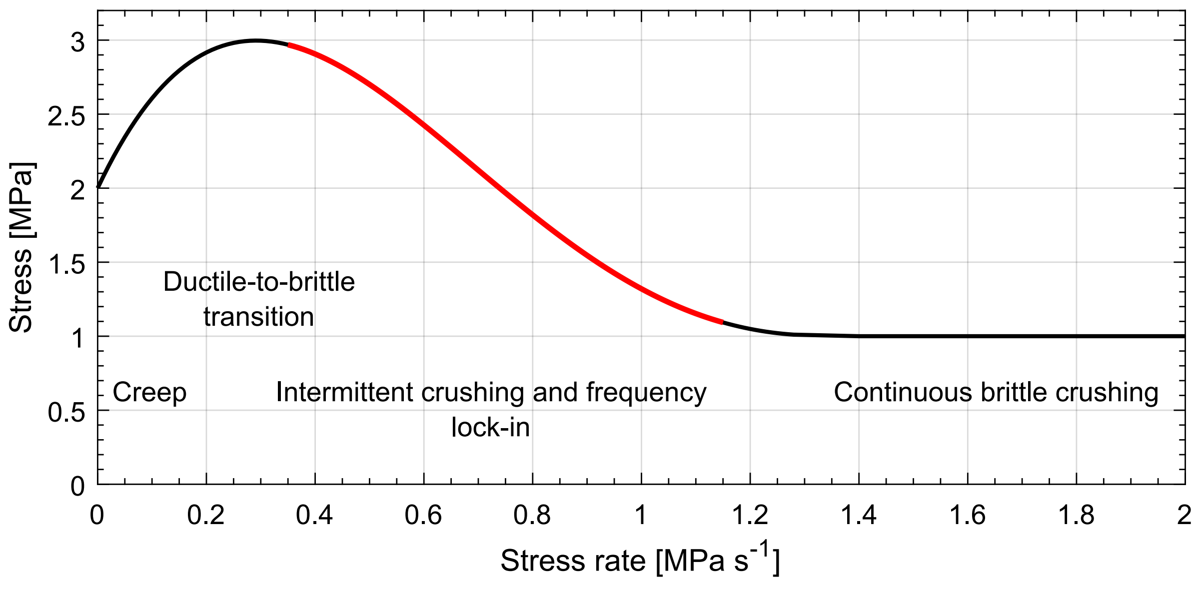

Figure 2.7: The polynomial curve fitted to the full-scale measurements from Cook Inlet, which were described by Blenkarn (1970). The curve represents ice crushing stress as a function of stress rate. Different ice failure zones are named (creep, ductile-to-brittle transition, intermittent crushing, frequency lock-in, continuous brittle crushing). The interaction region marked with red color can be simulated by the Määttänen-Blenkarn model.

The stress rate is expressed in terms of the relative velocity between the ice cover and the structure:

$$\dot{\sigma} = (\dot{u}_{\text{ice}} - \dot{x}_{\text{s}}) \frac{8\sigma_{\text{ref}}}{\pi D} \tag{2.9}$$

where $\dot{u}_{\text{ice}}$ is the constant velocity of the ice cover under the assumption that the inertia of the ice cover is high; $\dot{x}_{\text{s}}$ is the velocity of the structure at the ice level; σ_{ref} is the reference crushing strength of ice; and D is the diameter of the structure.

Eq. 2.9 can be used for narrow and wide structures, as well. According to Määttänen (1998), in case of wide structures the diameter, D, might be replaced by one or two times the ice thickness, h_{ice}. However, Määttänen does not define the aspect ratio, D/h_{ice}, that would help to classify the structure as wide or narrow.

The model may predict the lock-in vibrations at intermediate ice velocities. The random response of structure at higher ice velocities, where brittle crushing occurs, cannot be simulated. However, such capability could potentially be added by including a random generator function to simulate variation of the ice force in the continuous brittle crushing mode.

The model may produce realistic results when the relationship between the stress and the stress rate is known, as it is proved in Section 3.2. However, the need to use the in situ full-scale data for its calibration makes this model rather unsuitable for determining ice loads on OWTs.

Procedure for Soil-Structure-Ice-Interaction

The Procedure for Soil-Structure-Ice-Interaction (PSSII) was invented by Kärnä (1992); Kärnä et al. (1999). The ice cover is divided into far- and near-field parts, as shown in Figure 2.8. The far-field part is modeled as a rigid body. The near-field is modeled as a number of individual elements (contact zones), where forces and relative displacements between ice and the structure are defined at two contact points of each element — at the front and at the back. The calculation of ice forces relies on the dependence of the ice strength and the loading velocity — similar assumption to the one in the Määttänen-Blenkarn model (see Section 2.5.2). Furthermore, formulas for calculation of ice forces involve several coefficients and multiple assumptions for estimation of these coefficients. Unfortunately, the source code of PSSII is not available in the public domain. Also, there is no proper documentation concerning the input parameters, which are used in PSSII. Therefore, it is not possible to implement an own formulation of this code.

Those who would like to utilize PSSII must rely on cooperation with VTT Technical Research Centre of Finland who owns the copyrights and is able to introduce changes in the source code. The results of PSSII simulations generated at VTT have been used by many industrial players, such as DNV GL, DONG, Ramboll, for the assessment of sea ice loads on OWTs. Those companies relied on the sequential approach, which is described in detail in Section 2.2.

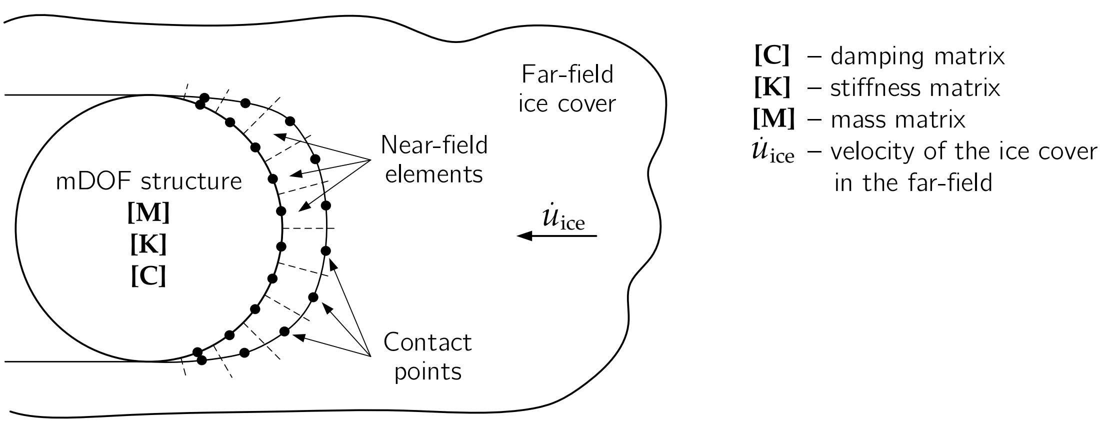

Figure 2.8: Scheme of PSSII model with the far- and near-field elements.

The ice load time series generated in PSSII was interfaced to OneWind[44] by Jussila, Popko, and Heinonen (2013) using the superposition method. This was realized within the BRICE project. A full coupling with an OWT simulation tool would be very complicated, if possible at all, as the PSSII solver is not compatible with the time-domain solvers used in the OWT simulation tools. According to Jussila (2018), VTT is still using this model in the context of measurement validations from ice tank tests and bottom-fixed structures, such as lighthouses. Though, there has been no further effort to fully couple PSSII with any OWT simulation tool.

To sum up, PSSII seems to be a powerful tool though its applicability is severely constrained due to a black box, proprietary source code and the lack of comprehensive documentation.

Hendrikse model

A phenomenological model for ice-structure interaction was developed by Hendrikse and Metrikine (2015, 2016); Hendrikse (2017) and extensively validated against scaled ice tank tests by Hendrikse et al. (2018); Owen and Hendrikse (2019). The model can simulate all ice-structure interaction modes (see Section 2.3), including creep and buckling (the buckling mode is not accounted for in this dissertation). The scheme of this model is shown in Figure 2.9.

Figure 2.10 presents eight ice properties, which are required for the calculation of the parameters describing the creep-crushing elements (stripes). The equations relating these ice properties with the ice model parameters can be found in Hendrikse and Metrikine (2015, pp. 340–341) and Hendrikse and Metrikine (2016, pp. 131–133).

[44] OneWind and OnWind are the former names of MoLWiT, which is the aero-hydro-servo-elastic tool developed by IWES (Strobel et al., 2012; Wihlfahrt et al., 2015). See Table 2.1 for simulation capabilities of MoLWiT.

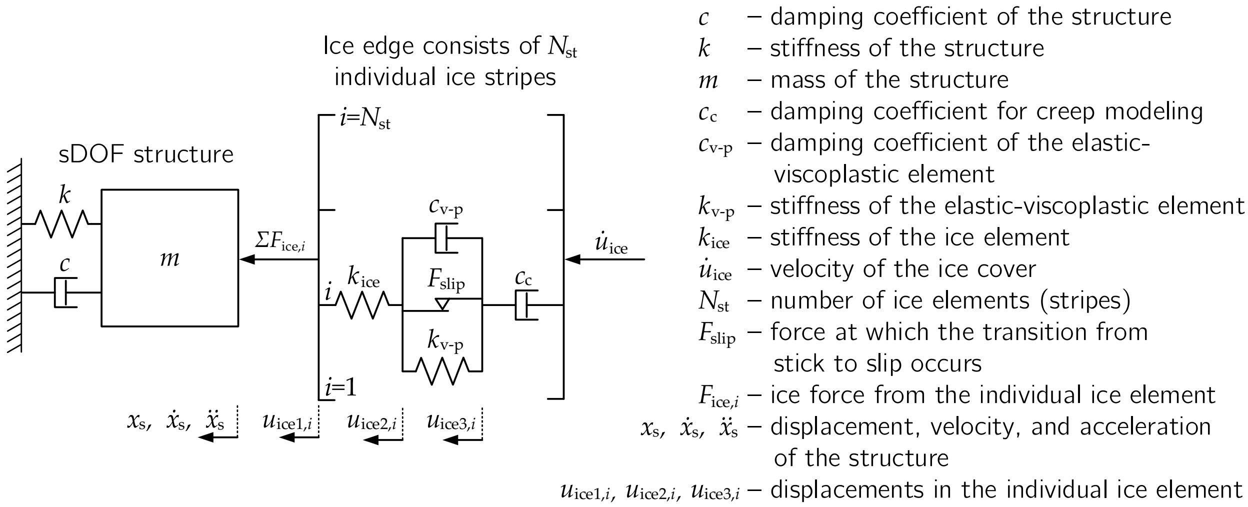

Figure 2.9: Scheme of the Hendrikse ice model. The ice edge is divided in to N_{st} individual creep-crushing elements (stripes).

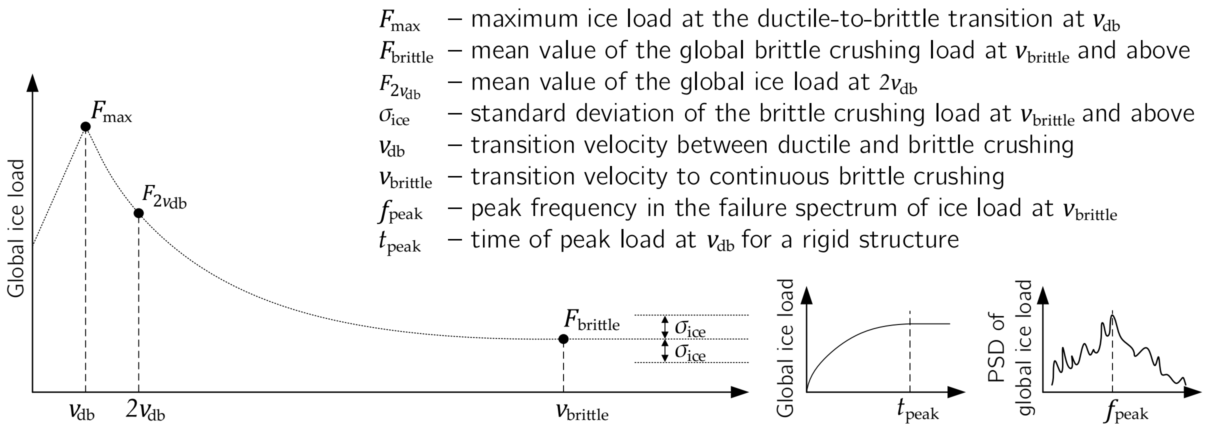

Figure 2.10: Ice properties required for calculation of parameters for creep-crushing elements. These properties should be obtained from measurements of ice action on a rigid structure. For more details refer to Hendrikse and Metrikine (2016).

The structure is modeled as an sDOF system described by mass, damping, stiffness, and diameter. The ice cover is modeled as a number of individual and independent creep-crushing elements, called stripes. Those individual stripes are necessary to account for varying loading area during the ice-structure interaction — such effect is not included in Matlock's and Sodhi's models. The total ice force, F_{ice}, imposed on the structure is a summation of force contributions from individual stripes, $\sum F_{ice,i}$.

The equations of motion for a single stripe are the following:

$$u_{\text{ice1},i}(t) = \begin{cases} u_{\text{ice2},i}(t) & \text{no ice-structure contact} \\ x_{\text{s}}(t) & \text{contact} \end{cases} \tag{2.10}$$

$$\dot{u}_{\text{ice2},i}(t) = \begin{cases} \dot{u}_{\text{ice}} & \text{no ice-structure contact} \\ \frac{k_{\text{ice}}}{c_{\text{c}}}\left[x_{\text{s}}(t) - u_{\text{ice2},i}(t)\right] + \dot{u}_{\text{ice}} & \text{contact stick} \\ \frac{k_{\text{ice}}}{c_{\text{v-p}}}\left[x_{\text{s}}(t) - u_{\text{ice2},i}(t)\right] & \\ \quad + \frac{k_{\text{v-p}}}{c_{\text{v-p}}}\left[u_{\text{ice3},i}(t) - u_{\text{ice2},i}(t)\right] & \\ \quad + \frac{k_{\text{ice}}}{c_{\text{c}}}\left[x_{\text{s}}(t) - u_{\text{ice2},i}(t)\right] + \dot{u}_{\text{ice}} + \frac{F_{\text{slip}}}{c_{\text{v-p}}} & \text{contact slip} \end{cases} \tag{2.11}$$

$$\dot{u}_{\text{ice3},i}(t) = \begin{cases} \dot{u}_{\text{ice}} & \text{no ice-structure contact} \\ \frac{k_{\text{ice}}}{c_{\text{c}}}\left[x_{\text{s}}(t) - u_{\text{ice2},i}(t)\right] + \dot{u}_{\text{ice}} & \text{contact} \end{cases} \tag{2.12}$$

where $u_{\text{ice1},i}$, $u_{\text{ice2},i}$, and $u_{\text{ice3},i}$ are the displacements of different parts of an individual ice stripe (see Figure 2.9); x_{s} is the structural displacement at ice level; $k_{\text{v-p}}$ is the stiffness and $c_{\text{v-p}}$ is the damping coefficient of the viscoplastic deformation of the stripe at low loading rates; c_{c} is the damping coefficient of the dashpot for modeling of ice creep; k_{ice} is the spring stiffness; F_{slip} is the slip force, which defines the force of the sliding stripe; and $\dot{u}_{\text{ice}}$ is the constant velocity of the ice under the assumption that the inertia of the ice cover is high.

The ice model accounts for the stick-slip phenomenon, which occurs when the cross-sectional surface of ice is in contact with the structure. Both surfaces can stick to each other or can slide one over another. More information about stic-slip can be found in e.g., Blackford et al. (2012); Schulson (2018).

A single stripe fails once the spring, k_{ice}, compresses exceeding a critical deformation, δ_{crit}, which is defined as:

$$\delta_{\text{crit}} = u_{\text{ice2},i}(t) - u_{\text{ice1},i}(t) \tag{2.13}$$

Once the stripe is broken, its new initial position with respect to the structure equilibrium is defined based on the uniform distribution function. This is an important distinction to Matlock's model, where ice failure is always governed by the same characteristic length (see Figure 2.5 and Eq. 2.4).

The Hendrikse ice model is applicable to vertical offshore structures, such as monopiles. Its may also be applicable to jacket support structures, if there is no accumulation of ice debris between the jacket legs and braces, which may affect loading conditions and cannot be simulated by this ice model.

2.5.3 High-fidelity models

High-fidelity ice models are often based on FEM, smoothed particle hydrodynamics (SPH) or discrete element method (DEM). They are focused on a detailed representation of ice failure processes or ice accumulation around the structure. Some examples of such models can be found in Suquet et al. (2012); Llorens et al. (2016); N. Zhang et al. (2017); Kolari (2017); Tuhkuri and Polojärvi (2018). The implementation of these models in OWT simulation tools would be difficult due to their complexity. Furthermore, these models are computationally demanding; and therefore not suitable for the full-load envelope simulation. For this reason, the OWT simulation tools are mainly based on the mid-fidelity, engineering-level models, as discussed in detail in Section 2.1.

2.6 Research projects focused on ice-structure interaction

This section presents an overview of some of the most recent research projects, which are focused on the ice-structure interaction. In the last ten years, an increase in the research interest in this topic can be observed. This research interest has been mainly driven by the oil and gas industry activities in the Arctic where around 13% of the world's undiscovered oil and 30% of the world's undiscovered gas deposits exist, as reported by Gautier et al. (2009). Also, the offshore wind industry is getting more interested in the ice-structure interaction topic — mostly due to the huge investments in the Baltic Sea where multiple new wind farms will be built in the upcoming years (see Section 1.1). The know-how flow and synergies have been observed between these industries in the last decade. This can be observed in multiple research projects, where new ice models are used in the offshore wind applications.

"BReaking the ICE"

The BReaking the ICE (BRICE) project was focused on the influence of sea ice loads on OWT support structures. It was executed in cooperation between IWES, the Hamburg Ship Model Basin (HSVA), and the VTT Technical Research Centre of Finland. The project was initiated in 2011 and lasted until the end of 2014. In the BRICE project, two phenomenological sea ice models were integrated and interfaced for the first time into an aero-hydro-servo-elastic tool for simulation of OWT by Hetmanczyk et al. (2011) and Jussila et al. (2013).

The Määttänen-Blenkarn ice model was validated by Popko and Georgiadou (2015) against ice tank tests performed at HSVA by Onken et al. (2013). The procedure and results of this validation are also included in Chapter 3. The shortcoming of the current industrial approach, where time series of sea ice loads are applied on the substructure was shown in Popko (2014) and are also included in Chapter 3. Furthermore, diverse ice conditions in the Baltic Sea, which may lead to high ultimate loads on OWTs, were investigated in BRICE. During the ice tank test campaign at HSVA new methods were developed for comparison of numerical simulations, experimental results, and full-scale measurements. Detailed information summarizing project findings can be found in Popko et al. (2015) and Tikanmäki et al. (2015).

The knowledge gathered in the BRICE project was utilized by the author to set up a follow-up project focused on the ice-structure interaction — see SeaLOWT below. HSVA utilized the gathered experience in other projects — for example IVOS, FATICE, and SAMCoT, which are also described below.

“Sea ice Loads on Offshore Wind Turbines”

The Sea ice Loads on Offshore Wind Turbines (SeaLOWT) project is intended to improve the design process of OWT support structures by considering sea ice loads in the coupled simulation. It is a follow-up project focused on sea ice that was initiated by the author together with Ramboll and Hamburg University of Technology (TUHH). The project started in 2016 and has been accomplished in 2020. The main goals of the project are:

- To set up an OWT numerical model with a support structure that is used in the most recent, commercial projects where Ramboll is involved. This also accounts for the real met-ocean condition data.
- To develop and implement new ice models, which are based on the experiments and the full-scale measurements. (1) TUHH has developed a full-scale ice load simulation model using the representative volume element (RVE) method; and (2) IWES and Ramboll have implemented the Hendrikse ice model (see Section 2.5.2) in their in-house simulation tools — MoLWiT and Ramboll Offshore Structural Analysis Package (ROSAP), respectively.
- To analyze the impact of sea ice loads on the global dynamics of OWTs. Such impact is barely studied and known.

“Ice loads in FAST”

The research focused on accounting for sea ice loads in the numerical analysis of OWTs was performed by the University of Michigan and the National Renewable Energy Laboratory (NREL), both from the United States. Several existing, static sea ice load formulas and phenomenological sea ice models were implemented by Yu et al. (2013, 2014) in FAST — a coupled simulation tool for analysis of OWTs (see Table 2.1). Those static formulas are not applicable for analysis of dynamic effects on OWTs, as the imposed ice loads are independent of time and there is no coupling between ice and the structure. On the other hand, simple coupled models, which were used in this research, are based on rather outdated theories — for example, the Matlock model described in Section 2.5.2. Furthermore, those implemented models were neither validated nor verified. Also, the mitigation of the load effects caused by sea ice loads through different control techniques was not investigated. Yu et al. (2013, p. 10) summarized their research as: “Of particular importance is the development of new ice/structure interaction models which include effects of ice sheet deformation and failure coupled with the dynamic response of the turbine structure”.

"Sustainable Arctic Marine and Coastal Technology"

The Sustainable Arctic Marine and Coastal Technology (SAMCoT)[45] was an international research project coordinated by the Norwegian University of Science and Technology (NTNU) and supported by oil and gas industry operating in the Arctic. It lasted from 2011 until 2019. SAMCoT covered a wide spectrum of ice-related topics, such as ice mechanics, fixed and floating structures in ice, ice-structure interaction, measurements collection and processing, and ice management. The project was not intended to focus on OWTs and their global dynamics. However, the phenomenological sea ice model developed by Hendrikse and Metrikine (2013, 2015, 2016) within SAMCoT is also suitable for analysis of OWTs. The source code of this sea ice model was made available by Dr. Hendrikse to the author of this dissertation. For the description of the model, the reader should refer to Section 2.5.2.

"Ice-induced Vibrations of Offshore Structures"

The Ice-induced Vibrations of Offshore Structures (IVOS) project was initiated by HSVA and was closely related to research realized in Work Package 3 of the SAMCoT project. IVOS lasted from 2015 until mid of 2018. Its aim was to increase the understanding of the physical process behind the structure lock-in vibrations induced by ice. Several scale model tests with flexible and rigid structures were performed in the ice tank at HSVA. The shape, size, and stiffness of the structures were varied. Also, the ice properties were altered. Tactile sensors were used for measuring ice loads, pressure distribution, and size of the contact area between ice and the structure. These properties are considered as the most influential for the occurrence of the lock-in vibrations. The phenomenological sea ice model developed by Hendrikse and Metrikine (2013, 2015, 2016) within SAMCoT was validated against those measurements from the ice tank. More information about this project and its results can be found in Ziemer (2017) and Owen (2017).

"FATigue damage from dynamic ICE action"

The FATtigue damage from dynamic ICE action (FATICE) project is coordinated by NTNU and is executed in cooperation with HSVA, TUHH, DIMB Engineering, and Siemens Wind Power.[46] The project was initiated in the middle of 2018. It aims for assessment of fatigue load effects on bottom-fixed offshore structure with emphasize on the support structures for OWTs. At the time when this dissertation was written, there was not much information available in the public domain concerning this research.

2.7 Summary of the state-of-the-art chapter

The aero-hydro-servo-elastic tools are necessary for the design process and certification of OWTs. They are often based on mid-fidelity, engineering-level models, as described in Section 2.1. There is a sophisticated interaction among those models, which are utilized in the coupled simulation

[45] https://www.ntnu.edu/web/samcot/about-samcot (Last accessed: June 1, 2020)

[46] https://www.martera.eu/projects/fatice (Last accessed: June 1, 2020)

tools. The development of these tools is driven by new OWT concepts, new design concepts for OWT subsystems, and environmental challenges at the deployment sites, such as ice loads. All these require relevant numerical models, which are computationally efficient and can adequately represent OWT dynamics and load effects — the simulation efficiency is crucial for calculation of a full-load envelope consisting of thousands of individual load cases, whereas the correct representation of structural dynamics and load effects is important for the design and certification of OWTs.

Sea ice is an important, but not a well-examined source of loading for highly dynamic OWTs. Its impact on the OWT dynamics is accounted for by using a superposition method or the sequential approach, as presented in Section 2.2. Standards for certification of OWTs provide superficial information on how to account for dynamic action of sea ice loads. Suggested methods are often outdated or not suitable for the dynamic analysis of OWTs. On the one hand, this is understandable, as standards are often lagging behind the state-of-the-art knowledge. It usually takes a couple of years, before new theories and models are recognized by the standards. On the other hand, this implies large uncertainty during the load analysis. The load analysts have difficulties with choosing an appropriate ice model and interpreting obtained results.

Many of the existing phenomenological ice models are based on questionable assumptions, such as the characteristic failure length (Sodhi's and Matlock's models) or the negative damping effect (Määttänen-Blenkarn's and PSSII models), as it was presented in Section 2.5. Many of these models are not always suitable for dynamic analysis of OWTs, as (1) They often require measurements for tuning of unphysical coefficients; and (2) Many of them cannot simulate all failure modes of ice and transitions between these failure modes. The recently developed Hendrikse model is currently considered as the state-of-the-art phenomenological ice model, which can be applied for dynamic analysis of OWTs. It accounts for all dynamic modes of ice-structure interaction, which were described in Section 2.3. Furthermore, it can also simulate creep and buckling of the ice cover. High-fidelity FEM-, SPH- or DEM-based ice models are computationally too expensive for simulation of the full-load envelope. So far, they have not been utilized in the context of OWT dynamics.

The understanding of the effect of sea ice loads on the global dynamics of offshore structures, including OWTs, is relatively poor. Multiple research projects dealing with ice-structure interaction have been initiated in the last decade, as presented in Section 2.6. The considerable synergy between those projects is also observed, where findings from one project are utilized in another.

Chapter 3

Validation of simulations against full- and model-scale measurements

The results presented in this chapter are part of extensive research realized in the framework of the BRICE project focused on the analysis of OWTs dynamics influenced by sea ice loads (see Section 2.6). Work Package 3 of this project deals with the analysis of ice-structure interaction where full-scale measurements, numerical models, and results of scaled ice tank tests are compared against each other. The basic principles of structural dynamics, also applicable to OWT support structures, can be studied based on the full-scale measurements from the Norströmsgrund lighthouse, which is shown in Figure 3.1b.

The measurements of the dynamic response of the lighthouse and ice loading time histories are well documented and available within the BRICE project. Therefore, the Norströmsgrund lighthouse is used as a full-scale reference structure in Section 3.1. This section is focused on the influence of the lack of coupling — between ice and the structure — on the global dynamics of the lighthouse numerical model. The numerical model is set up in Abaqus[47] and subjected to time histories of measured ice forces. Then, the results of numerical simulations are compared against the full-scale measurements. The comparison is made in terms of the probability density functions (PDFs) and the PSDs of accelerations at the two distinct heights of the lighthouse.

A scaled and simplified model of the Norströmsgrund lighthouse was built by HSVA and used for ice tank tests of ice-structure interaction. The results of these tests are used in Section 3.2 for

Section 3.1 is based on the paper of Popko (2014). The explicit written permission to reuse full or parts of this publication in this dissertation was granted by the American Society of Mechanical Engineers (ASME) on September 16, 2019.

Section 3.2 is based on the paper of Popko and Georgiadou (2015). The explicit written permission to reuse full or parts of this publication in this dissertation was granted by the International Society of Offshore and Polar Engineers (ISOPE) on August 30, 2019.

The reuse of already published materials in the dissertation is in conformity with §2 Promotionsleistungen of the *Promotionsordnung der Fakultät für Bauingenieurwesen und Geodäsie der Gottfried Wilhelm Leibniz Universität Hannover* from September 30, 2019.

[47] Abaqus is a proprietary, commercial FEA software developed by Dassault Systèmes. For more information see https://www.3ds.com/products-services/simulia/products/abaqus/ (Last accessed: June 1, 2020)

the validation of the Määttänen-Blenkarn ice model [48]. Both the ice model and the numerical representation of the HSVA structure are implemented and coupled in MoLWiT — an in-house aeroelastic tool developed at IWES (see Table 2.1). The basic dynamic properties of the numerical structure model are validated against the measurements. The scaling procedure for the ice model is proposed by the author. Finally, the results of the coupled simulation are compared against the HSVA measurements in terms of the time series of structural velocities and reaction forces.

(a) Location of the Norströmsgrund lighthouse in the north part of the Gulf of Bothnia. Figure adapted from Google Earth (2020b).

(b) The Norströmsgrund lighthouse during winter 2003 (Kolari, 2003). Picture reproduced with permission from D.Sc. (Tech.) Kari Kolari.

Figure 3.1: The Norströmsgrund lighthouse is located in the north part of the Gulf of Bothnia, around 55 km south from Luleå at the borderline of fast ice and drifting ice.

3.1 Uncoupled simulation of ice loading

The aim of this section is to examine how accurately a numerical model of the lighthouse can mimic the dynamic response of the full-scale Norströmsgrund lighthouse when subjected to a predefined, measured loading data.

[48] At the time when the work in Section 3.2 was realized, the development of the Hendrikse ice model had just been starting at the Delft University of Technology. The Määttänen-Blenkarn ice model was considered as one of the best simple phenomenological ice models due to its simplicity in the numerical application and quite realistic representation of ice-structure interaction.

Over the years, some of the standards for design and certification of OWTs (e.g., IEC, 2009; DNV, 2014) have suggested the application of predefined ice loading time histories for the analysis of the dynamic response of OWTs. This has been in contradiction to the commonly suggested approach for addressing load effects on OWT support structures by taking into account the coupled interaction of all environmental loads and the entire OWT assembly (see Sections 2.1 and 2.2).

The application of predefined (uncoupled) ice loading time histories on the numerical model of the structure might not always be suitable, which is shown in this section.

3.1.1 Full-scale measurements

The full-scale measurements of ice forces were performed during winter seasons from 1999 to 2003 in the scope of two projects funded by the European Union (EU): Validation of Low Level Ice Forces on Coastal Structures (LOLEIF)[49] and Measurements on Structures in Ice (STRICE)[50], respectively. At that time, the Norströmsgrund lighthouse was equipped with a set of load panels, which were attached at the MSL and enclosed 162° of its circumference, as described by Jochmann (2003a, p. 11). The load panels embraced the north-east and the east side of the lighthouse, as these were the predominant directions, from which sea ice was approaching. Figure 3.2 shows the arrangement of the load panels, which were installed during the STRICE project[51].

The arc length of a single load panel is 18°. Eight out of nine load panels are 1.21 m long and 2.8 m high, whereas the last one is assembled out of eight smaller load panels. Ice forces on the load panels were recorded with three different sampling frequencies, depending on the type of ice action: 1 Hz for static ice loads, 10 Hz for ice buckling and mixed failure modes (crushing and buckling), and 30 Hz for ice crushing.

The dynamic response of the Norströmsgrund lighthouse was measured in terms of horizontal accelerations that were recorded in two directions — north-south (along the x-axis) and east-west (along the z-axis). The accelerometers were located at the center of two decks of the lighthouse at 16.5 m and 37.1 m above the seabed, as shown in Figure 3.3. Acceleration time series were correlated with the measurements of ice forces on individual load panels[52]. The data recording was automatically triggered whenever an ice action on the lighthouse was detected. Subsequently, those sets of measurements (called ice events) were stored in multi-column files containing time histories of ice forces on individual load panels and structural accelerations. To give a full picture of an ice event, these recordings were accompanied by measurements of the average ice thickness, air temperature, wind speed, and wind direction. These additional measurements were collected in separate log files.

[49] https://cordis.europa.eu/project/rcn/37827/factsheet/en (Last accessed: June 1, 2020)

[50] https://cordis.europa.eu/project/rcn/54171/factsheet/en (Last accessed: June 1, 2020)

[51] Selected measurements from the STRICE project were provided by HSVA to IWES within the BRICE project.

[52] Until March 6, 2001 accelerations of the Norströmsgrund lighthouse were not recorded. Therefore, only the data sets recorded after this date can be used for the analysis.

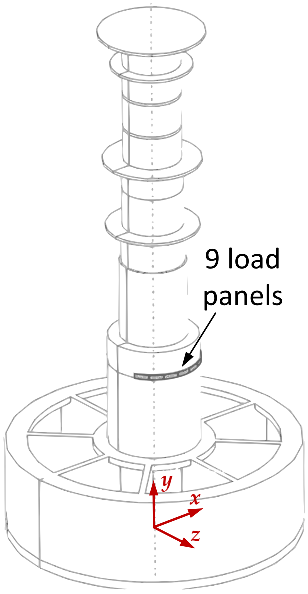

(a) Isometric view of the lighthouse with load panels at MSL.

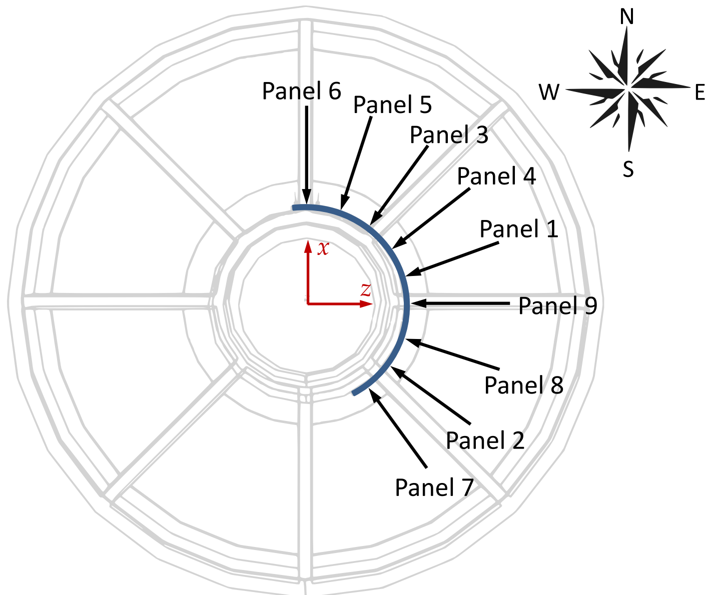

(b) Top view of the lighthouse with numbered load panels around its circumference at MSL. Modified figure from Popko (2014).

Figure 3.2: Arrangement of load panels on the Norströmsgrund lighthouse and their position with respect to true north. The right hand Cartesian coordinate system is placed at the bottom of the lighthouse model, where x-axis points true north, z-axis points east, and y-axis upward.

3.1.2 Numerical model of Norströmsgrund lighthouse

A three-dimensional (3D) numerical model of the Norströmsgrund lighthouse (Figure 3.3) is set up in Abaqus. The majority of its structural and geometrical properties are derived from Heinonen et al. (2004). The modification of several parameters presented in that report is necessary to obtain a desirable dynamic response of the numerical model. This section describes the most important aspects that are considered in the numerical implementation of the Norströmsgrund lighthouse.

Material density is varied at different heights of the lighthouse model to account for supplementary masses of thermal insulation, equipment, and hydrodynamic added mass. Values of material density presented by Heinonen et al. (2004, pp. 5–6) are used directly, as no other, precise estimates are available.

The numerical model of the lighthouse is supported at the central node of the foundation plate, which is also the origin of the coordinate system, as shown in Figure 3.3. The vertical translation of this node is constrained, whereas the remaining two translation and three rotational DOFs are free. Soil stiffness is modeled with two translation springs in the horizontal plane and three torsional springs — all attached at the central foundation node. The values of spring constants are iterated in order to obtain the frequency response of the numerical model comparable to frequencies obtained from the full-scale measurements and other numerical models (see Section 3.1.3). The

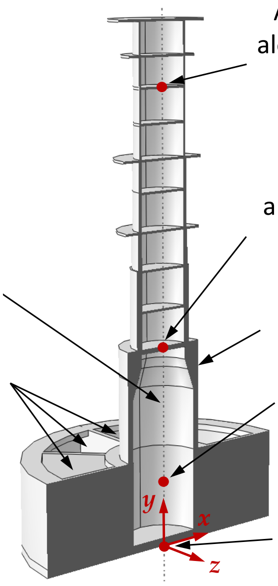

Figure 3.3: Vertical cross-section of the Norströmsgrund lighthouse model set up in Abaqus. The right hand Cartesian coordinate system is placed at the bottom of the lighthouse model, where x-axis points true north, z-axis points east, and y-axis points upward. Modified figure from Popko (2014, p. 3).

finally obtained spring constants are listed in Table 3.1. They are slightly smaller than those reported by Heinonen et al. (2004, p. 6). The difference in the obtained values comes from the fact that this particular model of the lighthouse may differ in certain aspects from the one presented by Heinonen. For example, such parameters as geometry and mass distribution can deviate compared to Heinonen's numerical model, as their description in his report is not too comprehensive.

Soil mass and soil moments of inertia are also attached to the central foundation node. Their values are directly taken from Heinonen et al. (2004, p. 6) and are listed in Table 3.1.

Table 3.1: Mass, moments of inertia, and stiffness values for modeling of soil and sand filling.

Soil	Sand filling	Unit	Description
1.52×10^6	4.76×10^6	kg	Point mass
4.51×10^8	2.72×10^8	$\mathrm{kg\,m^2}$	Moment of inertia with respect to horizontal x-axis
4.51×10^8	2.69×10^8	$\mathrm{kg\,m^2}$	Moment of inertia with respect to vertical y-axis
4.51×10^8	2.72×10^8	$\mathrm{kg\,m^2}$	Moment of inertia with respect to horizontal z-axis
6.00×10^9	–	$\mathrm{N\,m^{-1}}$	Spring stiffness for translations in horizontal x- and z-directions
8.00×10^{11}	–	N m	Spring stiffness for torsion around x-, y-, and z-axis

The external and internal caissons of the Norströmsgrund lighthouse are filled with sand up to the heights of 7.0 m and 16.1 m, respectively. In Abaqus, the sand filling is modeled as a point mass and three moments of inertia attached to a single node located at the center of gravity of the sand filling, as shown in Figure 3.3. This node is rigidly connected to the origin of the coordinate system. The calculated properties of the sand filling are listed in Table 3.1. Such an approach neglects the sand stiffness but also simplifies the numerical model. Implementation of the 3D sand filling and its interaction with caissons' walls would increase the number of DOFs in the model; and therefore, would require more computational effort. The negligence of the sand filling stiffness can be justified, as the stiffness of sand is much lesser than the stiffness of the concrete walls of the large diameter caissons (23 m in diameter), which are additionally reinforced with the bulkheads (see Figure 3.3).

The calculated values of mass and moments of inertia of sand filling are around 50% lower compared to those presented by Heinonen et al. (2004, p. 7). Furthermore, the obtained values are confirmed independently with both numerical and analytical calculations. This finding is surprising as the same sand density of 2000 m kg^{-3}, as proposed by Heinonen et al. (2004, p. 7), was used for the calculation of mass and moments of inertia in this research. This indicates that Heinonen might use different input parameters for the calculation of the sand filling properties.

Sensors recording accelerations, displacements, and velocities are located at the center of the two decks of the numerical model at 16.5 m and 37.1 m, as shown in Figure 3.3. These locations correspond to the physical locations of accelerometers in the Norströmsgrund lighthouse.

The load panels are modeled as massless and rigid. They are attached to the numerical model of the lighthouse at the MSL level ($y = 14.25$ m) and arranged in the same way as in the Norströmsgrund lighthouse, as shown in Figure 3.2. The outer radius of each load panel is 3.76 m, which corresponds to dimensions of real load panels, as reported by Jochmann (2003a, p. 7). The height of numerical load panels can be varied according to the average ice thickness in a particular ice event. Herein, an ice event with an average ice thickness of 0.4 m is analyzed.

The entire lighthouse model is meshed with the 10-node quadratic tetrahedral elements. They converge much better in terms of accuracy than the first-order tetrahedral elements and are easier to implement on complex geometries than the hexagonal elements (Benzley et al., 1995).

In Abaqus, the modal dynamic procedure is used for the analysis of the transient linear dynamics of the lighthouse model. The response of the lighthouse model is based on a subset of the eigenmodes. This approach provides accurate results for linear systems represented by a sufficient number of eigenmodes. In this case, ten eigenmodes below 20 Hz are accounted for in the analysis. These eigenmodes incorporate 98.9% of the total effective modal mass of the structure, which is considered sufficient[53] to capture the global dynamics of the model adequately. The response of the lighthouse model was obtained in the time domain, based on a time-dependent loading (measured time histories of ice force). The simulation results are presented in Section 3.1.5.

[53]The American Society of Civil Engineers (ASCE) requires the combined modal mass participation of at least 90% of the total mass in orthogonal horizontal directions of response (ASCE, 2017, p. 104). Priestley et al. (1996) confirmed that a sum of effective modal masses between 80% and 90% of the total mass could be considered sufficient to capture the global dynamic response of the structure.

3.1.3 Comparison of frequencies

Throughout the years, various damped natural frequencies[54] of the Norströmsgrund lighthouse have been reported by different scientists during the in situ measurements. Engelbrektson (1987) registered the lowest frequency at around 3.5 Hz, which was obtained from the tugboat pull test in the open water conditions. Other tests were conducted in the scope of the STRICE project, where Luo (2003, p. 3) indicated the lowest frequency at 2.0 Hz, whereas Kärnä et al. (2003) reported the following set of subsequent frequencies: 2.6–2.9 Hz, 6.5 Hz, and 12 Hz. These frequencies were induced by the ice splitting failure, which created an impulse load on the structure.

The discrepancy between the lowest (2.0 Hz measured in 2003) and the highest (3.5 Hz measured in 1987) value of the first frequency is significant. There are several reasons for it. For example, properties of concrete have degraded through the years. First crack formations on the walls of the lighthouse were reported by Björk (1981). Since that time, these cracks have developed even further, contributing to the reduced structural stiffness, and thus decreased frequencies. These cracks are located in the region where the highest stresses occurred during the dynamic ice action, as proved in numerical simulations performed by Bjerkås et al. (2010).

The natural frequencies and the corresponding mode shapes were calculated for an undamped lighthouse model and without account for gravity. It is experienced that the influence of structural damping and gravity on the eigenvalues is low (Popko et al., 2014, p. 5). A slight decrease of frequency could be expected, especially for the global modes, since gravity tends to reduce the bending stiffness of a vertical beam, as shown by e.g., Jonkman (2003, p. 44). For this particular eigenanalysis, the negligence of damping and gravity is justified as there are other, more important sources of uncertainty in the model setup (see Section 3.1.2).

The results of the eigenanalysis performed in Abaqus are presented in Figure 3.4. Only eigenmodes of odd numbers are shown — the eigenmodes of even numbers are orthogonally symmetric.

The 1st eigenmode shown in Figure 3.4a, is characterized by bending of the tower and slight rotation of the foundation caisson. The 3rd eigenmode presented in Figure 3.4b, is associated with the horizontal translation of the caisson and bending of the upper part of the tower. The 5th eigenmode in Figure 3.4c, is dominated by rotation of the caisson around the horizontal axis and the second bending mode of the tower. The 7th eigenmode shown in Figure 3.4d, is dominated by the second mode of the tower with almost no translation or rotation of the caisson. The 9th eigenmode is the global torsion of the lighthouse, as presented in Figure 3.4e.

The comparison of calculated eigenfrequencies against those from other numerical models and the full-scale measurements is presented in Table 3.2, where:

- Column 1 shows numbers of odd eigenmodes (modes of even numbers are orthogonally symmetric to those).

[54] The real physical system is described by damped natural frequencies, which are slightly lower than the undamped natural frequencies (also called eigenfrequencies). The relation between damped natural frequency, f_{d}, and eigenfrequency, f_{n}, is described as $f_{\mathrm{d}} = f_{\mathrm{n}}\sqrt{1-\zeta^2}$, where ζ is the damping ratio.

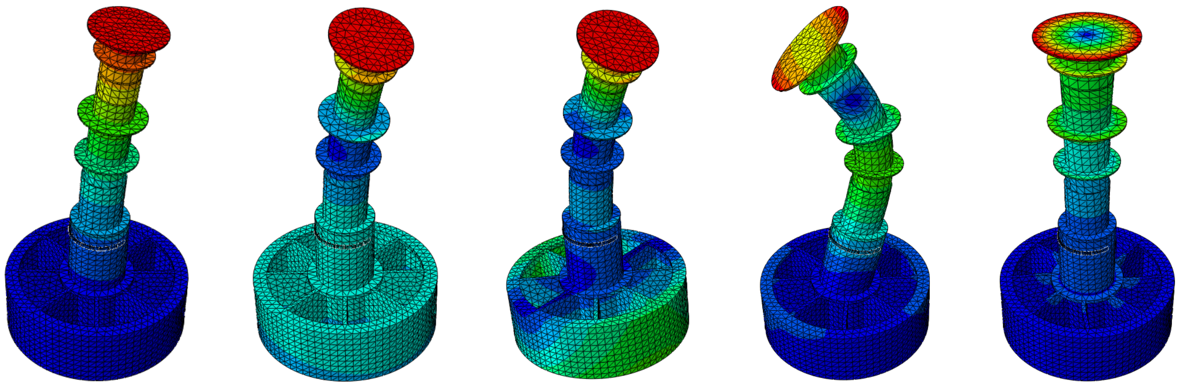

(a) 1st Eigenmode, 2.83 Hz **(b)** 3rd Eigenmode, 4.17 Hz **(c)** 5th Eigenmode, 5.62 Hz **(d)** 7th Eigenmode, 12.97 Hz **(e)** 9th Eigenmode, 18.09 Hz

Figure 3.4: Eigenmodes and corresponding eigenfrequencies of the Norströmsgrund lighthouse model set up in Abaqus (Popko, 2014, p. 4).

- Column 2 shows eigenfrequencies calculated in Abaqus in the scope of this research.
- Column 3 shows mean, minimum, and maximum eigenfrequencies for the given mode from other numerical models.
- Column 4 shows measured mean, minimum, and maximum damped frequencies for the given mode from the full-scale measurements from the STRICE project.
- Column 5 shows the percentage change between the values calculated in this research (column 2) and other numerical models (column 3).
- Column 6 shows the percentage change between the values calculated in this research (column 2) and the full-scale measurements (column 4).

The percentage change is calculated as:

$$\frac{value_2 - value_1}{value_1} 100\% \tag{3.1}$$

where $value_1$ is the frequency from this work, $value_2$ is the frequency obtained from another numerical model from the literature.

A very good match is obtained for the 1st frequency between the Abaqus model and other numerical models (mean difference of −0.7%), and between the Abaqus model and the full-scale measurements (mean difference of −2.8%). The match of the 1st frequency is the most important, as the Norströmsgrund lighthouse primarily responds in its first eigenmode, which carries the most energy. Higher modes are less pronounced in the frequency spectrum.

Also, a very good match is obtained for the 3rd frequency between the Abaqus model and other numerical models (mean difference of 1.2%). It is interesting that this frequency has not been

Table 3.2: Comparison of frequencies for the first four odd modes — numerical models and the full-scale measurements.

Mode No	Eigenfrequencies – numerical model (Popko, 2014)	Eigenfrequencies – numerical models (Heinonen et al., 2004, p. 8)	Damped frequencies – STRICE measurements	Percentage change – column 2 vs. 3	Percentage change – column 2 vs. 4
1st	2.83 Hz	mean 2.81 Hz min 2.61 Hz max 3.01 Hz	mean 2.75 Hz min 2.60 Hz max 2.90 Hz	mean −0.7% min −7.8% max 6.4%	mean −2.8% min −8.1% max 2.5%
3rd	4.17 Hz	mean 4.26 Hz min 3.47 Hz max 5.04 Hz	N/A	mean 1.2% min −18.5% max 20.9%	N/A
5th	5.62 Hz	mean 5.36 Hz min 4.55 Hz max 6.16 Hz	6.50 Hz	mean −4.7% min −19.0% max 9.6%	15.7%
7th	12.97 Hz	11.74 Hz	12.00 Hz	−9.5%	−7.5%

N/A – not available, values not recorded

captured in the full-scale measurements — perhaps, due to the fact that the 3rd mode is mainly associated with the horizontal translation of the very heavy caisson (cf. Figure 3.4b).

A good match is obtained for the 5th frequency between the Abaqus model and other numerical models (mean difference of −4.7%). The discrepancy increases for the full-scale measurements (mean difference of 15.7%). The reason for this difference might be that the measured frequency was recorded during the ice splitting event when the lighthouse was surrounded and constrained by sea ice at MSL. This would explain why the measured frequency (6.50 Hz) is higher than the simulated one (5.62 Hz).

A reasonable match is obtained for the 7th frequency between the Abaqus model and other numerical models (difference of −9.5%), and also between the Abaqus model and the full-scale measurements (difference of −7.5%).

To sum up — the obtained eigenfrequencies are in a good agreement with other numerical models and with the full-scale measurements. The most important is to obtain a good match for the 1st frequency, which caries the most energy and at which the Norströmsgrund lighthouse tends to respond. A more precise assessment of higher frequencies would be difficult due to: (1) Limited information concerning the conditions, under which the full-scale measurements of frequencies were conducted; (2) The limited number of sensors along the height of the lighthouse; and (3) The very limited knowledge concerning the soil properties under the lighthouse.

3.1.4 Application of measured ice forces on numerical model

A Python script is developed to preprocess measured time histories of ice forces and to apply them on individual load panels of the numerical model of the lighthouse. The script automatizes the following steps:

Step 1. Reading of measured ice forces

Measured time histories of ice forces for individual load panels are read from the comma-separated value (CSV) files delivered by HSVA.

Step 2. Screening time series and removing repeated time steps

It is found out that some of the time step indices are repeated in the measured time histories of ice forces. These duplicated indices lead to the abort of Abaqus solver. Therefore, it is necessary to find duplicated data entries and to remove them from the measured time histories of ice forces.

Step 3. Correction of offsets and signs

Some of the measured time histories of ice forces are found to have negative force values. This effect was caused by a drift in load cell electronics, not a physical pulling force on the load panel, as the load peaks direction is still positive. Therefore, the correction of some of these time series is necessary. This finding and the necessity for correction is additionally confirmed by HSVA.

Step 4. Detection of sampling rate

The sampling rate of the measured loading data is detected automatically based on the analyzed ice event. The simulation time step is adjusted to fulfill the Nyquist-Shannon sampling theorem (Nyquist, 1928; Shannon, 1948), which states that the sampling frequency should be at least twice the highest frequency of the measured signal. In the case of the analyzed ice event (see Section 3.1.5), the simulation time step (0.003 s) is ten times less than the sampling frequency (30 Hz) in order to avoid aliasing.

Step 5. Rescaling of measured ice forces

The measured time histories of ice forces have the unit of kN. They are rescaled from kN to N for the sake of simulation.

Step 6. Conversion of measured ice forces to pressure

The measured time histories of ice forces are converted to pressure, as this can easily be applied to individual load panels specified in Abaqus. The conversion is done according to the following equation:

$$P_{\text{ice},i} = \frac{F_{\text{ice},i}}{A} = \frac{10F_{\text{ice},i}}{h_{\text{ice}}\pi R} \tag{3.2}$$

where $F_{\text{ice},i}$ is the measured time history of ice force recorded on individual panels $(i = 1:9)$; A is the loading area calculated based on the average ice thickness of the analyzed ice event and the circumferential length of a single load panel $(2\pi R\ 18^\circ/360^\circ)$; h_{ice} is the average ice thickness for the analyzed ice event; and R is the panel radius.

Step 7. Application of pressure time histories to individual load panels

In the last step, pressure time histories are applied to individual load panels and the time domain simulation is executed.

3.1.5 Comparison of dynamic response of Norströmsgrund lighthouse and its numerical model

The numerical model of the lighthouse is subjected to measured time histories of ice loading coming from an ice event No. 1303_0702 registered on March 13, 2001 (Jochmann, 2003b, p. 175), where ice action lasting for around one hour was recorded.

This particular event was preselected based on the logbook data and the limited data sets of crushing failure events available for IWES within the BRICE project. The logbook data distinguishes different failure modes such as crushing, bending, or mixed failure. However, it does not provide information about the interaction type during the crushing failure (intermittent, frequency lock-in or continuous brittle crushing).[55] The final selection was based on: (1) The quality of the recorded time series (2) And the direction, from which the ice cover was approaching the structure. In the analyzed event the ice cover comes from the East. The eastern side of the lighthouse was equipped with the load panels as shown in Figure 3.2b.

The average ice cover thickness in this event is estimated to 0.4 m and the average ice velocity is $0.1\,\mathrm{m\,s^{-1}}$. This ice velocity is at the threshold between the frequency lock-in and the continuous brittle crushing modes of ice-structure interaction (see Section 2.3).

Ice loading and acceleration data were sampled with the frequency of 30 Hz. Those full-scale loading time histories are converted to pressure histories (see Eq. 3.2), which are individually applied to nine load panels of the numerical model. The simulation time step is set to 0.003 s, which is ten times less than the sampling time of the loading data, to capture the dynamic response of the lighthouse model adequately. The simulation time is set to 300 s.

The influence of structural damping on the dynamic response of the lighthouse model is examined to find out the most suitable damping ratio for the numerical model that would mimic the response of the full-scale structure. The Rayleigh viscous damping (Rayleigh, 1877) is used in the numerical model of the lighthouse. The damping matrix consists of a linear combination of mass and stiffness matrices:

$$[\boldsymbol{C}] = \alpha[\boldsymbol{M}] + \beta[\boldsymbol{K}] \tag{3.3}$$

where $[\boldsymbol{M}]$ is the mass matrix; $[\boldsymbol{K}]$ is the stiffness matrix; α is the mass proportional Rayleigh damping coefficient; and β is the stiffness proportional Rayleigh damping coefficient. Damping coefficients α and β are calculated as follows:

$$\alpha = 2\omega_1\omega_3\zeta\frac{\omega_3-\omega_1}{\omega_3^2-\omega_1^2} \tag{3.4}$$

$$\beta = 2\zeta\frac{\omega_3-\omega_1}{\omega_3^2-\omega_1^2} \tag{3.5}$$

[55] Refer to Section 2.3 for detailed information about ice failure modes and ice-structure interaction modes.

where $\omega_1 = 2\pi f_{n,1}$ is the 1st angular frequency; $\omega_3 = 2\pi f_{n,3}$ is the 3rd angular frequency; and ζ is the damping ratio.

The coefficients α and β are calculated for the frequency region limited by the two lowest eigenfrequencies of the subsequent eigenmodes: $f_{n,1} = 2.83$ Hz and $f_{n,3} = 4.17$ Hz (see Figure 3.4). Within this frequency region the desired damping ratio should be achieved. Several damping ratios, ζ, in the range from 0.01 to 0.05 are examined in order to tune the dynamic response of the numerical model to the response of the full-scale lighthouse. The calculated α and β coefficients for different damping ratios, ζ, are listed in Table 3.3.

Table 3.3: Rayleigh damping coefficients α and β as a function of damping ratio, ζ, (Popko, 2014).

Damping ratio, ζ	**0.01**	**0.02**	**0.03**	**0.04**	**0.05**
α	0.2119	0.4238	0.6357	0.8476	1.0595
β	0.0005	0.0009	0.0014	0.0018	0.0023

The dynamic responses of the numerical models and the full-scale lighthouse are compared in terms of accelerations, which are registered at two levels of the structure (Figure 3.5a). The results are shown in Figures 3.5b, 3.5c, 3.5d, and 3.5e in terms of PDFs.

The response of the full-scale structure at the tower top fits well to the response of the numerical models with the damping ratio of 0.05 in the north-south direction (Figure 3.5b) and 0.02 in the east-west direction (Figure 3.5c). However, those values are higher than the typical values of the damping ratio for concrete structures, which are usually in the range of 0.005 to 0.012 (Bachmann et al., 1995, p. 4).

PDF of the tower top acceleration in the east-west direction (Figure 3.5c) has a flatter distribution compared to the acceleration in the north-south direction (Figure 3.5b). This is observed for both the full-scale structure and the numerical model. Such a response is expected, as the ice loading mostly acts on the eastern side of the structure resulting in higher tower top accelerations in the east-west direction.

PDF of acceleration in the north-south direction at the lower level of the lighthouse ($y = 16.5$ m) fits quite well to the numerical model with the damping ratio of 0.01, as observed in Figure 3.5d. However, much stronger damping in the case of the full-scale lighthouse is observed in the east-west direction, from where the ice approaches. Its PDF is narrow and high, as shown in Figure 3.5e. The numerical model would require a much higher damping ratio — more than 0.05 — to mimic the behavior of the full-scale structure. Swaying of the full-scale lighthouse, and thus its acceleration, is additionally damped by interaction with the ice cover that encloses the structure from the eastern direction. In the numerical model, where the predefined ice forces are applied, such interaction is not accounted for.

Dynamic response of the lighthouse model is also analyzed in terms of PSDs of accelerations. The results of PSDs are presented in Figure 3.6.

The energy content of the acceleration signal of the full-scale lighthouse is quite equally distributed — relatively to the numerical model — within the analyzed range of frequencies from 0 Hz to 15 Hz.

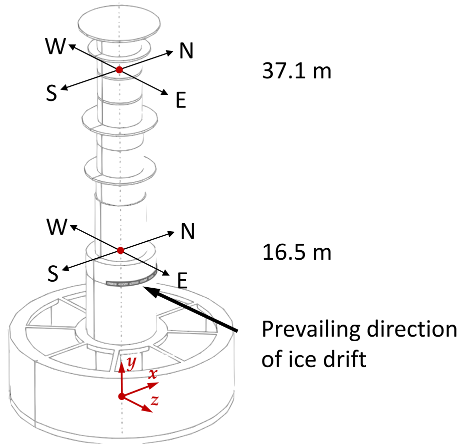

(a) Location of two accelerometers at 16.5 m and at 37.1 m above the seabed.

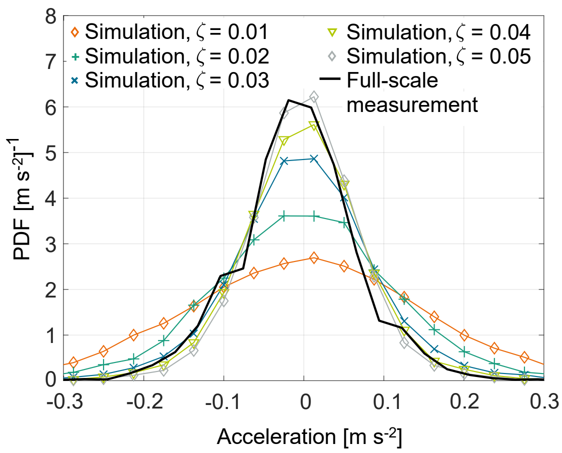

(b) PDF of acceleration at 37.1 m above the seabed, north-south direction (x-axis).

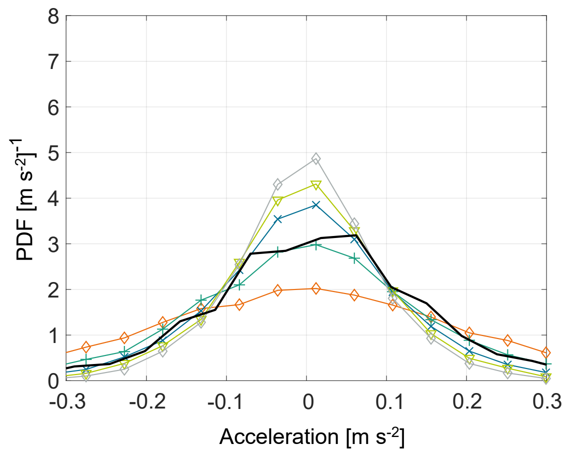

(c) PDF of acceleration at 37.1 m above the seabed, east-west direction (z-axis).

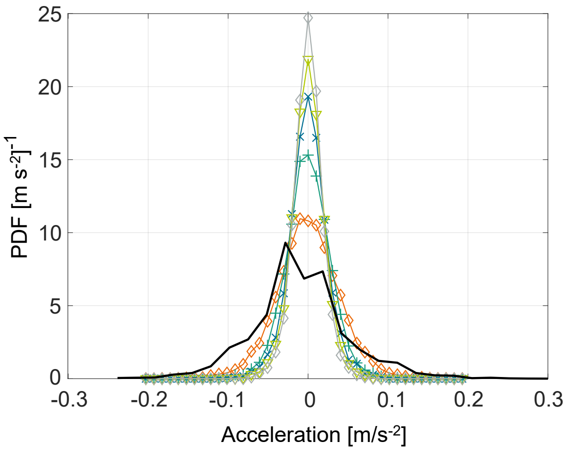

(d) PDF of acceleration at 16.5 m above the seabed, north-south direction (x-axis).

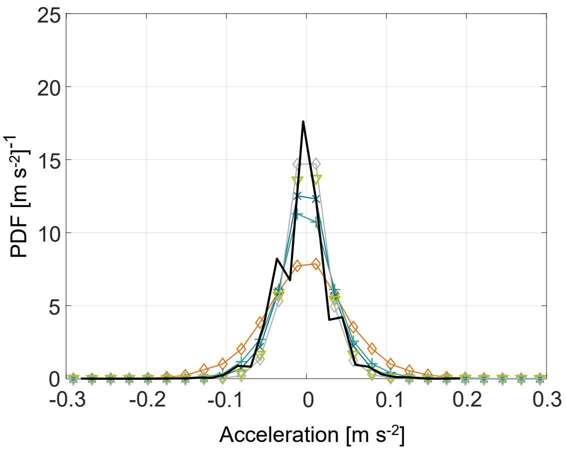

(e) PDF of acceleration at 16.5 m above the seabed, east-west direction (z-axis).

Figure 3.5: PDFs of accelerations at 16.5 m and 37.1 m above the seabed. The structural damping ratio, ζ, of the numerical model is varied from 0.01 to 0.05. Modified subfigures (b), (c), (d), and (e) from Popko (2014, pp. 5–6).

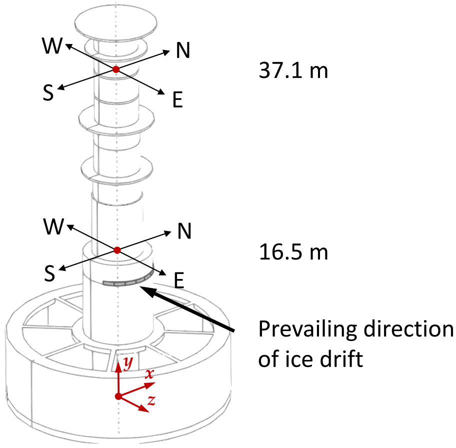

(a) Location of two accelerometers at 16.5 m and at 37.1 m above the seabed.

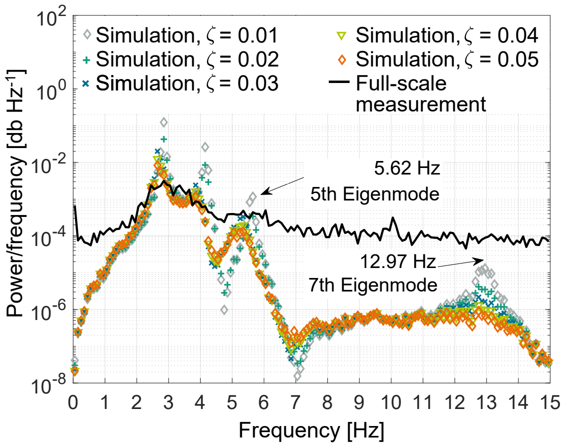

(b) PSD of acceleration at 37.1 m above the seabed, north-south direction (x-axis).

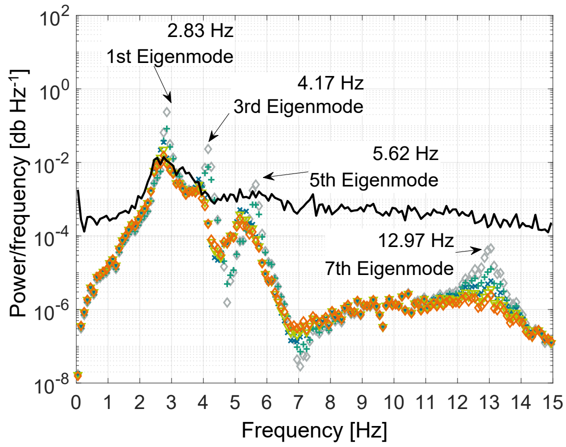

(c) PSD of acceleration at 37.1 m above the seabed, east-west direction (z-axis).

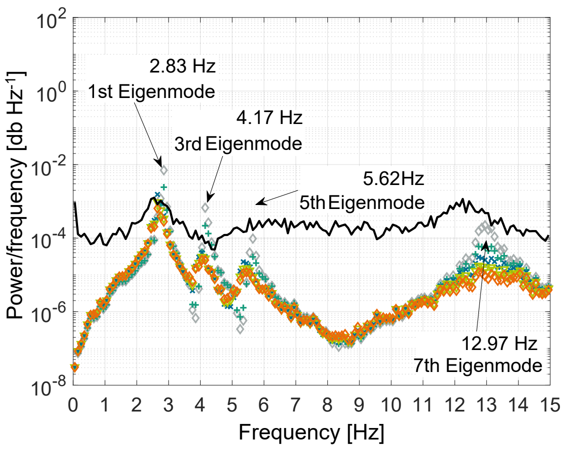

(d) PSD of acceleration at 16.5 m above the seabed, north-south direction (x-axis).

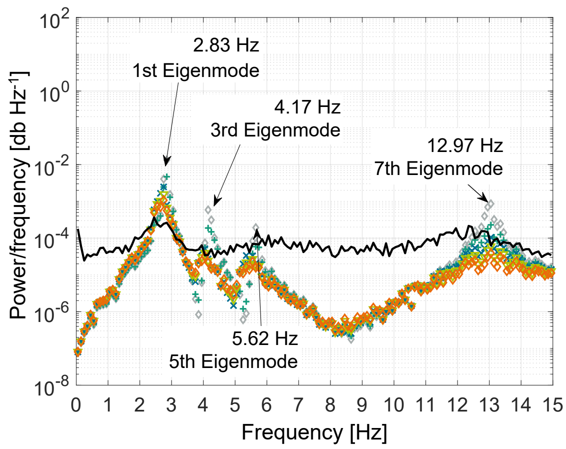

(e) PSD of acceleration at 16.5 m above the seabed, east-west direction (z-axis).

Figure 3.6: PSDs of accelerations at 16.5 m and 37.1 m above the seabed. The structural damping ratio, ζ, of the numerical model is varied from 0.01 to 0.05. Modified subfigures (b), (c), (d), and (e) from Popko (2014, p. 7).

This can be explained by the fact that the full-scale structure experiences random stationary vibrations and responds in a broadband spectrum when ice fails in a continuous brittle crushing mode (Kärnä et al., 2013). This happens at ice velocities from around $0.1\,\mathrm{m\,s^{-1}}$ (Jefferies et al., 2008). On the other hand, in PSDs of accelerations of the numerical models, there are significant spectral gaps, which are pronounced as deep valleys located in-between global eigenfrequencies of the structure. The numerical model with a predefined time series of ice loading is not able to properly mimic the dynamic response of the full-scale lighthouse. This happens due to the lack of the coupling between ice cover and the structure.

Higher energy content is visible at frequency peaks corresponding to first eigenfrequencies of the numerical models. Numerical models are more excited than the real full-scale lighthouse, as the essential coupling; and therefore damping, between the relative movement of the structure and ice is neglected.

3.1.6 Conclusions

The numerical model of the Norströmsgrund lighthouse is set up in Abaqus. The computed eigenfrequencies are in a good agreement with the frequencies measured in situ and those obtained from other numerical models — the difference is below 3% for the first two modes, and increases to around 9.5% for higher modes. Such agreement is achieved after tuning of soil and sand filling properties, which are poorly known and not well documented in other reports.

Numerical models of the lighthouse with different values of structural damping were analyzed to find the best fit to the full-scale response of the Norströmsgrund lighthouse. The numerical models with various damping ratios could only reproduce the dynamic response at a single level (height) and at a certain swaying direction (north-south or east-west). None of them was really able to mimic the response of the Norströmsgrund lighthouse at the two distinct heights simultaneously. It was found out that the structural damping ratio at the top deck (37.1 m above the seabed) should be between 0.02 and 0.05 to account for the additional damping contribution from ice.

Higher damping of the full-scale Norströmsgrund lighthouse is observed from the accelerometer located at the deck close to the MSL (16.5 m above the seabed) and parallel to the direction of ice loading. Such additional damping resulted from the ice-structure interaction. In the analyzed numerical models, such interaction was not accounted for. Therefore, a direct application of any predefined load time histories to the numerical model of the structure might not be the best solution, as important damping from ice is neglected.

Random stationary vibrations could not be properly mimicked by the numerical model, where predefined time series of ice loading were utilized. Due to the lack of ice-structure coupling, the broad range of frequencies (relatively flat spectrum), at which the Norströmsgrund lighthouse responded, could not be reproduced in the simulations. Instead, distinct energy peaks were visible at the dominant frequencies (2.83 Hz, 4.17 Hz, 5.62 Hz, and 12.97 Hz) with deep spectral gaps in-between these frequencies.

This finding is especially important for the numerical analysis of OWTs, which are more dynamic compared to lighthouses. The amplification of certain frequencies in the simulation may affect the fatigue life; and therefore the design requirements for OWTs, as shown by Popko et al. (2013).

The outcome of this research (Popko, 2014) has been used for the revision of Annex D *Recommendations for design of offshore wind turbine support structures with respect to ice loads* in the IEC 61400-3-1 standard (IEC, 2019b). Also, the importance of ice-structure coupling is highlighted by the author in this revision of the standard. Furthermore, several phenomenological ice models for ice-structure interaction (Matlock et al., 1969; Kärnä, 1992; Määttänen, 1998; Hendrikse & Metrikine, 2016) have been suggested by the author in the IEC standard[56].

3.2 Coupled simulation of ice loading

This section describes the validation of the Määttänen-Blenkarn phenomenological ice model[57] for ice-structure interaction against scaled ice tank tests. A simplified, scaled model of the Norströmsgrund lighthouse was built by HSVA. Several ice-structure interaction tests were performed by HSVA with various thicknesses and velocities of the ice cover. The results of those tests are compared against the numerical simulations in MoLWiT performed in the framework of the presented research.

3.2.1 Scaled ice tank tests

Only information concerning the setup of ice tank tests, which are relevant for author's numerical studies, are provided in this section. Therefore, such aspects as a detailed design of the scaled physical model, preparation of the ice cover, and the calibration of sensors for measurements are not covered. The detailed description of the HSVA tests is available in Onken (2012); Onken et al. (2013); Ziemer and Evers (2014).

Scaling laws used for model testing are not discussed in detail herein. A comprehensive explanation of the dimensional analysis and various scaling laws can be found in e.g., Langhaar (1951) or Wolowicz et al. (1979). Scaling issues with respect to ice tank tests are addressed by e.g., Schwarz (1977); Masterson and Spencer (2000); Palmer and Dempsey (2009).

Scaled physical model of the Norströmsgrund lighthouse

A simplified, scaled model of the Norströmsgrund lighthouse was built by HSVA. Its aim was to reproduce the dynamic response at the first dominant frequency of the full-scale lighthouse at the

[56]See Section 2.5.2 for information concerning capabilities and limitations of phenomenological ice models.
[57]Refer to Section 2.5.2 for more information concerning the Määttänen-Blenkarn ice model.

ice level. The physical, scaled model consists of a stiff hollow cylinder, mounting carriage, rigid base, and a set of springs and bearings. The sketch of its assembly is shown in Figure 3.7. The movement of the hollow cylinder is constrained to the unidirectional horizontal displacement.

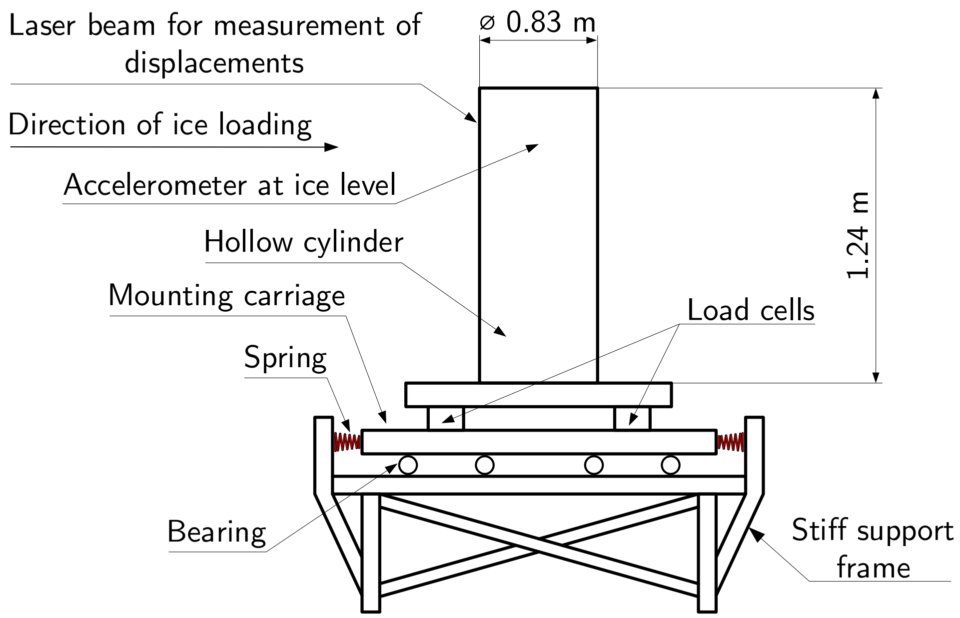

Figure 3.7: Sketch of the simplified, scaled model of the Norströmsgrund lighthouse built by HSVA. Basic components of the model are described and location of the measuring equipment is indicated. Modified figure from Popko and Georgiadou (2015, p. 1815).

The geometric scale factor[58], λ, of 8.67 was used for the design of the physical, scaled model of the Norströmsgrund lighthouse. The Froude scaling[59] of the spring stiffness according to the given λ was not feasible due to several technical reasons reported by Onken (2012, p. 30). Therefore, HSVA decided to reduce the stiffness of springs, while keeping the correctly scaled value of the first dominant frequency of the Norströmsgrund lighthouse.

The main properties of the scaled physical model that are important for its numerical implementation are listed in Table 3.4. Froude scale ratios between different physical values in the model- and full-scale are listed in Table 3.5.

[58]Geometric scale factor implies that the ratios of full-scale characteristic lengths to scaled model lengths are equal.

[59]The Froude number, Fr, is a dimensionless number expressed as a ratio of inertia forces to gravity forces: $Fr = \frac{F_{\text{inertia}}}{F_{\text{gravity}}} = \frac{ma}{mg} = \frac{mv^2/L}{\rho g L^3} = \frac{\rho L^3 v^2/L}{\rho g L^3} = \frac{\rho L^2 v^2}{\rho g L^3} = \frac{v}{\sqrt{gL}}$, where m is the mass; g is the gravitational acceleration; L is the length; ρ is the density; and v is the characteristic flow velocity.

Table 3.4: Main properties of the physical, scaled model of the Norströmsgrund lighthouse built by HSVA (Popko & Georgiadou, 2015).

Parameter	Value	Unit	Description
D	0.83	m	Cylinder diameter at the ice level
m	1544	kg	Oscillating mass including hydro added mass
k	4×10^6	$\mathrm{N\,m^{-1}}$	Stiffness of all springs in horizontal x-direction
c	9431	$\mathrm{kg\,s^{-1}}$	Damping coefficient in horizontal x-direction
ζ	0.06	–	Damping ratio
f_d	8.1	Hz	First damped natural frequency in open water

Table 3.5: Froude scale ratios between different physical values in model- and full-scale.

Physical value	Unit	Model-scale	Full-scale
Frequency	Hz	f_ms	$f_\mathrm{fs} = \lambda^{-0.5} f_\mathrm{ms}$
Density	$\mathrm{kg\,m^{-3}}$	ρ_ms	$\rho_\mathrm{fs} = \lambda^{0} \rho_\mathrm{ms}$
Acceleration	$\mathrm{m\,s^{-2}}$	$\ddot{x}_\mathrm{ms}$	$\ddot{x}_\mathrm{fs} = \lambda^{0} \ddot{x}_\mathrm{ms}$
Time	s	t_ms	$t_\mathrm{fs} = \sqrt{\lambda}\, t_\mathrm{ms}$
Velocity	$\mathrm{m\,s^{-1}}$	$\dot{x}_\mathrm{ms}$	$\dot{x}_\mathrm{fs} = \sqrt{\lambda}\, \dot{x}_\mathrm{ms}$
Stress rate	$\mathrm{Pa\,s^{-1}}$	$\dot{\sigma}_\mathrm{ms}$	$\dot{\sigma}_\mathrm{fs} = \sqrt{\lambda}\, \dot{\sigma}_\mathrm{ms}$
Length	m	L_ms	$L_\mathrm{fs} = \lambda\, L_\mathrm{ms}$
Stress, strength	Pa	σ_ms	$\sigma_\mathrm{fs} = \lambda\, \sigma_\mathrm{ms}$
Force	N	F_ms	$F_\mathrm{fs} = \lambda^{3} F_\mathrm{ms}$
Power	W	P_ms	$P_\mathrm{fs} = \lambda^{3.5} P_\mathrm{ms}$

Summary of ice tank test results

Four series of ice tank tests were conducted by Onken (2012) at HSVA. In the first series, the ice thickness varied between 0.025 m and 0.035 m, and the average flexural strength of ice was 9.85×10^4 Pa. The ice sheet was pushed against the structure with the constant acceleration of $0.002\,\mathrm{m\,s^{-2}}$ to find out different ice-structure interaction modes[60] based on the relative speed of the ice cover. Bending of the ice sheet, ductile crushing, intermittent crushing with frequency lock-in, and continuous brittle crushing were identified during this test.

Continues brittle crushing began at the ice velocity of around $0.11\,\mathrm{m\,s^{-1}}$, when ice started to fail randomly around the circumference of the cylinder. This resulted in the random stationary response of the structure in a broad spectrum of frequencies. Therefore, it was concluded that the ice velocities below $0.11\,\mathrm{m\,s^{-1}}$ might be relevant for the study of frequency lock-in vibrations.

In the second test series, the ice cover thickness was 0.032 m and its flexural strength was around 6.5×10^4 Pa. The events with constant ice sheet velocities of $0.08\,\mathrm{m\,s^{-1}}$, $0.09\,\mathrm{m\,s^{-1}}$, and

[60]The concept of different ice-structure interaction modes is discussed in Section 2.3.

$0.10\,\mathrm{m\,s^{-1}}$ were examined. However, there was no clear pattern of the frequency lock-in vibrations observed (cf. Figure 2.4).

In the third test series, ice thickness was 0.033 m and its average flexural strength was increased to 9.8×10^4 Pa. It was noticed that the intermittent crushing occurred at ice velocities up to $0.04\,\mathrm{m\,s^{-1}}$, where some small structural vibrations were detected.

In the last, fourth series of tests, the ice thickness was increased to 0.049 m to prevent bending of the ice cover and to generate more severe vibrations of the structure. Additionally, the ice strength was reduced to 6.85×10^4 Pa. In the fourth series of tests, multiple frequency lock-in vibrations with large displacement amplitudes of the structure were detected for the ice cover velocity[61] being in the range of $0.01\,\mathrm{m\,s^{-1}}$ to $0.04\,\mathrm{m\,s^{-1}}$.

This model-scale velocity range fits well to the range of the full-scale ice velocities of $0.05\,\mathrm{m\,s^{-1}}$ to $0.12\,\mathrm{m\,s^{-1}}$, where lock-in vibrations were observed at the Norströmsgrund lighthouse by Kärnä et al. (2003, pp. 38, 55, 69). This is confirmed by Eq. 3.6, which describes the relationship between the model-scale and full-scale velocities in case of the Froude scaling:

$$\dot{u}_{\mathrm{fs}} = \dot{u}_{\mathrm{ms}}\sqrt{\lambda} \tag{3.6}$$

The fourth series of HSVA ice tank tests seems to be the most interesting for the validation of the Määttänen-Blenkarn ice model[62] implemented in MoLWiT. According to Määttänen (1998), the model can predict the lock-in vibrations at intermediate ice velocities and the saw-tooth response at low ice velocities.

Further investigation of HSVA results showed that only a limited number of events from the fourth test series could be used for the validation of the numerical ice model in MoLWiT. For example, some transverse vibrations of the cylinder to the ice loading direction were registered, as the physical system had too high transverse flexibility, which was unintentional. Such events were neglected, as they could not be reproduced by the unidirectional ice model. Table 3.6 summarizes the set of events, which might be applicable for the validation of the numerical model.

Palmer et al. (2010) introduced an unifying dimensionless parameter, ψ, to indicate the mode of vibration based on different kinds of dynamic behavior from a number of full- and model-scale tests for vertical structures:

$$\psi = \frac{\dot{u}_{\mathrm{ice}}}{h_{\mathrm{ice}}\, f_{\mathrm{d}}} \tag{3.7}$$

where $\dot{u}_{\mathrm{ice}}$ is the ice cover velocity; h_{ice} is the ice thickness; and f_{d} is the lowest damped natural frequency of the structure.

[61] Ice cover velocity was not measured directly in the vicinity of the structure. Presented values refer to the velocity of the carriage rig that was pushing the ice sheet. The carriage velocity can be assumed to correspond to the ice velocity in the far-field in front of the structure.

[62] See Section 2.5.2 for detailed description of the Määttänen-Blenkarn ice model.

Table 3.6: Ice tank test events with the unidirectional response of the structure from the fourth series of ice tank tests. Table reproduced from Popko and Georgiadou (2015, p. 1816).

Event No	**Ice velocity,** $\dot{u}_{\mathrm{ice}}$ [m s^{-1}]	**Ice thickness,** h_{ice} [m]	**Compressive strength,** σ_{c} [Pa]	**Unifying parameter,** ψ [–]
04100-01	0.010	0.051	1.49×10^5	0.024
04100-03	0.010	0.051	1.49×10^5	0.024
04100-06	0.020	0.051	1.49×10^5	0.048
04100-09	0.030	0.051	1.49×10^5	0.072
04200-06	0.060	0.050	1.14×10^5	0.148
04400-01	0.045	0.047	1.29×10^5	0.118

According to Palmer et al. (2010), the lock-in vibrations occur when ψ is within the range of 0.01 to 0.40. This range matches ψ values calculated for the HSVA model for the lock-in events, as shown in the fifth column of Table 3.6.

Some of the data outputs that were recorded during the ice tank tests are: carriage (ice cover) velocity, $\dot{u}_{\mathrm{ice}}$; the structure displacement at the ice level, x_{s}; structure acceleration, $\ddot{x}_{\mathrm{s}}$; and reaction force at the structure base, F. All measurements were sampled with the average frequency of 56 Hz. These variables are essential for the comparison of dynamic responses of physical and numerical models. The indicative locations of the measuring equipment are shown in Figure 3.7.

Compressive strength tests of ice were conducted with the constant speed of the crosshead of 0.0022 m s^{-1} after the accomplishment of each individual ice tank test. The velocity in the compressive strength test corresponded to the lower range of the ice cover velocity in the ice tank. For the sake of comparability, the same crosshead speed was used for all compressive strength tests throughout the campaign. It should be emphasized that the compressive strength at low ice velocities where the creep failure dominates is around 1.5 to 3 times higher than the crushing strength at higher velocities, where brittle crushing occurs.

3.2.2 Numerical implementation

The multi-component, 3D physical model built at HSVA (see Figure 3.7) is reduced to an equivalent numerical sDOF model, which is implemented in MoLWiT. The numerical sDOF model of the structure is represented by a rigid mass, a spring, and a damper. Its components are depicted in Figure 3.8.

Such simplification is justified as: (1) The numerical implementation of a 3D geometry would not bring extra information to the analysis; (2) The structure designed at HSVA was constrained to the unidirectional motion; and (3) The analyzed ice model is relatively simple (only point force, constant loading area, no ice rubble clearance process). Therefore, the numerical implementation is made as simple as possible to reduce the modeling and computational effort. The governing equation for the sDOF system interacting with the ice model is:

$$m\ddot{x}_s + c\dot{x}_s + kx_s = F_{ice} \tag{3.8}$$

where m is the oscillating mass of the system (see Table 3.4); k is the spring stiffness (see Table 3.4); c is the damping coefficient (see Table 3.4); x_s is the displacement; $\dot{x}_s$ is the velocity; and $\ddot{x}_s$ is the acceleration.

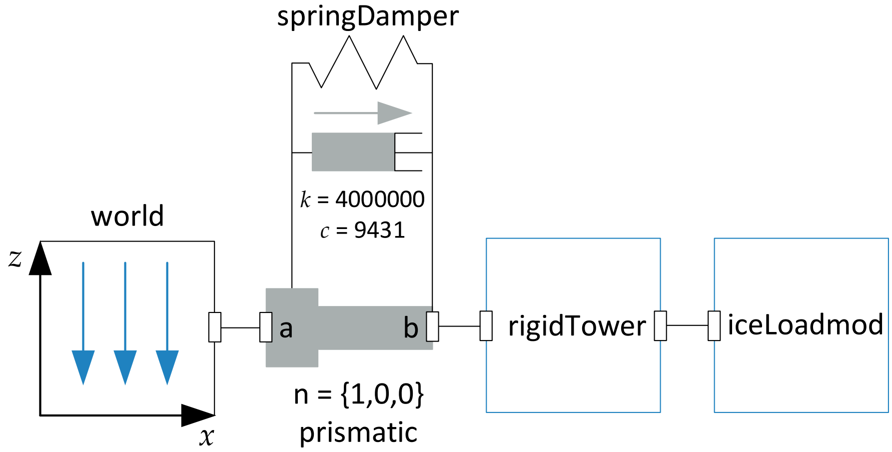

Figure 3.8: Component diagram in Dymola®—a simulation environment used for MoLWiT. Spring and damper are connected through the unidirectional prismatic joint to the rigid cylinder and to the global coordinate system. The Määttänen-Blenkarn ice model is directly connected to the rigid cylinder. Modified figure from Popko and Georgiadou (2015, p. 1817).

Validation of sDOF model

The basic properties of the numerical sDOF model implemented in MoLWiT are validated against the HSVA test results in terms of the static deflection, damped natural frequency, and the free decay response.

A constant horizontal force of 5000 N is applied to the cylinder to examine the static deflection in MoLWiT. The static deflection of the numerical sDOF model is 0.001 25 m. This agrees well with the deflection of the physical, scaled model (Onken, 2012, p. 36).

The numerical sDOF model oscillates with a frequency of around 8.1 Hz, as shown in Figure 3.9a. This is an exact match to the damped natural frequency of the physical, scaled model, which was obtained in the open water environment (Onken, 2012, p. 38). A set of additional frequencies was reported by Onken, as the physical, scaled model was not infinitely stiff (rigid). However, the energy content of those frequencies was considerably lower than the energy present in the dominant frequency of 8.1 Hz. Therefore, these additional frequencies are disregarded in the numerical modeling.

The damping ratio, ζ, of the numerical sDOF model is found to be 0.06, which is the same value as the one obtained from the physical measurements performed at HSVA (Onken, 2012, p. 39).

The result of the free decay simulation in MoLWiT is shown in Figure 3.9b. The oscillation of the mass-spring-damper system diminishes with a damping ratio calculated from the following equation:

$$\zeta = \frac{1}{\sqrt{1+(\frac{2\pi}{\delta})^2}} \tag{3.9}$$

where δ is the logarithmic decrement defined as:

$$\delta = \frac{1}{n} \ln \frac{x_s(t)}{x_s(t+nT)} \tag{3.10}$$

where $x_s(t)$ is the peak amplitude at time, t; $x_s(t+nT)$ is the amplitude of the nT peak period away; and n is the integer number of any successive, positive peak.

To sum up — the basic dynamic properties of the numerical sDOF model implemented in MoLWiT are successfully validated against the measurements of the scaled, physical model built at HSVA.

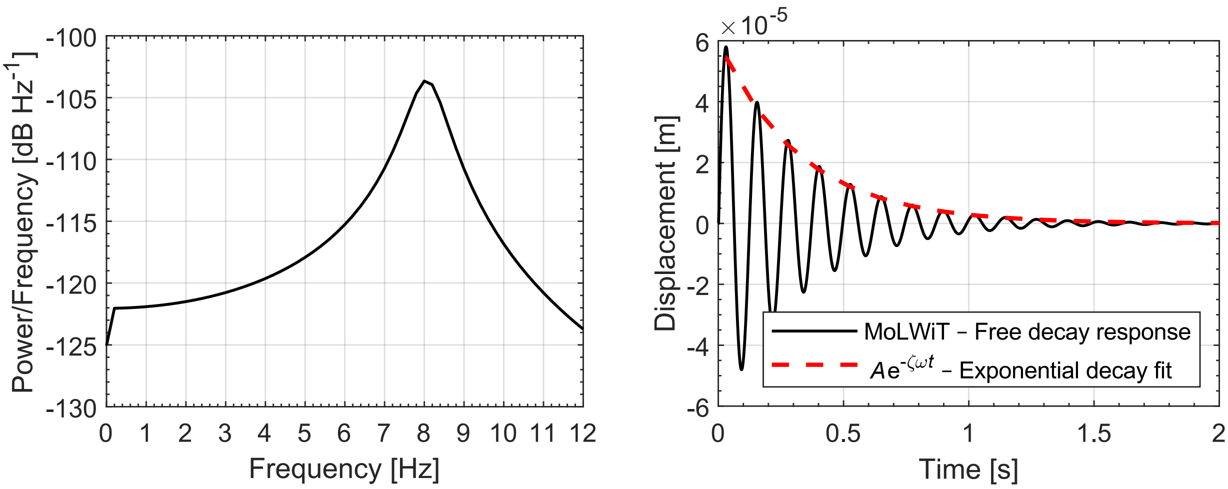

(a) Damped frequency response of the numerical sDOF model to force excitation in MoLWiT.

(b) Free decay response of the numerical sDOF model to force excitation in MoLWiT. The exponential decay curve is plotted with red dashed line.

Figure 3.9: Frequency and free decay response — simulation results from MoLWiT. Modified subfigures from Popko and Georgiadou (2015, pp. 1817–1818).

3.2.3 Calibration of Määttänen-Blenkarn ice model

The original polynomial from Eq. 2.8 (see Section 2.5.2) cannot be directly used for validation of the numerical model against scale tests from HSVA — note that Määttänen tuned his ice model to the full-scale measurements in Cook Inlet.

In order to apply the stress vs. stress rate relation to the scale test data, new stress levels should be calculated as a function of ice velocity at different stress rates. Then, a new polynomial approximation could be fitted to those data. Unfortunately, the unconfined compressive strength tests under different ice cover speeds were not performed at HSVA. Based on such tests it would be possible to derive the stress vs. stress rate relation for the scaled ice created in the ice tank.

Therefore, a new way for estimation of the stress vs. stress rate relation is proposed herein, solely based on the available measurement. The following measurements delivered by HSVA can be used for estimation of the stress vs. stress rate relation:

- Ice cover (carriage) velocity, $\dot{u}_{\mathsf{ice}}$,
- Ice thickness, h_{ice},
- Ice compressive strength, σ_{c},
- Structural acceleration, $\ddot{x}_{\mathsf{s}}$,
- Structural displacement, x_{s},
- Reaction force at the structure base, F.

The compressive strength of ice, σ_{c}, at each time step, can be approximated by relating it to the reaction force at the structure base, F, and to the loading area, A:

$$\sigma_{\mathsf{c}}(t) = \frac{F(t)}{A} \tag{3.11}$$

The loading area, A, is assumed to be constant and determined by the average ice thickness, h_{ice}, multiplied with the structure diameter, D, as no other precise assessment is available from the measurements. This assumption is rather conservative. The real effective contact area is smaller, as most of the ice load is imposed on the structure through a line-like zone in the middle part of the ice sheet, as observed by e.g., Joensuu and Riska (1989); Määttänen et al. (2012). This would translate to higher σ_{c} in Eq. 3.11.

The stress rate for each time step can be approximated from the following equation:

$$\dot{\sigma}(t) = \left[\dot{u}_{\mathsf{ice}}(t) - \dot{x}_{\mathsf{s}}(t)\right] \frac{4\sigma_{\mathsf{c}}}{\pi h_{\mathsf{ice}}} \tag{3.12}$$

where the structure velocity, x_{s}, and the ice cover velocity, $\dot{u}_{\mathsf{ice}}$, were measured at each time step. The average compressive strength, σ_{c}, and the ice thickness, h_{ice}, are kept constant.

Having $\sigma_{\mathsf{c}}(t)$ from Eq. 3.11 and $\dot{\sigma}(t)$ from Eq. 3.12, a cloud of stress-stress rate points can be plotted for each analyzed ice event from Table 3.6.

All charts shown in Figure 3.10 are plotted with 1:1 aspect ratio between units of the stress and the stress rate axis. The analyzed events represent the frequency lock-in mode.

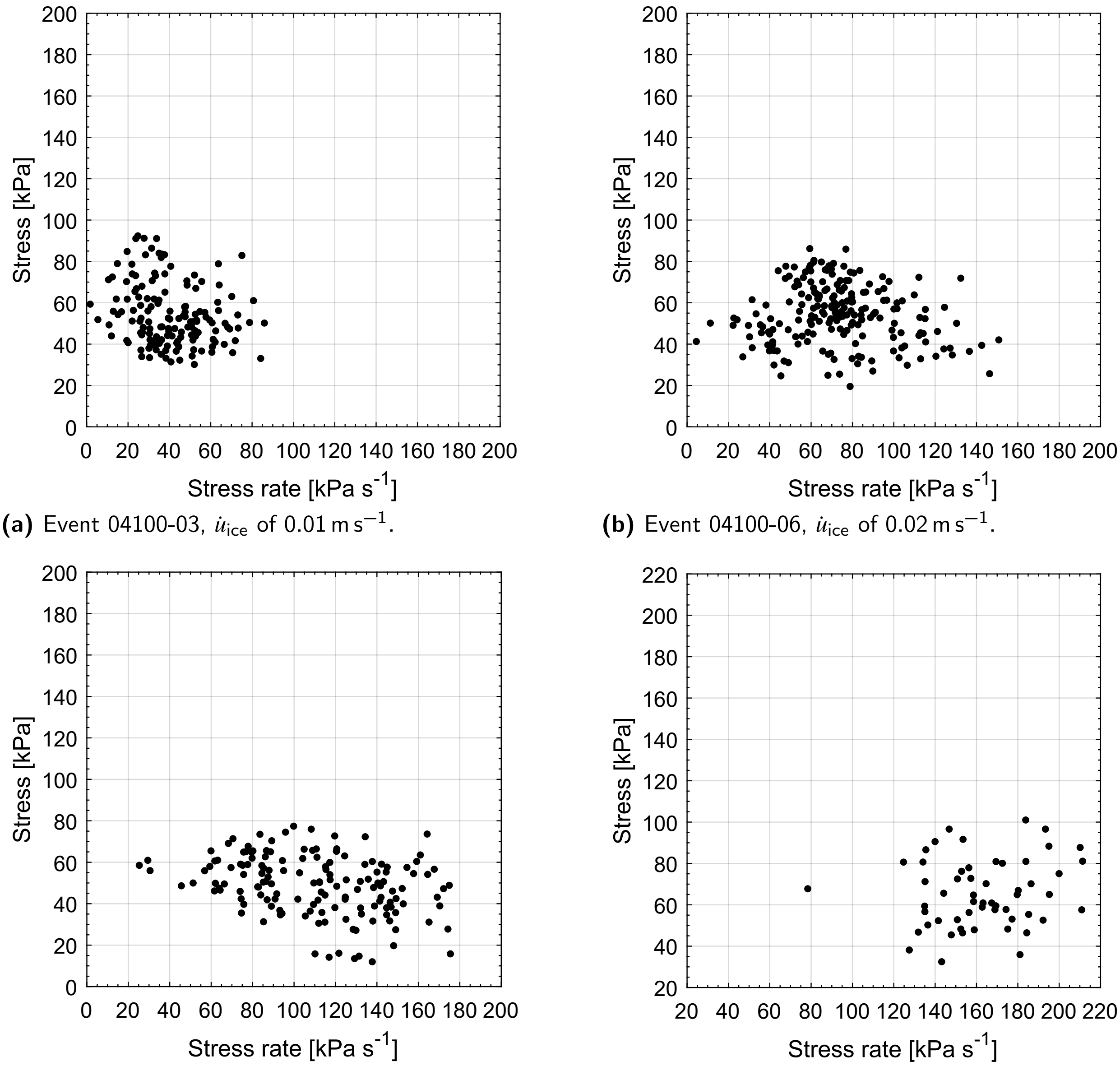

(a) Event 04100-03, $\dot{u}_{\text{ice}}$ of 0.01 m s^{-1}.

(b) Event 04100-06, $\dot{u}_{\text{ice}}$ of 0.02 m s^{-1}.

(c) Event 04100-09, $\dot{u}_{\text{ice}}$ of 0.03 m s^{-1}.

(d) Event 04200-06, $\dot{u}_{\text{ice}}$ of 0.06 m s^{-1}.

Figure 3.10: Stress-stress rate relationship, where every point in the cloud represents a single time step. Rescaled subfigures from Popko and Georgiadou (2015, p. 1818).

In the case of intermittent crushing of full-scale ice, a high variability in stress level might be expected for the relatively low change in stress rate. This is shown in Figure 3.11a, where the stress-stress rate relationship based on Määttänen's fit to the full-scale data from Cook Inlet is plotted. The steeply declining slope characterizing the intermittent crushing of ice and the steady-state response of a structure is indicated with an arrow. However, for scaled ice created at HSVA the slope would decline more gently, as shown in Figure 3.11b.

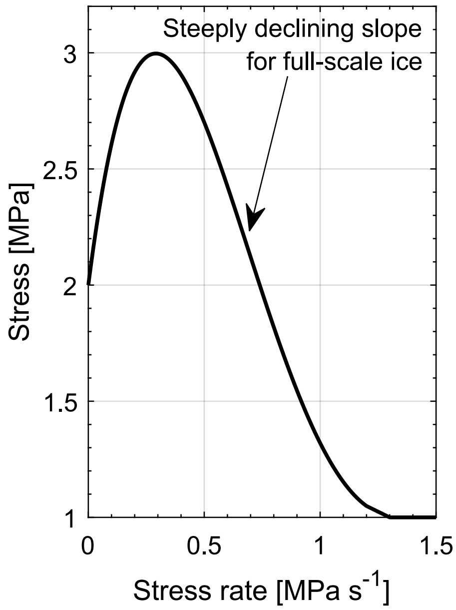

(a) Määttänen's fit to the full-scale measurements from Cook Inlet (see Eq. 2.8).

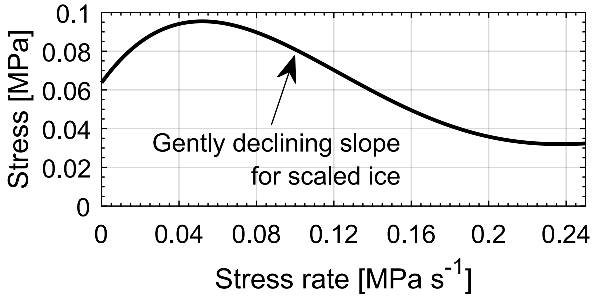

(b) Määttänen-Blenkarn curve scaled with λ of 31.4 to match the highest value of stress (0.095 MPa) from ice tank test events.

Figure 3.11: Stress-stress rate relationship for full-scale and for scaled ice plotted with 1:1 aspect ratio between units on stress and stress rate axis. Modified subfigures from Popko and Georgiadou (2015, p. 1818).

According to the Froude scaling, the relationship between a prototype (full-scale) and a model (scaled) stress is linearly scaled with λ, whereas stress rate is scaled with $\sqrt{\lambda}$, as shown in Table 3.5. This would explain why there is no steeply declined pattern visible in the stress-stress rate charts in Figure 3.10 for the ice tank test data — dots are scattered in clouds of horizontal shape. In other words — in the measurements of scaled ice there is less variability of stress but a lot of variability in the stress rate. This is opposite to the full-scale measurements from Cook Inlet (Blenkarn, 1970, p. 33).

The original Määttänen-Blenkarn curve was scaled with λ of 31.4 to match the highest stress value of 0.095 MPa that was observed in Figure 3.10 during various ice tank test events.

3.2.4 Validation of coupled simulations against measurements

The dynamic analysis of the simplified sDOF numerical model of the structure built at HSVA was executed in the time domain. The relative velocity between the ice cover and the structure was calculated at each time step resulting in variation of the stress rate. An explicit time integration scheme was utilized with a sufficiently small time step to ensure proper accuracy. The convergence of the results was achieved with a simulation time step of 0.001 s.

The locked-in vibrations lasted for around 3 s in the ice tank events 04100-03, 04100-06, and 04100-09. The time duration of the lock-in vibrations in the events 04200-06 and 04400-01 was even shorter. Therefore, the results of these two latter events are considered as too short and not presented herein.

Comparison of structural velocities

The comparison between measured and simulated time histories of the structural velocity component in the horizontal plane is shown in Figures 3.12a, 3.12c, and 3.12e for events 04100-03, 04100-06, and 04100-09, respectively.

The simulated results are in a relatively good agreement in terms of the maximum peak amplitudes with the measured ones. The maximum values of the simulated velocities are slightly overestimated compared to the measured values — usually in the range of 4% to 10%. The differences diminish for higher ice velocities. Peak-to-peak amplitudes of structural velocities during the lock-in vibrations are in the range of 0.8 to 1.0 of the ice cover velocity for both the numerical simulation and the measured time histories. This range is slightly lower than the one (1.0 to 1.4) observed by Kärnä and Muhonen (1990) in other model-scale tests.

In Figure 3.12a, the measured velocity signal has two distinct frequency components — the first one at around 6.9 Hz and the second one at around 2.3 Hz. The first frequency is around 15% lower than the natural damped frequency (8.1 Hz) obtained in the open water conditions (see Figure 3.9) — this is well aligned with observations of different full-scale measurements (Kärnä & Turunen, 1989; Kärnä et al., 2003; Heinonen et al., 2004). The second frequency is associated with the coupling between the dominant frequency of the structure and the crushing frequency of ice. Once the ice cover velocity increases to $0.03\,\mathrm{m\,s^{-2}}$ (Figure 3.12e), the structural velocity signal is mostly governed by the frequency close to the dominant structural frequency.

It must be emphasized that there is no proper understanding among the researcher community on how the ice-structure interaction influences the dominant frequency. This phenomenon is not captured correctly in the simulation results due to the oversimplification of the ice model, which can only predict a constant oscillation amplitude at the dominant structural frequency during the lock-in event.

Comparison of reaction forces

Figures 3.12b, 3.12d, and 3.12f show the simulated and measured force time histories for the events 04100-03, 04100-06, and 04100-09, respectively.

A good match of the upper bound of reaction forces for the simulated and measured data is observed for the lowest ice velocity of $0.01\,\mathrm{m\,s^{-2}}$ in Figure 3.12b. The discrepancy increases for higher velocities, where the simulated results overestimate forces recorded during the tank test.

Similar conclusions concerning the frequency content in the force measurements — as for the velocity measurements — can be made when looking at the force plots.

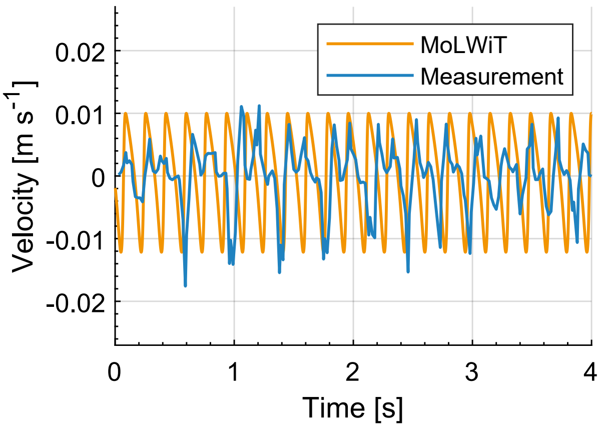

(a) Event 04100-03, $\dot{u}_{\mathrm{ice}}$ of 0.01 m s^{-1}.

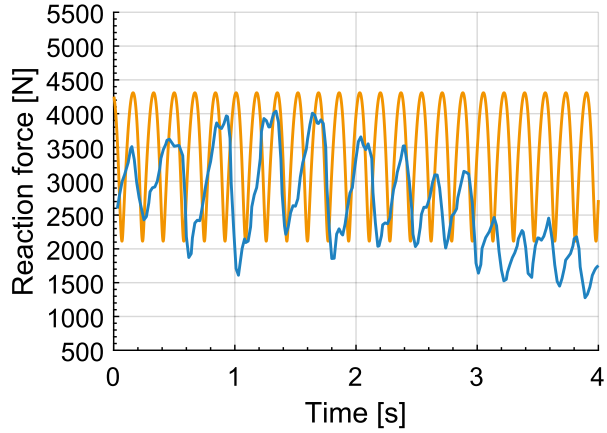

(b) Event 04100-03, $\dot{u}_{\mathrm{ice}}$ of 0.01 m s^{-1}.

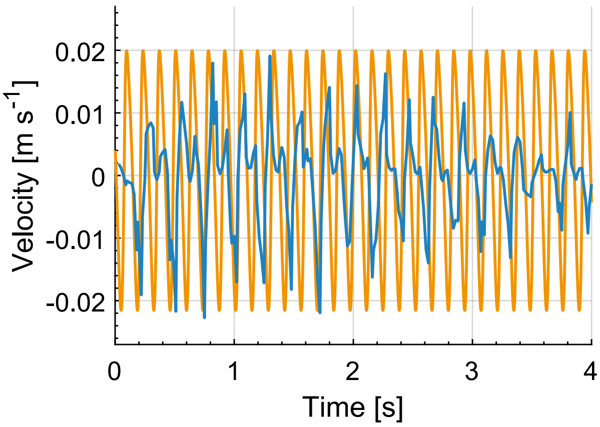

(c) Event 04100-06, $\dot{u}_{\mathrm{ice}}$ of 0.02 m s^{-1}.

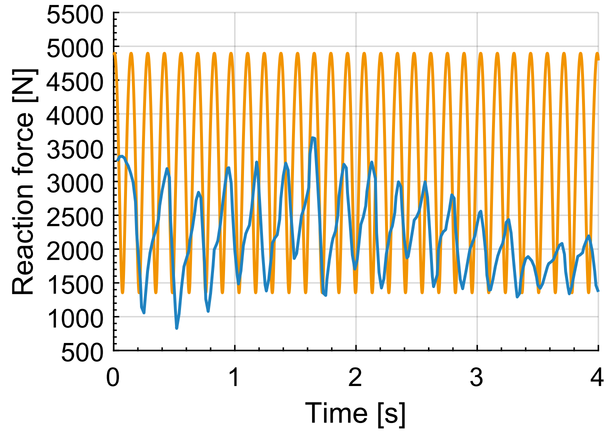

(d) Event 04100-06, $\dot{u}_{\mathrm{ice}}$ of 0.02 m s^{-1}.

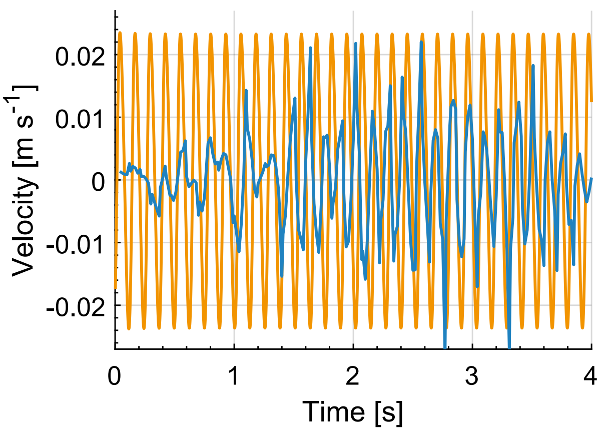

(e) Event 04100-09, $\dot{u}_{\mathrm{ice}}$ of 0.03 m s^{-1}.

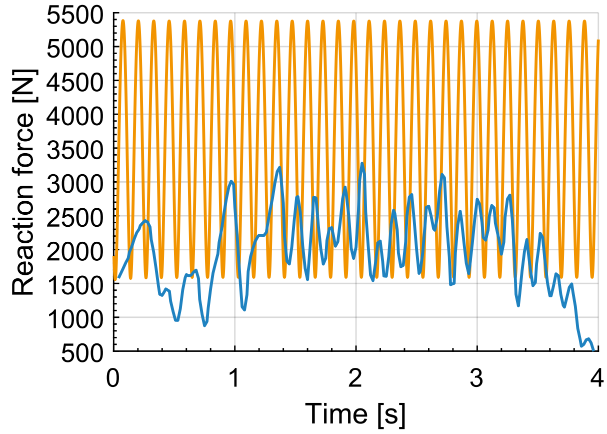

(f) Event 04100-09, $\dot{u}_{\mathrm{ice}}$ of 0.03 m s^{-1}.

Figure 3.12: Structure velocities (left column) and reaction forces (right column) at three ice events. Simulation results are marked with orange color, measurements with blue. Modified subfigures from Popko and Georgiadou (2015, p. 1820).

3.2.5 Conclusions

A simplified sDOF numerical model of the lighthouse is implemented in MoLWiT based on the design data from HSVA. Its basic dynamic properties are successfully validated against the physical model data.

Only a limited set of ice tank test measurements can be used for the validation of the Määttänen-Blenkarn ice model. Its applicability is limited to a particular type of ice-structure interaction problems, such as frequency lock-in vibrations or the saw-tooth response. Therefore, measurements with brittle crushing events at higher ice velocities, characterized by the random response of the structure could not be reproduced by this ice model. However, such capability could potentially be added by including a random generator function to simulate the variation of the ice force in the continuous brittle crushing mode.

In many cases, transverse vibrations of the cylinder to the ice loading direction were registered by HSVA. Such behavior cannot be reproduced with an sDOF numerical model of the structure and the unidirectional ice load model.

The Määttänen-Blenkarn model is tuned to the scaled ice tests based on the indirect way of finding stress vs. stress rate relationship, solely based on the measured ice-structure interaction data — as the uniaxial compressive strength at different ice velocities has not been measured at HSVA.

Nevertheless, the peak amplitudes of simulation structural velocities match well with the physical measurements. Even closer alignment could potentially be reached if the stress vs. stress rate curve was individually scaled to every single event.

It must be emphasized that there is no proper understanding among the researcher community on how the ice-structure interaction influences the dominant frequency of the structure. This phenomenon is not captured correctly in the simulation results due to the oversimplification of the ice model, which can only predict a constant oscillation amplitude at the dominant structural frequency during the lock-in event.

The scaled ice model failed in predicting reaction forces. The upper bound of the reaction force was only matched for one event with a relatively low ice velocity. The discrepancies between the simulation results and the measurements increased for higher ice velocities.

To sum up — the Määttänen-Blenkarn ice model might provide reasonable results once the relationship between the ice stress and stress rate is well known. However, such full-scale measurements are very difficult to obtain in situ and are usually not available. This is a severe limitation in the application of this ice model in the design process and load certification for OWTs. Nevertheless, it can be used for studying basic dynamics of OWTs, but rather on a theoretical, academic level.

Chapter 4

Verification and extension of Hendrikse ice model

This chapter presents the results of the verification of the Hendrikse ice model (Hendrikse & Metrikine, 2015, 2016), which has been implemented (fully-integrated) in MoLWiT against its source code in MATLAB®.[63] A stepwise procedure for the verification is utilized to mitigate and to trace back possible errors coming from the new implementation of the ice model in MoLWiT.

Section 4.1 shows the verification of the ice model interacting with an sDOF structure. The results obtained from the source code in MATLAB® and the new implementation in MoLWiT are compared and discussed.

The parameters of the ice model source code were derived based on the scaled ice properties. It is necessary to retune these ice properties in order to obtain the properties that would be representative for the southern Baltic Sea. Section 4.2 presents a derivation of the ice properties suitable for the simulation of the ice-structure interaction in full-scale.

In Section 4.3 an FEM code for modeling mDOF structures is implemented in MATLAB®. The source code of the ice model is extended to interact with the newly implemented mDOF structure. And finally, the mDOF structure and the extended ice model are coupled in one fully-integrated simulation. The coupling is cross-verified against fully-integrated simulations in MoLWiT in Section 4.4. For these simulations, the full-scale ice parameters are used, which have been estimated in Section 4.2.

4.1 Ice model interacting with sDOF structure

The verification of the ice model interacting with the sDOF structure is divided in two steps (cases) of increasing complexity:

[63] The MATLAB® source code of the ice model — version No. 25-09-2016 — was provided by Dr. Hendrikse from the Delft University of Technology. See Section 2.5.2 for more information concerning the ice model.

Case 1. To test the implementation of the deterministic equations for the ice stripe and the coupling between the ice stripe and the sDOF structure in MoLWiT.
The ice model is simplified to a single ice stripe. The random number generator is disabled, which means that the initial position of the ice stripe with respect to the structure is predefined. The results are compared in terms of time series.

Case 2. To test the implementation of the random number generator in MoLWiT and the ability to simulate different ice-structure interaction modes.
The ice model uses multiple ice stripes, which initial positions with respect to the equilibrium position of the sDOF structure, are derived from uniformly distributed random numbers. The results are compared in terms of time series, PDFs, and PSDs.

Table 4.1 lists properties of the sDOF structure that are used for the verification simulations. These properties are derived from the source code of the ice model.

Table 4.2 lists the reference ice properties, which are utilized as an input for the calculation of the derived parameters that are used by the ice model (cf. Figure 2.10).

The derived parameters of the ice model for the verification Case 1 and Case 2 are listed in Table 4.3 (cf. Figure 2.9 and Eqs. 2.10–2.12). All equations describing the derived parameters, their explanations, and assumptions are presented in Hendrikse and Metrikine (2015, 2016).

Table 4.1: Structural and geometrical properties of the sDOF model used in simulations.

Parameter	Value	Unit	Description
D	0.2	m	Cylinder diameter at the ice level
m	1.58×10^4	kg	Mass
k	2.50×10^6	$\mathrm{N\,m^{-1}}$	Spring stiffness
c	3.98×10^3	$\mathrm{kg\,s^{-1}}$	Damping coefficient
f_n	2.0	Hz	Natural frequency

Table 4.2: Reference ice parameters, which characterize the ice type — extracted from the source code (cf. Figure 2.10).

Parameter	Value	Unit	Description
h_ice	0.05	m	Ice thickness
F_brittle	5000	N	Mean value of the global brittle crushing load at v_brittle and above
F_max	25 000	N	Maximum ice load at the ductile-to-brittle transition
$F_{2v\mathrm{db}}$	15 000	N	Mean value of the global ice load at $2v_\mathrm{db}$
σ_ice	800	N	Standard deviation of the brittle crushing load, F_brittle
v_db	0.001	$\mathrm{m\,s^{-1}}$	Transition velocity between ductile and brittle crushing regions
v_brittle	0.1	$\mathrm{m\,s^{-1}}$	Transition velocity to continuous brittle crushing
f_peak	20	Hz	Peak frequency in the failure spectrum of ice at v_brittle
t_peak	60	s	Time of peak load at v_db for a rigid structure
c_ref	0.3	–	Fraction of the ice stripe deformation when visco-plasticity initiates
f_n	0.95	–	Peak load factor at v_db

Table 4.3: Derived parameters, which are used for the definition of ice stripes in the ice model in the verification Cases 1 and 2 (cf. Figure 2.9).

Parameter	Value (Case 1)	Value (Case 2)	Unit	Description
N_{st}	1	92	–	Number of individual ice stripes, see Hendrikse and Metrikine (2016, p. 133) for equation
k_{ice}	1.25×10^7	1.36×10^5	$\mathrm{N\,m^{-1}}$	Front stiffness of the individual ice stripe, see Hendrikse and Metrikine (2016, p. 133) for equation
c_{c}	2.50×10^7	2.72×10^5	$\mathrm{kg\,s^{-1}}$	Rear creep damper in the individual ice stripe, see Hendrikse and Metrikine (2016, p. 131) for equation
$k_{\mathrm{v\text{-}p}}$	2.50×10^6	2.72×10^4	$\mathrm{N\,m^{-1}}$	Stiffness of the viscoplastic element in the ice stripe, see Hendrikse and Metrikine (2015, p. 341) for equation
$c_{\mathrm{v\text{-}p}}$	7.50×10^6	8.15×10^4	$\mathrm{kg\,s^{-1}}$	Damping of the viscoplastic element in the ice stripe, see Hendrikse and Metrikine (2015, p. 341) for equation
F_{slip}	7.50×10^3	81.52	N	Load at which the viscoplastic element is activated, see Hendrikse and Metrikine (2016, p. 132) for equation
δ_{crit}	0.002	0.002	m	Critical deformation of the ice stripe upon its failure, see Hendrikse and Metrikine (2015, p. 340) for equation
u_{init}	0.0003	$u_{\mathrm{init}} \sim U(0,\ 0.01)$	m	Offset of the individual ice stripe upon its failure (with respect to the structure equilibrium position)

Verification results for Case 1

Figure 4.3 shows time series obtained with the source code of the ice model in MATLAB®, its modified version, and the MoLWiT implementation. Simulations are performed for $\dot{u}_{\mathrm{ice}}$ of $0.003\,\mathrm{m\,s^{-1}}$, h_{ice} of 0.05 m, and the output time step of 0.001 s. In Dymola® explicit ordinary differential equations (ODEs) are solved[64] by the variable time step LSODAR method with both relative[65] and absolute[66] tolerances of 1.0×10^{-5}. In MATLAB® the ODE45 variable time step solver[67] is used with a relative tolerance of 1.0×10^{-5} and an absolute tolerance of 1.0×10^{-7}.

A problem in the MATLAB® source code of the ice model was discovered during the verification. It was found that the event detection function[68] is not working properly. The cause of the problem is nested in MATLAB® ODE solver and is related to the limitations of this solver[69]. During the

[64] MoLWiT utilizes Dymola® as a simulation environment. For this work Dymola® 2020 was used.
[65] Relative tolerance is the error relative to the size of the state.
[66] Absolute tolerance is the largest error when the state approaches zero.
[67] An explicit Runge-Kutta (4,5) formula developed by Dormand and Prince (1980) is used in ODE45 solver.
[68] The ODEs solver should determine an appropriate time to stop the solution. For example, the ODE solver should stop once the individual ice stripe breaks. However, the ODE solver does not know beforehand when the breaking of the ice stripe will occur — as the breaking may occur at any time during the solution. The event location function helps to find out the exact time point at which the ice stripe breaks.
[69] According to MATLAB® online documentation, the root-finding mechanism employed by the ODE solver has the following limitations: (1) "If a terminal event occurs during the first step of the integration, then the solver registers the event as nonterminal and continues integrating"; (2) "If more than one terminal event occurs during the first step, then only the first event registers and the solver continues integrating"; and (3) "Zeros are determined by sign crossings between steps. Therefore, zeros of functions with an even

iteration process, the ice speed at the back of the ice sheet ($\dot{u}_{\text{ice}}$) was occasionally computed as greater than the initially prescribed value. This is an obvious mistake, as $\dot{u}_{\text{ice}}$ is defined as the constant velocity of the ice under the assumption that the inertia of the ice cover is high (cf. Figure 2.9). Two additional *if-else statements* were added in the source code to make sure that the *contact* and *contact slip* conditions are correctly fulfilled, as shown in pseudocodes in Figures 4.1 and 4.2.

Such problem has not been observed in MoLWiT where these additional *if statements* were not included. After the modification of the source code in MATLAB® an exact match between the results of MATLAB® (blue curve) and MoLWiT (orange curve) is achieved as shown in Figure 4.3. The MATLAB® results before the modification are depicted with the grey curve.

It should be emphasized that the discovered limitation is minor and it does not impair the simulation capabilities of the source code. Despite this limitation, the source code can correctly reproduce different regions of ice-structure interaction. Nevertheless, it is recommended to apply the suggested correction.

if *contact* condition is fulfilled **then**
    if $[u_{\text{ice2}} - x_{\text{s}}] \frac{k_{\text{ice}}}{c_{\text{c}}} < 0$ **then**
        $\dot{u}_{\text{ice3}} = \dot{u}_{\text{ice}}$
    else
        $\dot{u}_{\text{ice3}} = \dot{u}_{\text{ice}} - [u_{\text{ice2}} - x_{\text{s}}] \frac{k_{\text{ice}}}{c_{\text{c}}}$
    end
end

Figure 4.1: Pseudocode where the inner if-else statement is introduced to prevent $\dot{u}_{\text{ice3}}$ becoming larger than $\dot{u}_{\text{ice}}$ if elastic part of the individual ice stripe is lesser than 0.

if *contact slip* condition is fulfilled **then**
    if $\frac{F_{\text{slip}}}{c_{\text{v-p}}} + \frac{k_{\text{v-p}}}{c_{\text{v-p}}} [u_{\text{ice3}} - u_{\text{ice2}}] + \frac{k_{\text{ice}}}{c_{\text{v-p}}} [x_{\text{s}} - u_{\text{ice2}}] < 0$ **then**
        $\dot{u}_{\text{ice2}} = \dot{u}_{\text{ice3}} + \frac{F_{\text{slip}}}{c_{\text{v-p}}} + \frac{k_{\text{v-p}}}{c_{\text{v-p}}} [u_{\text{ice3}} - u_{\text{ice2}}] + \frac{k_{\text{ice}}}{c_{\text{v-p}}} [x_{\text{s}} - u_{\text{ice2}}]$
    else
        $\dot{u}_{\text{ice2}} = \dot{u}_{\text{ice3}}$
    end
end

Figure 4.2: Pseudocode where the inner if-else statement is introduced to prevent $\dot{u}_{\text{ice2}}$ becoming larger than $\dot{u}_{\text{ice}}$ if viscoplastic part of the individual ice stripe is larger than 0.

number of crossings between steps can be missed". Information cited from the MathWorks® web page: https://de.mathworks.com/help/matlab/math/ode-event-location.html (Last accessed: June 1, 2020).

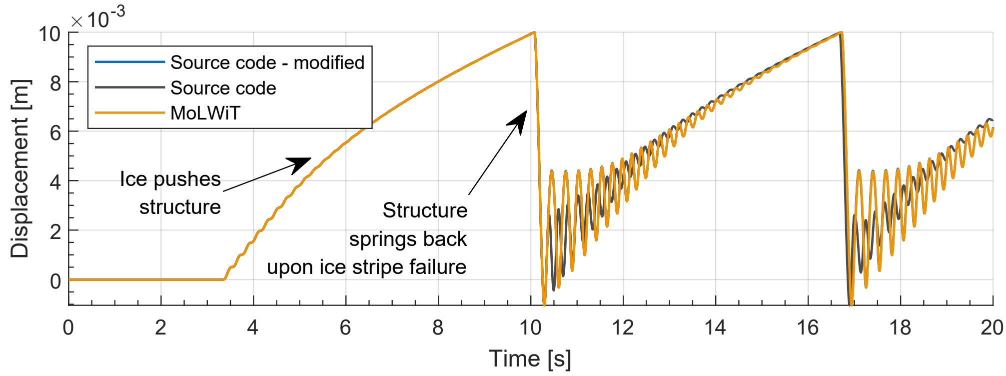

(a) Displacement of the sDOF structure.

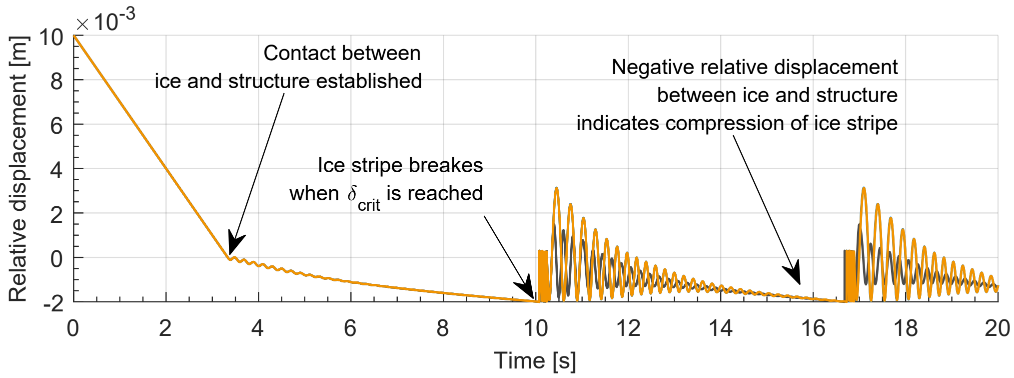

(b) Relative displacement between the front of the ice stripe and the sDOF structure.

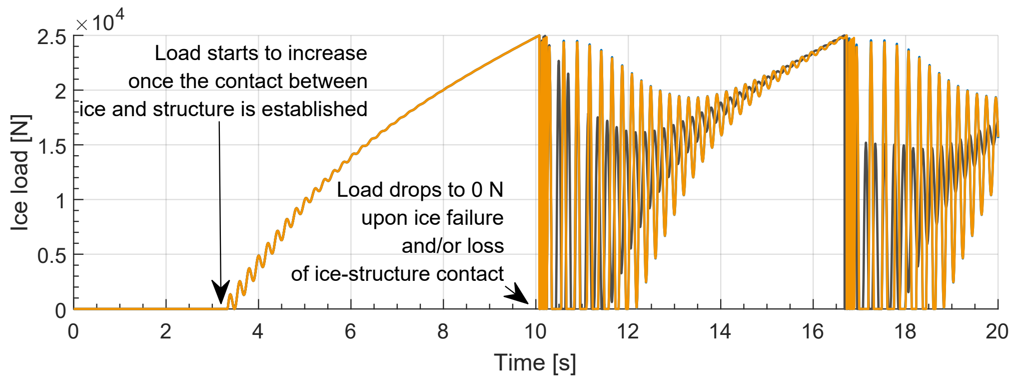

(c) Ice load imposed on the sDOF structure.

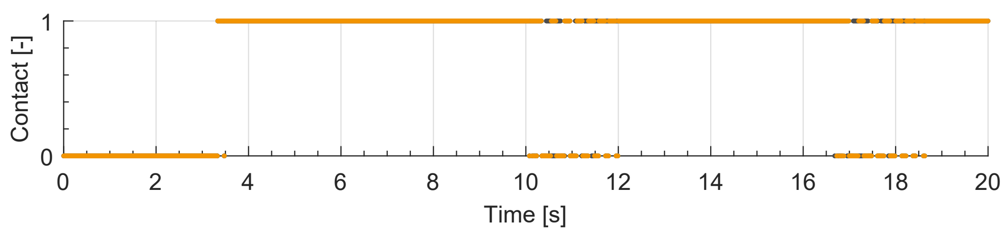

(d) Contact between the front of the ice stripe and the sDOF structure. 1 – contact, 0 – no contact.

Figure 4.3: Comparison of time series obtained with the source code of the ice model and the MoLWiT implementation. Simulations performed for $\dot{u}_{\text{ice}}$ of 0.003 m s^{-1}, h_{ice} of 0.05 m, 1 ice stripe, and output time step of 0.001 s.

Verification results for Case 2

Figures 4.4, 4.5, and 4.6 show verification results of the sDOF structure interacting with the ice cover modeled with 92 ice stripes, at three distinct ice velocities ($0.001\,\mathrm{m\,s^{-1}}$, $0.03\,\mathrm{m\,s^{-1}}$, and $0.2\,\mathrm{m\,s^{-1}}$) corresponding to the main three ice-structure interaction modes[70]. The results are difficult to interpret by visual inspection of the time series due to their stochastic nature. Therefore, the comparison is supplemented with PDF and PSD analysis of those time series. Also, basic statistical properties — such as mean and standard deviation of signals — are compared in terms of the percentage differences between them. The percentage difference is calculated as:

$$\left|\frac{value_1 - value_2}{(value_1 + value_2)/2}\right| 100\% \tag{4.1}$$

In Dymola® explicit ODEs are solved by the LSODAR method with both relative and absolute tolerances of 1.0×10^{-5} and the variable time step. In MATLAB® the ODE45 variable time step solver is used with a relative tolerance of 1.0×10^{-5} and an absolute tolerance of 1.0×10^{-7}. The output time step is set to 0.001 s in both tools. The simulation time is set to 600 s to assure statistically comparable results. The first 20 s are cut out from the simulation results for $\dot{u}_{\mathrm{ice}}$ of $0.03\,\mathrm{m\,s^{-1}}$ and $0.2\,\mathrm{m\,s^{-1}}$. This is necessary to remove initial numerical transients, which would impact the PSD and PDF analysis.

The intermittent crushing mode is simulated with a low ice velocity of $0.001\,\mathrm{m\,s^{-1}}$. The displacement of the sDOF structure and the ice load increase nonlinearly due to creep and viscoplastic deformation in ice stripes, as shown in Figures 4.4a and 4.4c. The time series results from the source code and MoLWiT overlap almost entirely. Small offsets in the time series can be caused by the random number generators, which define initial positions of the ice stripes at the beginning of the simulation in both MoLWiT and MATLAB®. There is also a very good match in PDFs and PSDs computed out of all time series shown in Figure 4.4.

The frequency lock-in mode is captured at the ice velocity of $0.03\,\mathrm{m\,s^{-1}}$. The frequency lock-in is identified when the structural velocity is in the range of 1 to 1.5 of the ice cover velocity (see Section 2.3). This is visible in PDF of the bimodal shape, as shown in Figure 4.5b. Furthermore, distinct frequency peaks are visible at around 2 Hz and 4 Hz in PSDs of displacement, velocity, and load. There is a very good match of all results obtained from both tools.

The brittle crushing mode is captured at the ice velocity of $0.2\,\mathrm{m\,s^{-1}}$. It is characterized by a very small amplitude of the structural velocity — in the analyzed case, it is one order lower than the ice velocity. Furthermore, PDF of the structure velocity (Figure 4.6b) has a normal distribution shape in contradiction to the bimodal shape that is observed in the case of the frequency lock-in mode (Figure 4.5b). Also, the PSD signal of the structural velocity (Figure 4.6b) carries much less energy — a difference of two orders of magnitude — compared to the PSD signal at the frequency lock-in mode (Figure 4.5b).

[70]See Section 2.3 for description and classification of ice-structure interaction modes.

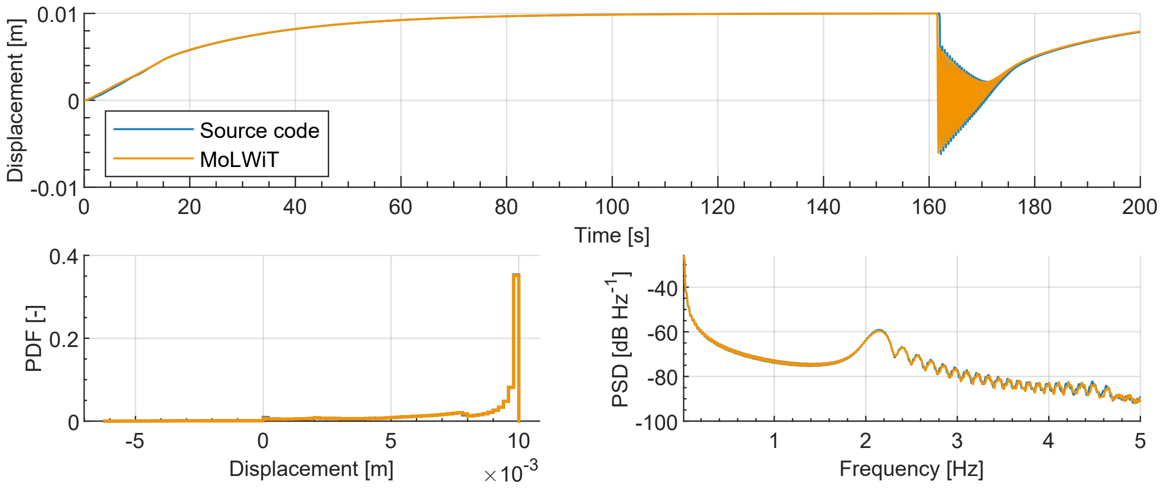

(a) Structure displacement at ice creep followed by intermittent crushing — zoomed time series, PDF, and PSD.

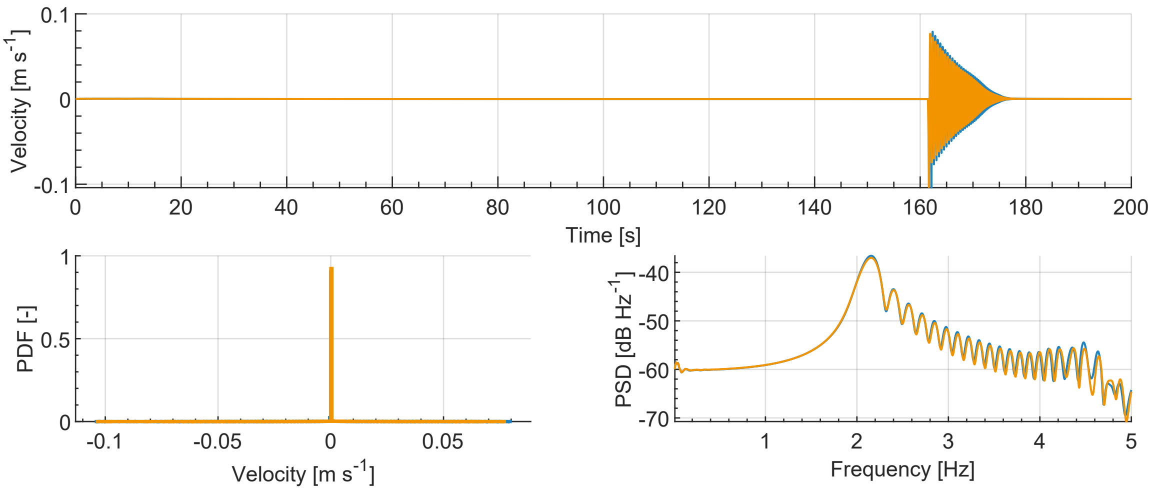

(b) Structure velocity at ice creep followed by intermittent crushing — zoomed time series, PDF, and PSD.

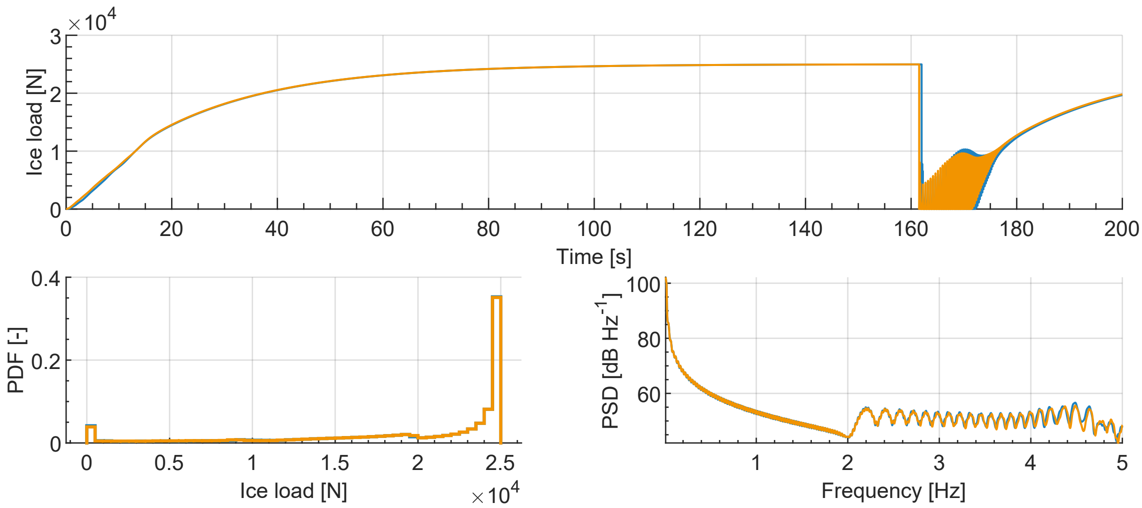

(c) Ice load creep followed by intermittent crushing — zoomed time series, PDF, and PSD.

Figure 4.4: Creep followed by intermittent crushing. Simulations performed for $\dot{u}_{\text{ice}}$ of 0.001 m s^{-1}, h_{ice} of 0.05 m, 92 ice stripes, output time step of 0.001 s, and simulation length of 600 s.

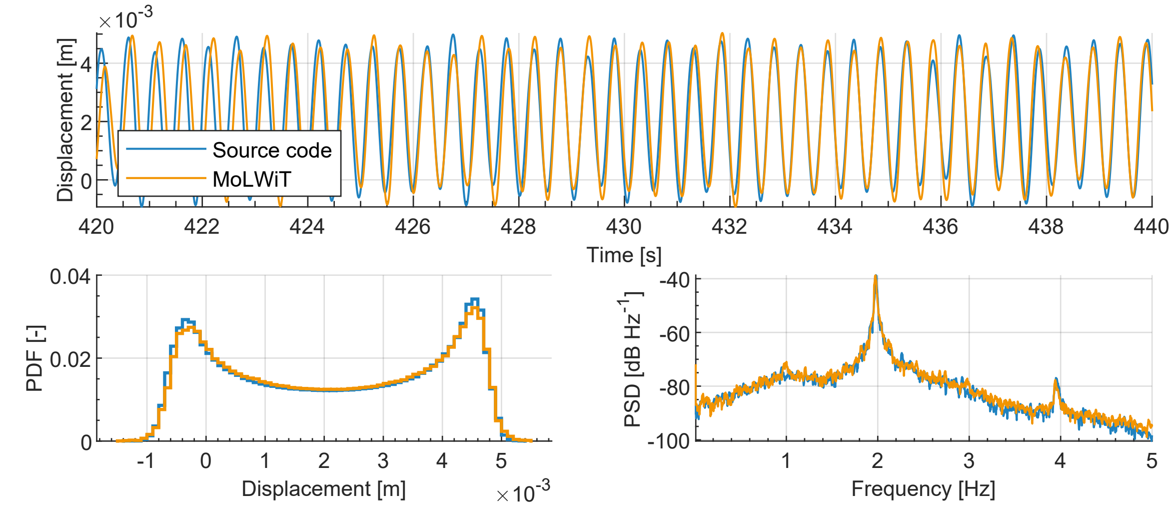

(a) Structure displacement at frequency lock-in mode — zoomed time series, PDF, and PSD.

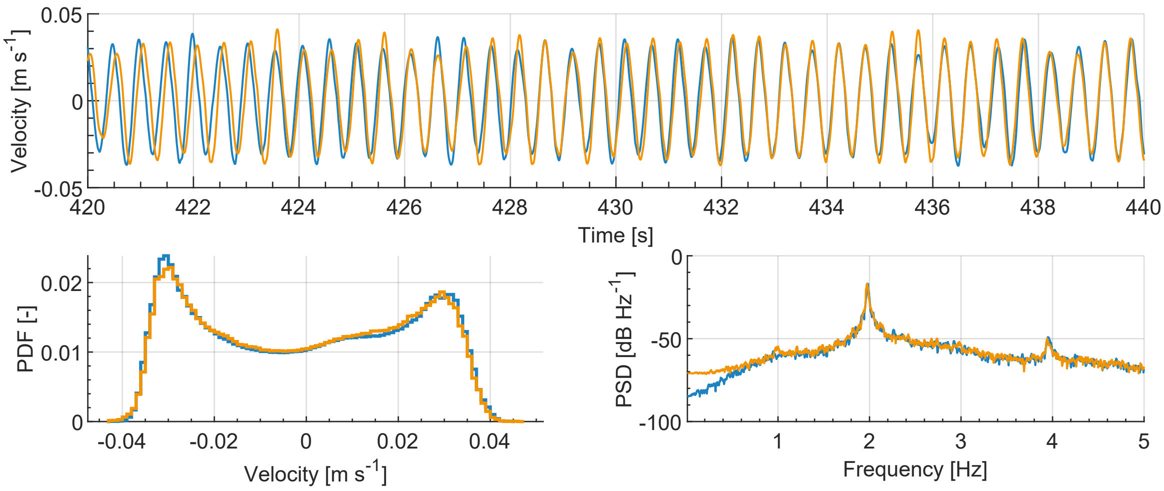

(b) Structure velocity at frequency lock-in mode — zoomed time series, PDF, and PSD.

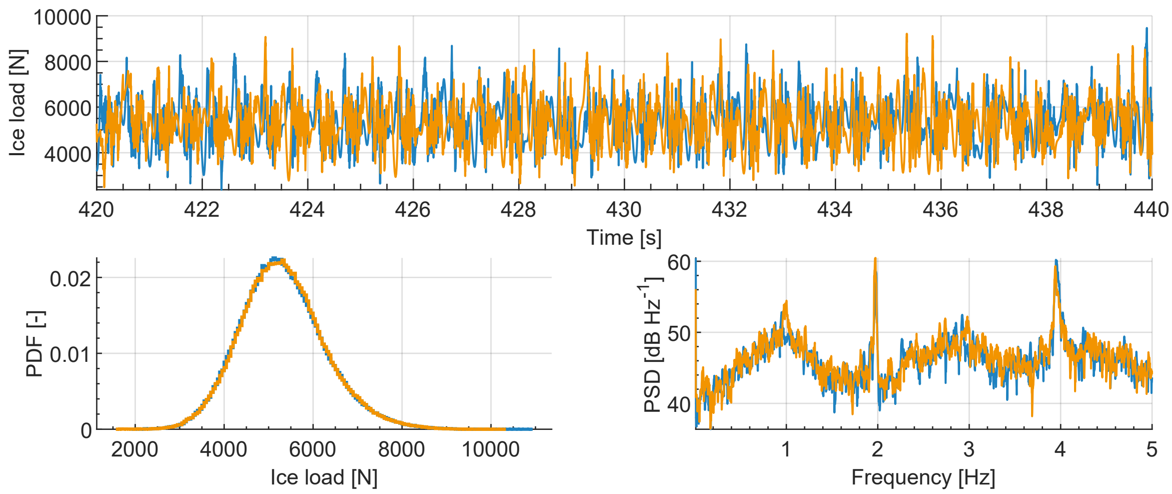

(c) Ice load at frequency lock-in mode — zoomed time series, PDF, and PSD.

Figure 4.5: Frequency lock-in mode. Simulations performed for $\dot{u}_{\text{ice}}$ of 0.03 m s^{-1}, h_{ice} of 0.05 m, 92 ice stripes, output time step of 0.001 s, and simulation length of 600 s.

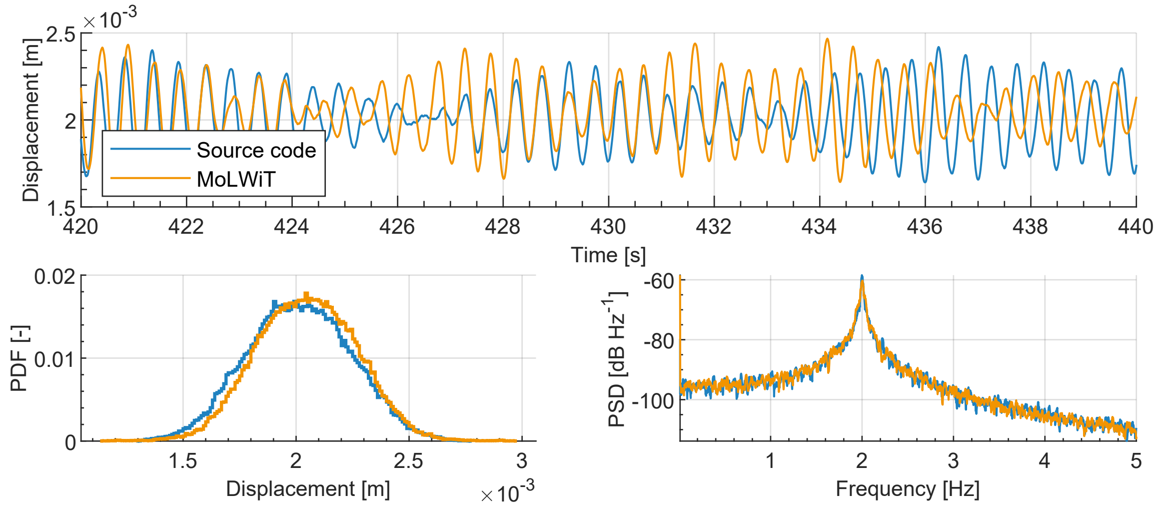

(a) Structure displacement at continuous brittle crushing mode — zoomed time series, PDF, and PSD.

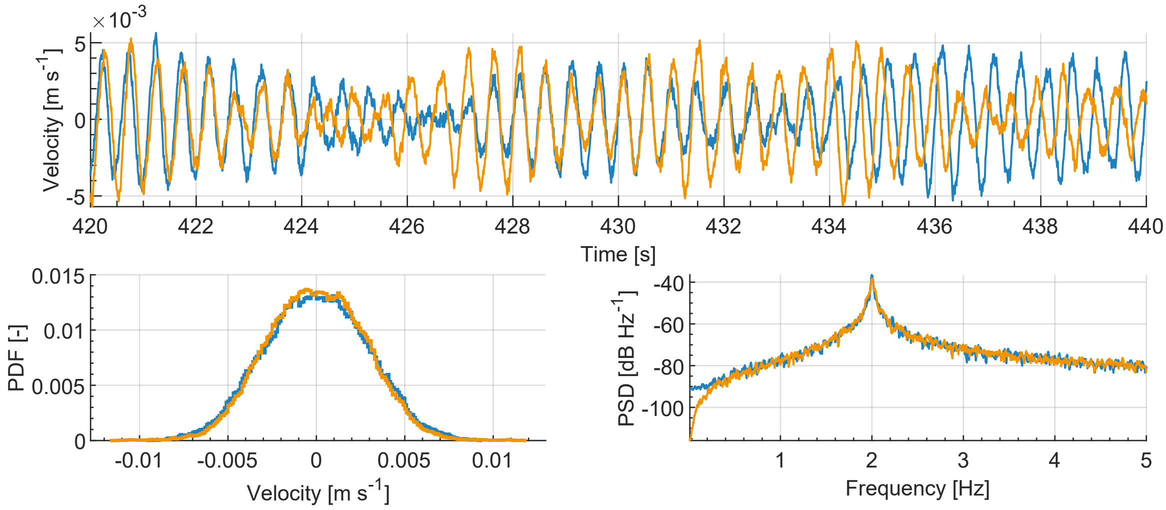

(b) Structure velocity at continuous brittle crushing mode — zoomed time series, PDF, and PSD.

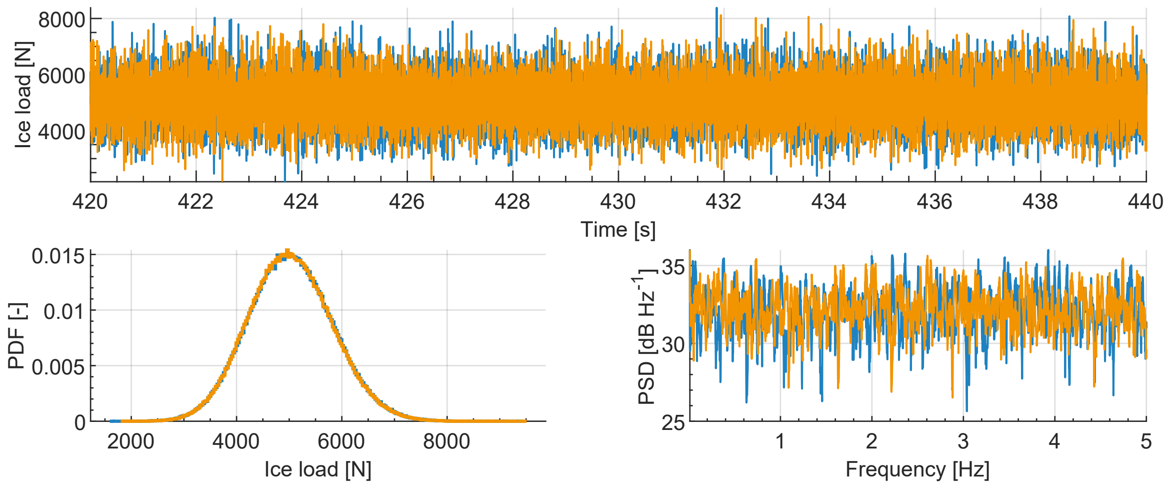

(c) Ice load at continuous brittle crushing mode — zoomed time series, PDF, and PSD.

Figure 4.6: Continuous brittle crushing mode. Simulations performed for $\dot{u}_{\text{ice}}$ of 0.2 m s^{-1}, h_{ice} of 0.05 m, 92 ice stripes, output time step of 0.001 s, and simulation length of 600 s.

The PSD signal of the ice load is entirely flat, as shown in Figure 4.6c. This is in contradiction to PSD of the ice load during the lock-in event (Figure 4.5c), where frequency peaks at around 2 Hz and 4 Hz are pronounced.

The percentage difference between the mean values of the ice load obtained from both tools is below 0.2% at each interaction region. The percentage difference between the standard deviation values of the ice load obtained from both tools is below 0.75% at each interaction region.

The percentage differences of mean and standard deviation values of displacements between both tools are usually below 1% at individual interaction regions. Similar conclusions can be derived when comparing statistics of the velocity signals.

4.1.1 Conclusions

The ice model and the sDOF structure implemented and coupled in MoLWiT have been successfully verified against the source code in MATLAB®. The agreement between the simulation results obtained from both simulation tools is very good. The ice model implemented in MoLWiT can reproduce three main ice-structure interaction modes — intermittent crushing, frequency lock-in, and continuous brittle crushing.

Furthermore, a minor problem in the source code has been discovered and mitigated, although its presence did not hamper the functionality of the source code. The problem is caused by the limitations of the root-finding mechanism employed by the ODE solver in MATLAB®.

4.2 Estimation of ice properties for the southern Baltic Sea

The source code of Hendrikse ice model was tuned based on the ice properties derived from scaled ice tank tests (cf. Figure 2.10 and Table 4.2). Therefore, it is necessary to retune its input properties for the full-scale application in the southern Baltic Sea[71]. The estimation of full-scale properties is done based on a literature study, own experiments, and the data from the SeaLOWT project. Table 4.4 shows the recommended range of indicative ice properties for the realistic simulations of ice-structure interaction in full-scale. Their choice is justified in the following subsections. Note that the listed ice properties might not always be representative for all locations in the southern Baltic Sea. For the load certification application, the ice properties should be derived from in situ measurements.

[71]The term *southern Baltic Sea* is not precisely defined in the literature. For this work, the southern Baltic Sea spans between two parallels from around N 54° to around N 56°, including the Danish straits, the Bay of Kiel, the Mecklenburg Bay, the Arkona Basin, the Bornholm Basin, and the Eastern Gotland Basin (cf. Figure 1.2).

Table 4.4: Indicative sea ice properties applicable to the southern Baltic Sea.

Parameter	Unit	Value	Comment
$\dot{u}_{\text{ice}}$	$\mathrm{m\,s^{-1}}$	0.0 to 0.6	Ice velocity range with occurrence probability > 99.94%
h_{ice}	m	0.1 to 0.3	Mean sea ice thickness
F_{brittle}	N	1.1×10^6 to 3.1×10^6	Brittle crushing load of sea ice at v_{brittle} and above (calculated for the reference SeaLOWT monopile support structure with the diameter of 7.3 m at MSL)
F_{max}	N	$3\,F_{\text{brittle}}$ to $5\,F_{\text{brittle}}$	Maximum ice load at the ductile-to-brittle transition
σ_{ice}	N	$0.1\,F_{\text{brittle}}$ to $0.5\,F_{\text{brittle}}$	Standard deviation of the brittle crushing load
v_{db}	$\mathrm{m\,s^{-1}}$	0.001 to 0.003	Ductile-to-brittle transition velocity at F_{max}
v_{brittle}	$\mathrm{m\,s^{-1}}$	0.10 to 0.13	Transition velocity to intermittent brittle crushing
f_{peak}	Hz	5.0 to 12.5	Frequency peak of ice load at v_{brittle} and above

4.2.1 Ice velocity

Gravesen et al. (2003, p. 2) estimate a maximum ice velocity to $1\,\mathrm{m\,s^{-1}}$ for the ice floes in the Danish straits, where Middelgrunden, Nysted, and Rødsand wind farms are located (see Figure 1.1).

According to the SeaLOWT Design Basis (Ramboll, 2018, p. 18), wind is the main driving force of ice floes in the southern Baltic Sea. Table 4.5 shows relation between the wind speed and the ice velocity with the assumption that the ice velocity is around 2.5% of the wind speed measured at 10 m above MSL — according to Lilover et al. (2018, p. 178) the ice floe is usually driven with a speed of 2% to 3% of the wind speed.

Table 4.5: Mean ice velocity and its probability as a function of wind speed measured at 10 m above MSL. Indicative data for the southern Baltic Sea (Ramboll, 2018, p. 18).

Wind speed bin	$\mathrm{m\,s^{-1}}$	$0 \le V < 3$	$3 \le V < 6$	$6 \le V < 9$	$9 \le V < 12$	$12 \le V < 16$	$16 \le V < 20$	$20 \le V$
Ice velocity	$\mathrm{m\,s^{-1}}$	0.04	0.11	0.19	0.26	0.36	0.46	0.55
Probability	%	10.43	28.87	32.81	19.20	7.65	0.98	0.06

To sum up — based on the analyzed data it can be concluded that the ice floe velocity can reach up to $1\,\mathrm{m\,s^{-1}}$ in the southern Baltic Sea. However, this is an extreme value. In the vast majority of cases (probability of around 99.94%), the ice floe velocity should not exceed $0.6\,\mathrm{m\,s^{-1}}$.

4.2.2 Ice thickness

Figure 4.7 shows the mean and maximum sea ice thickness during winter seasons at different locations of the southern Baltic Sea along the German coast. The average sea ice thickness, h_{ice}, varies from around 0.1 m to 0.3 m, and the maximum thickness can reach 0.6 m, as reported by

Schmelzer et al. (2012, p. 87). The mean range of the ice thickness will be used in the simulations, as presented in Table 4.4.

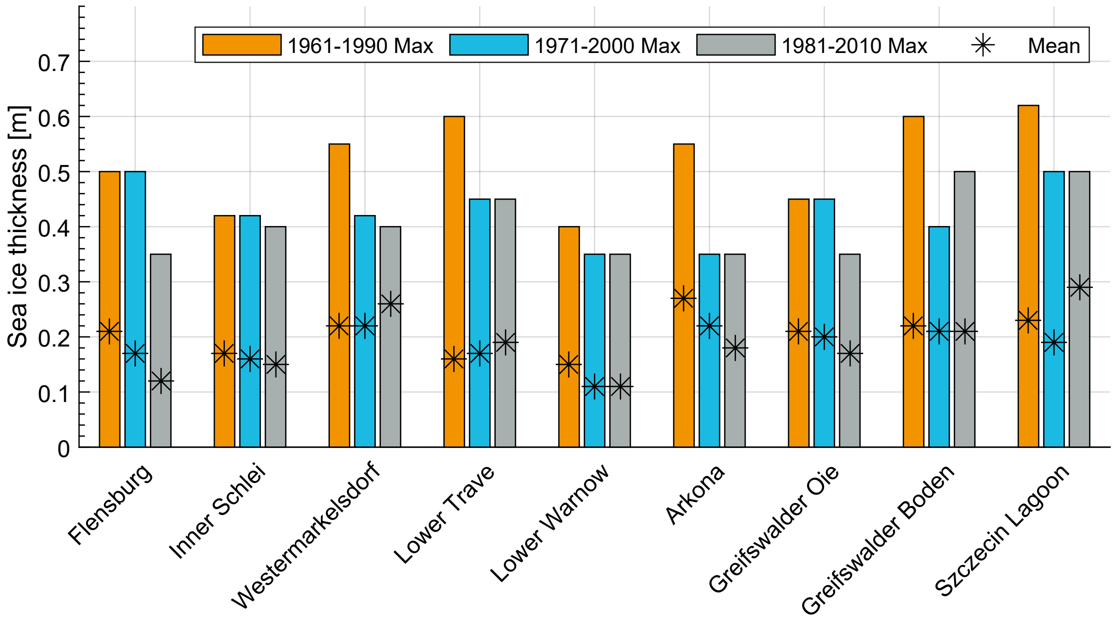

Figure 4.7: Mean and maximum sea ice thickness during winter seasons at the southern Baltic Sea along the German coast for different 30-year periods. Figure created based on the data from Schmelzer et al. (2012, p. 87).

4.2.3 Mean brittle crushing load

The level of mean brittle crushing load, F_{brittle}, can be estimated from Eq. 2.3 derived from ISO (2019, p. 199). The ISO standard suggests the sea ice strength, C_{R}, of 1.8 MPa. It should be emphasized that:

- This value is applicable for the Baltic Sea for extreme sea ice occurring every 100 years. Note that the extreme environmental conditions for the design of OWTs are defined with a 50-year recurrence period, which is two times less than the period specified in ISO.
- The value was determined based on the lighthouse measurements in the Gulf of Bothnia, in the north part of the Baltic Sea. It might be too conservative for the southern part of the Baltic Sea, where the sea ice is warmer compared to the sea ice in the Gulf of Bothnia.
- The value was derived from the spectral model developed by Kärnä et al. (2006). This model does not account for a mixed ice failure (bending and crushing). The mixed ice failure can further limit the load imposed on the structure. This failure type is important for relatively thin sea ice and structures of large diameters — both common in the southern Baltic Sea.

In contradiction to the ISO standard, Gravesen and Kärnä (2009) recommend C_R of 1 MPa, which represents the annual maximum strength of the sea ice cover in the southern Baltic Sea for the sea ice thickness less than 0.6 m. Figure 4.8 shows the global sea ice pressure and force as a function of sea ice thickness calculated with C_R recommended in ISO (2019, p. 200) and suggested by Gravesen and Kärnä (2009, p. 11) for the southern Baltic Sea. The calculations are performed for the reference SeaLOWT monopile support structure with the diameter of 7.3 m at MSL (see Appendix A.2 for structural and geometrical properties).

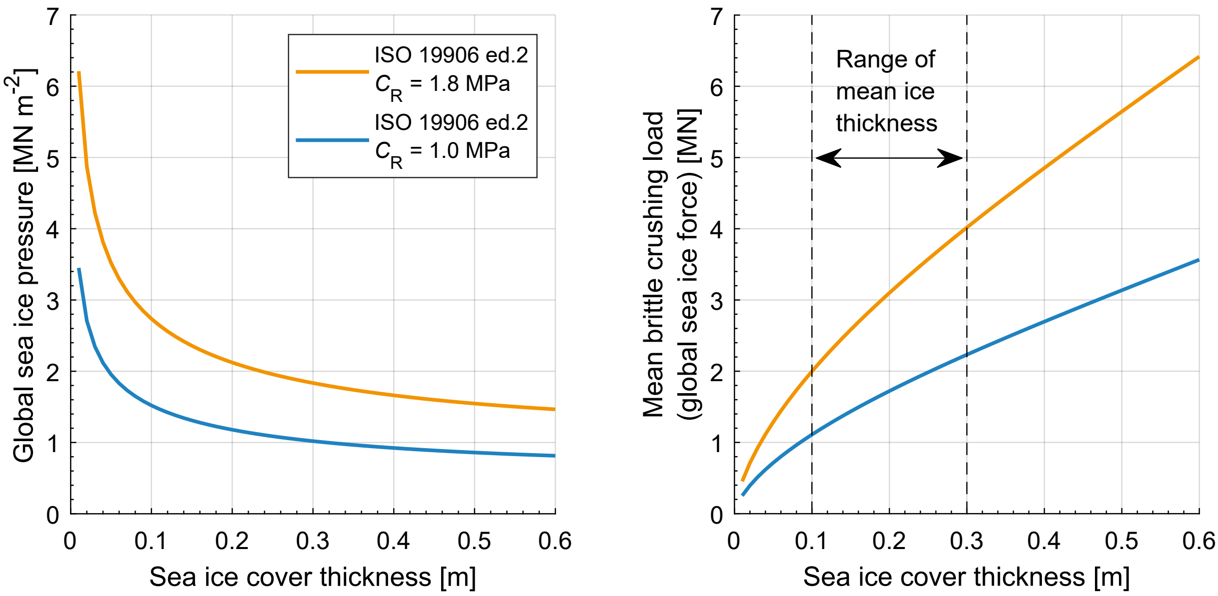

(a) Global sea ice pressure. **(b)** Mean brittle crushing load.

Figure 4.8: Global ice pressure and force as function of ice thickness calculated for different C_R values: 1.8 MPa suggested by ISO (2019, p. 200) and 1.0 MPa recommended by Gravesen and Kärnä (2009, p. 11). The calculations are performed for the reference SeaLOWT monopile support structure with 7.3 m diameter at MSL.

To sum — $F_{brittle}$ in the range of around 1.1 MN to 3.1 MN can be used for the simulation of sea ice loads in the southern Baltic Sea, as shown in Figure 4.8b. This range is defined by the range of the mean ice thickness presented in Section 4.2.2.

4.2.4 Standard deviation of brittle crushing load

The standard deviation of the sea ice load, σ_{ice}, during brittle crushing at high ice velocities (at $v_{brittle}$ and above) can vary significantly. The analysis of the full-scale measurements of the Norströmsgrund lighthouse revealed that σ_{ice} could reach up to 40% of $F_{brittle}$, as reported by Kärnä and Yan (2009, pp. 48–52). Määttänen (1983, p. 10) reported σ_{ice} of around 50% of $F_{brittle}$ for scaled tests performed at the Ice Engineering Facility of the Cold Regions Research and Engineering Laboratory (CRREL). Nord et al. (2013) analyzed scaled test data from the

EU-HYDRALAB Deciphering Ice Induced Vibrations (DIIV) project and found σ_{ice} of 10% of F_{brittle}. Sodhi (1998) also reported a similar σ_{ice} for other scaled test experiments.

To sum up — σ_{ice} in the range from 10% to 50% of F_{brittle} might be used for the simulation of ice loads in the southern Baltic Sea (see Table 4.4), as there are no other, more precise estimates available.

4.2.5 Relation between mean brittle crushing load and maximum load

Pressure at continuous brittle crushing (see Section 4.2.3) is much smaller than the maximum pressure peak when the ductile-to-brittle (DB) transition occurs. According to various full-scale measurements (e.g., Wright & Timco, 1994), the ice pressure exerted on the structure during continuous brittle crushing is usually in the range of around 1 MPa to 3 MPa (see Figure 4.8a). This effective pressure is three to five times smaller than the maximum pressure — and thus the maximum force F_{max} — that is observed at DB. The reasons for the reduction in effective pressure are the following:

- The actual contact area between ice and the structure during continuous brittle crushing is much smaller than the full contact area during ice creep.
- The ice pressure generated at local high-pressure zones[72] is responsible for the local flaking failure of ice. This was observed by e.g., Sodhi (2001), who analyzed pressure measurements from small-scale indentation tests.

To sum up — F_{max} can be modeled as three to five times larger than F_{brittle} for the simulation of ice loads in the southern Baltic Sea (see Table 4.4).

4.2.6 Transition velocity from ductile to brittle failure

The velocity region where DB transition occurs is of high interest in the analysis of sea ice-structure interaction, as it governs different interaction modes. The concept of such modes depending on different velocity regions was introduced by Sodhi (1991) and is discussed in Section 2.3.

The ice capacity can be characterized by the yield stress and the maximum strength. The yield stress is defined as the maximum stress that ice can withstand in its elastic region before the permanent deformation takes place. Whereas, the maximum strength defines the maximum load that ice can withstand.

[72] Local high-pressure zones are denoted with different names in various publications. For example, *hot spots* and *critial zones* terms are often used interchangeably with the term *local high-pressure zones*. A detailed overview of local high-pressure zones formation was presented by e.g. Dempsey et al. (2001).

A set of uniaxial compression tests was performed by the author on October 30, 2014 at the University Centre in Svalbard (UNIS) cold laboratory, located in Svalbard — a Norwegian archipelago in the Arctic Ocean. Several ice specimens were investigated under different strain rates, as shown in Figure 4.9. The ice specimens were made out of drilled ice cores extracted from a fjord nearby Svea — a mining settlement in Svalbard. Each specimen was loaded axially with the constant strain rate up to its failure.

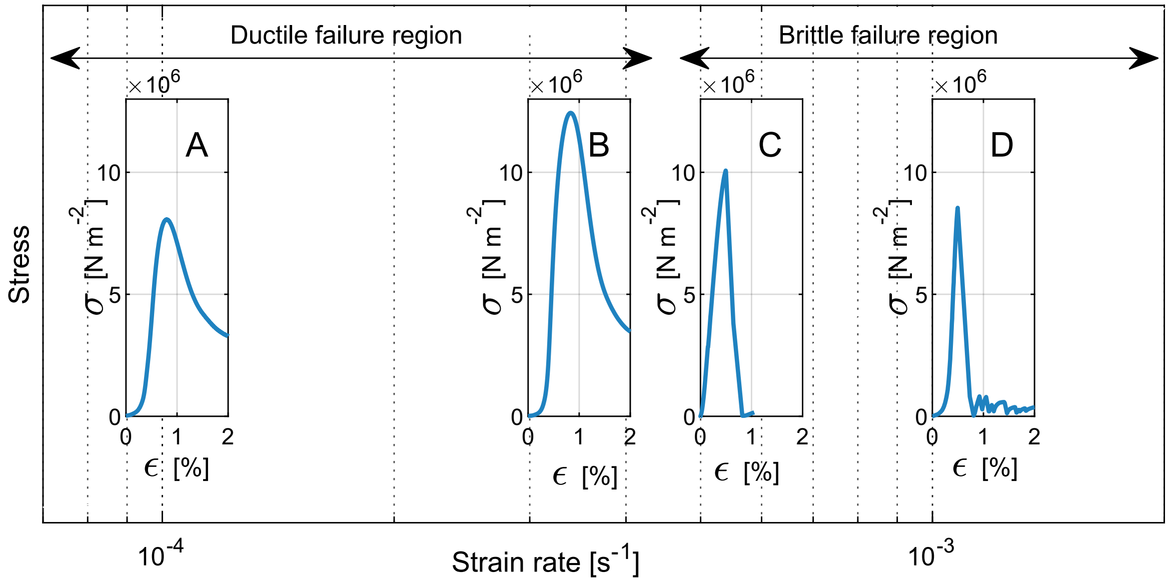

Figure 4.9: Transition between ductile and brittle failure regions governed by different strain rates, $\dot{\varepsilon}$, for different ice specimens. Their stress-strain curves are denoted as A, B, C, and D.

When the ice specimen is loaded with a relatively slow strain rate, $\dot{\varepsilon}$, cracks do not propagate and the stress, σ, reaches its maximum level at the strain, ε, of around 0.8%, as shown in Figure 4.9 (curves A and B). In this case, creep deformation allows stresses to relax — ice grain boundaries can slide with respect to each other after crossing the yield point. This can be described as a ductile behavior. On the other hand, the brittle behavior is characterized by elastic deformation followed by a sudden failure of the material — there is no yield period — as shown in Figure 4.9 (curves C and D). The instantaneous elastic deformation occurs at the strain, ε, of around 0.5%, due to the elastic response of the crystal lattice caused by the applied stress. Consequently, the maximum threshold stress level is reached and the strain energy is released, followed by the movement of dislocations in ice crystals. The transition region presented in Figure 4.9 fits well to the data presented by Schulson (2001) and Schulson and Duval (2009, p. 240).

The transition between ductile and brittle failure occurs at the indentation speed, v_{db}, of around $0.001\,m\,s^{-1}$ to $0.003\,m\,s^{-1}$. A comprehensive overview of different tests was presented by Sodhi (2001). At the DB point, the maximum compressive strength of ice is reached.

To sum up — v_{db} of $0.001\,m\,s^{-1}$ to $0.003\,m\,s^{-1}$ can be used for the simulation of ice loads in the southern Baltic Sea (see Table 4.4).

4.2.7 Transition velocity to continuous brittle crushing

The continuous brittle crushing is initiated at the ice velocity, v_{brittle}, greater than around 0.10 m s^{-1} to 0.13 m s^{-1}. Such relation has been observed in many laboratory and full-scale tests by e.g., Rogers et al. (1986). Therefore, this range of values is also adapted for the simulation of ice loads in the southern Baltic Sea (see Table 4.4).

4.2.8 Frequency peak of ice load during continuous brittle crushing

The model- and full-scale tests with rigid structures indicate that the frequency peak, f_{peak}, of the ice load during the continuous brittle crushing at v_{brittle} can vary from around 5 Hz to 20 Hz (Sodhi & Morris, 1986; Schwarz, 1970; Neill, 1976). The frequency peak shows dependence on the ice velocity and thickness. On the other hand, it is independent of the structure diameter when $\dot{u}_{\text{ice}}/h_{\text{ice}} < 1.5\,\text{s}^{-1}$, as reported by Sodhi and Morris (1986, p. 11). The independence of the structure diameter might not always be satisfied in the case of OWTs located in the southern Baltic Sea, where the ice velocity can reach up to 1 m s^{-1} and the mean ice thickness can vary from around 0.1 m to 0.3 m — as discussed in Sections 4.2.1 and 4.2.2.

Due to the absence of better estimates, it is decided to use f_{peak} of 5.0 Hz to 12.5 Hz, which is the lower bound of the reported frequency range. This lower bound is often reported for different full-scale structures.

4.2.9 Uncertainties in assessment of ice properties

Uncertainties in the assessment of ice properties directly affect ice loads. The ice thickness, ice strength, and ice cover velocity are the main properties that would influence ice loads on OWTs with monopile support structures and their dynamic response. The ice thickness is mainly a function of the temperature, freezing time, and presence of snow cover atop the ice sheet[73]. The ice strength depends on the internal structure of sea ice, impurities, grain size, strain rate, ice temperature, and loading direction. The ice cover is driven by wind, sea current, and tides.

To quantify the uncertainty of sea ice properties, the Monte Carlo method can be used. An example of application of this method can be found in Sinsabvarodom et al. (2020).

[73] A snow cover can have an insulating effect leading to a slower increase of ice thickness.

4.3 Extension of ice model simulation capabilities and coupling with mDOF structure

The source code of the Hendrikse ice model[74] is only capable of simulating an interaction between ice and an sDOF structure. In the scope of this dissertation, an FEM code for modeling mDOF structures is implemented in MATLAB®. Subsequently, the source code of the ice model is modified and coupled with this newly developed mDOF code. This extended ice model in MATLAB® is used for the cross-verification of the simulation results from MoLWiT, where the ice model and a full-scale monopile support structure[75] are implemented.

4.3.1 Implementation of FEM code for modeling mDOF structures

This section describes the main aspects of the implementation of the FEM code for modeling mDOF structures and presents its verification results against MoLWiT and ROSAP. The MATLAB® source code of the FEM representation of the mDOF structure is available in Appendix A. The relations between different functions in the code are shown in Figure 4.10. This FEM code can also be coupled by other researchers with the public version of the Hendrikse ice model and used for further studies of ice-structure interaction.[76]

A procedure for building an FE structure can be divided into the following steps:

1. Define the geometrical and structural properties of the monopile support structure including foundation properties.
2. Build element matrices.
3. Connect all elements by assembling global system matrices.
4. Apply contributions from point masses and inertia.
5. Apply boundary conditions.
6. Perform modal analysis.
7. Perform modal reduction of the system.

[74] Ice model version No. 25-09-2016 provided to the author by Dr. Hendrikse.

[75] The support structure consisting of the foundation, monopile, transition piece (TP), and tower has been designed by Ramboll for the IWES Wind Turbine IWT-7.5-164 (Popko, Thomas, et al., 2018) within the scope of the SeaLOWT project.

[76] The MATLAB® source code of the Hendrikse ice model and the sDOF structure (Hendrikse, 2019) is available in the public domain: doi:10.17632/582m8565dj.2. Note that another non-public version (No. 25-09-2016) of the source code is used in this work.

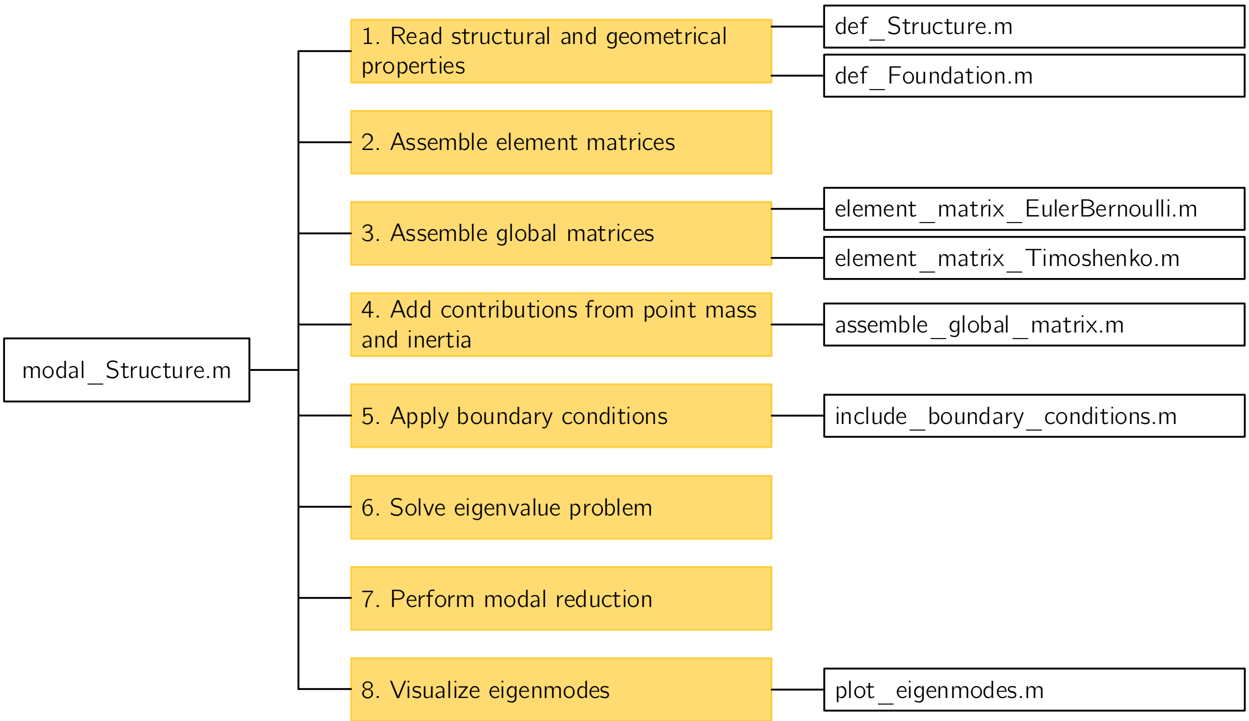

Figure 4.10: Scheme of the FEM code for modeling mDOF structures. Different sections of the code are marked orange. Branches extending from these sections indicate names of external functions, which are called by the main function, modal_Structure.

The definitions of the geometrical and structural properties of the monopile support structure, and foundation properties, mentioned in Step 1, are available in Appendices A.2 and A.3. The actions involved in Steps 2 to 7 are discussed in details on the following pages.

Definition of matrices for Euler-Bernoulli and Timoshenko beam elements

The most commonly used beam theories for the mathematical modeling of support structures in the coupled analysis of OWTs are Euler-Bernoulli and Timoshenko theories, which are described in Section 2.1.4. The vast majority of the modern aero-hydro-servo-elastic tools rely on 3D beam models, which are based on these two theories, as observed in Table 2.1.

The developed FEM code can handle both Euler-Bernoulli and Timoshenko beam elements consisting of two nodes with six DOFs at each node — three translation and three rotational — as shown in Figure 4.11.

The user can switch between these two models in the *User inputs* section of the main script (Appendix A.1). The source code listings with numerical implementations of element mass and

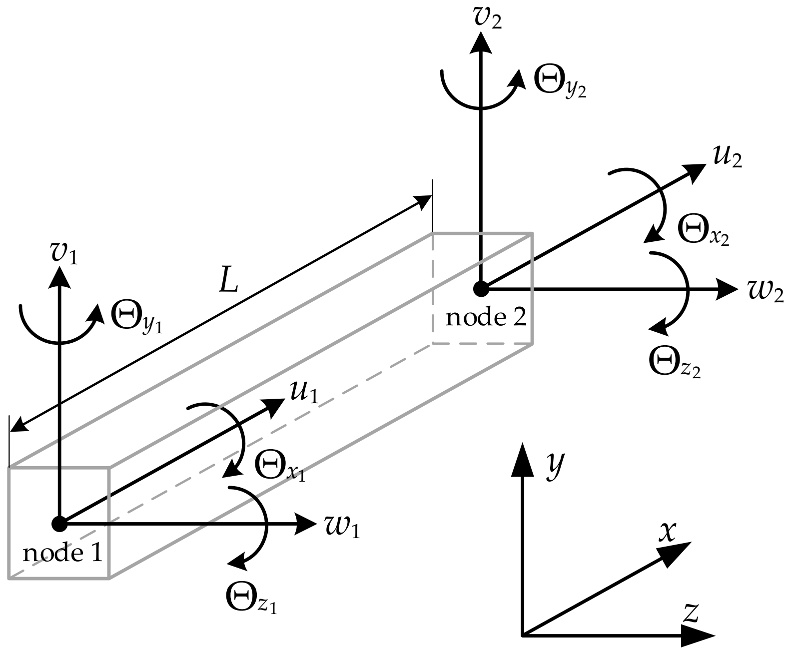

Figure 4.11: Beam element of length L with two nodes and six DOFs at each node (v, u, w — translation and Θ_x, Θ_y, Θ_z — rotational) in the 3D Euclidean space described by x, y, and z coordinates.

stiffness[77] matrices for both beam models are available in Appendices A.4 and A.5. Note that these matrices are symmetric with respect to their main diagonals.

The derivation of mass and stiffness matrices is merely tiresome algebra and is not be presented in this work. Derivations can be found in many books related to FEM and structural analysis, e.g., Przemieniecki (1968); Cook et al. (2001); Bauchau and Craig (2009).

Assemble of global mass and stiffness matrices

The direct stiffness method (DSM) is used for assembling the global system matrices out of the individual beam element matrices. The DSM was formulated by Turner et al. (1956) at Boeing and is still broadly used in the industry due to its implementation simplicity and efficiency in numerical computation.

[77] The element stiffness matrix can be split into elastic- and geometric stiffness contributions. The geometric stiffness, which accounts for the second-order effects of finite deformations (due to the influence of axial force) is not included herein. A small deformation theory has been adapted for the developed code. This theory describes the deformation of a solid body, in which the particle displacements are assumed as infinitesimal (arbitrarily close to zero). In practical application, the axial displacements between the element nodes can be assumed as negligibly small when elongation strains are smaller than around 0.1%. This value corresponds to the linear elastic range of structural steel.

All procedural steps involved in the DSM are covered in many books related to the FEM; and therefore they are not shown in this dissertation. One of the most comprehensive overviews of the DSM can be found in the lecture notes from Felippa (2004).

The DSM was implemented in the MATLAB® code, which listing is available in Appendix A.6. Figure 4.12 shows the assembly scheme of the global matrix for the monopile support structure including contributions from foundation and RNA at the first and the last node, respectively.

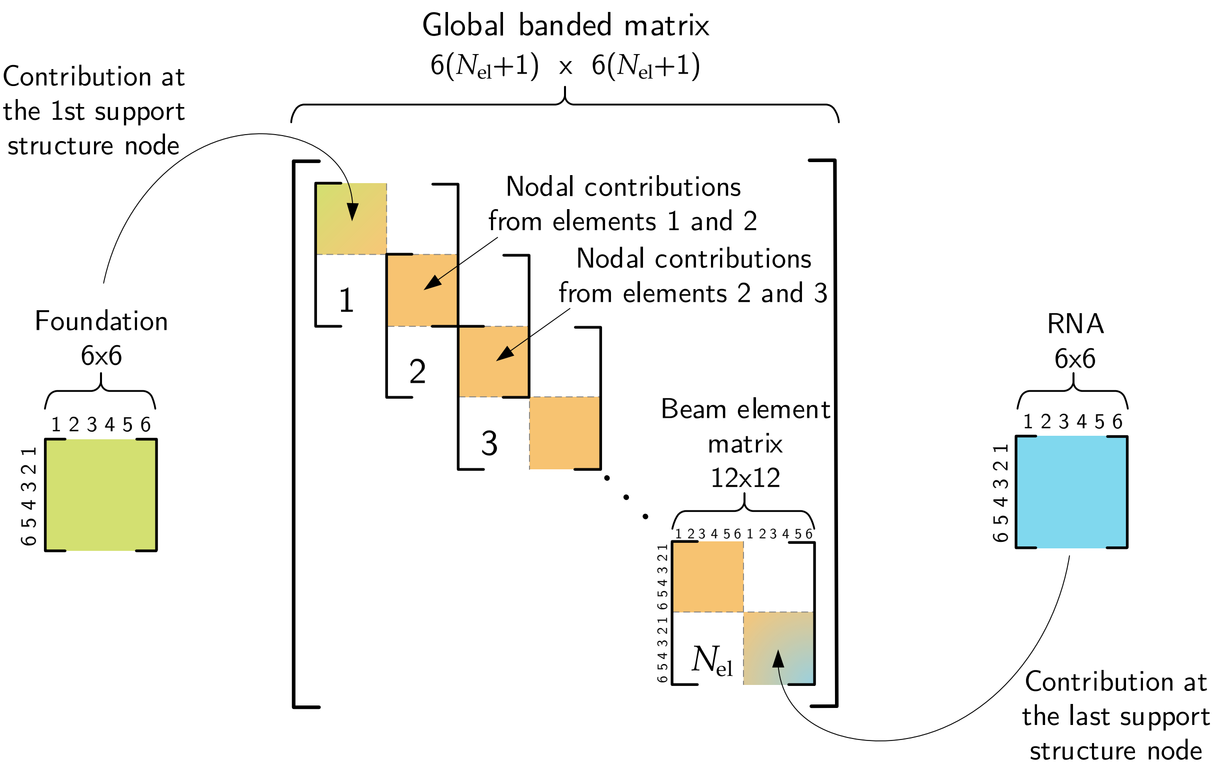

Figure 4.12: Assembly scheme of the global banded matrix for the monopile support structure including contributions from foundation and RNA at the first and last node, respectively.

The global mass $[\boldsymbol{M}]$ and stiffness $[\boldsymbol{K}]$ matrices are assembled by adding terms, which are associated with DOFs in the local element mass $[\boldsymbol{m}_\mathrm{e}]$ and elastic stiffness $[\boldsymbol{k}_\mathrm{e}]$ matrices, respectively:

$$[\boldsymbol{M}] = \sum_{i=1}^{N_\mathrm{el}} [\boldsymbol{m}_\mathrm{e}]_i \tag{4.2}$$

$$[\boldsymbol{K}] = \sum_{i=1}^{N_\mathrm{el}} [\boldsymbol{k}_\mathrm{e}]_i \tag{4.3}$$

where N_el is the number of elements in the structure. Note that the global mass $[\boldsymbol{M}]$ and stiffness $[\boldsymbol{K}]$ matrices are banded as their non-zero entries are confined to a diagonal band.

Contribution from point mass and inertia

The developed FEM code gives a possibility to include an additional contribution from point mass and inertia (translational, rotational, and coupled between translation and rotation due to eccentricity of the point mass) at any arbitrary node of the structure. Different DOFs are indicated with red color atop of the point mass and inertia matrix:

$$[\boldsymbol{M}_{\mathrm{p}}] = \begin{array}{c} \begin{array}{cccccc} x & y & z & \Theta_x & \Theta_y & \Theta_z \end{array} \\ \left[\begin{array}{ccc:ccc} m & 0 & 0 & 0 & mz_{\mathrm{m}} & -my_{\mathrm{m}} \\ & m & 0 & -mz_{\mathrm{m}} & 0 & mx_{\mathrm{m}} \\ & & m & my_{\mathrm{m}} & -mx_{\mathrm{m}} & 0 \\ \hdashline & & & I_x + m(y_{\mathrm{m}}^2 + z_{\mathrm{m}}^2) & I_{xy} - mx_{\mathrm{m}}y_{\mathrm{m}} & -I_{xz} - mx_{\mathrm{m}}z_{\mathrm{m}} \\ & \text{sym.} & & & I_y + m(x_{\mathrm{m}}^2 + z_{\mathrm{m}}^2) & -I_{yz} - my_{\mathrm{m}}z_{\mathrm{m}} \\ & & & & & I_z + m(x_{\mathrm{m}}^2 + y_{\mathrm{m}}^2) \end{array}\right] \end{array} \tag{4.4}$$

where m is the point mass; x_{m} is the mass offset from the node along the x-axis; y_{m} is the mass offset from the node along the y-axis; z_{m} is the mass offset from the node along the z-axis; I_x, I_y, I_z, are moments of inertia; and I_{xy}, I_{xz}, I_{yz} are product moments of inertia.

The point mass and inertia can be used for including contributions from the structural equipment, tower flanges, and RNA. The script is available in Appendix A.7.

Modeling of foundation

The developed FEM code can model both rigid and flexible foundations. In the case of the rigid foundation all DOFs at the first node of the support structure are constrained — they are eliminated from both global mass and stiffness matrices. The flexible foundation is modelled by including contributions from mass $[\boldsymbol{M}_{\mathrm{f}}]$ and stiffness $[\boldsymbol{K}_{\mathrm{f}}]$ foundation matrices to the global mass $[\boldsymbol{M}]$ and stiffness $[\boldsymbol{K}]$ matrices (see Figure 4.12). The source code for modeling both foundation types is available in Appendix A.8.

Generalized eigenvalue problem, modal reduction, and effective modal mass

The modal reduction algorithm belongs to the code listing in Appendix A.1. The eigenvalue problem is defined for each eigenvalue, ω_j, as:

$$\left([\boldsymbol{K}] - \omega_j^2[\boldsymbol{M}]\right)\{\boldsymbol{\phi}\}_j = 0 \tag{4.5}$$

where $\{\boldsymbol{\phi}\}_j$ is the mode shape vector for the eigenmode j; $[\boldsymbol{M}]$ and $[\boldsymbol{K}]$ are the global mass and stiffness matrices, respectively. Note that the mode shape vectors satisfy orthogonality conditions implying that both mass and stiffness modal matrices are diagonal:

$$\{\boldsymbol{\phi}\}_j^{\mathsf{T}}[\boldsymbol{M}]\{\boldsymbol{\phi}\}_k = m_j\delta_{jk} \tag{4.6}$$

$$\{\boldsymbol{\phi}\}_j^{\mathsf{T}}[\boldsymbol{K}]\{\boldsymbol{\phi}\}_k = k_j\delta_{jk} \tag{4.7}$$

where δ_{jk} is the Kronecker delta defined as:

$$\delta_{jk} = \begin{cases} 1 & \text{for} \quad j = k \\ 0 & \text{for} \quad j \neq k \end{cases} \tag{4.8}$$

The solution of the generalized eigenvalue problem consists of a corresponding set of an eigenvalue ω_j and eigenvector $\{\boldsymbol{\phi}\}_j$ for the given eigenmode j. The modal reduction is performed by trimming this number of sets to the number of the desired eigenmodes, N_m, and calculating diagonal modal reduced mass $[\boldsymbol{m}]$ and stiffness $[\boldsymbol{k}]$ matrices, each of size $N_\mathrm{m} \mathrm{x} N_\mathrm{m}$:

$$[\boldsymbol{m}] = [\boldsymbol{\phi}]^{\mathsf{T}}[\boldsymbol{M}][\boldsymbol{\phi}] \tag{4.9}$$

$$[\boldsymbol{k}] = [\boldsymbol{\phi}]^{\mathsf{T}}[\boldsymbol{K}][\boldsymbol{\phi}] \tag{4.10}$$

where $[\boldsymbol{\phi}]$ is the matrix with columnar eigenvectors, $\{\boldsymbol{\phi}\}$, of individual mode shapes.

The eigenfrequency ω_j for the eigenmode j of the modally reduced system of N_m modes can be expressed in the form of the generalized Rayleigh quotient:

$$\omega_j^2 = \frac{\{\boldsymbol{\phi}\}_j^{\mathsf{T}}[\boldsymbol{K}]\{\boldsymbol{\phi}\}_j}{\{\boldsymbol{\phi}\}_j^{\mathsf{T}}[\boldsymbol{M}]\{\boldsymbol{\phi}\}_j} = \frac{k_j}{m_j} \tag{4.11}$$

The concept of the effective modal mass was introduced by Wada et al. (1972). It is used for the quantification of the eigenmode importance in the multimode system. Eigenmodes with high effective masses can be easily excited by the base excitation; and therefore have a more significant impact on the structural dynamics than the eigenmodes with relatively low effective masses. The effective modal mass in the x-direction, which is involved in the eigenmode j is calculated as:

$$m_{x,j} = \frac{\left(\{\boldsymbol{\phi}\}_j^{\mathsf{T}}[\boldsymbol{M}]\{\boldsymbol{I}_x\}\right)^2}{\{\boldsymbol{\phi}\}_j^{\mathsf{T}}[\boldsymbol{M}]\{\boldsymbol{\phi}\}_j} \tag{4.12}$$

where $\{\boldsymbol{I}_x\}$ is the influence vector representing the displacement of mass in the x-direction resulting from the static application of unit ground displacement in the direction of the corresponding DOF. The same approach is used for calculation of effective modal masses in y- and z-directions.

Verification of eigenfrequencies and static deflections

The newly implemented MATLAB® code for modeling mDOF structures is verified against MoLWiT and ROSAP in terms of eigenfrequencies and static deflections. A monopile support structure with the RNA is defined in three simulation codes. Detailed structural and geometrical properties are listed in Appendix A.2.

The mass of the support structure is calculated as 1136.3 t in MATLAB®, 1136.1 t in MoLWiT, and 1135.6 t in ROSAP. Tiny differences (less than 0.06%) originate from different modeling techniques of the beam elements used in different codes. The RNA is modeled in all codes as a point mass of 536.78 t, which is rigidly attached with a vertical offset of 3.05 m from the tower top. The support structure is fixed at the seabed, where six DOFs are constrained.

Table 4.6 shows the comparison of eigenfrequencies obtained from MATLAB® (Timoshenko beam), MoLWiT (anisotropic beam)[78], and ROSAP (Timoshenko beam)[79]. Note that MATLAB® results for the Euler-Bernoulli beam elements are not included in this comparison — Timoshenko beams, as per definition, are more accurate; and therefore used in this verification. The last three columns of the table show the percentage difference between the results, which is calculated from Eq. 4.1.

Table 4.6: Comparison of eigenfrequencies of the monopile support structure calculated with MATLAB®, MoLWiT, and ROSAP. The monopile is fixed at the seabed, the RNA is modeled as a single point mass. Percentage differences between the results are shown in the last three columns.

Eigenmode	MATLAB® (Timoshenko) [Hz]	MoLWiT (Anisotropic) [Hz]	ROSAP (Timoshenko) [Hz]	MATLAB® vs. ROSAP (col. 2 vs. 4)	MATLAB® vs. MoLWiT (col. 2 vs. 3)	MoLWiT vs. ROSAP (col. 3 vs. 4)
1st fore-aft	0.266	0.267	0.266	0.04%	0.49%	0.53%
1st side-to-side	0.266	0.267	0.266	0.04%	0.49%	0.53%
2nd fore-aft	1.736	1.742	1.740	0.21%	0.35%	0.13%
2nd side-to-side	1.736	1.742	1.740	0.21%	0.35%	0.13%
3rd fore-aft	4.277	4.351	4.295	0.41%	1.71%	1.30%
3rd side-to-side	4.277	4.351	4.295	0.41%	1.71%	1.30%
1st torsion	6.412	6.406	6.407	0.07%	0.10%	0.02%
4th fore-aft	8.682	9.342	8.755	0.84%	7.33%	6.49%
4th side-to-side	8.682	9.342	8.755	0.84%	7.33%	6.49%

An excellent match is observed between MATLAB® and ROSAP results in column 5 of Table 4.6 — both models use the Timoshenko beam formulation. The difference is less than 0.5% for the majority of the eigenmodes. A very good match is also obtained for the results from MATLAB® and MoLWiT in column 6, and between MoLWiT and ROSAP in column 7 — in both cases different beam models are used. The first nine eigenmodes are visualized in Figure 4.13.

[78]See Section 2.1.4 and Kim et al. (2013) for more information about the anisotropic beam formulation.
[79]The ROSAP results were provided by Ramboll.

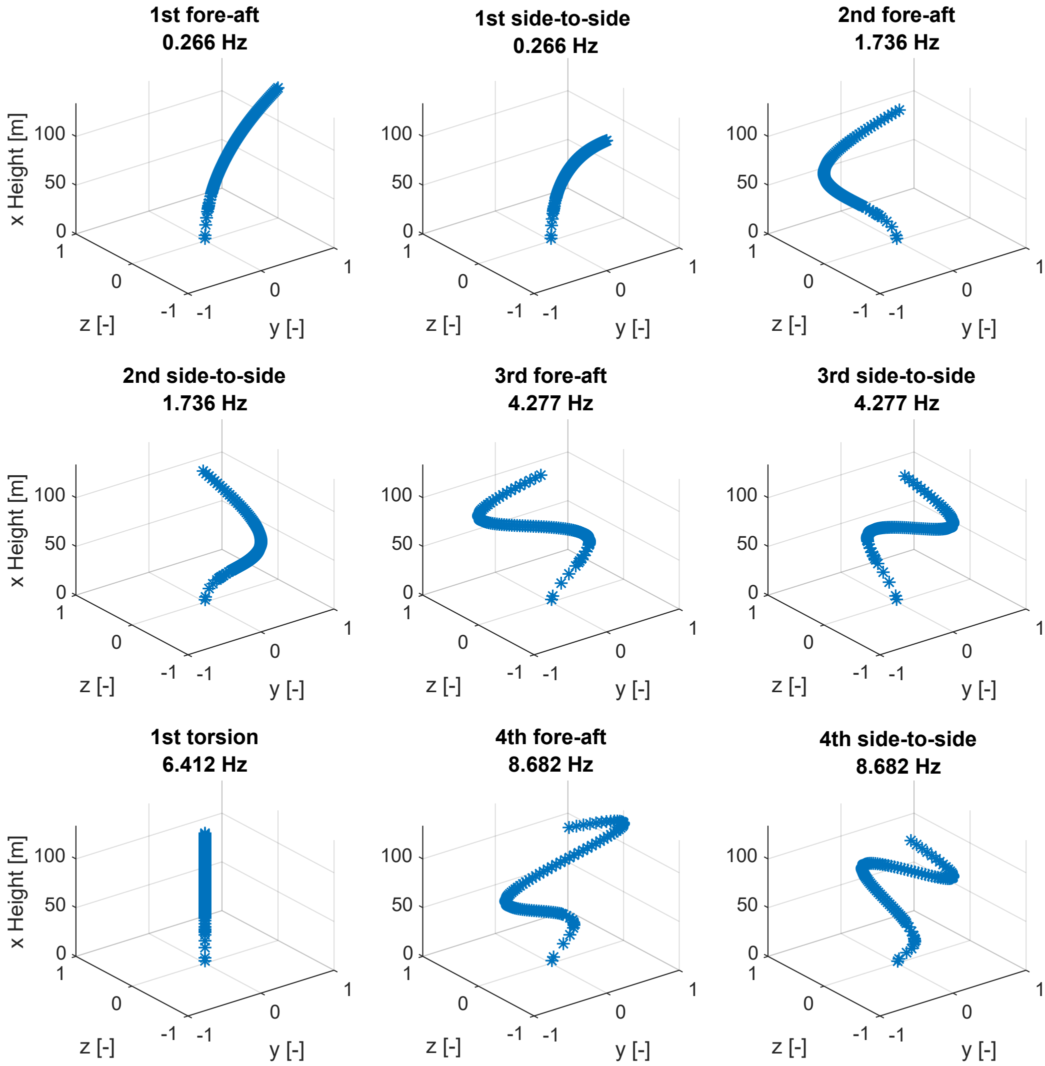

Figure 4.13: Visualization of the first nine eigenmodes calculated in MATLAB® for the support structure modeled with Timoshenko beam elements. The structure is fixed at the bottom, where six DOFs are constrained. The RNA is accounted for as a point mass in the eigenanalysis.

The global dynamics of the bottom-fixed OWTs is usually well captured when eigenmodes up to the cut-off frequency of around 5 Hz are included in the analysis.[80] This frequency usually constitutes an upper bound for the global dynamics analysis of the MW-class wind turbines — the energy of the higher modes is faster dissipated. This was often observed in the simulation results and the full-scale measurements of the MW-class wind turbines (Popko, Huhn, et al., 2018; Popko

[80] The definition of the frequency upper bound alone is not sufficient to claim that the global dynamics of an OWT is correctly reproduced. Note that the eigenmodes, which are involved in the analysis, should account for the combined modal mass of at least 90% of the total mass in orthogonal horizontal directions of response to correctly capture the global dynamic response of the structure (ASCE, 2017, p. 104).

et al., 2019). Therefore, a more significant discrepancy (6.5% to 7.3%) between the codes at both 4th fore-aft and side-to-side modes (above 8.5 Hz) is not considered to be an issue.

Table 4.7 shows horizontal deflections at the MSL, tower bottom (12.5 m above MSL), and tower top (98.5 m above MSL) upon the application of a static horizontal force of 1000 kN at the tower top. Deflections are computed with MATLAB®, MoLWiT, and ROSAP. Percentage differences between the results are calculated according to Eq. 4.1 and are shown in the last three columns.

Table 4.7: Comparison of horizontal deflections of the support structure at MSL, tower bottom at 12.5 m above MSL, and tower top at 98.5 m above MSL. Deflections are computed with MATLAB®, MoLWiT, and ROSAP. Percentage differences are shown in the last three columns.

Location	MATLAB® (Timoshenko) [m]	MoLWiT (Anisotropic) [m]	ROSAP (Timoshenko) [m]	MATLAB® vs. ROSAP (col. 2 vs. 4)	MATLAB® vs. MoLWiT (col. 2 vs. 3)	MoLWiT vs. ROSAP (col. 3 vs. 4)
MSL	0.02656	0.02601	0.02645	0.42%	2.11%	1.69%
TP	0.04913	0.04842	0.04907	0.12%	1.46%	1.33%
Tower top	0.53810	0.53288	0.53882	0.13%	0.98%	1.11%

An excellent match is observed between MATLAB® and ROSAP results in column 5 of Table 4.7. The percentage difference in deflections is less than 0.5% at all analyzed heights. A good match is observed between MATLAB® and MoLWiT (column 6), and MoLWiT and ROSAP (column 7), where the percentage difference varies from around 1% to 2.1% depending on the location.

To sum up — the newly developed FEM code for modeling mDOF structures has been successfully verified against MoLWiT and ROSAP. A very good match of eigenfrequencies and static deflections is obtained — especially when the Timoshenko beam elements are used in two codes. The verified FEM code is coupled in MATLAB® with the extended ice model, as described in Section 4.3.2.

4.3.2 Extension of simulation capabilities of ice model from sDOF to mDOF structures

The simulation capabilities of the Hendrikse ice model source code have been extended to cope with multi-mode mDOF structures, which behavior can be described by a superposition of a number of eigenmodes, N_m. This section presents a theoretical background of the modal system analysis in the time domain. The presented methodology has been applied to extend Eqs. 2.10–2.12 of the ice model in the solver of the source code. The cross-verification of the simulation results from the extended source code and MoLWiT is presented in Section 4.4.

Note that the dynamic response of any linear system consisting of N_dof can be described by second order differential equations:

$$[\boldsymbol{M}]\{\ddot{x}\} + [\boldsymbol{C}]\{\dot{x}\} + [\boldsymbol{K}]\{x\} = \{\boldsymbol{F}\} \tag{4.13}$$

where $[\boldsymbol{M}]$ is the global mass matrix; $[\boldsymbol{C}]$ is the global viscous damping matrix; $[\boldsymbol{K}]$ is the global stiffness matrix; $\{\boldsymbol{x}\}$ is the displacement vector of N_{dof}; symbols $\dot{}$ and $\ddot{}$ represent first and second derivative of displacement components with respect to time; and $\{\boldsymbol{F}\}$ is the load vector with loading time histories for individual DOFs.

Displacements of all DOFs can be represented in terms of a number of individual mode shape vectors $\{\boldsymbol{\phi}\}$, which are arranged in the mode shape matrix $[\boldsymbol{\phi}]$:

$$[\boldsymbol{\phi}] = [\{\boldsymbol{\phi}\}_1 \, \{\boldsymbol{\phi}\}_2 \ldots \{\boldsymbol{\phi}\}_{N_{\text{dof}}}] \tag{4.14}$$

Therefore, the displacement vector $\{\boldsymbol{x}\}$ from Eq. 4.13 can be represented in terms of the mode shape vectors $\{\boldsymbol{\phi}\}$, where the time variation is described by the modal coordinates $r_1(t), r_2(t), \ldots, r_{N_{\text{dof}}}(t)$:

$$\{\boldsymbol{x}\} = [\boldsymbol{\phi}]\,\{\boldsymbol{r}\} = \sum_{j=1}^{N_{\text{dof}}} \{\boldsymbol{\phi}\}_j r_j \tag{4.15}$$

The displacement representation from Eq. 4.15 can be substituted into Eq. 4.13, which is then premultiplied with $[\boldsymbol{\phi}]^{\mathsf{T}}$:

$$[\boldsymbol{\phi}]^{\mathsf{T}}[\boldsymbol{M}][\boldsymbol{\phi}]\{\ddot{\boldsymbol{r}}\} + [\boldsymbol{\phi}]^{\mathsf{T}}[\boldsymbol{C}][\boldsymbol{\phi}]\{\dot{\boldsymbol{r}}\} + [\boldsymbol{\phi}]^{\mathsf{T}}[\boldsymbol{K}][\boldsymbol{\phi}]\{\boldsymbol{r}\} = [\boldsymbol{\phi}]^{\mathsf{T}}\{\boldsymbol{F}\} \tag{4.16}$$

Note that the orthogonality relation in Eqs. 4.6 and 4.7 implies that mass and stiffness terms are diagonal and uncoupled. The same can be assumed for the modal damping:

$$\{\boldsymbol{\phi}\}_j^{\mathsf{T}}[\boldsymbol{C}]\{\boldsymbol{\phi}\}_k = 0 \qquad \text{for } j \neq k \tag{4.17}$$

Since Eqs. 4.6, 4.7, and 4.17 are diagonal and uncoupled, the entire modal equation of motion is also uncoupled:

$$[\boldsymbol{m}]\{\ddot{\boldsymbol{r}}\} + [\boldsymbol{c}]\{\dot{\boldsymbol{r}}\} + [\boldsymbol{k}]\{\boldsymbol{r}\} = [\boldsymbol{\phi}]^{\mathsf{T}}\{\boldsymbol{F}\} \tag{4.18}$$

where $[\boldsymbol{m}]$, $[\boldsymbol{c}]$, and $[\boldsymbol{k}]$ are the generalized modal mass, damping, and stiffness matrices, respectively. The size of each generalized modal matrix is $N_{\text{m}} \times N_{\text{m}}$.

The resulting ice load, F_{ice}, from N_{st} stripes is applied at the desired structural DOF and projected to each eigenmode, j, through the modal load vector, $\{\boldsymbol{f}_{\text{ice}}\}$:

$$\{\boldsymbol{f}_{\text{ice}}\} = \{\boldsymbol{\phi}\}_{\text{dof},j}^{\mathsf{T}} F_{\text{ice}} = \sum_{j=1}^{N_{\text{m}}} \phi_{\text{dof},j} \sum_{i=1}^{N_{\text{st}}} F_{\text{ice},i} \tag{4.19}$$

Work-energy principle

The total mechanical energy of the system, E_t, can be expressed as a sum of kinetic energy, E_k, and potential energy, E_p:

$$E_\mathrm{t} = E_\mathrm{k} + E_\mathrm{p} = \frac{1}{2}\{\dot{x}\}^\mathsf{T}[\boldsymbol{M}]\{\dot{x}\} + \frac{1}{2}\{x\}^\mathsf{T}[\boldsymbol{K}]\{x\} \tag{4.20}$$

where $\{x\}$ is the displacement vector defined in Eq. 4.15 and $\{\dot{x}\}$ is the velocity vector.

The total mechanical energy in the modally reduced system, consisting of N_m eigenmodes, can be expressed in terms of modal mass $[\boldsymbol{m}]$, modal stiffness $[\boldsymbol{k}]$, and modal coordinates $\{\boldsymbol{r}\}$:

$$E_\mathrm{t} = E_\mathrm{k} + E_\mathrm{p} = \frac{1}{2}\{\dot{r}\}^\mathsf{T}[\boldsymbol{m}]\{\dot{r}\} + \frac{1}{2}\{r\}^\mathsf{T}[\boldsymbol{k}]\{r\} = \frac{1}{2}\sum_{j=1}^{N_\mathrm{m}}(m_{jj}\dot{r}_j^2 + k_{jj}r_j^2) \tag{4.21}$$

Note that the total mechanical energy is the sum of mechanical energy in each eigenmode, j, without coupling effects as the mass and stiffness terms are uncoupled (see Eqs. 4.6 and 4.7).

Work done by ice on the structure at the node located at the MSL is calculated multiplying Eq. 4.19 by the modal coordinate vector $\{\boldsymbol{r}\}$, and integrating with respect to time:

$$W_\mathrm{ice} = \int F_\mathrm{ice}\,dx = \int \{\boldsymbol{f}_\mathrm{ice}\}\{\dot{r}\}\,dt = \sum_{j=1}^{N_\mathrm{m}}\int f_{\mathrm{ice},j}\,\dot{r}_j\,dt \tag{4.22}$$

The total energy dissipated by the structure per cycle is:

$$\Delta W_\mathrm{d} = -\oint F_\mathrm{d}\,dx = -\oint [c]\,\{\dot{r}\}\,dr = -\sum_{j=1}^{N_\mathrm{m}}\oint c_{jj}\,\dot{r}_j^2\,dt \tag{4.23}$$

where F_d is the viscous damping force, $[\boldsymbol{c}]$ is the modal damping matrix, $dx = \dot{x}dt$, and $dr = \dot{r}dt$.

4.4 Extended ice model interacting with modally reduced mDOF structure

In this section, both MoLWiT and a newly developed mDOF code (Section 4.3) that is coupled with the modified Hendrikse ice model (Section 4.3.2) are cross-verified against each other.

The parameters of the ice model are adapted to the full-scale ice according to the findings from Section 4.2. Table 4.8 lists a set of the reference ice parameters, from which the properties of individual ice stripes are derived. Table 4.9 presents the properties of individual ice stripes, which are used for the verification simulations.

Table 4.8: Reference ice parameters used for full-scale ice simulation.

Parameter	Value	Unit	Description
h_{ice}	0.1	m	Ice thickness
F_{brittle}	1 109 663	N	Mean value of the global brittle crushing load at v_{brittle} and above
F_{max}	5 548 315	N	Maximum ice load at the ductile-to-brittle transition
$F_{2v\text{db}}$	3 328 989	N	Mean value of the global ice load at $2v_{\text{db}}$
σ_{ice}	166 450	N	Standard deviation of the brittle crushing load, F_{brittle}
v_{db}	0.001	m s^{-1}	Transition velocity between ductile and brittle crushing regions
v_{brittle}	0.1	m s^{-1}	Transition velocity to continuous brittle crushing
f_{peak}	11	Hz	Peak frequency in the failure spectrum of ice at v_{brittle}
t_{peak}	150	s	Time of peak load at v_{db} for a rigid structure
c_{ref}	0.3	–	Fraction of the ice stripe deformation when visco-plasticity initiates
f_{n}	0.95	–	Peak load factor at v_{db}

The monopile support structure is fixed at the seabed, where six DOFs are constrained. The RNA is modeled as a point mass of 536 780 kg, which is connected above the tower top center with a vertical offset of 3.05 m. The RNA rolling, yaw, and nodding inertia are not included. Nine eigenmodes are accounted for in the analysis — four fore-aft, four side-to-side, and one torsional as visualized in Figure 4.13.

Marine growth and hydro loads are not accounted for. Two sets of results are provided from the MATLAB® code for the support structure modeled with Timoshenko and Euler-Bernoulli beam elements, respectively. The MoLWiT results are provided for the support structure modeled with anisotropic beam elements.

Simulations are performed for $\dot{u}_{\text{ice}}$ of 0.01 m s^{-1}, h_{ice} of 0.1 m, and 50 individual ice stripes. A new position of each ice stripe upon its failure is derived from uniformly distributed random numbers. In MATLAB® the *rand* function[81] based on the Mersenne Twister pseudorandom number generator (Matsumoto & Nishimura, 1998) is used, whereas in MoLWiT the *Xorschift64* pseudorandom number generator[82] is utilized. Both generators provide a high quality sequence of uniformly distributed pseudorandom numbers as observed by Gevorkyan et al. (2016).

The output time step is set to 0.01 s and the length of simulation is 600 s. In Dymola® explicit ODEs are solved[83] by the variable time step LSODAR method with both relative and absolute tolerances of 1.0×10^{-5}. In MATLAB® the ODE45 variable time step solver[84] is used with a relative tolerance of 1.0×10^{-5} and an absolute tolerance of 1.0×10^{-7}.

[81] https://de.mathworks.com/help/matlab/ref/rand.html (Last accessed: June 1, 2020)
[82] https://build.openmodelica.org/Documentation/Modelica.Math.Random.Generators.Xorshift64star.html (Last accessed: June 1, 2020)
[83] MoLWiT utilizes Dymola® as a simulation environment. For this work Dymola® 2020 was used.
[84] An explicit Runge-Kutta (4,5) formula developed by Dormand and Prince (1980) is used in ODE45 solver.

Table 4.9: Derived parameters, which are used for the definition of ice stripes for full-scale ice simulation.

Parameter	Value	Unit	Description
N_{st}	50	–	Number of individual ice stripes, see Hendrikse and Metrikine (2016, p. 133) for equation
k_{ice}	55.483×10^{6}	$\mathrm{N\,m^{-1}}$	Front stiffness of the ice stripe, see Hendrikse and Metrikine (2016, p. 133) for equation
c_{c}	110.966×10^{6}	$\mathrm{kg\,s^{-1}}$	Rear creep damper in the ice stripe, see Hendrikse and Metrikine (2016, p. 131) for equation
$k_{\mathrm{v\text{-}p}}$	11.097×10^{6}	$\mathrm{N\,m^{-1}}$	Stiffness of the viscoplastic element in the ice stripe, see Hendrikse and Metrikine (2015, p. 341) for equation
$c_{\mathrm{v\text{-}p}}$	33.290×10^{6}	$\mathrm{kg\,s^{-1}}$	Damping of the viscoplastic element in the ice stripe, see Hendrikse and Metrikine (2015, p. 341) for equation
F_{slip}	33.290×10^{3}	N	Load at which the viscoplastic element is activated, see Hendrikse and Metrikine (2016, p. 132) for equation
δ_{crit}	0.0036	m	Critical deformation of the ice stripe upon its failure, see Hendrikse and Metrikine (2015, p. 340) for equation
u_{init}	$u_{\mathrm{init}} \sim U(0,\ 0.011)$	m	Offset of the individual ice stripe upon its failure (with respect to the structure equilibrium position)

Horizontal fore-aft displacements of the monopile support structure are analyzed at three heights — at MSL, tower bottom (12.5 m above MSL), and tower top (98.5 m above MSL). They are shown in Figures 4.14, 4.15, and 4.16 in terms of time series, PDFs, and PSDs. All time series are zoomed to 30 s length time windows for clearer overview of the signals. Both PDFs and PSDs are calculated out of 550 s time series. The first 50 s are cut out to remove the impact of the initial numerical transients on PDF and PSD analysis.

Note that the time series signals are not overlapping — this is expected as the random number generators are used for the simulation of offsets of individual ice stripes upon their failures. Therefore, the most important is to obtain comparable statistics of the structural response at different heights. A very good match is observed between the time series of displacements obtained from MATLAB® (Euler-Bernoulli beam) and MoLWiT (anisotropic beam). The percentage differences — calculated from Eq. 4.1 — between the following statistics of both time series are:

- for mean values: 1.17% at MSL, 0.67% at the tower bottom, and 0.33% at the tower top;
- for standard deviations: 1.12% at MSL, 0.60% at the tower bottom, and 0.84% at the tower top;
- for skewness: 1.61% at MSL, 0.42% at the tower bottom, and 2.58% at the tower top.

The results obtained with MATLAB® (Timoshenko beam) are slightly off due to higher shear flexibility of the Timoshenko beam elements. An excellent match is also observed for PSDs of displacements at each analyzed height of the structure — the subsequent frequency peaks overlap.

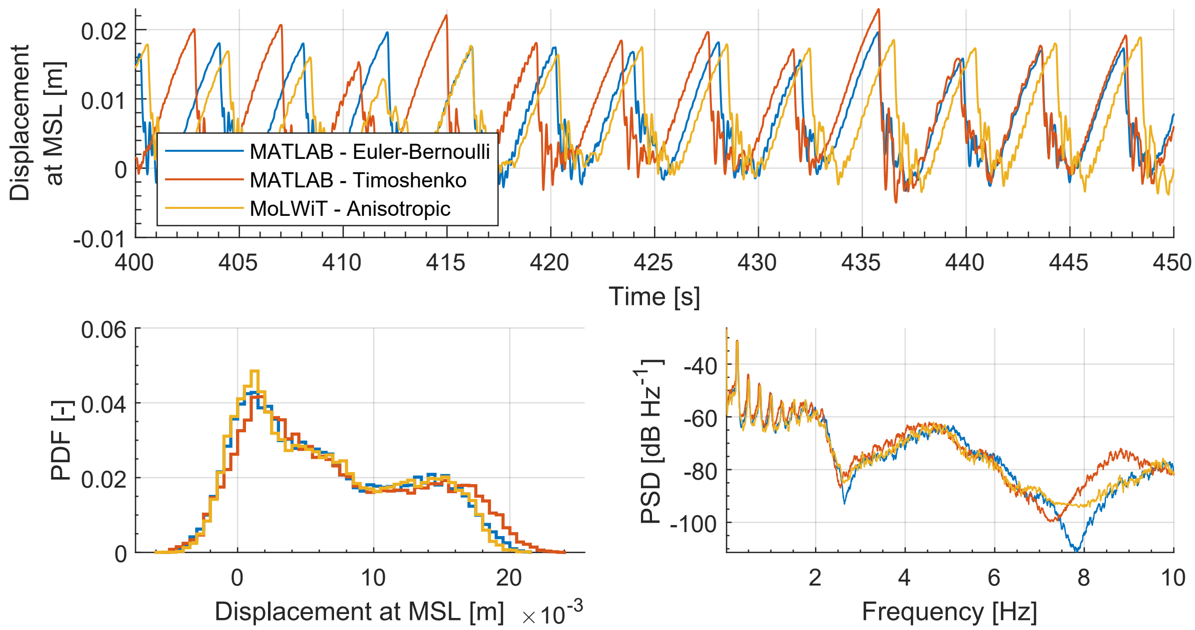

Figure 4.14: Fore-aft displacement at MSL — zoomed time series, PDF, and PSD. Simulations performed for $\dot{u}_{\text{ice}}$ of 0.01 m s^{-1}, h_{ice} of 0.1 m, and 50 ice stripes.

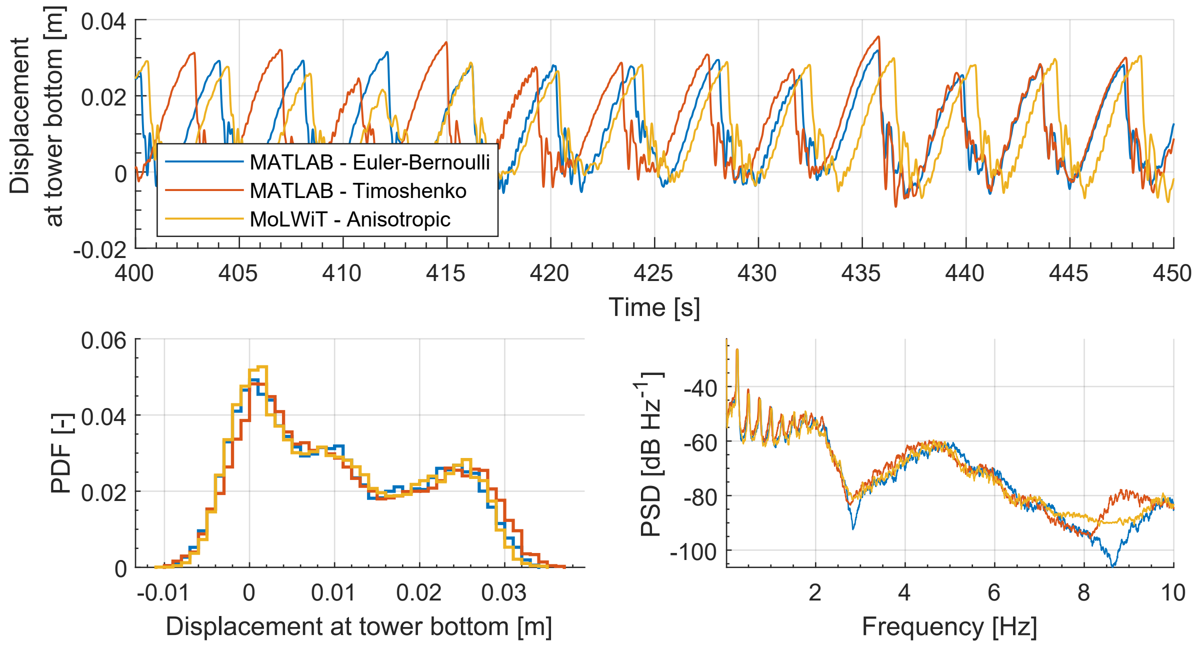

Figure 4.15: Fore-aft displacement at tower bottom (12.5 m above MSL) — zoomed time series, PDF, and PSD. Simulations performed for $\dot{u}_{\text{ice}}$ of 0.01 m s^{-1}, h_{ice} of 0.1 m, and 50 ice stripes.

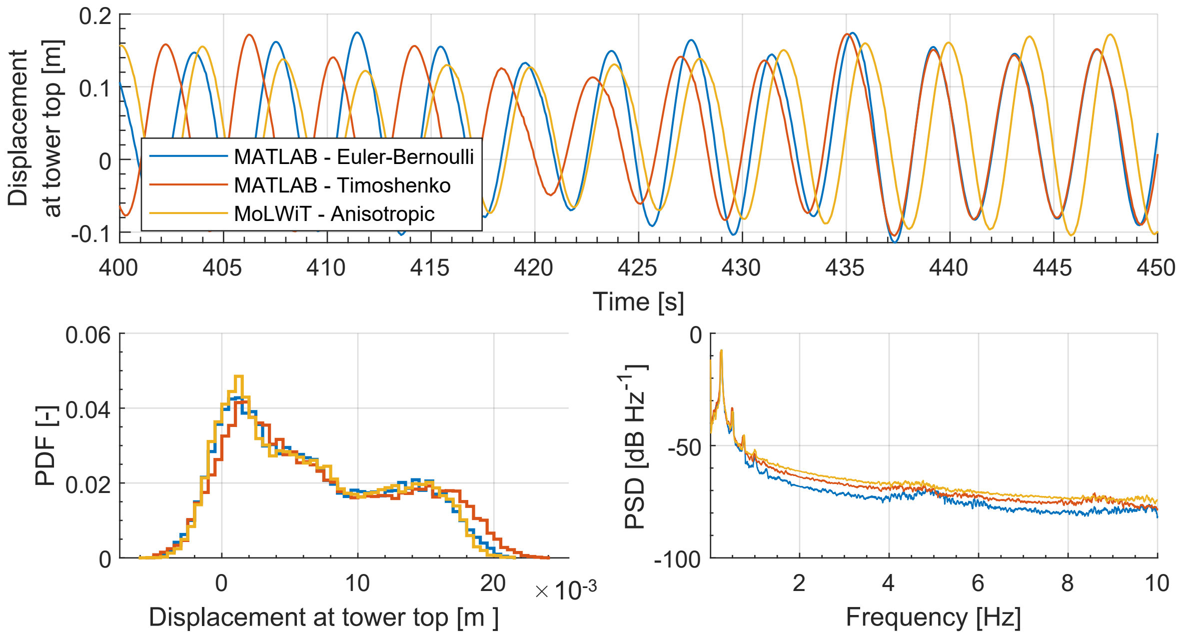

Figure 4.16: Fore-aft displacement at tower top (98.5 m above MSL) — zoomed time series, PDF, and PSD. Simulations performed for $\dot{u}_{\text{ice}}$ of 0.01 m s^{-1}, h_{ice} of 0.1 m, and 50 ice stripes.

Figure 4.17 shows the global ice load acting on the structure at the MSL level. There is a very good match of PDFs obtained from MATLAB® (Euler-Bernoulli beam) and MoLWiT (anisotropic beam). The results obtained with MATLAB® (Timoshenko beam) are slightly off due to higher shear flexibility of the Timoshenko beam elements. The energy content in the ice load spectrum at the intermittent ice crushing is dominated by a distinct peak at 0.23 Hz, which corresponds to the frequency of the global ice failure[85]. Deep spectral gaps are visible in PSDs of the ice load at the frequencies of around 1.75 Hz, 4.2 Hz–4.4 Hz, and 8.7 Hz–9.3 Hz. These set of frequencies corresponds to the 2nd, 3rd, and 4th fore-aft eigenmode, respectively.

[85] Once the critical ductile load is reached by the vast majority of ice stripes, they all fail almost at the same time (time scale of milliseconds) and the structure springs back vigorously. A pattern of this rapid motion resembles a saw-tooth shape (Figure 4.14) and is only observed when the first frequency of the structure is higher than this global failure of multiple ice stripes.

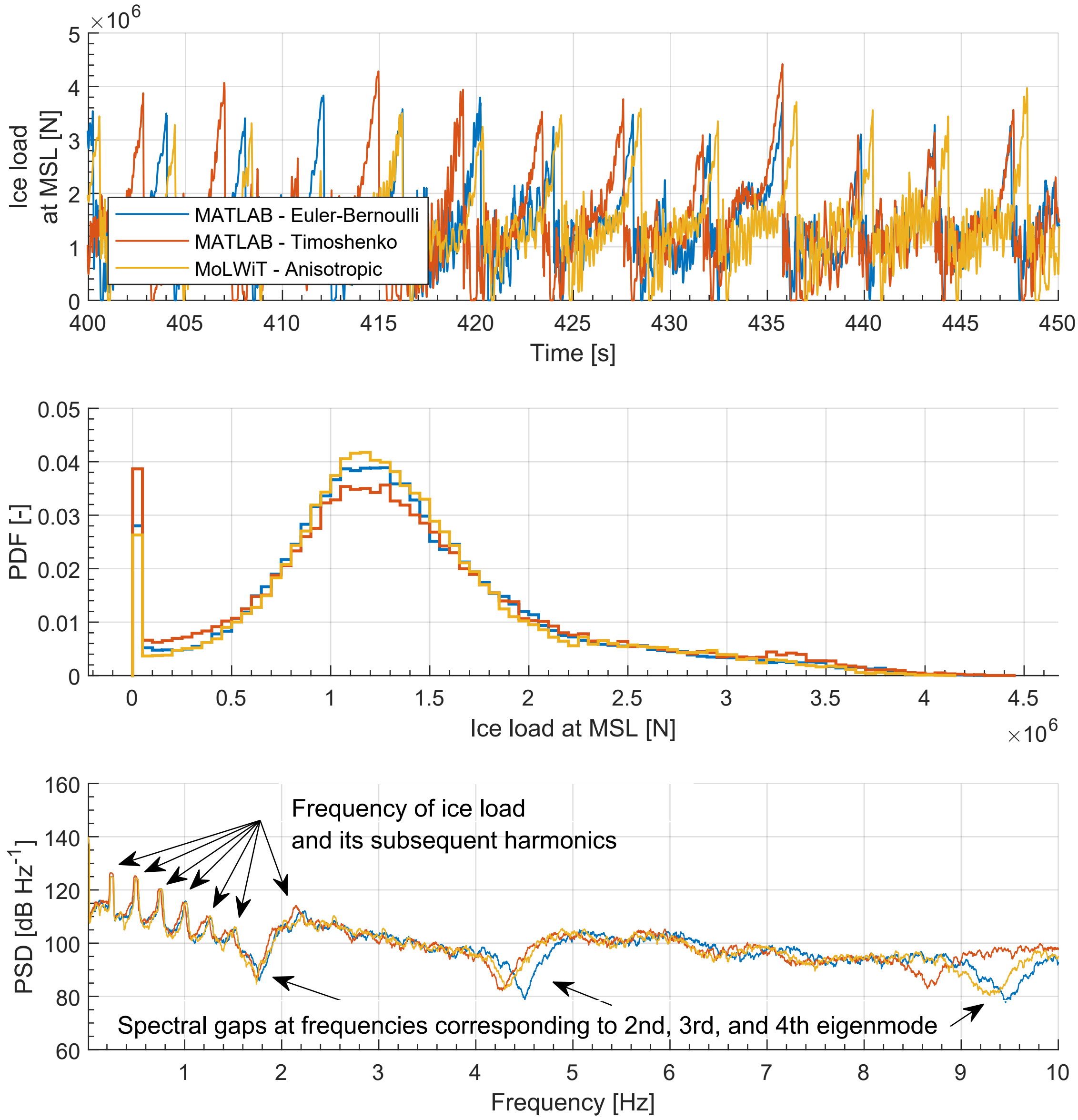

Figure 4.17: Ice load acting at MSL in fore-aft direction — zoomed time series, PDF, and PSD. Simulations performed for $\dot{u}_{\text{ice}}$ of 0.01 m s^{-1}, h_{ice} of 0.1 m, and 50 ice stripes.

4.5 Summary of the chapter

The following has been achieved in Chapter 4:

- The estimation of full-scale ice properties has been made based on the literature study, own experiments, and the data from the SeaLOWT project. A set of indicative sea ice properties applicable to the southern Baltic Sea has been provided in Section 4.2. These properties have been used for the derivation of full-scale parameters for the Hendrikse ice model.

- The Hendrikse ice model interacting with an sDOF structure has been implemented in MoLWiT and cross-verified against its source code in MATLAB® in Section 4.1. A limitation of the source code associated with the root-finding mechanism employed by the ODE solver has been identified.
- The FEM code for modeling mDOF structures has been implemented in MATLAB® in Section 4.3. It has been verified in terms of eigenfrequencies and static deflections against MoLWiT and ROSAP. An excellent match has been achieved between MATLAB® and ROSAP (both with Timoshenko beams), and between MATLAB® (Euler-Bernoulli beam) and MoLWiT (anisotropic beam).
- The newly developed FEM code has been coupled with the source code of the Hendrikse ice model, which simulation capabilities have been extended to cope with the modal representation of mDOF structures. The new coupling has been successfully cross-verified against MoLWiT simulations in Section 4.4. A very good match has been achieved between MATLAB® (Euler-Bernoulli beam) and MoLWiT (anisotropic beam), where the percentage differences between the statistics (mean, standard deviation, and kurtosis) computed from the time series of structural displacements are within 1%.

Chapter 5

Fully-integrated simulation of ice and offshore wind turbine

In Chapter 4, the coupling between the Hendrikse ice model and a modally reduced mDOF support structure has been successfully cross-verified in fully-integrated simulations in two independent simulation tools — MATLAB® and MoLWiT. The next step is to use the Hendrikse ice model for the fully-integrated simulation with the flexible OWT consisting of the support structure designed by Ramboll, the generic IWES Wind Turbine IWT-7.5-164 model (Popko, Thomas, et al., 2018), and the controller[86]. This setup is used for the simulation of the ice-OWT interaction in MoLWiT.

Section 5.1 presents the advantages of the fully-integrated simulation of the ice-OWT interaction and compares this approach with the coupled simulation where the ice model is encapsulated in the external DLL. The application of the latter approach might be impeded by the lack of the event detection mechanism, which is crucial for detecting ice failures at exact time points. In Section 5.2, multiple LCs are defined for the analysis of ice impact on the global dynamics of the OWT. The analysis is performed at three distinct design situations[87] — idling below the cut-in wind speed, power production below and above the rated wind speed. At each design situation, the influence of multiple ice velocities on the OWT dynamics is investigated. The simulated range of ice velocities covers three main ice-structure interaction modes — intermittent ice crushing, frequency lock-in, and continuous brittle crushing — which are defined in Section 2.3. Section 5.3 quantifies the impact of ice on the global dynamics of the OWT. The quantification is done in

[86] A new controller has been developed by the Advanced Control Systems group at IWES. As of June 2020, the controller consists of a torque regulator and both collective and individual pitch controllers. In this work, a collective pitch control is used. The generator torque is calculated from a relationship proportional to the squared generator speed for the partial-load region below the rated wind speed. A gain-scheduled, proportional-integral pitch controller is implemented for the full-load region above the rated wind speed, where the constant torque approach is utilized. A linear transition between the partial- and full-load regions around the rated wind speed is utilized. Additionally, low-pass and notch filters are used for removing specific global eigenfrequencies of the wind turbine from the control input and output signals to prevent system excitation.

[87] The term *design situation* is used in the standards in the context of DLCs. IEC (2019b, p. 44) defines it as: "For design purposes, the life of an offshore wind turbine can be represented by a set of design situations covering the most significant conditions that an offshore wind turbine may experience".

terms of DELs and PSDs. Section 5.4 presents the results of the work-energy principle. The work-energy transfer between ice and the OWT is analyzed at several design situations, such as idling and power production at different wind speeds. Finally, in Section 5.5, a contribution of different eigenmodes to DELs is investigated at different ice-structure interaction regions by switching off the contribution of a certain eigenmode to the system displacement at MSL but still preserving its contribution to the system stiffness.

5.1 Fully-integrated simulation approach versus other coupled approaches

According to the author's knowledge, the fully-integrated simulation[88] of ice loading and an operating OWT in an aero-hydro-servo-elastic tool has not been performed with the Hendrikse ice model yet.

At the time when this dissertation was written, Ramboll was working on the coupling of the Hendrikse ice model encapsulated in the external DLL with their in-house tool ROSAP. However, the results were not available for the comparison with MoLWiT at that time.

There were also several approaches to couple other ice models to different aeroelastic tools by using an external DLL (e.g., Yu et al., 2013, 2014; McCoy et al., 2014; Shi et al., 2016, 2018). Another approach is to couple two independent tools. For example, Willems and Hendrikse (2019) coupled the Variation of contact Area model for Numerical Ice Load Level Analyses (VANILLA) with the Bonus Horizontal axis wind turbine Code (BHawC)[89]. Such coupling can be realized through a communication protocol that shares a number of variables between both tools at regular time intervals (a similar way how the DLL communicates with an external tool).

It should be emphasized that the event detection[90] is not possible in such a configuration, as a DLL interface can only handle inputs and outputs at each time step of the integrator. Therefore, the event detection mechanism — potentially encapsulated in the DLL that contains the ice model — cannot halt the integrator in the main code before the next communication time step between the DLL and the code occurs. Therefore, the simulation of ice-structure interaction by means of the external DLL might not always provide reliable results and great care in their interpretation is required. Some of the ice-breaking events might be communicated with a certain delay to the solver or even be overlooked by the solver if ice stripes move very fast and several successive breaking events take place in-between the two subsequent DLL-code communication

[88] The differences between the fully-integrated simulation, full coupling, sequential approach, semi-integrated approach, and superposition method are defined and described by Böker (2010, pp. 26–31).

[89] An in-house aeroelastic tool from Siemens Gamesa Renewable Energy.

[90] The ODEs solver should determine an appropriate time to stop the solution. For example, the ODE solver should stop once the individual ice stripe breaks. However, the ODE solver does not know beforehand when the breaking of the ice stripe will occur — as the breaking may occur at any time during the solution. The event detection function helps to find out the exact time point at which the ice stripe breaks.

time points. Theoretically, these limitations might be overcome when using a very fine integrator time step and the communication interval between the DLL and the code. However, this would often come at the price of computational performance.

To sum up — the fully-integrated approach, which is utilized in this dissertation is in general more robust and superior to other approaches where an external DLL is used, or two individual tools are fully-coupled through an external interface.

5.2 Definition of test load cases and outputs

Three distinct design situations for the OWT are selected for the tests: (1) Idling below the cut-in wind speed; (2) Power production below the rated wind speed; and (3) Power production above the rated wind speed. The global dynamics of the OWT is analyzed at these design situations: (1) By accounting for ice loads; and (2) Without ice load contributions.

Twelve groups of LCs with increasing complexity are defined in Table 5.1. Six of them are simulated with a constant uniform wind, whereas the remaining six are simulated with turbulent wind fields.

Turbulent wind fields for stochastic LCs are generated with the Sandia method using the Kaimal spectrum. Six independent wind seeds, each 10 minutes long, are used for every LC to obtain statistically comparable results as recommended in IEC (2019a, p. 50). Standard deviations of longitudinal wind components, σ_{long}, are calculated from the turbulence intensities provided by Ramboll (2018, p. 9). Standard deviations of lateral and vertical components — σ_{lat} and σ_{vert} — are derived based on IEC (2019a, p. 70).

A set of 22 ice velocities, which grow logarithmically from $0.001\,\mathrm{m\,s^{-1}}$ to $0.400\,\mathrm{m\,s^{-1}}$, is simulated in conjunction with three distinct design situations for the wind turbine with both constant and turbulent wind. This range covers the vast majority of ice velocities (probability of occurrence exceeding 99%) in the southern Baltic Sea, as presented in Table 4.5. The reference ice parameters are listed in Table 4.8. The derived parameters, which are used for the definition of ice stripe properties, are presented in Table 4.9.

The direction of ice load is aligned with the wind direction in all LCs. This is a realistic assumption in the case when wind is the main driving force for the ice cover[91]. Mass of marine growth, water added masses, and buoyancy are not included for the sake of modeling simplicity. Also, wave loads[92] and sea current loads[93] are not accounted for in the simulations.

[91]It is the case for the reference site in the southern Baltic Sea (from which the met-ocean properties are used in this research), where the ice floe direction is aligned with the dominant wind direction (Ramboll, 2018, p. 18).

[92]Waves are not present, as the ice cover is modeled as a flat surface covering water at MSL.

[93]Sea current load is modeled in a simplified manner — as a time-invariant, vertical load profile — in the vast majority of aero-hydro-servo-elastic simulation tools. Therefore, it does not contribute to dynamic loads.

Table 5.1: Definition of test load cases for examination of ice-OWT interaction.

Load case set	Wind conditions	Design situation
LC_01 (1 subcase)	Constant uniform wind, no wind shear $V_{hub} = 1\,\mathrm{m\,s^{-1}}$	Idling below cut-in wind speed, Blades pitched to 90°, Ice is not included
LC_07 (1 subcase)	Constant uniform wind, no wind shear $V_{hub} = 7\,\mathrm{m\,s^{-1}}$	Power production below rated wind speed governed by external controller, Ice is not included
LC_15 (1 subcase)	Constant uniform wind, no wind shear $V_{hub} = 15\,\mathrm{m\,s^{-1}}$	Power production above rated wind speed governed by external controller, Ice is not included
LC_01_$\dot{u}_{ice}$ (22 subcases)	Constant uniform wind, no wind shear $V_{hub} = 1\,\mathrm{m\,s^{-1}}$	Idling below cut-in wind speed, Blades pitched to 90°, Ice acting on the support structure at MSL
LC_07_$\dot{u}_{ice}$ (22 subcases)	Constant uniform wind, no wind shear $V_{hub} = 7\,\mathrm{m\,s^{-1}}$	Power production below rated wind speed governed by external controller, Ice acting on the support structure at MSL
LC_15_$\dot{u}_{ice}$ (22 subcases)	Constant uniform wind, no wind shear $V_{hub} = 15\,\mathrm{m\,s^{-1}}$	Power production above rated wind speed governed by external controller, Ice acting on the support structure at MSL
LC_01seed (6 subcases)	Stochastic wind field modeled with Kaimal spectrum $V_{hub} = 1\,\mathrm{m\,s^{-1}}$ $\sigma_{long} = 0.625\,\mathrm{m\,s^{-1}}$, $\sigma_{lat} = 0.8\sigma_{long}$, $\sigma_{vert} = 0.5\sigma_{long}$ $\alpha_{NWP} = 0.12$	Idling below cut-in wind speed, blades pitched to 90°, Ice is not included
LC_07seed (6 subcases)	Stochastic wind field modeled with Kaimal spectrum $V_{hub} = 7\,\mathrm{m\,s^{-1}}$ $\sigma_{long} = 1.068\,\mathrm{m\,s^{-1}}$, $\sigma_{lat} = 0.8\sigma_{long}$, $\sigma_{vert} = 0.5\sigma_{long}$ $\alpha_{NWP} = 0.12$	Power production below rated wind speed governed by external controller, Ice is not included
LC_15seed (6 subcases)	Stochastic wind field modeled with Kaimal spectrum $V_{hub} = 15\,\mathrm{m\,s^{-1}}$ $\sigma_{long} = 1.658\,\mathrm{m\,s^{-1}}$, $\sigma_{lat} = 0.8\sigma_{long}$, $\sigma_{vert} = 0.5\sigma_{long}$ $\alpha_{NWP} = 0.12$	Power production above rated wind speed governed by external controller, Ice is not included
LC_01seed_$\dot{u}_{ice}$ (132 subcases)	Stochastic wind field modeled with Kaimal spectrum $V_{hub} = 1\,\mathrm{m\,s^{-1}}$ $\sigma_{long} = 0.625\,\mathrm{m\,s^{-1}}$, $\sigma_{lat} = 0.8\sigma_{long}$, $\sigma_{vert} = 0.5\sigma_{long}$ $\alpha_{NWP} = 0.12$	Idling below cut-in wind speed, Blades pitched to 90°, Ice acting on the support structure at MSL
LC_07seed_$\dot{u}_{ice}$ (132 subcases)	Stochastic wind field modeled with Kaimal spectrum $V_{hub} = 7\,\mathrm{m\,s^{-1}}$ $\sigma_{long} = 1.068\,\mathrm{m\,s^{-1}}$, $\sigma_{lat} = 0.8\sigma_{long}$, $\sigma_{vert} = 0.5\sigma_{long}$ $\alpha_{NWP} = 0.12$	Power production below rated wind speed governed by external controller, Ice acting on the support structure at MSL
LC_15seed_$\dot{u}_{ice}$ (132 subcases)	Stochastic wind field modeled with Kaimal spectrum $V_{hub} = 15\,\mathrm{m\,s^{-1}}$ $\sigma_{long} = 1.658\,\mathrm{m\,s^{-1}}$, $\sigma_{lat} = 0.8\sigma_{long}$, $\sigma_{vert} = 0.5\sigma_{long}$ $\alpha_{NWP} = 0.12$	Power production above rated wind speed governed by external controller, Ice acting on the support structure at MSL

σ_{long} – standard deviation of longitudinal wind component
σ_{lat} – standard deviation of lateral wind component
σ_{vert} – standard deviation of vertical wind component
$\dot{u}_{ice}$ = 0.001, 0.002, 0.003, 0.004, 0.005, 0.006, 0.007, 0.008, 0.009, 0.010, 0.020, 0.030, 0.040, 0.050, 0.060, 0.070, 0.080, 0.090, 0.100, 0.200, 0.300, 0.400 $\mathrm{m\,s^{-1}}$ – ice cover velocity

V_{hub} – mean wind speed at the hub height
α_{NWP} – power law exponent for wind shear
seed = a,b,c,d,e,f – six turbulent wind seeds

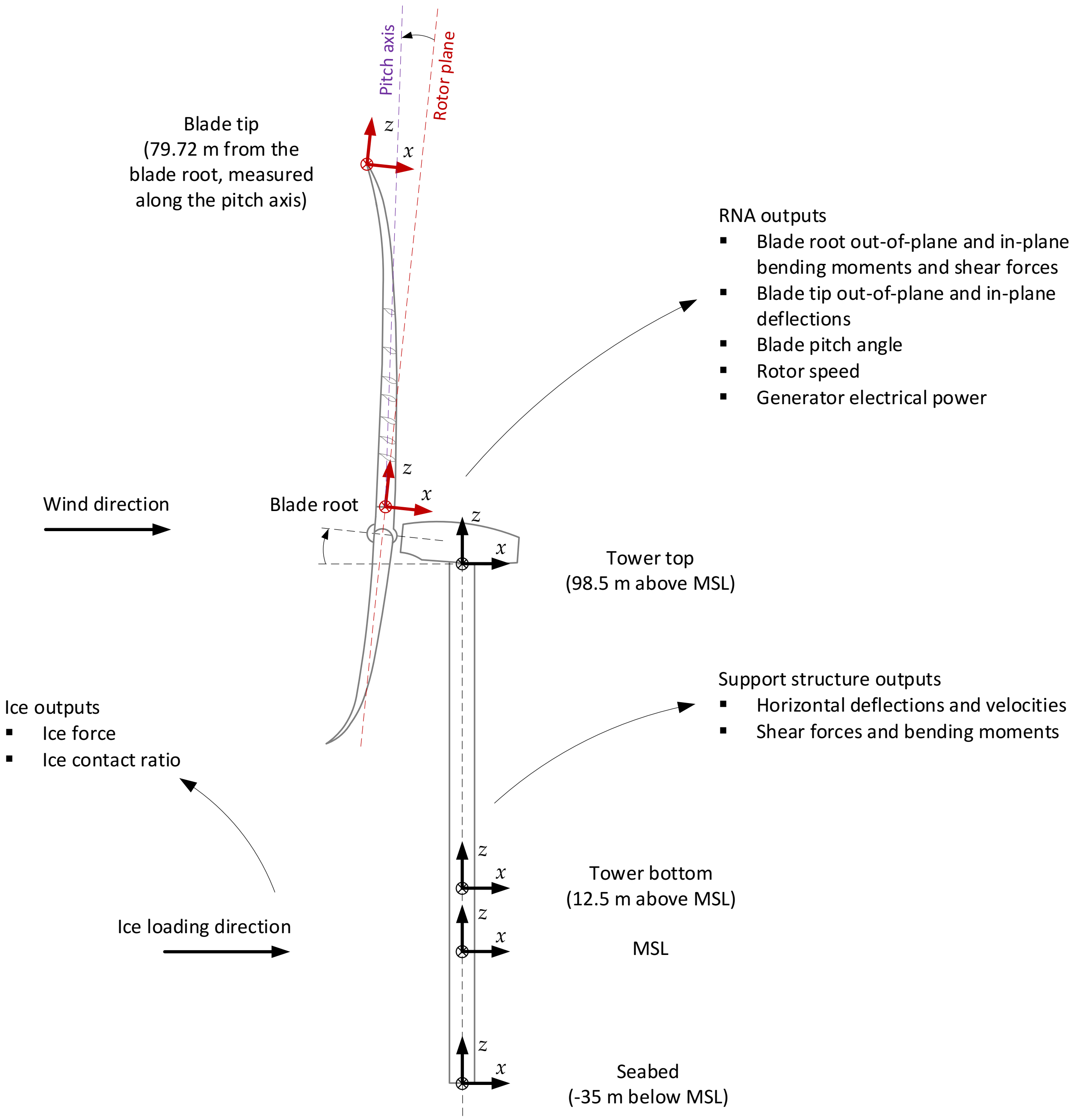

Figure 5.1: Schematic drawing of the analyzed OWT model consisting of the offshore monopile support structure designed by Ramboll and the IWES Wind Turbine IWT-7.5-164. The main outputs and the coordinate systems are indicated. The support structure outputs are provided in the right hand Cartesian coordinate system, where the x-axis points downwind; the y-axis points to the side; and the z-axis points vertically upwards. The blade outputs are provided in the right hand Cartesian coordinate system, where the x-axis points out-of-plane, downwind along the tilted rotor axis; the y-axis points in-plane of the rotor; and the z-axis points radially outwards.

The monopile support structure is fixed at the seabed, where six DOFs are constrained. Nine support structure eigenmodes (four fore-aft, four side-to-side, and one torsional) and seven blade eigenmodes (four flapwise and three edgewise) with frequencies up to around 6 Hz are accounted for in the analysis.

The total simulation time for each LC is set to 700 s. The first 100 s are cut out from the results to remove initial simulation transients. The time step for data output is 0.01 s. The explicit ODEs are solved in MoLWiT by the 4th order Runge-Kutta method with both relative and absolute tolerances of 1.0×10^{-5}.

For each LC, the outputs are recorded at a number of nodal points, which are placed at the critical locations for capturing the global dynamics of the OWT. Figure 5.1 shows a schematic drawing of the analyzed OWT model and its main outputs. The simulation results are analyzed in terms of time series, short-term DELs, and PSDs. For turbulent LCs, short-term DELs and PSDs are computed from six aggregated time series, each simulated with an individual wind seed. Furthermore, short-term DELs are calculated for each wind speed and ice velocity with the same probability — not weighted with the wind speed distribution — for easier quantification of the ice load impact.

5.3 Quantification of ice impact on OWT dynamics

This section presents selected results of the ice-OWT interaction. The impact of ice loads on the global dynamics of the OWT is quantified in terms of short-term DELs and PSDs of the fore-aft bending moment at MSL.

5.3.1 Classification of ice-OWT interaction regions

Figures 5.2 and 5.3 present short-term DELs of the fore-aft bending moment at MSL for LCs with constant and turbulent wind fields, and at different design situations of OWT, respectively. In both figures, four distinct ice-structure interaction regions can be distinguished:

- The first region, where ice load is not applied to the support structure of the OWT.
- The second region (grey shaded plot background), for ice velocities from $0.001\,\mathrm{m\,s^{-1}}$ to $0.010\,\mathrm{m\,s^{-1}}$, where intermittent ice crushing occurs and short-term DELs are the largest.
- The third region, for ice velocities from $0.020\,\mathrm{m\,s^{-1}}$ to $0.100\,\mathrm{m\,s^{-1}}$, where frequency lock-in is present. Herein, short-term DELs are lower than in the intermittent crushing region but larger than those in the brittle crushing region.
- The fourth region (green shaded plot background), for ice velocities from $0.200\,\mathrm{m\,s^{-1}}$, where continuous brittle crushing of ice occurs and short-term DELs are smaller than those in the frequency lock-in region.

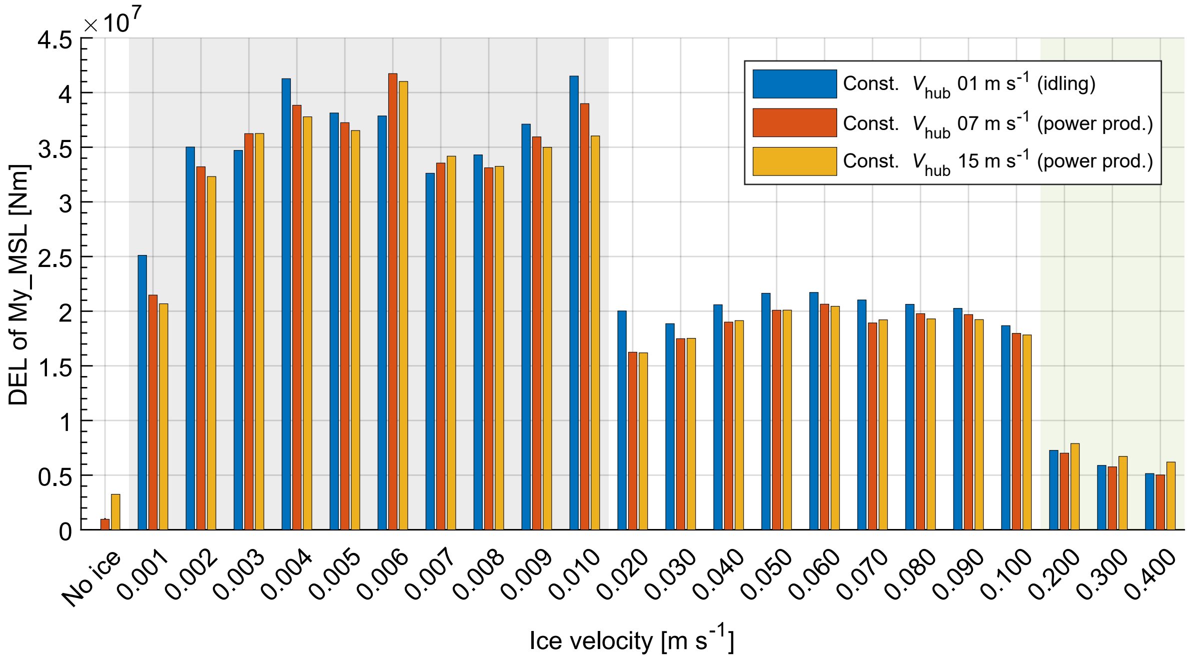

Figure 5.2: Short-term DELs of fore-aft bending moment at MSL. LCs are simulated with constant wind speed.

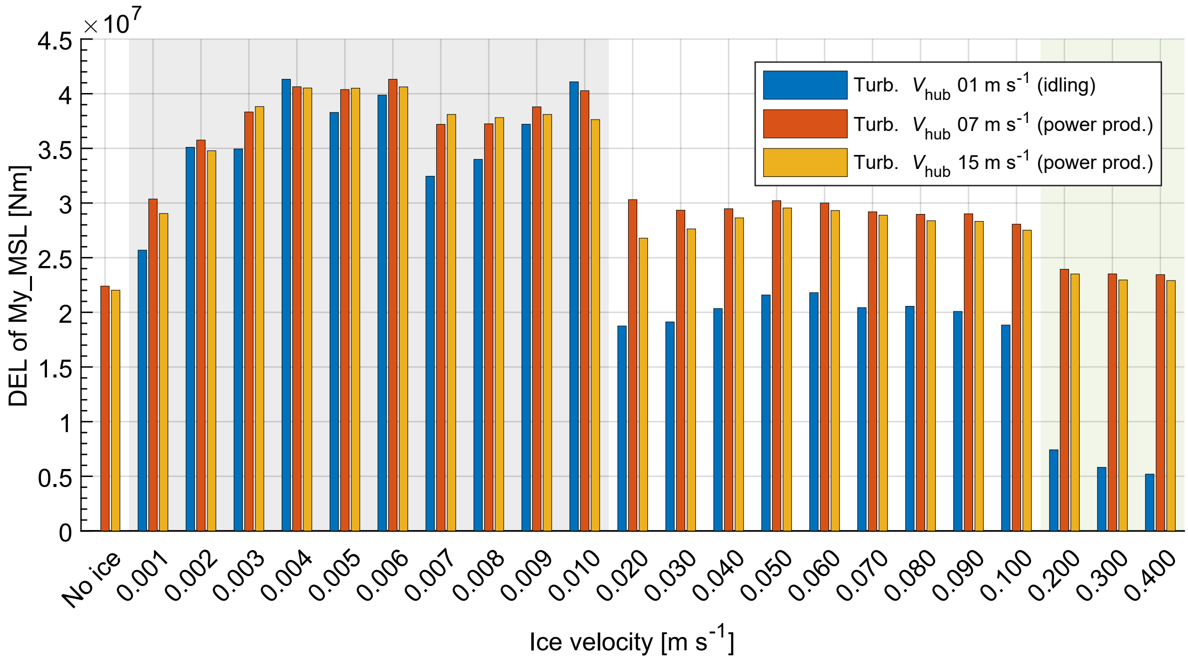

Figure 5.3: Short-term DELs of fore-aft bending moment at MSL. LCs are simulated with turbulent wind, where six independent seeds are used for each wind speed bin.

The classification of these regions is supported by the PSD analysis of both the fore-aft bending moment at MSL and the ice load for the turbulent LCs, as shown in Figures 5.4–5.9. The global eigenmodes of the OWT are indicated with vertical dashed lines. A name of the dominant mode shape[94] is displayed atop of each vertical line. It should be emphasized that frequencies of specific global mode shapes — especially those dominated by vibration of the blade — can slightly vary depending on the rotational speed of the rotor due to the effect of centrifugal stiffening and aeroelastic interaction between the blade and wind[95] during the time domain simulation. The 3P frequency[96] at the rated rotor speed — associated with the tower passage of the blades — is indicated with a red vertical dashed line and red text atop.

Ice load is not present

Figure 5.4 shows PSD of the fore-aft bending moment at MSL. When ice load is not present, the OWT tends to respond in the 1st and 2nd global fore-aft modes at around 0.27 Hz and 1.5 Hz, respectively. The peak of the global mode dominated by the 3rd flapwise frequency of the blade is also visible at around 3.5 Hz. However, its energy content is much lower when compared to the first two global fore-aft modes. Other global eigenmodes — dominated by the 1st/2nd flapwise and the 2nd edgewise vibrations of the blade — are less pronounced during the operation of the OWT when compared to the idling case. This can be explained by increased aerodynamic damping[97] during the power production. In the case of the IWT-7.5-164 wind turbine model that is used in this work, the aerodynamic damping can vary[98] from around 3.5% at the cut-in wind speed to around 7.2% above the rated wind speed. The aerodynamic damping is several times larger than the structural damping — the structural damping of the blade of a modern MW-class wind turbine

[94] A mode shape of the component, which contributes the highest energy to the global coupled mode of OWT. In MoLWiT, the eigenmodes are calculated separately for the support structure and blades during the modal analysis. Afterwards, they are linked in the time domain simulation through equations of motion resulting in coupled modes of the entire system (OWT). Note that the frequencies of the coupled modes can differ compared to the frequencies of uncoupled modes.

[95] Flapwise and edgewise bending moments of the rotating blade are counteracted by centrifugal and aerodynamic forces. The effect of centrifugal stiffening has less impact on the torsional mode than on both bending modes.

[96] The 1P rotor frequency is not depicted as the imbalance of blades is not accounted for in this analysis. 1P can also be induced by turbulent eddies passing through the rotor.

[97] It is difficult to directly quantify “pure” aerodynamic damping within time domain simulations as the aerodynamic damping is a feature of the modeling that arises from the coupled aeroelastic nature of the simulations; therefore, it contains contributions from the wind turbine dynamics and its non-linear control system. The most reliable way to estimate “pure” aerodynamic damping is to linearize the wind turbine model. It has to be emphasized that control dynamics is not used in linearized calculations. More information about various methods for estimation of the aerodynamic damping can be found in Cerda Salzmann and van der Tempel (2005); Passon (2015).

[98] The estimation based on a steady-state simulation and a linearized turbine model with a steady controller. Note that the BEM theory relies on lookup tables for steady-state lift, drag, and moment coefficients as a function of the angle of attack. However, these steady curves are generally not sufficient to model the dynamic response of a flexible rotor to variable inflow conditions. Therefore, a dynamic stall model should be used in the model linearization. Also, a dynamic wake model should be included in the model linearization, as it introduces a lagged response in induction to changes in operating conditions.

is usually in the range from around 0.25% to 0.8%, the structural damping of a monopile support structure is usually from around 0.4% to around 1%.

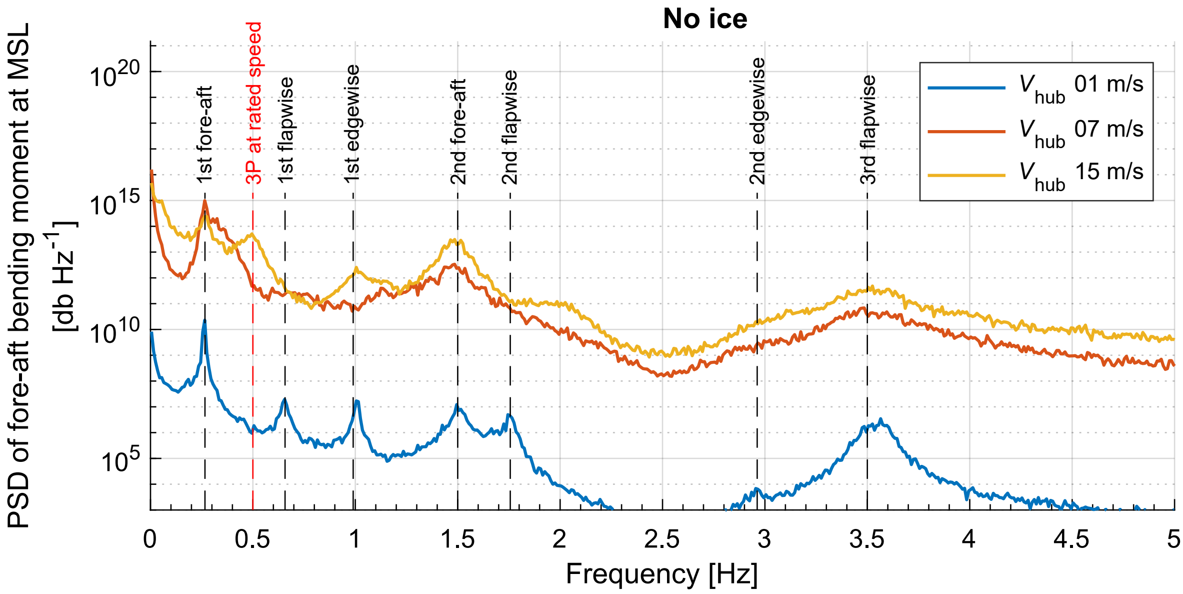

Figure 5.4: PSDs of fore-aft bending moment at MSL. Global coupled eigenmodes are indicated with vertical dashed lines and named according to the dominant mode shape. Rotor 3P frequency at rated rotational speed is indicated with red vertical dashed line.

Furthermore, the spectrum of the idling OWT carries much lower energy — around five orders of magnitude less — when compared to the operating wind turbine. The 3P frequency is pronounced at around 0.5 Hz when the OWT operates above the rated wind speed with the constant rotational speed[99]. The 3P frequency peak is not clearly pronounced when the wind turbine operates in the partial-load region, where the rotor speed varies with the turbulent wind speed to maintain the constant tip-speed ratio. The fluctuating rotor speed results in smeared and less intense 3P excitation.

Intermittent ice crushing region

In the intermittent ice crushing region, global eigenmodes of the OWT can be excited by higher harmonics of the global ice failure[100] when frequencies of these structural eigenmodes are in the vicinity of ice load harmonics.

[99] The rated rotational speed of the IWT-7.5-164 rotor is 10 rpm.

[100] Once the critical ductile load is reached by the vast majority of ice stripes, they all fail almost at the same time (time scale of milliseconds) and the structure springs back vigorously. A pattern of this rapid motion resembles a saw-tooth shape and is only observed when the first frequency of the structure is higher than the frequency of global failure of multiple ice stripes, as shown for example in Figures 2.4 and 4.14.

The energy content in the ice load spectrum at the intermittent ice crushing (Figure 5.5) is dominated by a distinct peak at 0.09 Hz, which corresponds to the frequency of the global ice failure when a saw-tooth like shape of the structural response is observed (cf. Figures 2.4 or 4.14). The subsequent distinct peaks are the higher harmonics of the global ice failure (related to the sawtooth shape of the ice load time history, which is not sinusoidal but contains harmonics). They are especially pronounced when the OWT is idling. When the OWT is operating, these higher harmonics are still visible, though their amplitudes are much smaller when compared to the idling case. This can be explained by increased aerodynamic damping from the spinning rotor. This observation indicates the importance of the coupled load analysis and shows the complexity of the entire system consisting of the OWT interacting with ice and wind loads.

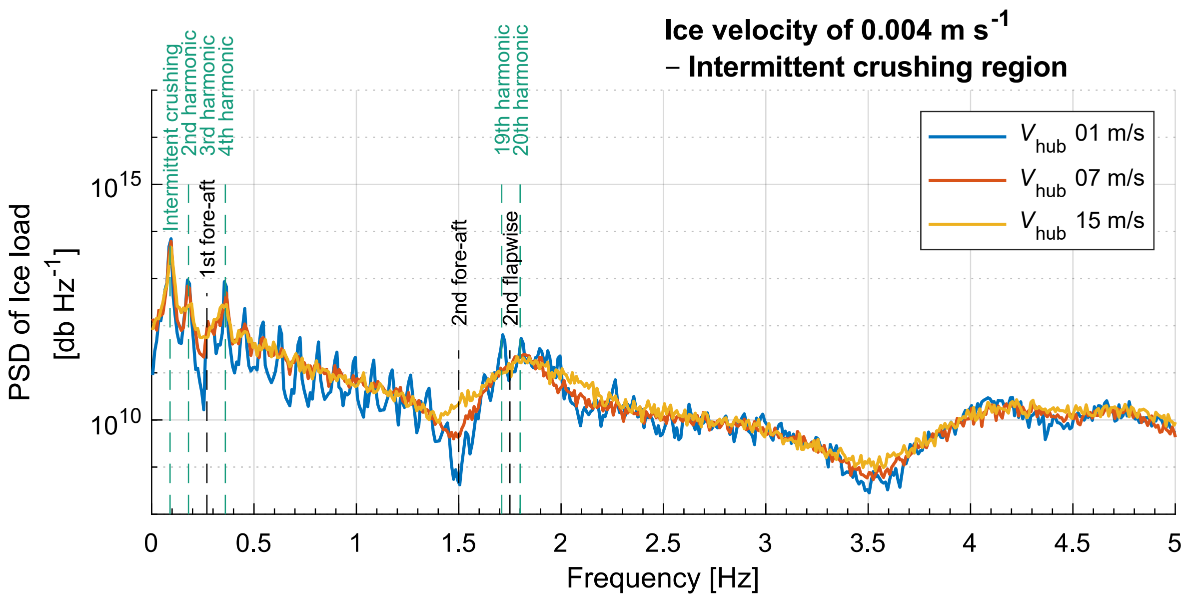

Figure 5.5: PSDs of ice load at MSL. Global coupled eigenmodes are indicated with vertical dashed lines and named according to the dominant mode shape. The fundamental frequency of intermittent ice crushing and some of its higher harmonics are indicated with green text and green dashed lines.

Figure 5.6 shows spectrum of the bending fore-aft moment at MSL. The OWT response is governed by the 1st fore-aft global mode at around 0.27 Hz, which frequency overlaps with the 3rd harmonic of the global ice failure. A global mode dominated by the 2nd flapwise vibration of the blade at 1.75 Hz lies in the close vicinity of the 19th and 20th harmonics of the global ice load.

There are no apparent peaks associated with higher structural modes at frequencies above 2.0 Hz. Above that frequency, higher harmonics of the ice load also diminish; and therefore do not carry enough energy to excite higher OWT modes. The harmonics of the global ice load are especially pronounced in the bending moment spectrum when ice acts on the idling OWT (blue curve in Figure 5.6).

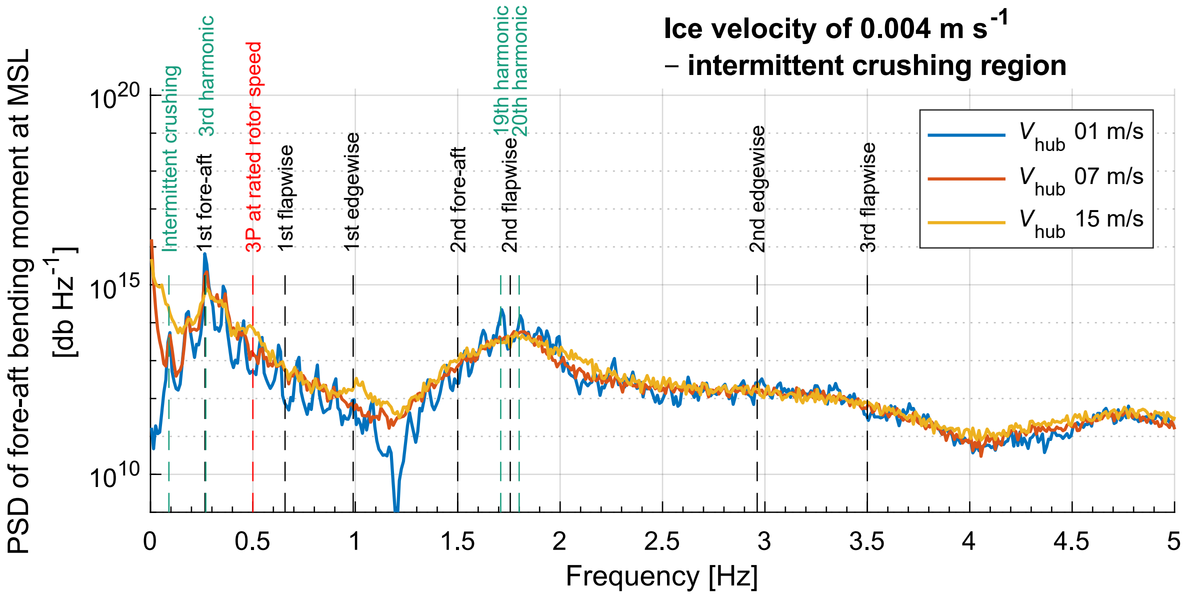

Figure 5.6: PSDs of fore-aft bending moment at MSL. Global coupled eigenmodes are indicated with vertical dashed lines and named according to the dominant mode shape. The fundamental frequency of intermittent ice crushing and some of its higher harmonics are indicated with green text and green vertical dashed lines.

Frequency lock-in region

It is astonishing that the energy content in the ice load spectrum at the lock-in region is significantly lower[101] when compared to the intermittent ice crushing region (cf. Figure 5.5 vs. 5.7) but short-term DELs of the fore-aft bending moment are only around 20% lower (Figure 5.3).

Furthermore, in the ice load spectrum there are no frequency peaks, which could be attributed to the frequency of the breaking ice stripes distinct from the OWT frequencies. The energy peaks are only visible at the frequencies corresponding to the 2nd global fore-aft mode and the global mode dominated by the 3rd flapwise vibration of the blade — that is why this interaction region is defined as the frequency lock-in (see Section 2.3). The frequency of the later mode is slightly shifted.

It is interesting that the energy of ice spectrum is monotonically increasing until it reaches the first frequency peak at 1.5 Hz where it sharply drops. Then the monotonic increase starts again until the second peak at around 3.4 Hz is reached. This phenomenon is also observed in load spectra at other ice velocities in the frequency lock-in region.

In the frequency lock-in region (Figure 5.8), the OWT response is governed by the 1st and 2nd global fore-aft modes, and the global mode dominated by the 3rd flapwise vibration of the blade.

[101] Around three orders of magnitude lower in the frequency range up to 0.5 Hz.

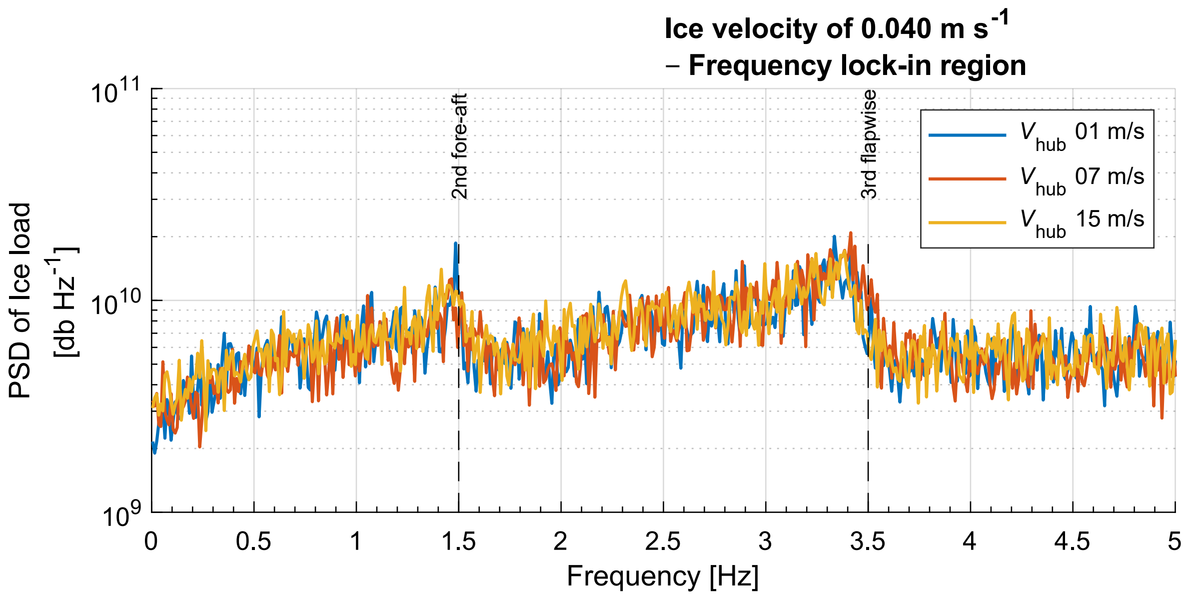

Figure 5.7: PSDs of ice load at MSL at three distinct design situations of the OWT. Global structural modes, which are visible in the ice load spectrum are indicated with black vertical dashed lines and named according to the dominant mode shape.

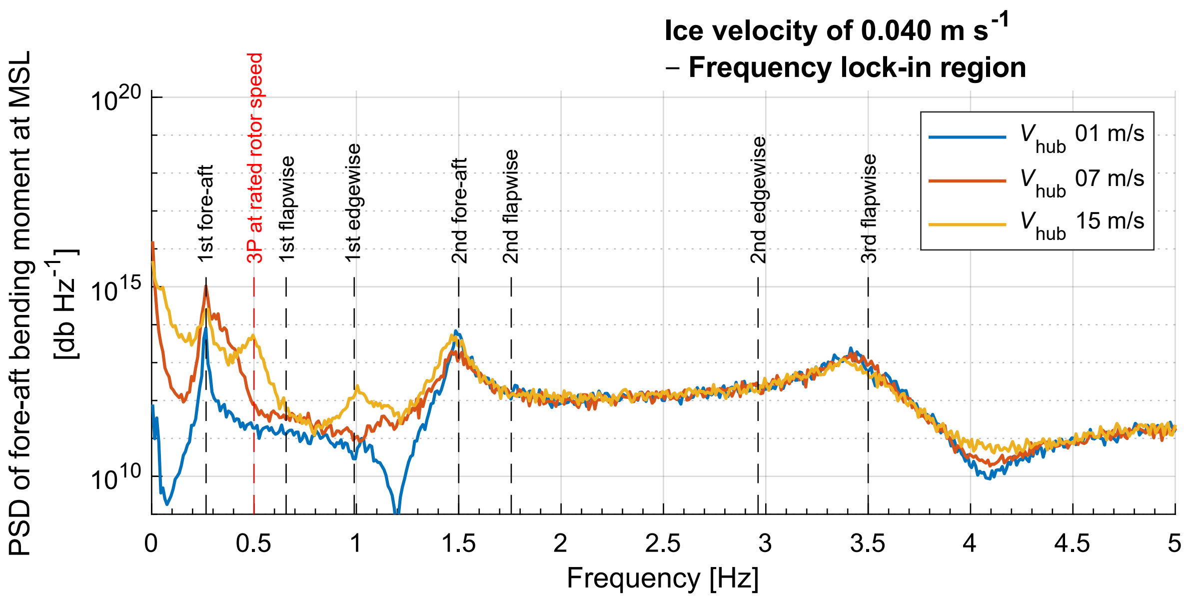

Figure 5.8: PSDs of fore-aft bending moment at MSL at three distinct design situations of the OWT. Global coupled eigenmodes are indicated with vertical dashed lines and named according to the dominant mode shape. Rotor 3P frequency at rated rotational speed is indicated with red vertical dashed line.

The sharp peaks of these three modes are pronounced at around 0.26 Hz, 1.5 Hz, and 3.4 Hz, respectively. The 1st, 2nd, and 3rd peaks have very similar energy content regardless of whether the OWT is idling or producing power.

Continuous brittle crushing region

The ice load spectrum at the continuous brittle crushing at high ice velocities is flat, as shown in Figure 5.9. The energy is equally redistributed through the entire frequency bandwidth regardless of whether the OWT is idling or producing power.

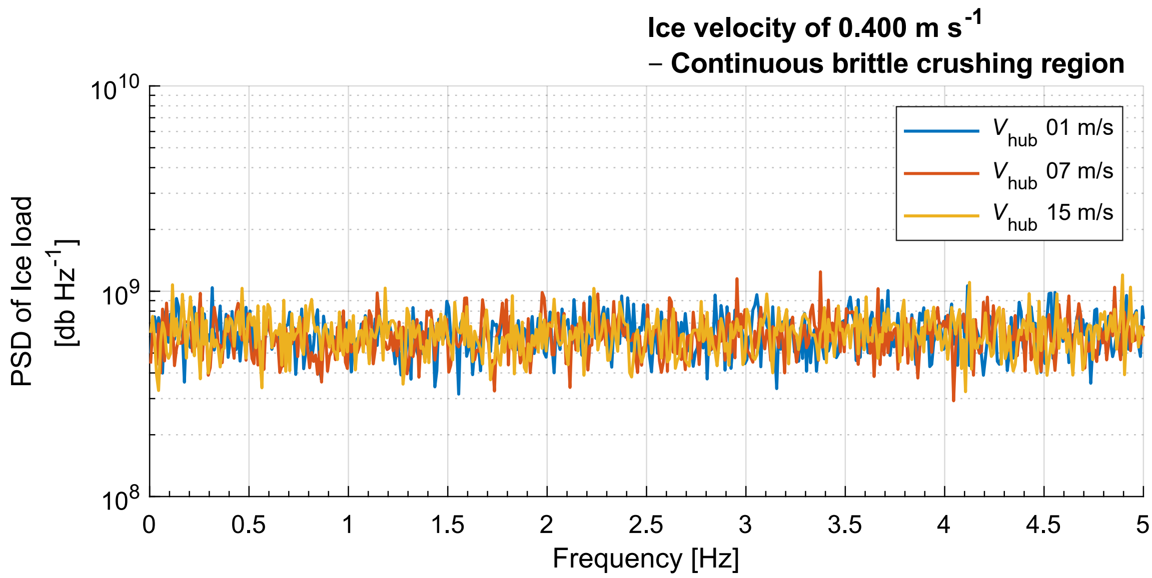

Figure 5.9: PSDs of ice load at MSL at three distinct design situations of the OWT.

In the continuous brittle crushing region, the energy spectrum of the fore-aft bending moment (Figure 5.10) of the operating OWT is very similar to the spectrum of the operating OWT without ice loads (Figure 5.4). The difference is visible for the idling OWT, where the energy content in the spectrum is increased when compared to the idling OWT without ice loads.

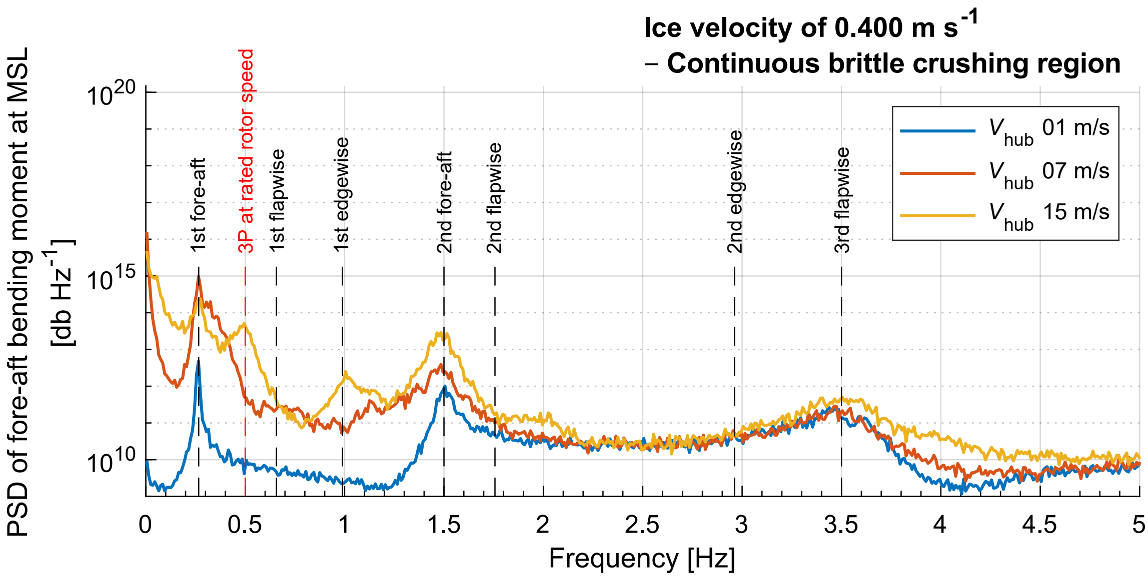

Figure 5.10: PSDs of fore-aft bending moment at MSL at three distinct design situations of the OWT. Global coupled eigenmodes are indicated with vertical dashed lines and named according to the dominant mode shape. Rotor 3P frequency at rated rotational speed is indicated with red vertical dashed line.

5.3.2 Ice loads combined with constant and turbulent wind — impact on DELs at different design situations of OWT

Short-term DELs, which are calculated for the idling OWT at constant and turbulent wind LCs, have comparable magnitudes — the mean difference of around 0.2% at all corresponding ice velocities (cf. Figures 5.2 and 5.3).

On the other hand, in the power production cases, short-term DELs calculated for LCs with the turbulent wind are much larger than those at the corresponding LCs with the constant wind. When there is no ice, DELs in the turbulent LCs are around 2000% larger at wind of 7 $m\,s^{-1}$ and around 500% larger at wind of 15 $m\,s^{-1}$.

In the intermittent crushing region, short-term DELs from the turbulent, power production LCs are around 10% larger than DELs obtained from the corresponding constant wind LCs for the same ice velocities.

In the lock-in region, short-term DELs from the turbulent, power production LCs are around 52% larger than DELs obtained from the corresponding constant wind LCs for the same ice velocities.

In the continuous brittle crushing region, short-term DELs from the turbulent, power production LCs are around 295% and 233% larger than DELs obtained from the corresponding constant wind LCs of 7 $m\,s^{-1}$ and 15 $m\,s^{-1}$, respectively.

Now let us compare the percentage increase of short-term DELs at different ice-structure interaction regions with respect to the reference turbulent case, where there is no ice load applied to the OWT. The percentage increase is calculated as:

$$\frac{value_{\text{new}} - value_{\text{ref}}}{value_{\text{ref}}} 100\% \tag{5.1}$$

where $value_{\text{ref}}$ is the reference DEL value at the given wind speed when there is no ice load and $value_{\text{new}}$ is the DEL value calculated for the OWT with ice load and the same wind speed.

For the power production cases, the increase of around 74% is observed at the intermittent ice crushing, for frequency lock-in around 30% increase, and only around 5% increase at the continuous brittle crushing. A dramatic increase in short-term DELs occurs when the idling OWT is subjected to ice action on its support structure when compared to the idling OWT without ice loads (8200% increase at intermittent ice crushing, 4650% increase at frequency lock-in, and 1400% increase at continuous brittle crushing).

Very similar trends are also observed at multiple other outputs along the OWT.[102] For example, at short-term DELs of the blade root bending moment in the out-of-rotor-plane direction as shown in Figure 5.11. At the blade root, the largest DELs are always observed during the power production above the rated wind speed, where the pitch control is used.

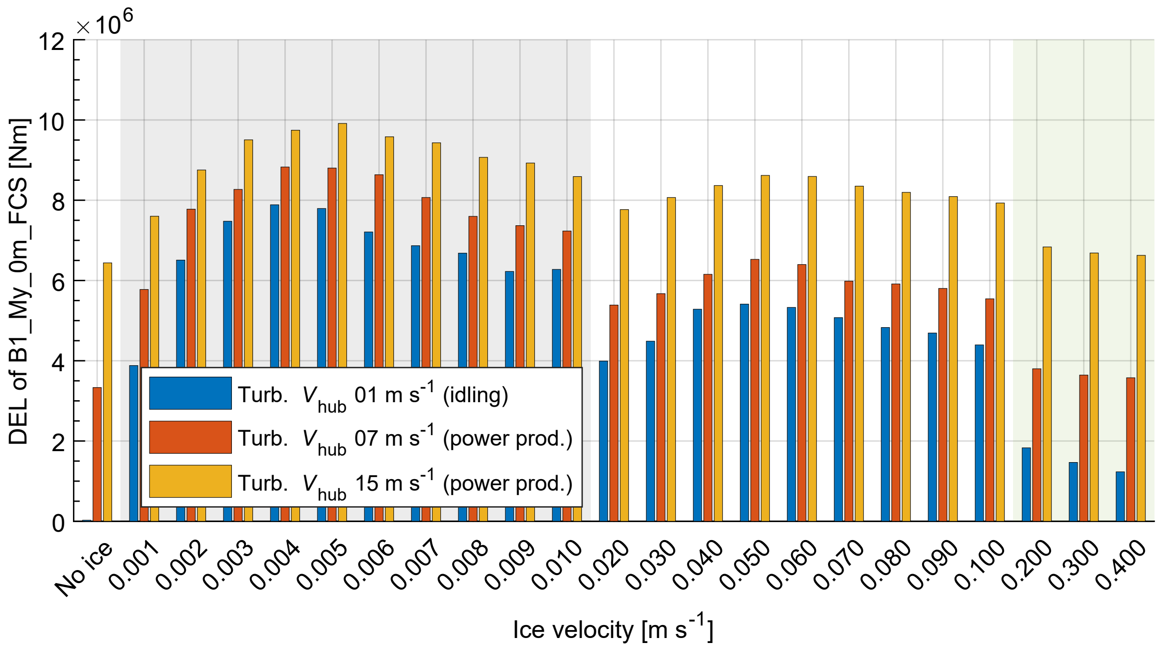

Figure 5.11: Short-term DELs of the blade root bending moment in the out-of-rotor-plane direction. LCs are simulated with turbulent wind.

[102] See Appendix B for plots of short-term DELs at other heights of the support structure.

5.3.3 Conclusions

The quantification of ice impact on the OWT dynamics can be summarized as follows:

- The most severe fatigue load effects are always caused by intermittent ice crushing, regardless of whether the OWT is idling or operating.
- The highest increase of fatigue load effects occurs when the OWT is idling and there is an ice action on its support structure, regardless of the ice velocity. During the OWT operation, the increased aerodynamic damping can effectively mitigate load effects resulting from the ice load action at MSL.
- Fatigue load effects calculated for the operating OWT during continuous brittle crushing are only around 5% larger than those obtained for the reference case with the operating OWT with no ice loads. Therefore, the continuous brittle crushing region is not a design driver in terms of fatigue load effects.
- During intermittent ice crushing, ice fails with the frequency lower than the frequency of the 1st global mode of the OWT. Furthermore, structural frequencies are not pronounced in the spectrum of ice load in the intermittent ice crushing region. The load spectrum rather contains frequency peaks corresponding to the higher harmonics of the global ice failure. This is in contrast to the frequency lock-in region, where energy peaks — corresponding to the OWT frequencies — are visible in the spectrum of ice load.
- The energy content in the ice load spectrum at frequency lock-in is relatively low compared to the energy content during intermittent crushing.

5.4 Work-energy flow between ice and OWT

In this section, the energy flow during ice-OWT interaction is analyzed at three distinct design situations at the turbulent wind (idling, power production below the rated wind speed, and power production above the rated wind speed) and at multiple ice velocities where different ice-structure interaction modes occur — intermittent crushing, frequency lock-in, and continuous brittle crushing.

Mean values of work done by ice on the first four fore-aft eigenmodes of the support structure and at different ice velocities are shown in Figure 5.12.

The external work done by ice on the OWT support structure can either be positive or negative. If both the ice force and the structural displacement at MSL are in the same direction, the positive work is done on the OWT (it gains mechanical energy). On the other hand, if the structural displacement is in the opposite direction to the ice force, the negative work is done and as a consequence the OWT loses mechanical energy.

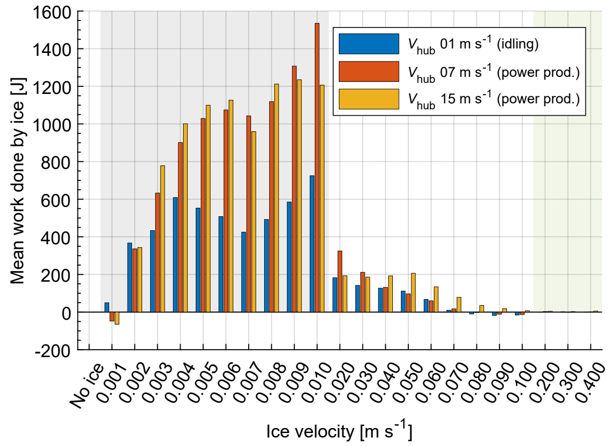

(a) Work done by ice on the 1st fore-aft eigenmode

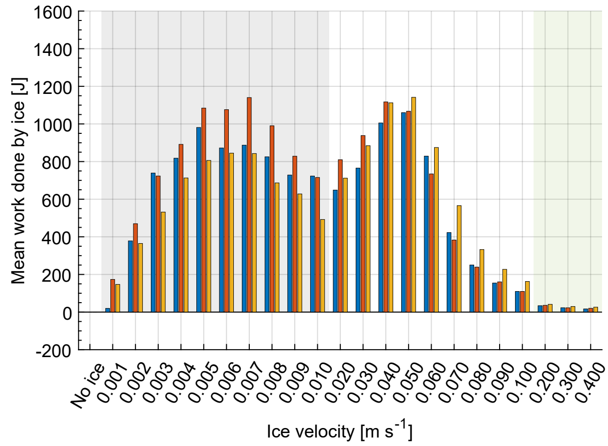

(b) Work done by ice on the 2nd fore-aft eigenmode

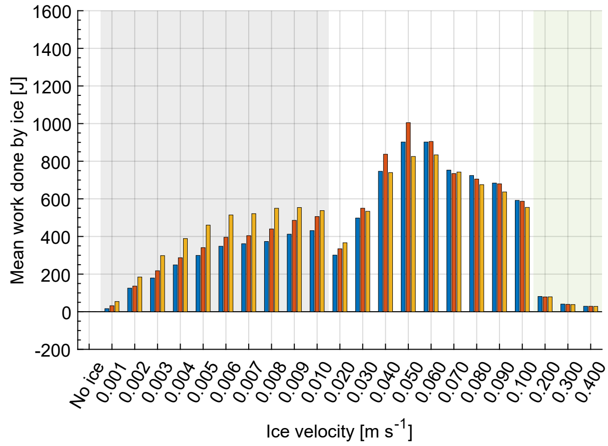

(c) Work done by ice on the 3rd fore-aft eigenmode

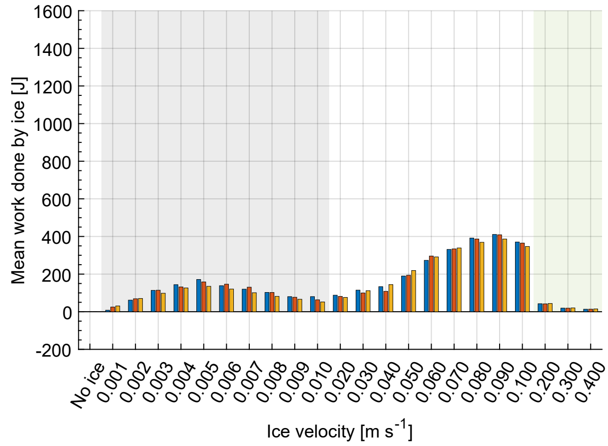

(d) Work done by ice on the 4th fore-aft eigenmode

Figure 5.12: Mean work done by ice on the first four fore-aft eigenmodes of OWT support structure at different ice velocities. The grey shaded plot background corresponds to the intermittent crushing mode, the green shaded background to continuous brittle crushing mode, and the white area in-between is the frequency lock-in mode.

Mean values of energy dissipated in the first four fore-aft eigenmodes through viscous damping are presented in Figure 5.13. The energy dissipation in individual eigenmodes is computed according to Eq. 4.23.

And finally, the ratio of the mean work done by ice to the mean energy dissipated in individual eigenmodes is shown in Figure 5.14. When work is done by external[103] ice forces on the support

[103] The external forces can also be called nonconservative as they alter the total mechanical energy of a structure.

structure, the total mechanical energy of the OWT is changed. When the ratio is greater than 1, more energy is transferred into the given eigenmode (Eq. 4.22) than it is dissipated through viscous damping (Eq. 4.23)[104]. On the other hand, when the ratio is lower than 1, more energy is dissipated in the eigenmode. When the ratio equals 1, the mean energy is conserved.

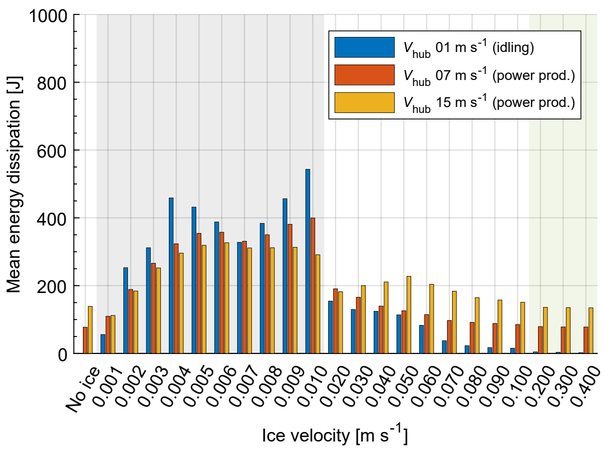

(a) Energy dissipated in the 1st fore-aft eigenmode

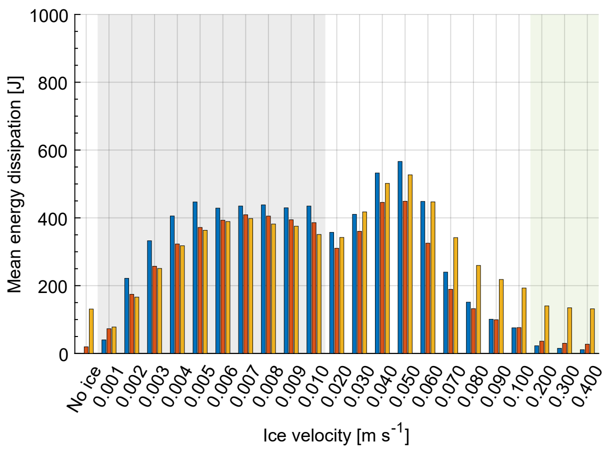

(b) Energy dissipated in the 2nd fore-aft eigenmode

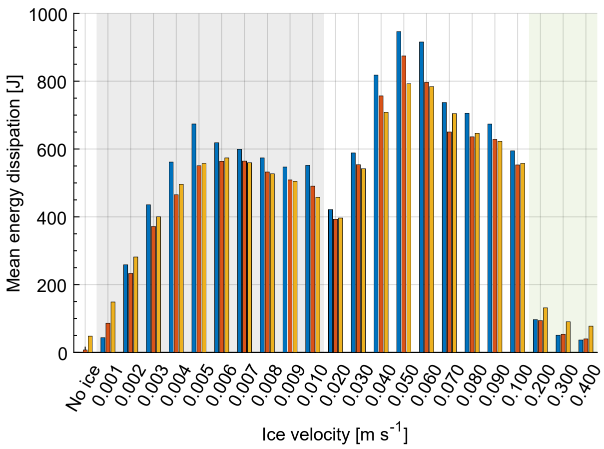

(c) Energy dissipated in the 3rd fore-aft eigenmode

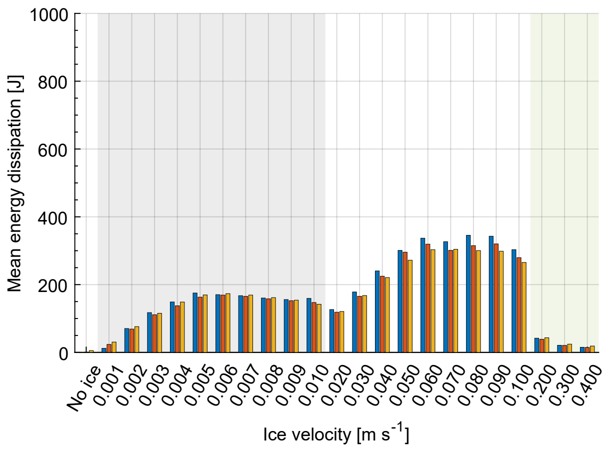

(d) Energy dissipated in the 4th fore-aft eigenmode

Figure 5.13: Mean energy dissipated in the first four fore-aft eigenmodes of OWT support structure at different ice velocities. The grey shaded plot background corresponds to the intermittent crushing mode, the green shaded background to continuous brittle crushing mode, and the white area in-between is the frequency lock-in mode.

All subfigures within individual figures are plotted with the same scale for the sake of clarity and the ease of results interpretation. Each mean value (individual vertical bar in the plot) is calculated

[104]Note that energy dissipation through the aerodynamic damping is not accounted for in Eq. 4.23.

from the aggregated statistics of six time series (each of 600 s length) simulated with individual turbulent seeds, as presented in Table 5.1. This results in a one-hour stochastic realization for each analyzed case, as recommended by IEC (2019a, p. 50). The grey shaded plot background corresponds to the intermittent crushing mode, the green shaded background to the continuous brittle crushing mode, and the white area in-between is the frequency lock-in mode.

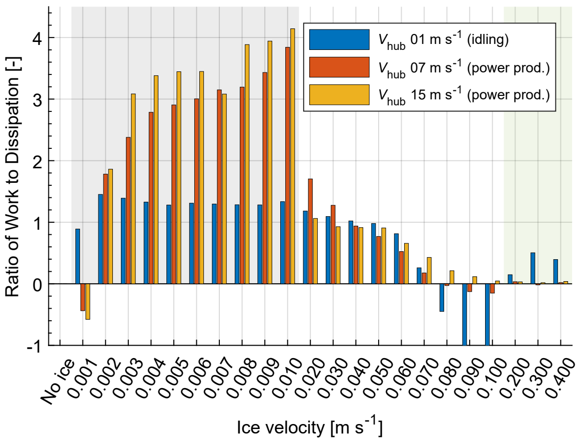

(a) Ratio of external work done by ice to energy dissipated in the 1st fore-aft eigenmode

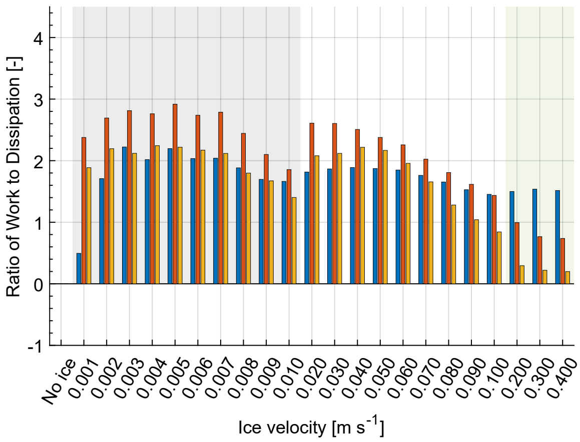

(b) Ratio of external work done by ice to energy dissipated in the 2nd fore-aft eigenmode

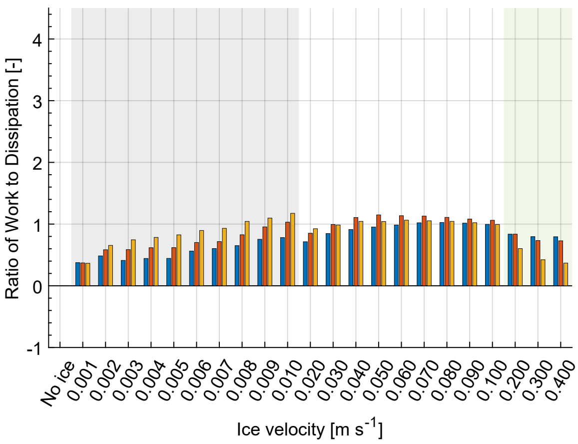

(c) Ratio of external work done by ice to energy dissipated in the 3rd fore-aft eigenmode

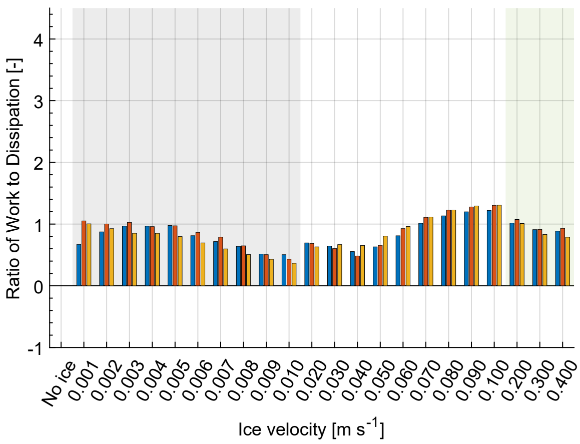

(d) Ratio of external work done by ice to energy dissipated in the 4th fore-aft eigenmode

Figure 5.14: Ratio of mean external work done by ice to mean energy dissipated in fore-aft eigenmodes of OWT support structure at different ice velocities. The grey shaded plot background corresponds to the intermittent crushing mode, the green shaded background to continuous brittle crushing mode, and the white area in-between is the frequency lock-in mode.

5.4.1 Intermittent crushing region

Mean work done by ice on eigenmodes

In the intermittent crushing region (grey shaded plot background), most of the work is done on the 1st and the 2nd fore-aft eigenmodes, as shown in Figures 5.12a and 5.12b, respectively. The work done on the 3rd and the 4th eigenmodes is around two and three times smaller, as presented in Figures 5.12c and 5.12d.

At the very low ice velocity of $0.001\,\mathrm{m\,s^{-1}}$, work done by ice on the 1st eigenmode becomes negative in the case of power production (Figure 5.12a). This basically means that ice can also have a certain damping effect on this eigenmode.

It is striking that work done by ice on the 1st eigenmode of the operating OWT is much larger than on the idling OWT for the ice velocities between $0.002\,\mathrm{m\,s^{-1}}$ and $0.010\,\mathrm{m\,s^{-1}}$. This is related to the definition of work, which is a product of force and displacement (see Eq. 4.22). During the power production, the wind turbine experiences larger displacements — mainly governed by its 1st eigenmode — due to the contribution of high aerodynamic forces acting on the spinning rotor. A similar pattern is observed in the 3rd eigenmode (Figure 5.12c), where more energy is transferred during the power production than at idling.

Note that in the middle of the intermittent crushing region — at the ice velocity of around $0.007\,\mathrm{m\,s^{-1}}$ — there is a decrease in work done on the 1st eigenmode and an increase of work done on the 2nd eigenmode (cf. Figures 5.12a vs. 5.12b).

Mean energy dissipated in eigenmodes

Most of the energy is dissipated in the 3rd eigenmode, as shown in Figure 5.13c. However, this mode is not governing the structural response at the intermittent crushing region. The 1st and the 2nd eigenmodes (Figures 5.13a and 5.13b) dissipate on average around 30% less energy — at the ice velocities between $0.002\,\mathrm{m\,s^{-1}}$ and $0.010\,\mathrm{m\,s^{-1}}$ — than the 3rd eigenmode. The 4th eigenmode (Figure 5.13d) dissipates on average around three times less energy when compared to the 3rd one. Note that most of the energy is dissipated in the intermittent crushing region when the OWT is idling.

Ratio of work done by ice to energy dissipated in eigenmodes

In the intermittent crushing region, the 1st and the 2nd eigenmodes receive more energy than they can dissipate through viscous damping (positive energy balance), as shown in Figures 5.14a and 5.14b, respectively. This means that the first two eigenmodes govern the structural response in the intermittent crushing region. The 3rd and the 4th eigenmodes dissipate more energy than they receive from ice in the majority of analyzed ice velocities between $0.001\,\mathrm{m\,s^{-1}}$ and $0.010\,\mathrm{m\,s^{-1}}$, as presented in Figures 5.14c and 5.14d.

5.4.2 Frequency lock-in region

Mean work done by ice on eigenmodes

In the frequency lock-in region — at the ice velocities between $0.020\,\mathrm{m\,s^{-1}}$ and $0.100\,\mathrm{m\,s^{-1}}$ — the mean work done by ice on the 1st eigenmode drops dramatically (around five times) when compared to the intermittent crushing region. This transition is visible in Figure 5.12a at the ice velocities of $0.010\,\mathrm{m\,s^{-1}}$ and $0.020\,\mathrm{m\,s^{-1}}$. Furthermore, work done by ice on the 1st eigenmode becomes negative in the upper bound of the frequency lock-in region, at the ice velocities from around $0.080\,\mathrm{m\,s^{-1}}$ to $0.100\,\mathrm{m\,s^{-1}}$. This happens when the OWT is idling and operating in the partial-load region. This means that ice can also have some damping effect on this eigenmode.

In the case of the 2nd, the 3rd and the 4th eigenmodes the transition from the intermittent crushing to the frequency lock-in region is also pronounced at the ice velocities between $0.020\,\mathrm{m\,s^{-1}}$ and $0.100\,\mathrm{m\,s^{-1}}$ (Figures 5.12b, 5.12c, and 5.12d). For these eigenmodes, the work done by ice increases significantly. As a result, the 2nd and the 3rd eigenmodes start to dominate in the frequency lock-in region.

At the upper bound of the frequency lock-in region — at the ice velocities from around $0.080\,\mathrm{m\,s^{-1}}$ to $0.100\,\mathrm{m\,s^{-1}}$ — the mean work done on the 2nd eigenmode is diminishing (Figure 5.12b). At the same time, a considerable amount of work is transferred from ice to the 4th eigenmode (Figure 5.12d). According to author's knowledge, this phenomenon has not been observed before.

Mean energy dissipated in eigenmodes

In the frequency lock-in region — at the ice velocities between $0.020\,\mathrm{m\,s^{-1}}$ and $0.100\,\mathrm{m\,s^{-1}}$ — most of the energy is dissipated in the 3rd eigenmode (Figure 5.13c), followed by the 2nd and 4th eigenmodes (Figures 5.13b and 5.13d). In the case of the 1st and the 2nd eigenmodes, energy dissipation is significant when the OWT is operating in the full-load region above the rated wind speed. During idling and in the partial-load region, energy dissipation is considerably smaller.

Ratio of work done by ice to energy dissipated in eigenmodes

The ratio of the mean work done by ice to the mean energy dissipated drops significantly in the frequency lock-in region in the case of the 1st fore-aft eigenmode (Figure 5.14a).

In the case of the 2nd eigenmode (Figure 5.14b), the ratio in the entire frequency lock-in region is around 2, which means that on average twice as much energy is transferred to this eigenmode than dissipated (positive energy balance).

In the 3rd and the 4th eigenmodes (Figures 5.14c and 5.14d) the ratio is around 1. There is an increasing trend for the 4th eigenmode in the upper bound of the frequency lock-in region at the ice velocities between $0.070\,\mathrm{m\,s^{-1}}$ and $0.100\,\mathrm{m\,s^{-1}}$.

5.4.3 Continuous brittle crushing region

Mean work done by ice on eigenmodes

In the continuous brittle crushing region at high ice velocities above $0.100\,\mathrm{m\,s^{-1}}$, the mean value of work done by ice on all individual eigenmodes is around one order of magnitude lower than at the intermittent crushing and lock-in regions, as shown in Figure 5.12 (green shaded plot background). The 1st eigenmode receives the least amount of energy from ice — the bar plots are almost invisible. Some small amount of energy is transferred to the 2nd, the 3rd, and the 4th eigenmodes.

Mean energy dissipated in eigenmodes

In the continuous brittle crushing region, the energy dissipated in the 1st and the 2nd eigenmode during the power production is very comparable to the reference case where there is no ice load applied to the OWT (Figures 5.13a and 5.13b).

Ratio of work done by ice to energy dissipated in eigenmodes

In the continuous brittle crushing region — at the ice velocities above $0.100\,\mathrm{m\,s^{-1}}$ — more energy is dissipated than transferred to the structure from the ice cover. The only exception is observed at the 2nd eigenmode when the OWT is idling (Figures 5.14b).

5.4.4 Conclusions

Mean work done by ice on individual eigenmodes:

- Mean work done by ice on the fore-aft eigenmodes of the support structure varies significantly depending on the interaction region. Even within a specific interaction region, the amount of work done on the subsequent eigenmodes can drift alternating the dominant eigenmode if the ice velocity is slightly altered.
- In the intermittent crushing region, most of work is done by ice on the 1st fore-aft eigenmode.
- In the lock-in region, most of work is done by ice on the 3rd and the 2nd fore-aft eigenmodes of the support structure. The 1st and the 4th fore-aft eigenmodes receive around one order of magnitude energy less.

- In the continuous brittle crushing region at high ice velocities, the mean value of work done by ice on individual eigenmodes is one order of magnitude lower than at intermittent crushing and lock-in regions.

Mean energy dissipated through viscous damping in individual eigenmodes:

- In the intermittent crushing region, most of the energy is dissipated in the 3rd eigenmode. However, this eigenmode is not governing the structural response at low ice velocities. The 1st and the 2nd eigenmodes dissipate around 30% less energy than the 3rd eigenmode. The 4th eigenmode dissipates around three times less energy compared to the 3rd one. Most of energy is dissipated when the OWT is idling.
- In the frequency lock-in region, the most of the energy is dissipated in the 3rd eigenmode. In the case of the 1st and the 2nd eigenmodes, energy dissipation is more significant when the OWT is operating in the full-load region above the rated wind speed, than during idling or in the partial load region.
- In the continuous brittle crushing region, the energy dissipated in the 1st and the 2nd eigenmodes during the power production is very comparable to the reference case where there is no ice load applied to the OWT.

Ratio of work done by ice to energy dissipated in eigenmodes:

- In the intermittent crushing region, the 1st and the 2nd eigenmodes receive more energy than they can dissipate through viscous damping. This means that the first two eigenmodes govern the structural response in the intermittent crushing region. The 3rd and the 4th eigenmodes dissipate more energy than they receive from ice.
- In the frequency lock-in region, the ratio of the mean work done by ice to the mean energy dissipated is around 1 for the 1st, the 3rd, and the 4th fore-aft eigenmodes. In the case of the 2nd eigenmode, the ratio in the entire frequency lock-in region is around 2, which means that on average twice as much energy is transferred to this eigenmode than dissipated through viscous damping. This means that the 2nd eigenmode governs the structural response in the frequency lock-in region.
- In the continuous brittle crushing region, more energy is dissipated through viscous damping than transferred to the structure from ice. The only exception is observed at the 2nd eigenmode when the OWT is idling.

5.5 Sensitivity analysis of eigenmodes contribution to short-term DELs

In this section, a sensitivity analysis of eigenmodes contribution to short-term DELs is investigated at different ice-structure interaction regions by switching off the contribution of an individual eigenmode to the system displacement at MSL but still preserving its contribution to the system stiffness. This investigation is done at the postprocessing stage (once the simulations are accomplished) by superposition of different combinations of individual modal displacements.

Note that the displacement vector $\{\boldsymbol{x}\}$ from Eq. 4.13 can be represented in terms of the mode shape vectors $\{\boldsymbol{\phi}\}$, where the time variation is described by the modal coordinates $r_1(t), r_2(t), \ldots, r_{N_\mathrm{m}}(t)$, as it is shown in Eq. 4.15. Therefore, the horizontal displacement of the support structure DOF located at MSL is calculated from a superposition of displacement contributions from individual eigenmodes:

$$\{\boldsymbol{x}\} = \sum_{j=1}^{N_\mathrm{m}} \{\boldsymbol{\phi}\}_{\mathrm{dof},j}\, r_j \tag{5.2}$$

The time history of horizontal displacement at MSL from Eq. 5.2 — which is the result of superposition of individual modal displacements — would have a different pattern of peaks and troughs, depending on the number of eigenmodes that are superpositioned.

The rainflow-counting algorithm counts peaks and throughs. Once all the cycles are counted, DELs can be calculated using Miner's rule (Miner, 1945). The displacement is directly related to the shear force. Therefore, it is a reasonable assumption to examine the impact of different eigenmodes on DELs by calculating DELs of displacements.

Figure 5.15 shows short-term DELs, which are calculated for different combinations (superpositions) of displacements at MSL coming from the first four fore-aft eigenmodes of the support structure. Calculations are performed for four distinct interaction regions — no ice load, intermittent ice crushing, frequency lock-in, and continuous brittle crushing.

The first set of results (reference case) contains all four eigenmodes contributing to the horizontal displacement at MSL. In the second set, the first three eigenmodes are superpositioned, whereas the 4th eigenmode is switched off. In the third case, the 1st, the 2nd, and the 4th eigenmodes are accounted for, whereas the 3rd one is excluded. In the fourth case, the last three eigenmodes are included, whereas the 1st one is switched off.

The percentage change (Eq. 3.1) — calculated with respect to the corresponding design situation from the reference case, including all eigenmodes — is printed atop of each bar.

The 4th eigenmode is switched off

The contribution of displacement from the 4th eigenmode to DELs is relatively small at each interaction region and design situation, as visible in Figure 5.15. Once the 4th eigenmode is switched off, DEL values alter between −3.7% and 2.7% with respect to the reference case. This is expected as cycle amplitudes of the 4th eigenmode are the smallest when compared to the first three eigenmodes.

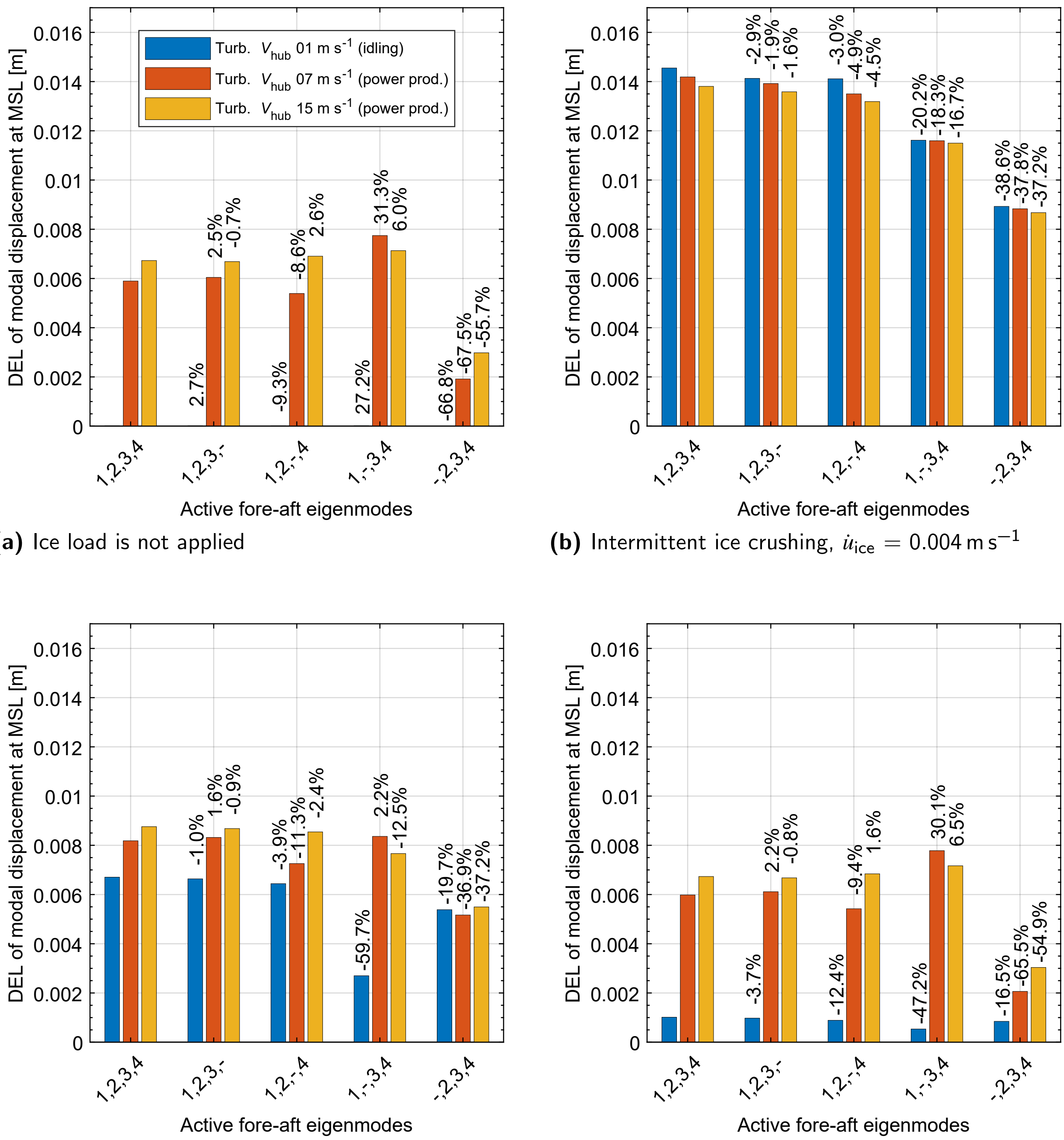

(a) Ice load is not applied

(b) Intermittent ice crushing, $\dot{u}_{ice} = 0.004\,\mathrm{m\,s^{-1}}$

(c) Frequency lock-in, $\dot{u}_{ice} = 0.040\,\mathrm{m\,s^{-1}}$

(d) Continuous brittle crushing, $\dot{u}_{ice} = 0.400\,\mathrm{m\,s^{-1}}$

Figure 5.15: Short-term DELs of modal displacements at MSL resulting from different combinations (superpositions) of eigenmodes.

The 3rd eigenmode is switched off

The contribution of displacement from the 3rd eigenmode to DELs is a bit more considerable than the 2nd mode. Once the 3rd eigenmode is switched off, the DELs are reduced up to around 12%.

Some small increase of DELs (up to around 2.5%) is visible when the OWT is producing power above the rated wind speed and there is no ice load (Figure 5.15a) or ice fails in the continuous brittle crushing mode (Figure 5.15d).

The 2nd eigenmode is switched off

When there is no ice load, a significant increase of DELs is visible (around 27% and 31%) for two design situations — idling and power production below the rated wind speed, respectively — when the 2nd eigenmode is switched off (Figure 5.15a). This means that the presence of the 2nd eigenmode has a mitigating effect on load effects at these two design situations. This mitigating effect is explained by the facts that the modal displacement of the 2nd eigenmode is in the opposite phase to the modal displacement of the 1st eigenmode at MSL, as shown in Figure 5.16a. Once both modal displacements are superpositioned, the resulting vibration amplitudes in the time series are lower, which has a direct impact on DELs.

During the intermittent ice crushing, a significant decrease of DELs is visible (ca. −20%, −18%, and −17%) at three design situations — idling, power production below and above the rated wind speed, respectively — as shown in Figure 5.15b. This means that a significant portion of DELs during the intermittent ice crushing is attributed to the 2nd eigenmode.

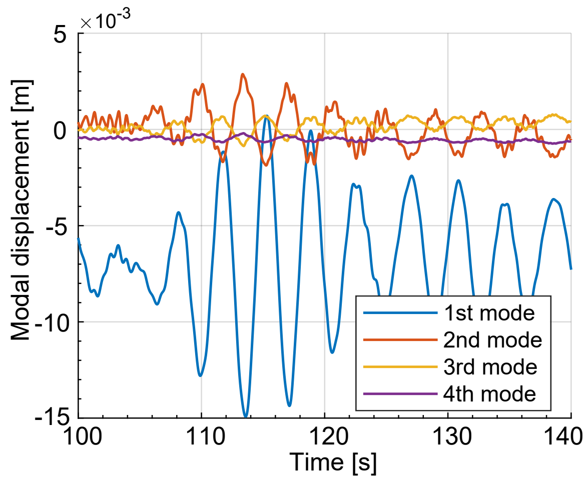

(a) No ice load and power production at turbulent wind with the mean wind speed of 7 m s^{-1} at hub height

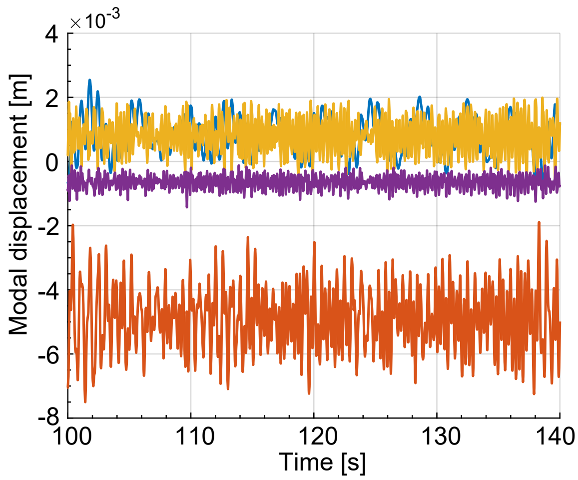

(b) Frequency lock-in and idling at turbulent wind with the mean wind speed of 1 m s^{-1} at hub height

Figure 5.16: Modal displacements at MSL for fore-aft eigenmodes. Selected time series for illustration of modal displacements at distinct design situations and ice-structure interaction regions.

In the frequency lock-in region, a dramatic decrease of DELs is visible (around −60%) at idling, as shown in Figure 5.15c, when the 2nd eigenmode has the largest contribution to the system displacement (see Figure 5.16b). This means that a substantial portion of DELs is attributed to the 2nd eigenmode when the turbine is idling and subjected to frequency lock-in. Much less impact is observed when OWT is producing power and significant aerodynamic damping is present.

During the continuous brittle crushing, on the one hand, a dramatic decrease of DELs is visible (around −47%) at idling, and on the other hand a very significant increase of DELs is visible (around 30%) at power production below the rated wind speed.

The 1st eigenmode is switched off

The contribution of the 1st eigenmode to DELs is always very significant, as visible in Figure 5.15. The most dramatic decrease of DELs is observed when there is no ice load applied to the structure and during the continuous brittle crushing.

5.5.1 Conclusions

The 1st eigenmode of the support structure has always a significant contribution to DELs. This is expected, as this eigenmode is the easiest to excite and has the highest vibration amplitudes. The impact of the 2nd eigenmode of the support structure on DELs is also very considerable, though it might have mitigating effect at certain design situations, as it vibrates with the opposite phase. The 3rd and the 4th eigenmodes have less impact than the first two eigenmodes. Nevertheless, their presence is important as they are often coupled with blade eigenmodes.

Chapter 6

Conclusions

Support structures for OWTs are designed and certified site-specific based on the calculated load effects. These load effects originate from static, cyclic, stochastic, and transient loads from the met-ocean environment and rotating components of the wind turbine. The met-ocean environment of the Baltic Sea accounts for variable wind and marine conditions. Sea ice is part of marine conditions — which among others — should be included in the design process of OWTs support structures.

The load analysis and design of OWTs, including its components, rely on the time-domain based, coupled aero-hydro-servo-elastic simulation tools. Only this approach can provide an accurate prediction of the OWT dynamic response, as discussed in Chapter 2. Dynamic interaction between an OWT and external loads — including ice loads — cannot be disregarded as it may result in considerable loss of accuracy.

A proper understanding of sea ice impact on the global dynamics of OWTs — involving the fully-integrated simulation approach — is necessary within the offshore wind research community, industry, and certification authorities. So far, they all had to rely on the ice experts, whose methods for ice loads calculation were not fully transparent and not always compatible with the design and certification methodologies for OWTs.

6.1 Contributions to the state-of-the-art

The main contributions of this work to the state-of-the-art are summarized as follows:

- A simple phenomenological Määttänen-Blenkarn ice model has been validated against scaled ice tank tests from HSVA in Chapter 3. Over the years, this model had been considered as one of the state-of-the-art phenomenological ice models. It has been shown that the Määttänen-Blenkarn ice model might provide reasonable results once the relationship between the ice stress and stress rate is well known. However, such full-scale measurements are very difficult to obtain in situ and are usually not available. This is a severe limitation in the application of this ice model in the design process and load certification for OWTs. Nevertheless, it has been shown that it can be used for studying OWT dynamics but rather on a theoretical, academic level.

- At the time when the validation work with the Määttänen-Blenkarn ice model was accomplished, a new advanced phenomenological ice model was released by Dr. Hendrikse and its source code was made available to the author. This new ice model has been fully integrated into an aero-hydro-servo-elastic tool (MoLWiT) for the first time, as presented in Chapter 4.
- The implementation of the Hendrikse ice model in MoLWiT has been successfully cross-verified against its source code in Chapter 4.
- Furthermore, the simulation capabilities of the source code have been extended to accommodate modally reduced mDOF structures. The extended source code of the ice model has been coupled with a newly developed FEM code for modeling mDOF structures. This FEM code is available in Appendix A. It can be coupled by other researchers with the publicly available version of the Hendrikse ice model source code (for sDOF structures) upon the extension of its simulation capabilities to cope with multi-mode structures. The extension procedure has been described in Section 4.3.2.
- The fully-integrated implementation of the Hendrikse ice model in MoLWiT has been used for advanced studies of ice-OWT interaction in Chapter 5. The analysis has been performed at three distinct design situations — idling below the cut-in wind speed, power production below the rated wind speed, and power production above the rated wind speed. Each design situation has been simulated with multiple ice velocities covering three main ice-structure interaction modes — intermittent ice crushing, frequency lock-in, and continuous brittle crushing. The impact of ice on the OWT dynamics has been investigated in terms of short-term DELs and PSDs. It has been shown that:
  - The most severe fatigue load effects are always caused by intermittent ice crushing, regardless of whether the OWT is idling or operating.
  - The highest increase of fatigue load effects occurs when the OWT is idling and there is an ice action on its support structure, when compared to the corresponding reference design situation where ice loads are not present (around 8200% increase at the intermittent ice crushing mode, around 4600% increase at the frequency lock-in mode, and around 1400% increase at the continuous brittle crushing mode). However, in terms of the absolute values, DELs at idling are usually smaller than those obtained at power production.
  - During the OWT operation, the increase of short-term DELs is not that dramatic as for the idling case, as the increased aerodynamic damping can effectively mitigate load effects resulting from the ice load action at MSL. Nevertheless, this increase is still noticeable: the increase of around 74% is observed at the intermittent ice crushing mode, around 30% at the frequency lock-in mode, and around 5% for the continuous brittle crushing mode — when compared to the corresponding reference design situations without ice loads. Note that, the continuous brittle crushing region is not a design driver in terms of fatigue load effects.
  - During intermittent ice crushing, ice fails with the frequency lower than the frequency of the 1st global mode of the OWT. Furthermore, structural frequencies are not

pronounced in the spectrum of ice load in the intermittent ice crushing region. The load spectrum rather contains frequency peaks corresponding to the higher harmonics of the global ice failure. This is in contrast to the frequency lock-in region, where energy peaks — corresponding to the OWT frequencies — are visible in the spectrum of ice load.

  - The energy content in the ice load spectrum at frequency lock-in is relatively low compared to the energy content during intermittent crushing.

- The work-energy flow between ice and the OWT at different design situations has been analyzed for the first time. It has been shown that:
  - The work done by ice on the fore-aft eigenmodes of the support structure varies significantly depending on the ice-OWT interaction region. Even within a specific interaction region, the amount of work done on the subsequent eigenmodes can drift alternating the dominant eigenmode if the ice velocity is slightly altered.
  - In the intermittent crushing region, most of the work is done by ice on the 1st and the 2nd fore-aft eigenmodes.
  - In the lock-in region, most of the work is done on the 2nd and the 3rd fore-aft eigenmodes. The 1st and the 4th fore-aft eigenmodes receive around one order of magnitude energy less.
  - In the continuous brittle crushing region, the mean value of work done by ice on individual eigenmodes is one order of magnitude lower than at the intermittent crushing and lock-in regions.
  - It has been noticed that at certain ice velocities (at very low ice velocity in the intermittent crushing region and in the upper bound of velocities in the frequency lock-in region), negative work was done by ice on the 1st eigenmode. This means that ice can also have a certain damping effect.

- The sensitivity analysis of eigenmodes contribution to short-term DELs has been performed. It has been shown that the 1st eigenmode always has a significant contribution to DELs. The impact of the 2nd eigenmode on DELs is also very considerable, though it might have mitigating effect at certain design situations, as it vibrates with the opposite phase to other eigenmodes. The 3rd and the 4th eigenmodes have less impact on DELs than the first two eigenmodes. Nevertheless, their presence is important from the perspective of the OWT global dynamics. Those modes are usually coupled with blade flapwise modes.

- Last but not least, the ice properties in the source code of the Hendrikse ice model had been based on the scale ice tank tests. Therefore, it was necessary to retune its input properties for the full-scale application in the southern Baltic Sea. A set of indicative ice properties for the southern Baltic Sea has been estimated in Chapter 4. These properties can be directly used as an input to the ice model for the simulation of the full-scale ice-OWT interaction.

6.2 Recommendations for load analysts

The following recommendations are given for the load analysts who are dealing with simulations of ice loads on OWTs:

- The simulation time for a single load case of 10 minutes long can be considerable due to the event detection mechanism, which is used for detecting ice failures at the exact time points. In the case of MoLWiT, it took between 12 and 18 hours to simulate a single load case, depending on the ice velocity. The most severe fatigue loads are caused during the intermittent crushing of ice. Therefore, it is recommended to focus first on this ice-structure interaction mode.
- Higher modes of the support structure (the 3rd and the 4th one) play an important role in the OWT global dynamics, as they are often coupled with blade eigenmodes. Therefore, they should be included in the analysis.
- The load analysis involving ice loads should, in general, be performed with turbulent wind fields. Especially for the OWT producing power, short-term DELs calculated for load cases with the turbulent wind and ice are much larger than those at the corresponding load cases with the constant wind and ice (during frequency lock-in and continuous brittle crushing). The only exception can be made when a rough assessment of ice loads impact on the OWT dynamics is performed in the intermittent crushing region, where the impact of turbulent wind field is comparable to the constant wind.
- It is necessary to consider ice loads in the design process of OWT support structures, even if the probability of encountering ice is not very significant in the southern Baltic Sea. The impact of ice loads is especially important in idling cases. It might become important when the wind turbine is idling for an extended period, for example, due to delays in the construction phase or fault.

6.3 Recommendations for future work

The following research ideas are suggested for future work in the context of ice-OWT interaction:

Implementation of a mixed failure mode combining ice crushing and buckling
The Hendrikse ice model can simulate a mixed ice failure mode of crushing and buckling. This work has only been focused on crushing loads, which is a conservative approach. From an engineering point of view, buckling of ice does not impose significant forces on a structure, as the flexural strength of ice is much lower than the crushing strength.

Extension of the ice model to account for two-dimensional load
The current version of the ice model can only generate one-dimensional loads (only one force component in the horizontal plane). This is a correct assumption for the interaction with the vertical flat structure when ice load is perpendicular to its face across the entire

width. However, for cylindrical structures, such as monopiles, two-dimensional ice model would be more appropriate.

Investigation of semi-active damping device for mitigation of ice-induced vibrations
This work has shown that the increase in fatigue load effects due to ice action is most significant when the OWT is idling. During idling, the effect of aerodynamic damping is much lower than in power production when the rotor is spinning. A semi-active damping system based on the magnetorheological fluid may help to mitigate both fatigue and ultimate load effects at different idling and operational regions of OWT. A magnetorheological damper contains a carrier fluid with suspended iron particles. The fluid viscosity can be controlled by varying the intensity of the magnetic field generated by an electromagnet. The damping characteristic can be instantly adapted to the excitation conditions, as the response time of the magnetorheological fluid is measured in milliseconds. The magnetorheological damping technology is broadly used in various automotive and civil engineering applications — such as an active suspension in vehicles (e.g., Sun et al., 2019), a seismic control of tall buildings (e.g., Dyke et al., 1998), mitigation of cable vibrations in bridges (e.g., Wang et al., 2019). In recent years, several papers have been published describing a potential application of magnetorheological dampers to wind turbines (e.g., Kirkegaard et al., 2002; Martynowicz, 2015; Rezaee & Aly, 2018; Caterino, 2015; Caterino et al., 2020).

Investigation of active control systems for mitigation of ice-induced vibrations
The aforementioned semi-active damping is a straightforward solution but not ideal, as it does not mitigate the external ice load but rather only a global load effect caused by the external ice load. It might be supported by active control during the OWT operation. For example, a larger swaying of the wind turbine might be induced by active control of thrust (through blade pitch and generator torque control) in order to initiate a global failure of the ice cover before the maximum ice load is reached. This might be beneficial in the intermittent crushing region, where the global failure frequency is lower than the first natural frequency of OWT.

Full-scale measurements of ice loads on OWT support structures
There is neither a full-scale nor a scale test data of an operating OWT under the ice loads excitation available for the investigation. Such measurements are necessary for the validation of numerical models for ice-OWT interaction. The full-scale measurements from offshore structures, such as lighthouses or oil and gas platforms, are not fully representative for OWTs, which dynamics is highly influenced by aerodynamic damping during the operation. Therefore, a measuring campaign of ice loads on OWT and OWT response to these loads would further help to understand this complex interaction. The organization of this task would also include the design of measuring equipment, its calibration, and deployment.

Verification of the Hendrikse ice model against more complex ice models
When this work was realized, other researchers at TUHH were developing a new, high complexity ice model based on the RVE method. The model has been developed and calibrated based on the full-scale laboratory experiments and measurements of ice-ship interaction gathered from various icebreaker voyages. A comparison of OWT load effects obtained from the phenomenological Hendrikse ice model and a high complexity TUHH ice

model should answer the question of whether more complex ice models are really necessary for a more realistic representation of global OWT dynamics.

References

Airy, G. B. (1845). On tides and waves. In *Encyclopædia Metropolitana* (Vol. 5, pp. 241–396). London: William Clowes and Sons.

API. (1995). *API RP 2N: Recommended practice for planning, designing, and constructing structures and pipelines for Arctic conditions* (2nd ed.). Washington, DC: American Petroleum Institute.

API. (2015). *API RP 2N: Planning, designing, and constructing structures and pipelines for Arctic conditions* (3rd ed.). Washington, DC: American Petroleum Institute.

ASCE. (2017). *ASCE Standard ASCE/SEI 7-16 Minimum design loads and associated criteria for buildings and other structures*. Reston, VA: American Society of Civil Engineers. doi: 10.1061/9780784414248

Bachmann, H., Ammann, W. J., Deischl, F., Eisenmann, J., Floegl, I., Hirsch, G. H., ... Steinbeisser, L. (1995). *Vibration problems in structures: Practical guidelines*. Basel: Birkhaüser Verlag Basel. doi: 10.1007/978-3-0348-9231-5

Baltic Sea Region Energy Co-operation. (2012, April). *Conditions for deployment of wind power in the Baltic Sea region. Analysis part I Enabling studies* (Tech. Rep.). Berlin & Stockholm: Baltic Sea Region Energy Co-operation.

Bauchau, O. A., & Craig, J. I. (2009). *Structural analysis*. Springer, Dordrecht. doi: 10.1007/978-90-481-2516-6

Behera, A., & Gambier, A. (2018, June). Multi-objective optimal tuning of the multi-loop pitch control systems of a wind turbine. In *Annual American Control Conference, AAC 2018* (pp. 3068–3073). Milwaukee, WI: Institute of Electrical and Electronics Engineers. doi: 10.23919/ACC.2018.8431803

Belyi, M. V. (1993, July). Superelement method for transient dynamic analysis of structural systems. *International Journal for Numerical Methods in Engineering*, *36*(13), 2263–2286. doi: 10.1002/nme.1620361308

Benzley, S. E., Perry, E., Merkley, K., Clark, B., & Sjaardema, G. (1995, October). A comparison of all hexagonal and all tetrahedral finite element meshes for elastic and elasto-plastic analysis. In *Proceedings of the 4th International Meshing Roundtable* (pp. 179–191).

Albuquerque, NM: Sandia National Laboratories. Retrieved June 1, 2020, from http://citeseerx.ist.psu.edu/viewdoc/download?doi=10.1.1.70.392&rep=rep1&type=pdf

Berg, J., Natarajan, A., Mann, J., & Patton, E. G. (2016, November). Gaussian vs non-Gaussian turbulence: impact on wind turbine loads. *Wind Energy*, *19*(11), 1975–1989. doi: 10.1002/we.1963

Bjerkås, M., Albrektsen, A., & Gürtner, A. (2010, June). Static and dynamic ice actions in the light of new design codes. In *Proceedings of the 29th International Conference on Ocean, Offshore and Arctic Engineering* (Vol. 4, pp. 733–739). Shanghai: American Society of Mechanical Engineers. doi: 10.1115/OMAE2010-20036

Björk, B. (1981). *Ice-induced vibrations of fixed offshore structures, marine structures and ships in ice, Part 2: Experiences with Baltic lighthouses* [Report No. 81-06/2.]. Stockholm: Ship Research Institute of Norway, Information Department.

Blackford, J. R., Skouvaklis, G., Pursera, M., & Koutsosa, V. (2012, July). Friction on ice: stick and slip. *Faraday Discussions*, 243–254. doi: 10.1039/C2FD00128D

Blenkarn, K. A. (1970, April). Measurement and analysis of ice forces on Cook Inlet structures. In *Proceedings of Offshore Technology Conference* (pp. 21–34). Houston, TX. doi: 10.4043/1261-MS

Böker, C. (2010). *Load simulation and local dynamics of support structures for offshore wind turbines* (Doctoral dissertation, Schriftenreihe des Instituts für Stahlbau der Universität Hannover, Gottfried Wilhelm Leibniz Universität Hannover, Hannover). Retrieved June 1, 2020, from http://d-nb.info/1124365036

Borg, M., Hansen, A. M., & Bredmose, H. (2016, September). Floating substructure flexibility of large-volume 10MW offshore wind turbine platforms in dynamic calculations. *Journal of Physics: Conference Series*, *753*, 1–10. doi: 10.1088/1742-6596/753/8/082024

Bossanyi, E. (2000, July). The design of closed loop controllers for wind turbines. *Wind Energy*, *3*(3), 149–163. doi: 10.1002/we.34

Bossanyi, E., & Witcher, D. (2009, July). *Controller for 5MW reference turbine* (11593/BR/04). Bristol: Garrad Hassan and Partners Limited.

Branlard, E. (2017, April). Examples of applications of vortex methods to wind energy. In *Wind Turbine Aerodynamics and Vorticity-Based Methods. Research Topics in Wind Energy* (Vol. 7, pp. 347–353). Springer, Cham. doi: 10.1007/978-3-319-55164-7_27

Branlard, E., & Gaunaa, M. (2014, December). Development of new tip-loss corrections based on vortex theory and vortex methods. *Journal of Physics: Conference Series*, *555*, 1–8. doi: 10.1088/1742-6596/555/1/012012

Bretschneider, C. L. (1959, August). *Wave variability and wave spectra for wind-generated gravity waves* (Technical Memorandum No.118). Washington, DC: Beach Erosion Board, U.S. Army Corps of Engineers. Retrieved June 1, 2020, from https://apps.dtic.mil/dtic/tr/fulltext/u2/227467.pdf

BSH. (2015). *Standard Design. Minimum requirements concerning the constructive design of offshore structures within the Exclusive Economic Zone (EEZ). BSH No 7005*. Hamburg and Rostock: Federal Maritime and Hydrographic Agency (BSH). Retrieved June 1, 2020, from https://www.bsh.de/DE/PUBLIKATIONEN/_Anlagen/Downloads/Offshore/Standards/Standard-Design_en.pdf

Byrne, B. W., Burd, H. J., Zdravković, L., McAdam, R. A., Taborda, D. M. G., Houlsby, G. T., ... Gavin, K. G. (2019, January). PISA: new design methods for offshore wind turbine monopiles. *Revue Française de Géotechnique*, *158*(3), 1–6. doi: 10.1051/geotech/2019009

Cammaert, A. B., & Muggeridge, D. B. (1988). *Ice interaction with offshore structures*. New York: Van Nostrand Reinhold.

Caterino, N. (2015, June). Semi-active control of a wind turbine via magnetorheological dampers. *Journal of Sound and Vibration*, *345*, 1–17. doi: 10.1016/j.jsv.2015.01.022

Caterino, N., Pugliano, G., Spizzuoco, M., & Robustelli, U. (2020, April). Variable dampers to mitigate structural demand to wind turbines: The role of the monitoring system features for the effectiveness of the control strategy. *Applied Sciences*, *10*(7), 1–20. doi: 10.3390/app10072498

Cerda Salzmann, D. J., & van der Tempel, J. (2005, October). Aerodynamic damping in the design of support structures for offshore wind turbines. In *Proceedings of the Copenhagen Offshore Wind 2005.* Copenhagen: European Wind Energy Association. Retrieved June 1, 2020, from http://citeseerx.ist.psu.edu/viewdoc/download?doi=10.1.1.613.7848&rep=rep1&type=pdf

Cook, R. D., Malkus, D. S., Plesha, M. E., & Witt, R. J. (2001). *Concepts and applications of finite element analysis* (4th ed.). John Wiley & Sons, Inc.

Coyle, H. M., & Reese, L. C. (1966, March). Load transfer for axially loaded pile in clay. *Journal of the Soil Mechanics and Foundations Division*, *92*(2), 1–26.

Craig, R. R., & Bampton, M. C. C. (1968, July). Coupling of substructures for dynamic analyses. *AIAA Journal — American Institute of Aeronautics and Astronautics*, *6*(7), 1313–1319. doi: 10.2514/3.4741

Croasdale, K. R., & Cammaert, A. B. (1994, March). An improved method for the calculation of ice loads on sloping structures in first-year ice. *Power Technology and Engineering (formerly Hydrotechnical Construction)*, *28*(3), 174–179. doi: 10.1007/BF01545935

Daley, C., & Riska, K. (1994). *Conceptual framework for an ice load model* (Tech. Rep.). Calgary: National Energy Board. Retrieved June 1, 2020, from http://citeseerx.ist.psu.edu/viewdoc/download?doi=10.1.1.560.2779&rep=rep1&type=pdf

Dean, R. G. (1965, September). Stream function representation of nonlinear ocean waves. *Journal of Geophysical Research*, *70*(18), 4561–4572. doi: 10.1029/JZ070i018p04561

De Klerk, D., Rixen, D. J., & Voormeeren, S. N. (2008, May). General framework for dynamic substructuring: History, review, and classification of techniques. *AIAA Journal — American Institute of Aeronautics and Astronautics*, *56*(5), 1169–1181. doi: 10.2514/1.33274

Dempsey, J. P., Palmer, A. C., & Sodhi, D. S. (2001, December). High pressure zone formation during compressive ice failure. *Engineering Fracture Mechanics*, *68*(17–18), 1961–1974. doi: 10.1016/S0013-7944(01)00033-9

DNV. (2014). *DNV-OS-J101 Design of offshore wind turbine structures*. Det Norske Veritas AS. Retrieved June 1, 2020, from https://rules.dnvgl.com/docs/pdf/DNV/codes/docs/2014-05/Os-J101.pdf

DNV GL. (2016). *DNVGL-ST-0437 Loads and site conditions for wind turbines*. DNV GL AS. Retrieved June 1, 2020, from https://rules.dnvgl.com/docs/pdf/DNVGL/ST/2016-11/DNVGL-ST-0437.pdf

Dormand, J. R., & Prince, P. J. (1980, March). A family of embedded Runge-Kutta formulae. *Journal of Computational and Applied Mathematics*, *6*(1), 19–26. doi: 10.1016/0771-050X(80)90013-3

Drnevich, V. P. (1978, July). *Resonant column test* (Tech. Rep.). Lexington, KY: Soil Dynamics Instruments, Inc. Retrieved June 1, 2020, from https://apps.dtic.mil/dtic/tr/fulltext/u2/a058902.pdf

Dyke, S. J., Spencer Jr, B. F., Sain, M. K., & Carlson, J. D. (1998, October). An experimental study of MR dampers for seismic protection. *Smart Materials and Structures*, *7*(5), 693–703. doi: 10.1088/0964-1726/7/5/012

Engelbrektson, A. (1987). *Methods for structural response measurements and their transformation to ice forces* (VBB Project M7334, Report No 3). Stockholm: The Swedish National Administration of Shipping and Navigation, Luleå University of Technology.

Faltinsen, O. M. (1993). *Sea loads on ships and offshore structures*. Cambridge: Cambridge University Press.

Felippa, C. A. (2004). *Introduction to finite element methods*. University of Colorado. (Material assembled from Lecture Notes for the course Introduction to Finite Elements Methods (ASEN 5007) offered from 1986 at the Aerospace Engineering Sciences Department of the University of Colorado at Boulder)

Frandsen, S., Gravesen, H., Jørgensen, L., Eriksson, C., Halling, K. M., Skjærbæk, P., ... Bjerregaard, E. T. D. (2001). *Recommendation for technical approval of offshore wind turbines*. Copenhagen: Danish Energy Agency. Retrieved June 1, 2020, from https://findit.dtu.dk/en/catalog/2389484118

Frenkiel, F. N., & Klebanoff, P. S. (1967, March). Higher-order correlations in a turbulent field. *Physics of Fluids*, *10*(3), 507–520. doi: 10.1063/1.1762145

Gautier, D. L., Bird, K. J., Charpentier, R. R., Grantz, A., Houseknecht, D. W., Klett, T. R., ... Wandrey, C. J. (2009, May). Assessment of undiscovered oil and gas in the Arctic. *Science*, *324*(5931), 1175–1179. doi: 10.1126/science.1169467

Gevorkyan, M. N., Demidova, A. V., Korolkova, A. V., Kulyabov, D. S., & Sevastianov, L. A. (2016, November). The stochastic processes generation in OpenModelica. In V. Vishnevskiy, K. Samouylov, & D. Kozyrev (Eds.), *Distributed Computer and Communication Networks. DCCN 2016. Communications in Computer and Information Science* (Vol. 678, pp. 538–552). Springer, Cham. doi: 10.1007/978-3-319-51917-3_46

Geyer, B., Weisse, R., Bisling, P., & Winterfeldt, J. (2015, December). Climatology of North Sea wind energy derived from a model hindcast for 1958–2012. *Journal of Wind Engineering and Industrial Aerodynamics*, *147*, 18–29. doi: 10.1016/j.jweia.2015.09.005

GL. (2005). *Guideline for the construction of fixed offshore installations in ice infested waters*. Hamburg: Germanischer Lloyd. Retrieved June 1, 2020, from http://rules.dnvgl.com/docs/pdf/gl/maritimerules/gl_iv-6-7_e.pdf

GL. (2012). *Guideline for the certification of offshore wind turbines*. Hamburg: GL Renewables Certification.

Glauert, H. (1926, November). *A general theory of the autogyro* (Reports and Memoranda No. 1111). H. M. Stationery Office. Retrieved June 1, 2020, from https://pdfs.semanticscholar.org/0b5c/822565db009f49cfc430d8e43dae8b42b1db.pdf

Glauert, H. (1935). Airplane propellers. In W. F. Durand (Ed.), *Aerodynamic theory* (Vol. 4, pp. 169–360). Berlin: Springer Verlag. doi: 10.1007/978-3-642-91487-4_3

Gontier, H., Schaffarczyk, A. P., Kleinhans, D., & Friedrich, R. (2007, July). A comparison of fatigue loads of wind turbine resulting from a non-Gaussian turbulence model vs. standard ones. *Journal of Physics: Conference Series*, *75*(1), 1–11. doi: 10.1088/1742-6596/75/1/012070

Google Earth. (2020a). *Baltic Sea, Data: SIO, NOAA, U.S. Navy, NGA, GEBCO IBCAO Landsat Copernicus.* Retrieved June 1, 2020, from https://www.google.com/earth/

Google Earth. (2020b). *Gulf of Bothnia, Image: IBCAO, Image: Landsat/Copernicus, Data: SIO, NOAA, U.S. Navy, NGA, GEBCO.* Retrieved June 1, 2020, from https://www.google.com/earth/

Gravesen, H., & Kärnä, T. (2009, June). Ice loads for offshore wind turbines in southern Baltic Sea. In *Proceedings of the 20th International Conference on Port and Ocean Engineering under Arctic Conditions.* Luleå. Retrieved June 1, 2020, from http://www.poac.com/Papers/POAC09_01-71.zip

Gravesen, H., Petersen, B., Sørensen, S. L., & Vølund, P. (2003, June). Ice forces to wind turbine foundations in Denmark. In *Proceedings of the 17th International Conference on Port and Ocean Engineering under Arctic Conditions* (Vol. 1, pp. 187–202). Trondheim. Retrieved June 1, 2020, from http://www.poac.com/Papers/POAC03_V1.zip

Gravesen, H., Sørensen, S. L., & Vølund, P. (2002, July). Extreme ice and wind loads to foundations. In *Proceedings of the 1st World Wind Energy Conference and Exhibition.* Berlin.

Gravesen, H., Sørensen, S. L., Vølund, P., Barker, A., & Timco, G. W. (2005, January). Ice loading on Danish wind turbines: Part 2. Analyses of dynamic model test results. *Cold Regions Science and Technology*, *41*(1), 25–47. doi: 10.1016/j.coldregions.2004.05.009

Guyan, R. J. (1965, February). Reduction of stiffness and mass matrices. *AIAA Journal — American Institute of Aeronautics and Astronautics*, *3*(2), 380–380. doi: 10.2514/3.2874

Haapala, J., Meier, H. E. M., & Rinne, J. (2001, August). Numerical investigations of future ice conditions in the Baltic Sea. *AMBIO: A Journal of the Human Environment*, *30*(4), 237–244. doi: 10.1579/0044-7447-30.4.237

Hansen, M. H., & Henriksen, L. C. (2013, January). *Basic DTU wind energy controller* (DTU Wind Energy E-0018). Roskilde: DTU Wind Energy. Retrieved June 1, 2020, from http://orbit.dtu.dk/files/56263924/DTU_Wind_Energy_E_0028.pdf

Hansen, M. O. L. (2015). *Aerodynamics of wind turbines* (3rd ed.). London: Routledge. doi: 10.4324/9781315769981

Hansen, M. O. L., & Madsen, H. A. (2011, November). Review paper on wind turbine aerodynamics. *Journal of Fluids Engineering*, *133*(11), 1–12. doi: 10.1115/1.4005031

Hansen, M. O. L., Sørensen, J. N., Voutsinas, S., Sørensen, N., & Madsen, H. A. (2006, June). State of the art in wind turbine aerodynamics and aeroelasticity. *Progress in Aerospace Sciences*, *42*(4), 286–330. doi: 10.1016/j.paerosci.2006.10.002

Hasselmann, K., Barnett, T. P., Bouws, E., Carlson, H., Cartwright, D. E., Enke, K., … Walden, H. (1973). Measurements of wind-wave growth and swell decay during the Joint North Sea Wave Project (JONSWAP). *Ergänzungsheft zur Deutschen Hydrographischen Zeitschrift Reihe*, *8*(12). Retrieved June 1, 2020, from https://repository.tudelft.nl/islandora/object/uuid:f204e188-13b9-49d8-a6dc-4fb7c20562fc/datastream/OBJ/download

Hauptmann, S., Bülk, M., Schön, L., Erbslöh, S., Boorsma, K., Grasso, F., ... Cheng, P. W. (2014, December). Comparison of the lifting-line free vortex wake method and the blade-element-momentum theory regarding the simulated loads of multi-MW wind turbines. *Journal of Physics: Conference Series*, *555*, 1–13. doi: 10.1088/1742-6596/555/1/012050

Heinonen, J., Hetmanczyk, S., & Strobel, M. (2011, July). Introduction of ice loads in overall simulation of offshore wind turbines. In *Proceedings of the 21st International Conference on Port and Ocean Engineering under Arctic Conditions* (pp. 359–372). Montréal. Retrieved June 1, 2020, from http://www.poac.com/Papers/POAC11_1-79.zip

Heinonen, J., Kärnä, T., & Luo, C. (2004, January). *STRICE Report: Dynamic behaviour of the Norstömsgrund lighthouse* (Deliverable No. D-6.2-A, Revision No. 1.1, EU FP5 EESD Project – Contract No. EVG1-CT-2000-00024). Espoo: VTT Technical Research Centre of Finland, Luleå University of Technology.

Hendrikse, H. (2017). *Ice-induced vibrations of vertically sided offshore structures* (Doctoral dissertation, Delft University of Technology, Delft). doi: 10.4233/uuid:325ebcfb-f920-400c-8ef6-21b2305b6920

Hendrikse, H. (2019, March). *Model for simulation of dynamic ice-structure interaction for vertically sided offshore structures – SDOF MATLAB implementation.* (Mendeley Data, v2) doi: 10.17632/582m8565dj.2

Hendrikse, H., & Metrikine, A. (2015, September). Interpretation and prediction of ice induced vibrations based on contact area variation. *International Journal of Solids and Structures*, *75–76*, 336–348. doi: 10.1016/j.ijsolstr.2015.08.023

Hendrikse, H., & Metrikine, A. (2016, November). Ice-induced vibrations and ice buckling. *Cold Regions Science and Technology*, *131*, 129–141. doi: 10.1016/j.coldregions.2016.09.009

Hendrikse, H., & Metrikine, A. V. (2013, June). The influence of friction at the ice-structure interface on ice induced vibrations. In *Proceedings of the 22nd International Conference on Port and Ocean Engineering under Arctic Conditions.* Espoo. Retrieved June 1, 2020, from http://www.poac.com/Papers/2013/pdf/POAC13_066.pdf

Hendrikse, H., Ziemer, G., & Owen, C. C. (2018, July). Experimental validation of a model for prediction of dynamic ice-structure interaction. *Cold Regions Science and Technology*, *151*, 345–358. doi: 10.1016/j.coldregions.2018.04.003

Hetmanczyk, S., Heinonen, J., & Strobel, M. (2011, June). Dynamic ice load model in overall simulation of offshore wind turbines. In *Proceedings of the 21st International Offshore and Polar Engineering Conference* (Vol. 1, pp. 347–352). Maui, HI: International Society of Offshore and Polar Engineers. Retrieved June 1, 2020, from https://www.onepetro.org/conference-paper/ISOPE-I-11-551

Hirayama, K., Schwarz, J., & Wu, H.-C. (1974, June). *An investigation of ice forces on vertical structures* (Issue 158 of IIHR report). Iowa City, IA: Iowa Institute of Hydraulic Research, University of Iowa. Retrieved June 1, 2020, from https://www.iihr.uiowa.edu/wp-content/uploads/2018/07/TR158.pdf

Höglund, A., Pemberton, P., Hordoir, R., & Schimanke, S. (2017, May). Ice conditions for maritime traffic in the Baltic Sea in future climate. *Boreal Environment Research*, *22*, 245–265. Retrieved June 1, 2020, from http://www.borenv.net/BER/pdfs/ber22/ber22-245-265.pdf

Højstrup, J., Hansen, K. S., Pedersen, B. J., & Nielsen, M. (1999, March). Non-Gaussian turbulence. In *Proceedings of the European Wind Energy Conference 1999* (pp. 1055–1057). Nice. Retrieved June 1, 2020, from https://www.osti.gov/etdeweb/servlets/purl/679629

Huang, Y., Shi, Q., & Song, A. (2007, August). Model test study of the interaction between ice and a compliant vertical narrow structure. *Cold Regions Science and Technology*, *49*(2), 151–160. doi: 10.1016/j.coldregions.2007.01.004

Hurty, W. C. (1965, May). Dynamic analysis of structural systems using component modes. *AIAA Journal — American Institute of Aeronautics and Astronautics*, *3*(4), 678–685. doi: 10.2514/3.2947

IEC. (2009). *IEC 61400-3 Wind turbines — Part 3: Design requirements for offshore wind turbines*. Geneva: International Electrotechnical Commission.

IEC. (2019a). *IEC 61400-1 Wind energy generation systems — Part 1: Design requirements* (4th ed.). Geneva: International Electrotechnical Commission.

IEC. (2019b). *IEC 61400-3-1 Wind energy generation systems — Part 3-1: Design requirements for fixed offshore wind turbines* (1st ed.). Geneva: International Electrotechnical Commission.

ISO. (2010). *ISO 19906 Petroleum and natural gas industries — Arctic offshore structures* (1st ed.). Geneva: International Organization for Standardization.

ISO. (2019). *ISO 19906 Petroleum and natural gas industries — Arctic offshore structures* (2nd ed.). Geneva: International Organization for Standardization.

Jefferies, M. G., Kärnä, T., & Løset, S. (2008, July). Field data on the magnification of ice loads on vertical structures. In *Proceedings of the 19th IAHR International Symposium on Ice* (Vol. 2, pp. 1325–1343). Vancouver: International Association for Hydro-Environment Engineering and Research. Retrieved June 1, 2020, from https://www.iahr.org/index/club/14

Jefferies, M. G., & Wright, W. H. (1988, February). Dynamic response of Molikpaq to ice-structure interaction. In *Proceedings of the 7th International Conference on Offshore Mechanics and Arctic Engineering* (Vol. 4, pp. 201–220). Houston, TX: American Society of Mechanical Engineers.

Jochmann, P. (2003a, October). *STRICE Report: Full scale measurements at lighthouse Norströmsgrund – Winter 2001 –* (Deliverable No. D-5.1.1, EU FP5 EESD Project – Contract No. EVG1-CT-2000-00024). Hamburg: Hamburgische Schiffbau-Versuchsanstalt GmbH.

Jochmann, P. (2003b, October). *STRICE Report: Full scale measurements at lighthouse Norströmsgrund – Winter 2001 – Appendix 3* (Deliverable No. D-5.1.1, EU FP5 EESD Project – Contract No. EVG1-CT-2000-00024). Hamburg: Hamburgische Schiffbau-Versuchsanstalt GmbH.

Joensuu, A., & Riska, K. (1989). *Jään ja rakenteen välinen kosketus: mittaustulokset yhteisistä jään murskauskokeista Wärtsilän arktisen teknologiakeskuksen kanssa keväällä 1988* [*Contact between ice and structure: measurement results from joint ice crushing tests with Wärtsilä Arctic Technology Center in spring 1988*] (Report M-88). Otaniemi: Helsinki University of Technology, Laboratory of Naval Architecture and Marine Engineering. Retrieved June 1, 2020, from http://urn.fi/URN:NBN:fi:bib:me:W00065127800 (In Finnish)

Jonkman, J. (2003, December). *Modeling of the UAE wind turbine for refinement of FAST AD* (NREL / TP-500-34755). Golden, CO: National Renewable Energy Laboratory. Retrieved June 1, 2020, from http://www.nrel.gov/docs/fy04osti/34755.pdf

Jussila, V. (2018, June). General principles of the Procedure for Ice-Structure-Interaction (PSSII). In *Proceedings of the 28th International Ocean and Polar Engineering Conference* (pp. 1630–1637). Sapporo: International Society of Offshore and Polar Engineers. Retrieved June 1, 2020, from https://www.onepetro.org/conference-paper/ISOPE-I-18-476

Jussila, V., Popko, W., & Heinonen, J. (2013, June). Interfacing of ice load simulation tools for cylindrical and conical structure with OneWind simulation tool for offshore wind turbines. In *Proceedings of the 22nd International Conference on Port and Ocean Engineering under Arctic Conditions.* Espoo. Retrieved June 1, 2020, from http://www.poac.com/Papers/2013/pdf/POAC13_045.pdf

Kaimal, J. C., Wyngaard, J. C., Izumi, Y., & Coté, O. R. (1972, July). Spectral characteristics of surface-layer turbulence. *Quarterly Journal of the Royal Meteorological Society*, *98*(417), 563–589. doi: 10.1002/qj.49709841707

Kärnä, T. (1992, June). A Procedure for dynamic Soil-Structure-Ice Interaction. In *Proceedings of the 2nd International Offshore and Polar Engineering Conference* (Vol. 2, pp. 764–771). San Francisco, CA: International Society of Offshore and Polar Engineers. Retrieved June 1, 2020, from https://www.onepetro.org/conference-paper/ISOPE-I-92-207

Kärnä, T., Andersen, H., Gürtner, A., Metrikine, A., Sodhi, D., Loo, M., . . . Jefferies, M. (2013, June). Ice-induced vibrations of offshore structures — Looking beyond ISO 19906. In

Proceedings of the 22nd International Conference on Port and Ocean Engineering under Arctic Conditions. Espoo. Retrieved June 1, 2020, from http://www.poac.com/Papers/2013/pdf/POAC13_226.pdf

Kärnä, T., Jochmann, P., & Kolari, K. (2003, October). *STRICE Report: Observed ice-structure interactions in winters 2000 and 2001* (Deliverable No. D-3.1-A1, EU FP5 EESD Project – Contract No. EVG1-CT-2000-00024). Hamburg: VTT Technical Research Centre of Finland, Hamburgische Schiffbau Versuchsanstalt GmbH.

Kärnä, T., Kamesaki, K., & Tsukuda, H. (1999, August). A numerical model for dynamic ice-structure interaction. *Computers & Structures*, *72*(4–5), 645–658. doi: 10.1016/S0045-7949(98)00337-X

Kärnä, T., & Muhonen, A. (1990, August). Preliminary results from ice indentation tests using flexible and rigid indentors. In *Proceedings of the 10th IAHR International Symposium on Ice* (Vol. 3, pp. 261–275). Espoo: International Association for Hydro-Environment Engineering and Research. Retrieved June 1, 2020, from https://www.iahr.org/index/club/14

Kärnä, T., Qu, Y., Bi, X., Yue, Q., & Kuehnlein, W. (2006, May). A spectral model for forces due to ice crushing. *Journal of Offshore Mechanics and Arctic Engineering*, *129*(2), 138–145. doi: 10.1115/1.2426997

Kärnä, T., & Turunen, R. (1989, December). Dynamic response of narrow structures to ice crushing. *Cold Regions Science and Technology*, *17*(2), 173–187. doi: 10.1016/S0165-232X(89)80007-2

Kärnä, T., & Yan, Q. (2009, August). *Analysis of the size effects in ice crushing — Edition 2* (RTEU50-IR-6/2005). Helsinki: VTT Technical Research Centre of Finland. Retrieved June 1, 2020, from https://www.yumpu.com/en/document/view/23771713/analysis-of-the-size-effect-in-ice-crushing-edition-1-karnaeu

Kelley, N. D., & Jonkman, B. J. (2007, April). *Overview of the TurbSim stochastic inflow turbulence simulator. Version 1.21.* (NREL/TP-500-41137). Golden, CO: National Renewable Energy Laboratory. Retrieved June 1, 2020, from https://www.nrel.gov/docs/fy07osti/41137.pdf

Kellner, L., Herrnring, H., & Ring, M. (2017, June). Review of ice load standards and comparison with measurements. In *Proceedings of the ASME 2017 36th International Conference on Ocean, Offshore and Arctic Engineering.* Trondheim: American Society of Mechanical Engineers. doi: 10.1115/OMAE2017-61735

Kim, T., Hansen, A. M., & Branner, K. (2013, November). Development of an anisotropic beam finite element for composite wind turbine blades in multibody system. *Renewable Energy*, *59*, 172–183. doi: 10.1016/j.renene.2013.03.033

Kirkegaard, P. H., Nielsen, S. R. K., Poulsen, B. L., Andersen, J., Pedersen, L. H., & Pedersen, B. J. (2002, September). Semiactive vibration control of a wind turbine tower using an MR damper. In *Proceedings of The Fifth European Conference on Structural Dynamics: Eurodyn'02* (pp. 1575–1580). Munich: CRC Press/Balkema.

Kjetså, A., & Saaghus, L. J. (2010). *Local dynamics of offshore wind turbine jacket sub-structures* (Master's thesis, Norwegian University of Science and Technology, Trondheim). Retrieved June 1, 2020, from http://hdl.handle.net/11250/236598

Kolari, K. (2003, February). *Norstromsgrund_LH_03.jpg.* Retrieved June 1, 2020, from http://virtual.vtt.fi/virtual/proj6/arki/kuvat/strice/PICS/Norstromsgrund_LH_03.html

Kolari, K. (2017, June). A complete three-dimensional continuum model of wing-crack growth in granular brittle solids. *International Journal of Solids and Structures*, *115–116*, 27–42. doi: 10.1016/j.ijsolstr.2017.02.012

Korzhavin, K. N. (1971). *Action of ice on engineering structures* (No. CRREL Translation TL260). Hanover, NH: U.S. Army Cold Regions Research and Engineering Laboratory. Retrieved June 1, 2020, from https://apps.dtic.mil/dtic/tr/fulltext/u2/723169.pdf (Original work published in 1962)

Kühn, M. J. (2001). *Dynamics and design optimisation of offshore wind energy conversion systems* (Doctoral dissertation, Delft University of Technology, Delft). Retrieved June 1, 2020, from http://resolver.tudelft.nl/uuid:adc3b032-3dde-4e32-84c3-7b8e181e5263

Laks, J. H., Pao, L. Y., & Wrigh, A. D. (2009, June). Control of wind turbines: past, present, and future. In *Proceedings of the American Control Conference* (pp. 2096–2103). St. Louis, MO: American Control Conference. doi: 10.1109/ACC.2009.5160590

Langhaar, H. L. (1951). *Dimensional analysis and theory of models* (3rd ed.). John Wiley & Sons Canada, Limited.

Le Méhauté, B. (1976). *An introduction to hydrodynamics and water waves*. Springer-Verlag Berlin Heidelberg. doi: 10.1007/978-3-642-85567-2

Leishman, J. G., & Beddoes, T. S. (1989, July). A semi-empirical model for dynamic stall. *Journal of the American Helicopter Society*, *34*(3), 3–17. doi: 10.4050/JAHS.34.3

Lilover, M.-J., Kõuts, T., Pavelson, J., & Leppäranta, M. (2018, May). Characteristics of high-resolution sea ice dynamics in the Gulf of Finland, Baltic Sea. *Boreal Environment Research*, *23*, 175–191. Retrieved June 1, 2020, from http://www.borenv.net/BER/pdfs/ber23/ber23-175-191.pdf

Lio, W. H. (2017). *Blade-pitch control for wind turbine load reductions* (Doctoral dissertation, University of Sheffield, Sheffield). Retrieved June 1, 2020, from http://etheses.whiterose.ac.uk/16527/1/Lio_PhDthesis_final.pdf

Llorens, M.-G., Griera, A., Bons, P. D., Lebensohn, R. A., Jansen, L. A. E. D., & Weikusat, I. (2016, September). Full-field predictions of ice dynamic recrystallisation under simple shear conditions. *Earth and Planetary Science Letters*, *450*, 233–242. doi: 10.1016/j.epsl.2016.06.045

Løset, S., & Marchenko, A. (2009, August). Field studies and numerical simulations of ice bustles on vertical piles. *Cold Regions Science and Technology*, *58*(1–2), 15–28. doi: 10.1016/j.coldregions.2009.03.007

Luo, C. (2003, December). *STRICE Report: Numerical analysis of Norströmsgrund lighthouse* (Deliverable No. D-6.2-A, Revision 1.1, EU FP5 EESD Project – Contract No. EVG1-CT-2000-00024). Luleå: Luleå University of Technology.

Luomaranta, A., Ruosteenoja, K., Jylhä, K., Gregow, H., Haapala, J., & Laaksonen, A. (2014, April). Multimodel estimates of the changes in the Baltic Sea ice cover during the present century. *Tellus A: Dynamic Meteorology and Oceanography*, *66*(1), 1–17. doi: 10.3402/tellusa.v66.22617

Määttänen, M. (1983, February). *Dynamic ice-structure interaction during continuous crushing* (CRREL Report 83-5). Hanover, NH: U.S. Army European Research Office. Retrieved June 1, 2020, from https://apps.dtic.mil/dtic/tr/fulltext/u2/a126349.pdf

Määttänen, M. (1998, July). Numerical model for ice-induced vibration load lock-in and synchronization. In *Proceedings of the 14th IAHR International Symposium on Ice* (Vol. 2, pp. 923–930). Potsdam, NY: International Association for Hydro-Environment Engineering and Research. Retrieved June 1, 2020, from https://www.iahr.org/index/club/14

Määttänen, M. (2006, April). Future international Arctic offshore structures ice load code ISO 19906. In *Proceedings of the 5th European Seminar Offshore Wind and other marine renewable Energies in Mediterranean and European Seas* (pp. 211–216). Civitavecchia: OWEMES Association Onlus.

Määttänen, M., Løset, S., Metrikine, A., Evers, K.-U., Hendrikse, H., Lønøy, C., . . . Sukhorukov, S. (2012, June). Novel ice induced vibration testing in a large-scale facility: Deciphering ice induced vibrations, Part 1. In *Proceedings of the 21st IAHR International Symposium on Ice* (pp. 946–958). Dalian: International Association for Hydro-Environment Engineering and Research.

Määttänen, M., & Vähätaini, K. (2013, June). OWEC ice loads in landfast ice zone. In *Proceedings of the 22nd International Conference on Port and Ocean Engineering under Arctic Conditions.* Espoo. Retrieved June 1, 2020, from http://www.poac.com/Papers/2013/pdf/POAC13_019.pdf

MacCamy, R., & Fuchs, R. (1954, December). *Wave forces on piles: a diffraction theory* (Technical Memorandum No. 69). Berkeley, CA: U.S. Army Corps of Engineers. Retrieved

June 1, 2020, from https://usace.contentdm.oclc.org/digital/api/collection/p266001coll1/id/7401/download

Mann, J. (1994, August). The spatial structure of neutral atmospheric surface-layer turbulence. *Journal of Fluid Mechanics*, *273*, 141–168. doi: 10.1017/S0022112094001886

Mann, J. (1998, October). Wind field simulation. *Probabilistic Engineering Mechanics*, *13*(4), 269–282. doi: 10.1016/S0266-8920(97)00036-2

Martynowicz, P. (2015, June). Vibration control of wind turbine tower-nacelle model with magnetorheological tuned vibration absorber. *Journal of Vibration and Control*, *23*(20), 3468–3489. doi: 10.1177/1077546315591445

Masciola, M., Robertson, A., Jonkman, J., & Driscoll, F. (2011, October). *Investigation of a FAST-OrcaFlex coupling module for integrating turbine and mooring dynamics of offshore floating wind turbines* (NREL/CP-5000-52896). Golden, CO: National Renewable Energy Laboratory. Retrieved June 1, 2020, from https://www.nrel.gov/docs/fy12osti/52896.pdf

Masterson, D. M., & Spencer, P. A. (2000, June). Ice force versus aspect ratio. In *Proceedings of IUTAM Symposium on Scaling Laws in Ice Mechanics and Ice Dynamics* (pp. 31–42). Fairbanks, AK: Springer, Dordrecht. doi: 10.1007/978-94-015-9735-7_3

Matlock, H., Dawkins, W. P., & Panak, J. J. (1969, May). A model for the prediction of ice-structure interaction. In *Proceedings of the 1st Offshore Technology Conference* (Vol. 1, pp. 687–694). Houston, TX. doi: 10.4043/1066-MS

Matsumoto, M., & Nishimura, T. (1998, January). Mersenne Twister: A 623-dimensionally equidistributed uniform pseudo-random number generator. *ACM Transactions on Modeling and Computer Simulation*, *8*(1), 3–30. doi: 10.1145/272991.272995

McCoy, T. J., Brown, T., & Byrne, A. (2014, October). *Ice load project final technical report. Creation of a model for interaction of bottom-fixed wind turbines with surface ice for use with common simulation codes Award No. DE-EE0005477* (DDRP0133). Seattle, WA: DNV KEMA Renewables, Inc. doi: 10.2172/1303304

McQueen, H., & Srinil, N. (2016, February). A modified Matlock-Duffing model for two-dimensional ice-induced vibrations of offshore structures with geometric nonlinearities. *Journal of Offshore Mechanics Arctic Engineering*, *138*(1), 011501-1–011501-9. doi: 10.1115/1.4031927

Miner, M. A. (1945, September). Cumulative damage in fatigue. *Journal of Applied Mechanics*, *12*(3), 159–164.

Modarres, R. (2016). *Semi-empirical modeling of two-dimensional and three-dimensional dynamic stall* (Doctoral dissertation, Washington University, Saint Louis, MO). Retrieved June 1, 2020, from https://openscholarship.wustl.edu/cgi/viewcontent.cgi?article=1161&context=eng_etds

Modelica Association. (2017, April). Modelica®— A unified object-oriented language for systems modeling. Language specification. Version 3.4 [Computer software manual]. Linköping. Retrieved June 1, 2020, from https://www.modelica.org/documents/ModelicaSpec34.pdf

Moriarty, P. J., & Hansen, A. C. (2005, January). *AeroDyn theory manual* (NREL/TP-500-36881). Golden, CO: National Renewable Energy Laboratory. Retrieved June 1, 2020, from https://www.nrel.gov/docs/fy05osti/36881.pdf

Morison, J. R., O'Brien, M. P., Johnson, J. W., & Schaaf, S. A. (1950, May). The force exerted by surface waves on piles. *Journal of Petroleum Technology*, *2*(5), 149–154. doi: 10.2118/950149-G

Mücke, T., Harkness, C., & Argyriadis, K. (2012, April). Offshore wind turbulence model versus measurement. In *Proceedings of EWEA.* Copenhagen: European Wind Energy Association. Retrieved June 1, 2020, from http://proceedings.ewea.org/annual2012/allfiles2/989_EWEA2012presentation.pdf

Mücke, T., Kleinhans, D., & Peinke, J. (2011, March). Atmospheric turbulence and its influence on the alternating loads on wind turbines. *Wind Energy*, *14*(2), 301–316. doi: 10.1002/we.422

Muhonen, A. (1996, September). *Evaluation of three ice-structure interaction models* (Licentiate of Technology). Espoo: Helsinki University of Technology. Retrieved June 1, 2020, from http://lib.tkk.fi/Lic/199X/isbn9512263351/isbn9512263351.pdf

Neill, C. R. (1976, June). Dynamic ice forces on piers and piles. An assessment of design guidelines in the light of recent research. *Canadian Journal of Civil Engineering*, *3*(2), 305–341. doi: 10.1139/l76-030

Nghiem, A., & Pineda, I. (2017, September). *Wind energy in Europe: Scenarios for 2030* (Tech. Rep.). Brussels: Wind Europe. Retrieved June 1, 2020, from https://windeurope.org/wp-content/uploads/files/about-wind/reports/Wind-energy-in-Europe-Scenarios-for-2030.pdf

Nichols, J., Camp, T., Jonkman, J., Butterfield, S., Larsen, T., Hansen, A., ... Kaufer, D. (2009, January). Offshore Code Comparison Collaboration within IEA Wind Annex XXIII: Phase III results regarding tripod support structure modeling. In *Proceedings of the 47th AIAA Aerospace Sciences Meeting.* Orlando, FL. Retrieved June 1, 2020, from https://www.nrel.gov/docs/fy10osti/47534.pdf

Nielsen, M., Hansen, K. S., & Pedersen, B. J. (2000, July). Gyldigheden af antagelsen om Gaussisk Turbulens: Risø-R-1195(DA). In *Gyldigheden on antagelsen om Gaussisk Turbulens, Risø-R-1195(DA)* (pp. 1–61). Forskningscenter Risø. Retrieved June 1, 2020, from https://www.osti.gov/etdeweb/servlets/purl/20086251 (In Danish)

Nielsen, M., Larsen, G. C., Mann, J., Ott, S., Hansen, K. S., & Pedersen, B. J. (2004, January). *Wind simulation for extreme and fatigue loads* (Risø–R–1437(EN)). Roskilde:

Risø National Laboratory for Sustainable Energy. Retrieved June 1, 2020, from https://backend.orbit.dtu.dk/ws/portalfiles/portal/57160513/ris_r_1437.pdf

Nord, T. S., Määttänen, M., & Øiseth, O. (2013, June). Frequency domain force identification in ice-structure interaction. In *Proceedings of the 22nd International Conference on Port and Ocean Engineering under Arctic Conditions.* Espoo. Retrieved June 1, 2020, from http://www.poac.com/Papers/2013/pdf/POAC13_080.pdf

Nyquist, H. (1928, April). Certain topics in telegraph transmission theory. *Transactions of the American Institute of Electrical Engineers*, *47*(2), 617–644. doi: 10.1109/T-AIEE.1928.5055024

O'Callahan, J. C. (1989, January). A procedure for an improved reduced system (IRS) model. In *Proceedings of the 7th International Modal Analysis Conference* (Vol. 1, pp. 17–21). Las Vegas, NV.

Ochi, M. K., & Hubble, E. N. (1976, July). Six-parameter wave spectra. In *Proceedings of the 15th Coastal Engineering Conference* (pp. 301–328). Honolulu, HI: American Society of Civil Engineers. doi: 10.9753/icce.v15.17

Ohlenforst, K., Sawyer, S., Dutton, A., Backwell, B., Fiestas, R., Lee, J., ... Balachandran, N. (2019, April). *GWEC Global wind report 2018* (Tech. Rep.). Brussels: Global Wind Energy Council. Retrieved June 1, 2020, from https://gwec.net/wp-content/uploads/2019/04/GWEC-Global-Wind-Report-2018.pdf

Onken, G. (2012). *Design of a physical analogous model for the study of dynamic ice-structure interaction* (Unpublished master's thesis). Technischen Universität Hamburg–Harburg, Hamburg. (M.Sc. thesis written at the Hamburg Ship Model Basin)

Onken, G., Evers, K.-U., Haase, A., & Jochmann, P. (2013, June). Ice model tests with a cylindrical structure to investigate dynamic ice-structure interaction. In *Proceedings of the 22nd International Conference on Port and Ocean Engineering under Arctic Conditions.* Espoo. Retrieved June 1, 2020, from http://www.poac.com/Papers/2013/pdf/POAC13_055.pdf

Owen, C. C. (2017). *Ice-induced vibrations of vertically sided model structures: Comparison of structures with circular and rectangular cross-section subjected to the frequency lock-in regime* (Master's thesis, Delft University of Technology and Norwegian University of Science and Technology, Delft). Retrieved June 1, 2020, from http://resolver.tudelft.nl/uuid:18b05231-6b53-4d1b-8531-caf3c31848ea

Owen, C. C., & Hendrikse, H. (2019, June). A study of the transition ice speed from intermittent crushing to frequency lock-in vibrations based on model-scale experiments. In *Proceedings of the 25th International Conference on Port and Ocean Engineering under Arctic Conditions.* Delft. Retrieved June 1, 2020, from https://www.poac.com/Papers/2019/pdf/POAC19-171.pdf

Øye, S. (1990, November). Dynamic stall simulated as time lag of separation. In *Proceedings of the fourth IEA Symposium on the Aerodynamics of Wind Turbines: IEA R&D WECS experts meeting* (Vol. 118). Rome: Energy Technology Support Unit (ETSU).

Øye, S. (1991, October). *Tjæreborg wind turbine. 4th dynamic inflow measurement* (VK-204). Lyngby: Department of Fluid Mechanics. Technical University of Denmark. Retrieved June 1, 2020, from https://orbit.dtu.dk/files/3524469/VK204.pdf

Øye, S. (1992, November). Induced velocities for rotors in yaw. In *Proceedings of the sixth IEA Symposium on the Aerodynamics of Wind Turbines.* Petten.

Page, A. M., Grimstad, G., Eiksund, G. R., & Jostad, H. P. (2018, November). A macro-element pile foundation model for integrated analyses of monopile-based offshore wind turbines. *Ocean Engineering*, *167*, 23–35. doi: 10.1016/j.oceaneng.2018.08.019

Page, A. M., Grimstad, G., Eiksund, G. R., & Jostad, H. P. (2019, February). A macro-element model for multidirectional cyclic lateral loading of monopiles in clay. *Computers and Geotechnics*, *106*, 314–326. doi: 10.1016/j.compgeo.2018.11.007

Page, A. M., Norén-Cosgriff, K., Skau, K. S., & Kaynia, A. M. (2019, June). REDWIN foundation models for integrated dynamic analyses of offshore wind turbines. In *Proceedings of the ASME 2019 38th International Conference on Ocean, Offshore and Arctic Engineering.* Glasgow: American Society of Mechanical Engineers. doi: 10.1115/OMAE2019-96168

Palmer, A., & Dempsey, J. (2009, June). Model tests in ice. In *Proceedings of the 20th International Conference on Port and Ocean Engineering under Arctic Conditions.* Luleå. Retrieved June 1, 2020, from http://www.poac.com/Papers/POAC09_01-71.zip

Palmer, A., Qianjin, Y., & Fengwei, G. (2010, March). Ice-induced vibrations and scaling. *Cold Regions Science and Technology*, *60*, 189–192. doi: 10.1016/j.coldregions.2009.11.005

Passon, P. (2015). *Offshore wind turbine foundation design. Selected topics from the perspective of a foundation designer* (Doctoral dissertation, Technical University of Denmark, Department of Wind Energy, Roskilde). Retrieved June 1, 2020, from https://backend.orbit.dtu.dk/ws/portalfiles/portal/122903957/Offshore_Wind_Turbine_Foundation_Design.pdf (DTU Wind Energy PhD-0044 (EN))

Paz, M. (1984, May). Dynamic condensation. *AIAA Journal — American Institute of Aeronautics and Astronautics*, *22*(5), 724–727. doi: 10.2514/3.48498

Paz, M. (1989, January). Modified dynamic condensation method. *Journal of Structural Engineering*, *115*(1), 234–238. doi: 10.1061/(ASCE)0733-9445(1989)115:1(234)

Peters, D. A., & He, C. J. (1991, July). Correlation of measured induced velocities with a finite-state wake model. *Journal of the American Helicopter Society*, *36*(3), 59–70. doi: 10.4050/JAHS.36.59

Peyton, H. R. (1966, November). Sea ice forces. In *Conference on Ice Pressure Against Structures* (pp. 117–123). Quebec: National Research Council of Canada. doi: 10.4224/40001154

Pierson, W. J., & Moskowitz, L. A. (1964, December). Proposed spectral form for fully developed wind seas based on the similarity theory of S. A. Kitaigorodskii. *Journal of Geophysical Research*, *69*(24), 5181–5190. doi: 10.1029/JZ069i024p05181

Pitt, D. M., & Peters, D. A. (1980, September). Theoretical prediction of dynamic-inflow derivatives. In *Sixth European Rotorcraft And Powered Lift Aircraft Forum* (pp. 1–19). Bristol. Retrieved June 1, 2020, from https://dspace-erf.nlr.nl/xmlui/bitstream/handle/20.500.11881/1796/ERF%201980-47.pdf?sequence=1

Popko, W. (2014, June). Comparison of full-scale and numerical model dynamic responses of Norströmsgrund lighthouse. In *Proceedings of the 33rd International Conference on Ocean, Offshore and Arctic Engineering* (Vol. 10). San Francisco, CA: American Society of Mechanical Engineers. doi: 10.1115/OMAE2014-23562

Popko, W., Antonakas, P., & Vorpahl, F. (2013, July). Investigation of local vibration phenomena of a jacket sub-structure caused by coupling with other components of an offshore wind turbine. In *Proceedings of the 23rd International Offshore and Polar Engineering Conference* (Vol. 1, pp. 336–344). Anchorage, AK: International Society of Offshore and Polar Engineers. Retrieved June 1, 2020, from https://www.onepetro.org/conference-paper/ISOPE-I-13-012

Popko, W., & Georgiadou, S. (2015, June). Validation of Määttänen-Blenkarn ice model for ice-structure interaction against ice tank tests. In *Proceedings of the 25th International Ocean and Polar Engineering Conference* (Vol. 1, pp. 1814–1821). Kona, HI: International Society of Offshore and Polar Engineers. Retrieved June 1, 2020, from https://www.onepetro.org/conference-paper/ISOPE-I-15-037

Popko, W., Georgiadou, S., Loukogeorgaki, E., & Vorpahl, F. (2016, February). Influence of joint flexibility on local dynamics of a jacket support structure. *Journal of Ocean and Wind Energy*, *3*(1), 1–9. doi: 10.17736/jowe.2016.jcr45

Popko, W., Heinonen, J., Hetmanczyk, S., & Vorpahl, F. (2012, June). State-of-the-art comparison of standards in terms of dominant sea ice loads for offshore wind turbine support structures in the Baltic Sea. In *Proceedings of the 22nd International Offshore and Polar Engineering Conference* (Vol. 1, pp. 426–435). Rhodes: International Society of Offshore and Polar Engineers. Retrieved June 1, 2020, from https://www.onepetro.org/conference-paper/ISOPE-I-12-094

Popko, W., Huhn, M. L., Robertson, A., Jonkman, J., Wendt, F., Müller, K., ... Cai, J. (2018, June). Verification of a numerical model of the offshore wind turbine from the alpha ventus wind farm within OC5 Phase III. In *Proceedings of the ASME 2018 37th International*

Conference on Ocean, Offshore and Arctic Engineering OMAE 2018. Madrid: American Society of Mechanical Engineers. doi: 10.1115/OMAE2018-77589

Popko, W., Robertson, A., Jonkman, J., Wendt, F., Thomas, P., Müller, K., ... Harries, R. (2019, June). Validation of numerical models of the offshore wind turbine from the alpha ventus wind farm against full-scale measurements within OC5 Phase III. In *Proceedings of the ASME 2019 38th International Conference on Ocean, Offshore and Arctic Engineering.* Glasgow: American Society of Mechanical Engineers. doi: 10.1115/OMAE2019-95429

Popko, W., Thomas, P., Sevinc, A., Rosemeier, M., Bätge, M., Braun, R., ... Reuter, A. (2018, December). *IWES Wind Turbine IWT-7.5-164 Rev 4* (Tech. Rep.). Bremerhaven: Fraunhofer Institute for Wind Energy Systems IWES. doi: 10.24406/IWES-N-518562

Popko, W., Vorpahl, F., Jonkman, J., & Robertson, A. (2012, September). OC3 and OC4 projects — Verification benchmark exercises of the state-of-the-art coupled simulation tools for offshore wind turbines. In *Proceedings of the 7th European Seminar Offshore Wind and other marine renewable Energies in Mediterranean and European Sea* (pp. 499–504). Rome: OWEMES Association Onlus. Retrieved June 1, 2020, from http://www.owemes-2012.eu/documents/v2013-proceedingsowemes-pdf.pdf

Popko, W., Vorpahl, F., Zuga, A., Kohlmeier, M., Jonkman, J., Robertson, A., ... von Waaden, H. (2014, February). Offshore Code Comparison Collaboration Continuation (OC4), Phase I — Results of coupled simulations of an offshore wind turbine with jacket support structure. *Journal of Ocean and Wind Energy*, *1*(1), 1–11. Retrieved June 1, 2020, from http://legacy.isope.org/publications/jowe/jowe-01-1/JOWE-01-1-p001-jcr07-Popko.pdf

Popko, W., Wächter, M., & Thomas, P. (2016, June). Verification of Continuous Time Random Walk wind model. In *Proceedings of the 26th International Ocean and Polar Engineering Conference* (Vol. 1, pp. 471–483). Rhodes: International Society of Offshore and Polar Engineers. Retrieved June 1, 2020, from https://www.onepetro.org/conference-paper/ISOPE-I-16-189

Popko, W., Ziemer, G., & Evers, K.-U. (2015, June). *Schlussbericht. BReaking the ICE (BRICE). Dynamische Untersuchungen von Offshore-Windenergieanlagen unter dem Einfluss von Meer-Eis FKZ 0325297A/B* (Tech. Rep.). Bremerhaven: Fraunhofer-Institut für Windenergie und Energiesystemtechnik IWES, Hamburgische Schiffbau-Versuchsanstalt GmbH. (In German) doi: 10.2314/GBV:859611647

Prandtl, L. (1923, January). *Applications of modern hydrodynamics to aeronautics* (Report No. 116). Göttingen: Göttingen University. Retrieved June 1, 2020, from https://ntrs.nasa.gov/archive/nasa/casi.ntrs.nasa.gov/19930091180.pdf (Translated from German by the staff of the National Advisory Committee for Aeronautics)

Priestley, M. J. N., Seible, S., & Calvi, G. M. (1996). *Seismic design and retrofit of bridges*. John Wiley and Sons. doi: 10.1002/9780470172858

Przemieniecki, J. S. (1968). *Theory of matrix structural analysis*. New York: McGraw-Hill.

Ralston, T. D. (1977, September). Ice force design considerations for conical offshore structures. In *Proceedings of the 4th International Conference on Port and Ocean Engineering under Arctic Conditions* (Vol. II, pp. 741–752). St. John's, NF. Retrieved June 1, 2020, from http://www.poac.com/Papers/POAC77_V2_all.pdf

Ramboll. (2018, August). *SeaLOWT — Impact of sea ice loads on global dynamics of offshore wind turbines. Design Basis* (301000334/SLOWT-311-006). Hamburg: Ramboll.

Rayleigh, J. W. S. (1877). *The theory of sound* (Vol. 1). London: Macmillan and co. Retrieved June 1, 2020, from https://ia800700.us.archive.org/17/items/theorysound06raylgoog/theorysound06raylgoog.pdf

Reese, L. C., Cox, W. R., & Koop, F. D. (1974, May). Analysis of laterally loaded piles in sand. In *Proceedings of the 6th Offshore Technology Conference* (pp. 473–483). Houston, TX: Offshore Technology Conference. doi: 10.4043/2080-MS

Reeves, P. M. (1969, November). *A non-Gaussian turbulence simulation* (AFFDL-TR-69-67). Ohio: Air Force Flight Dynamics Laboratory, Air Force Systems Command, Wright-Patterson Air Force Base. Retrieved June 1, 2020, from https://apps.dtic.mil/dtic/tr/fulltext/u2/701735.pdf

Rezaee, M., & Aly, A. M. (2018, September). Vibration control in wind turbines to achieve desired system-level performance under single and multiple hazard loadings. *Structural Control and Health Monitoring*, *25*(12), 1–31. doi: 10.1002/stc.2261

RIL. (2002). *RIL 144-2002 Rakenteiden kuormitusohjeet* [*Guideline for the loading of structures*]. Helsinki: Suomen Rakennusinsinöörien Liitto RIL [Finnish Association of Civil Engineers]. (In Finnish)

Robertson, A., Jonkman, J., Vorpahl, F., Popko, W., Qvist, J., Frøyd, L., … Guérinel, M. (2014, June). Offshore Code Comparison Collaboration, Continuation within IEA Wind Task 30: Phase II Results regarding a floating semisubmersible wind system. In *Proceedings of the 33rd International Conference on Ocean, Offshore and Arctic Engineering* (Vol. 9B). San Francisco, CA: American Society of Mechanical Engineers. doi: 10.1115/OMAE2014-24040

Robertson, A., Wendt, F., Jonkman, J. M., Popko, W., Borg, M., Bredmose, H., … Guérinel, M. (2016, September). OC5 Project Phase Ib: Validation of hydrodynamic loading on a fixed, flexible cylinder for offshore wind applications. *Energy Procedia*, *94*, 82–101. doi: 10.1016/j.egypro.2016.09.201

Robertson, A., Wendt, F., Jonkman, J. M., Popko, W., Dagher, H., Gueydon, S., ... Debruyne, Y. (2017, October). OC5 Project Phase II: Validation of global loads of the DeepCwind floating semisubmersible wind turbine. *Energy Procedia*, *137*, 38–57. doi: 10.1016/j.egypro.2017.10.333

Robertson, A., Wendt, F., Jonkman, J. M., Popko, W., Vorpahl, F., Stansberg, C. T., ... Bouy, L. (2015, June). OC5 Project Phase I: Validation of hydrodynamic loading on a fixed cylinder. In *Proceedings of the 25th International Ocean and Polar Engineering Conference* (Vol. 1, pp. 471–480). Kona, HI: International Society of Offshore and Polar Engineers. Retrieved June 1, 2020, from https://www.onepetro.org/conference-paper/ISOPE-I-15-116

Rogers, B. T., Hardy, M. D., Neth, V. W., & Metge, M. (1986). Performance monitoring of the Molikpaq while deployed at Tarsuit P-45. In *Proceedings of the 3rd Canadian Conference on Marine Geotechnical Engineering.* St. John's, NF: Canadian Geotechnical Society. Retrieved June 1, 2020, from https://openlibrary.org/works/OL12323308W/3rd_Canadian_Conference_on_Marine_Geotechnical_Engineering

Sanderson, T. J. O. (1988). *Ice Mechanics. Risks to offshore structures*. London: Graham and Trotman Limited.

Schafhirt, S., Hembre, J. M., & Muskulus, M. (2014, June). How to detect local out-of-plane vibrations in jacket support structures for offshore wind turbines. In *Proceedings of the ASME 2014 33rd International Conference on Ocean, Offshore and Arctic Engineering OMAE2014* (Vol. 9B). San Francisco, CA: American Society of Mechanical Engineers. doi: 10.1115/OMAE2014-24245

Schmelzer, N., Holfort, J., Sztobryn, M., & Przygrodzki, P. (2012). *Climatological Ice Atlas for the western and southern Baltic Sea (1961–2010)* (N. Schmelzer & J. Holfort, Eds.) (No. BSH-Nr. 2338). Hamburg und Rostock: Bundesamt für Seeschifffahrt und Hydrographie. Retrieved June 1, 2020, from https://www.bsh.de/download/Eisatlas_Ostsee_EN.pdf

Schulson, E. M. (2001, December). Brittle failure of ice. *Engineering Fracture Mechanics*, *68*(17–18), 1839–1887. doi: 10.1016/S0013-7944(01)00037-6

Schulson, E. M. (2018, August). Friction of sea ice. *Philosophical Transactions of the Royal Society*, *376*, 1–20. doi: 10.1098/rsta.2017.0336

Schulson, E. M., & Duval, P. (2009). *Creep and fracture of ice*. Cambridge: Cambridge University Press. doi: 10.1017/CBO9780511581397

Schwarz, J. (1970). Treibeisdruck auf Pfähle [Ice pressure on piles]. In *Mitteilungen des Franzius-Institutes für Grund- und Wasserbau der Technischen Universität Hannover, Heft 34* (pp. 83–193). Hannover. (In German)

Schwarz, J. (1971, September). The pressure of floating ice-fields on piles. In *Proceedings of the 1st IAHR International Symposium on Ice* (pp. 1–12). Reykjavik: International Association for Hydro-Environment Engineering and Research. Retrieved June 1, 2020, from https://www.iahr.org/index/club/14

Schwarz, J. (1977, September). New developments in modeling ice problems. In *Proceedings of the 4th International Conference on Port and Ocean Engineering under Arctic Conditions* (Vol. 1, pp. 45–61). St. John's, NF. Retrieved June 1, 2020, from http://www.poac.com/Papers/POAC77_V1_all.pdf

Seidel, M., & Hendrikse, H. (2018, July). Analytical assessment of sea ice-induced frequency lock-in for offshore wind turbine monopiles. *Marine Structures*, *60*, 87–100. doi: 10.1016/j.marstruc.2018.02.003

Seidel, M., & Kelma, S. (2012, September). Stochastic modelling of wind and wave induced loads on jacket piles. *Stahlbau*, *81*(9), 705–710. doi: 10.1002/stab.201201599

Seidel, M., von Mutius, M., Rix, P., & Steudel, D. (2005, October). Integrated analysis of wind and wave loading for complex support structures of offshore wind turbines. In *Conference Proceedings Offshore Wind 2005* (pp. 1–10). Copenhagen. Retrieved June 1, 2020, from http://www.marc-seidel.de/Papers/Seidel_Offshore_Wind_2005.pdf

Seidel, M., von Mutius, M., & Steudel, D. (2004, October). Design and load calculations for offshore foundations of a 5MW turbine. In *Proceedings of Deutsche Windenergie-Konferenz (DEWEK) 2004* (pp. 1–6). Wilhelmshaven: DEWI — German Wind Energy Institute. Retrieved June 1, 2020, from http://www.marc-seidel.de/Papers/Seidel_DEWEK2004_OffshoreFoundations.pdf

Shannon, C. E. (1948, July). A mathematical theory of communication. *Bell System Technical Journal*, *27*(3), 379–423. doi: 10.1002/j.1538-7305.1948.tb01338.x

Shi, W., Tan, X., Gao, Z., & Moan, T. (2016, March). Numerical study of ice-induced loads and responses of a monopile-type offshore wind turbine in parked and operating conditions. *Cold Regions Science and Technology*, *123*, 121–139. doi: 10.1016/j.coldregions.2015.12.007

Shi, W., Tan, X., Zhou, L., Ning, D., & Karimirad, M. (2018, June). Investigation on ice loads for offshore wind turbine in varying ice conditions. In *Proceedings of the 28th International Ocean and Polar Engineering Conference* (pp. 483–488). Sapporo: International Society of Offshore and Polar Engineers. Retrieved June 1, 2020, from https://www.onepetro.org/conference-paper/ISOPE-I-18-534

Sinsabvarodom, C., Chai, W., Leira, B. J., Høyland, K. V., & Naess, A. (2020, February). Uncertainty assessments of structural loading due to first year ice based on the

ISO standard by using Monte-Carlo simulation. *Ocean Engineering*, *198*, 1–23. doi: 10.1016/j.oceaneng.2020.106935

Snel, H. (1997, October). Heuristic modelling of dynamic stall characteristics. In *European Wind Energy Conference* (pp. 429–433). Dublin: European Wind Energy Association.

SNiP. (2018). СНиП 2.06.04-82* Нагрузки и воздействия на гидротехнические сооружения (волновые, ледовые и от судов) [*SNIP 2.06.04-82* Loads and impacts on hydraulic structures (from wave, ice and ships)*] (No. SP 38.13330.2018). Москва [Moscow]: Министерство строительства и жилищно-коммунального хозяйства Российской Федерации [Ministry of Construction Industry, Housing and Utilities Sector]. (In Russian)

Sodhi, D. S. (1988, August). Ice-induced vibrations of structures. In *Proceedings of the 9th IAHR International Symposium on Ice* (Vol. II, pp. 625–657). Sapporo: International Association for Hydro-Environment Engineering and Research. Retrieved June 1, 2020, from https://www.iahr.org/index/club/14

Sodhi, D. S. (1991). *Ice-structure interaction during indentation tests* (S. Jones, J. Tillotson, R. F. McKenna, & I. J. Jordaan, Eds.). Springer, Berlin, Heidelberg. doi: 10.1007/978-3-642-84100-2

Sodhi, D. S. (1994, February). A theoretical model for ice-structure interaction. In *Proceedings of the 13th International Conference on Offshore Mechanics and Arctic Engineering* (Vol. 4, pp. 29–34). Houston, TX: American Society of Mechanical Engineers.

Sodhi, D. S. (1998, June). Nonsimultaneous crushing during edge indentation of freshwater ice sheets. *Cold Regions Science and Technology*, *27*(3), 179–195. doi: 10.1016/S0165-232X(98)00010-X

Sodhi, D. S. (2001, December). Crushing failure during ice-structure interaction. *Engineering Fracture Mechanics*, *68*(17–18), 1889–1921. doi: 10.1016/S0013-7944(01)00038-8

Sodhi, D. S., & Morris, C. E. (1986, February). Characteristic frequency of force variations in continous crushing of sheet ice against rigid cylindrical structures. *Cold Regions Science and Technology*, *12*(1), 1–12. doi: 10.1016/0165-232X(86)90015-7

Steenfelt, J. S. (2016, September). Ice loads on structures in the Baltic environment. In *The 13th Baltic Sea Region Geotechnical Conference Historical Experience and Challenges of Geotechnical Problems in Baltic Sea Region* (pp. 129–136). Vilnius: Vilnius Gediminas Technical University Press Technika. doi: 10.3846/13bsgc.2016.018

Stokes, G. G. (1847, March). On the theory of oscillatory waves. *Transactions of the Cambridge Philosophical Society*, *8*, 441–473. Retrieved June 1, 2020, from http://pordlabs.ucsd.edu/wryoung/theorySeminar/pdf15/Stokes1847.pdf

Strobel, M., Hilmann, C., Wihlfahrt, U., Samlaus, R., Hetmanczyk, S., Zuga, A., . . . Vorpahl, F. (2012, February). *Abschlussbericht. Projekt OneWind (Phase 1). FKZ0325131* (Tech. Rep.). Bremerhaven: Fraunhofer-Institut für Windenergie und Energiesystemtechnik IWES. (In German) doi: 10.2314/GBV:735481504

Strobel, M., Vorpahl, F., Hillmann, C., Gu, X., Zuga, A., & Wihlfahrt, U. (2011, March). The OnWind Modelica library for offshore wind turbines — Implementation and first results. In *Proceedings of the 8th International Modelica Conference* (pp. 603–609). Dresden: Linköping University Electronic Press, Linköpings Universitet. doi: 10.3384/ecp11063603

Suarez, L. E., & Singh, M. P. (1992, December). Improved fixed interface method for modal synthesis. *AIAA Journal — American Institute of Aeronautics and Astronautics*, *30*(12), 2952–2958. doi: 10.2514/3.11642

Sun, S., Tang, X., Yang, J., Ning, D., Du, H., Zhang, S., & Li, W. (2019, August). A new generation of magnetorheological vehicle suspension system with tunable stiffness and damping characteristics. *IEEE Transactions on Industrial Informatics*, *15*(8), 4696–4708. doi: 10.1109/TII.2018.2890290

Suquet, P., Moulinec, H., Castelnau, O., Montagnat, M., Lahellec, N., Grennerat, F., . . . Brenner, R. (2012). Multi-scale modeling of the mechanical behavior of polycrystalline ice under transient creep. *Procedia IUTAM Symposium on Linking Scales in Computations: From Microstructure to Macro-scale Properties*, *3*, 76–90. doi: 10.1016/j.piutam.2012.03.006

The BACC II Author Team. (2015). *Second assessment of climate change for the Baltic Sea Basin*. Springer, Cham. doi: 10.1007/978-3-319-16006-1

Tibaldi, C., Hansen, M. H., & Henriksen, L. C. (2014, December). Optimal tuning for a classical wind turbine controller. *Journal of Physics: Conference Series*, *555*, 1–12. doi: 10.1088/1742-6596/555/1/012099

Tibaldi, C., Hansen, M. H., & Zahle, F. (2015, December). *Methods for systematic tuning of wind turbine controllers* (DTU Wind Energy E, No. 0100). Roskilde: DTU Wind Energy. Retrieved June 1, 2020, from https://orbit.dtu.dk/ws/files/118777390/Wind_Energy_E_0100.pdf

Tikanmäki, M., Jussila, V., Kurkela, J., Heinonen, J., & Marito, J. (2015, February). *Breaking the Ice (BRICE) Final Report* (VTT-R-00497-15). Espoo: VTT Technical Research Centre of Finland.

Timco, G. W., & Croasdale, K. R. (2006, August). How well can we predict ice loads? In *Proceedings of the 18th IAHR International Symposium on Ice* (Vol. 1, pp. 167–174). Sapporo: International Association for Hydro-Environment Engineering and Research. Retrieved June 1, 2020, from http://web2.clarkson.edu/projects/iahrice/IAHR%202006/contents/21_s39.pdf

Timco, G. W., Frederking, R., Kamesaki, K., & Tada, H. (1999, February). Comparison of ice load calculation algorithms for first-year ridges. In *Proceedings of International Workshop on Rational Evaluation of Ice Forces on Structures REIFS'99* (pp. 88–102). Mombetsu. Retrieved June 1, 2020, from https://nrc-publications.canada.ca/eng/view/accepted/?id=2ab9030c-b110-4ed2-8318-71522a08a55b

Timco, G. W., Irani, M. B., Tseng, J., Liu, L. K., & Zheng, C. B. (1992, October). Model tests of dynamic ice loading on the Chineses JZ-20-2 jacket platform. *Canadian Journal of Civil Engineering*, *19*(5), 819–832. doi: 10.1139/l92-093

Timco, G. W., & Weeks, W. F. (2010, February). A review of the engineering properties of sea ice. *Cold Regions Science and Technology*, *60*(2), 107–129. doi: 10.1016/j.coldregions.2009.10.003

Timoshenko, S. P. (1921). LXVI. On the correction for shear of the differential equation for transverse vibrations of prismatic bars. *The London, Edinburgh, and Dublin Philosophical Magazine and Journal of Science*, *41*(245), 744–746. doi: 10.1080/14786442108636264

Toyama, Y., Sensu, T., Minami, M., & Yashima, N. (1983, April). Model tests on ice-induced self-excited vibration of cylindrical structures. In *Proceedings of the 7th International Conference on Port and Ocean Engineering under Arctic Conditions* (Vol. 2, pp. 834–844). Helsinki. Retrieved from http://www.poac.com/Papers/POAC83_V2_all.pdf

Tran, C. T., & Petot, D. (1980, September). Semi-empirical model for the dynamic stall of airfoils in view of the application to the calculation of responses of a helicopter blade in forward flight. In *Sixth European Rotorcraft and Powered Lift Aircraft Forum* (pp. 1–23). Bristol. Retrieved June 1, 2020, from https://dspace-erf.nlr.nl/xmlui/bitstream/handle/20.500.11881/1835/ERF%201980-48.pdf?sequence=1&isAllowed=y

Tu, Y., & Vorpahl, F. (2014, June). Influence of superelement support structure modeling on the loads on an offshore wind turbine with a jacket support structure. In *Proceedings of the 24th International Offshore and Polar Engineering Conference* (Vol. 1, pp. 342–349). Busan: International Society of Offshore and Polar Engineers. Retrieved from https://www.onepetro.org/conference-paper/ISOPE-I-14-107

Tuhkuri, J., & Polojärvi, A. (2018, August). A review of discrete element simulation of ice-structure interaction. *Philosophical Transactions of the Royal Society*, *376*, 1–16. doi: 10.1098/rsta.2017.0335

Turner, M. J., Clough, R. W., Martin, H. C., & Topp, L. J. (1956, September). Stiffness and deflection analysis of complex structures. *Journal of the Aeronautical Sciences*, *23*(9), 805–823. doi: 10.2514/8.3664

Veers, P. S. (1988, March). *Three-dimensional wind simulation* (SAND88-0152 UC-261). Albuquerque, NM: Sandia National Laboratories. Retrieved June 1, 2020, from http://prod.sandia.gov/techlib/access-control.cgi/1988/880152.pdf

von Kármán, T. (1948, November). Progress in the statistical theory of turbulence. *Proceedings of the National Academy of Sciences*, *34*(11), 530–539. doi: 10.1073/pnas.34.11.530

Vorpahl, F., & Popko, W. (2014, October). An overview of current aero-elastic design tools — Benefits and limitations. In *Windpower Monthly: Future Offshore Foundations Forum 2014.* Hamburg. (PowerPoint presentation)

Vorpahl, F., Schwarze, H., Fischer, T., Seidel, M., & Jonkman, J. (2013, September). Offshore wind turbine environment, loads, simulation, and design. *Wiley Interdisciplinary Reviews: Energy and Environment*, *2*(5), 548–570. doi: 10.1002/wene.52

Vorpahl, F., Strobel, M., Jonkman, J. M., Larsen, T. J. L., Passon, P., & Nichols, J. (2014, April). Verification of aero-elastic offshore wind turbine design codes under IEA Wind Task XXIII. *Wind Energy*, *17*(4), 519–547. doi: 10.1002/we.1588

Vorpahl, F., van Wingerde, A., Blunk, M., Busmann, H.-G., Kleinhansl, S., Kossel, T., ... Munduate, X. (2009, June). Validation of a finite element based simulation approach for offshore wind turbines within IEA Wind Annex XXIII — Simulation challenges and results for a 5-MW turbine on a tripod substructure. In *Proceedings of the 19th International Offshore and Polar Engineering Conference* (Vol. 1, pp. 362–369). Osaka: International Society of Offshore and Polar Engineers. Retrieved June 1, 2020, from https://www.onepetro.org/conference-paper/ISOPE-I-09-411

VSN. (1988). ВСН 41.88 Проектирование морских ледостойких стационарных платформ [*VSN 41.88 Design of ice resistant stationary platforms*]. Москва [Moscow]: Министерство нефтяной промышленности СССР [Ministry of Petroleum Industry of the USSR]. (In Russian)

Wada, B. K., Bamford, R., & Garba, J. A. (1972, January). Equivalent spring-mass system: A physical interpretation. In *The Shock and Vibration Bulletin* (Vol. 42, pp. 214–225). Washington, DC: The Shock and Vibration Information Center. Naval Research Laboratory. Retrieved June 1, 2020, from https://apps.dtic.mil/dtic/tr/fulltext/u2/739578.pdf

Wang, W., Hua, X., Wang, X., Wu, J., Sun, H., & Song, G. (2019, January). Mechanical behavior of magnetorheological dampers after long-term operation in a cable vibration control system. *Structural Control and Health Monitoring*, *26*(1), 1–19. doi: 10.1002/stc.2280

Wessels, E., & Jochmann, P. (1991, September). Model/full scale correlation of ice forces on a jacket platform in Bohai Bay. In *Proceedings of the 11th International Conference on*

Port and Ocean Engineering under Arctic Conditions (Vol. 1, pp. 198–212). St. John's, NF. Retrieved June 1, 2020, from http://www.poac.com/Papers/POAC91_V1_all.pdf

Westendarp, E. (2016, April). *Pinwheel-offshore-wadden-sea-watts.* Retrieved June 1, 2020, from https://pixabay.com/photos/pinwheel-offshore-wadden-sea-watts-1317817/ (Pixabay License terms: Free for commercial use, no attribution required)

Wheeler, J. D. (1969, May). Method for calculating forces produced by irregular waves. In *Preprints 1969 Offshore Technology Conference* (Vol. I, pp. 83–94). Houston, TX: Offshore Technology Conference. doi: 10.4043/1006-MS

Wihlfahrt, U., Hillmann, C., Samlaus, R., & Thomas, P. (2015, February). *Schlussbericht. Projekt OneWind (Phase 2). FKZ0325131A* (Tech. Rep.). Bremerhaven: Fraunhofer-Institut für Windenergie und Energiesystemtechnik IWES. (In German) doi: 10.2314/GBV:848363280

Willems, T., & Hendrikse, H. (2019, June). Coupled simulation of ice-structure interaction of offshore wind turbines in BHawC using VANILLA. In *Proceedings of the 25th International Conference on Port and Ocean Engineering under Arctic Conditions.* Delft. Retrieved June 1, 2020, from https://www.poac.com/Papers/2019/pdf/POAC19-110.pdf

Withalm, M., & Hoffmann, N. P. (2010, February). Simulation of full-scale ice-structure-interaction by an extended Matlock-model. *Cold Regions Science and Technology*, *60*(2), 130–136. doi: 10.1016/j.coldregions.2009.09.006

Wolowicz, C. H., Bowman, J. S., & Gilbert, W. P. (1979, August). *Similitude requirements and scaling relationships as applied to model testing* (NASA Technical Paper 1435). National Aeronautics and Space Administration. Retrieved June 1, 2020, from https://ntrs.nasa.gov/archive/nasa/casi.ntrs.nasa.gov/19790022005.pdf

Wright, B. D., & Timco, G. W. (1994, August). A review of ice forces and failure modes on the Molikpaq. In *Proceedings of the 12th IAHR International Symposium on Ice* (Vol. 2, pp. 816–825). Trondheim: International Association for Hydro-Environment Engineering and Research. Retrieved June 1, 2020, from https://www.iahr.org/index/club/14

Yu, B., Karr, D. G., & Sirnivas, S. (2014, June). Ice nonsimultaneous failure, bending and floe impact modeling for simulating wind turbine dynamics using FAST. In *Proceedings of the ASME 2014 33rd International Conference on Ocean, Offshore and Arctic Engineering* (Vol. 10). San Francisco, CA: American Society of Mechanical Engineers. doi: 10.1115/OMAE2014-24320

Yu, B., Karr, D. G., Song, H., & Sirnivas, S. (2013, June). A surface ice module for wind turbine dynamic response simulation using FAST. In *Proceedings of the 32nd International Conference on Ocean, Offshore and Arctic Engineering* (Vol. 8). Nantes: American Society of Mechanical Engineers. doi: 10.1115/OMAE2013-11179

Zhang, N., Zheng, X., Ma, Q., & Hao, H. (2017, June). Numerical simulation of failure progress of ice using smoothed particle hydrodynamics. In *Proceedings of the 27th International Ocean and Polar Engineering Conference* (pp. 1305–1310). San Francisco, CA: International Society of Offshore and Polar Engineers. Retrieved June 1, 2020, from https://www.onepetro.org/conference-paper/ISOPE-I-17-277

Zhang, Y., Remmers, T. C., Yu, B., & Karr, D. G. (2016, May). Nonlinear contact dynamic response simulation of Matlock's ice-structure interaction model using Fourier analysis. In *Proceedings of the 23rd IAHR International Symposium on Ice.* Ann Arbor, MI: International Association for Hydro-Environment Engineering and Research.

Zhang, Y., & Yu, B. (2018, November). An ice-structure interaction model using Fourier series for offshore wind tower analysis. In *Proceedings of ASME 2018 1st International Offshore Wind Technical Conference.* San Francisco, CA: American Society of Mechanical Engineers. doi: 10.1115/IOWTC2018-1074

Ziemer, G. (2017, September). *Research Project IVOS — Ice-induced Vibrations of Offshore Structures* (Tech. Rep.). Hamburg: Hamburgische Schiffbau-Versuchsanstalt. Retrieved June 1, 2020, from https://www.researchgate.net/publication/320082967_IVOS_Project_Description

Ziemer, G., & Evers, K.-U. (2014, June). Ice model tests with a compliant cylindrical structure to investigate ice-induced vibrations. In *Proceedings of the 33rd International Conference on Ocean, Offshore and Arctic Engineering* (Vol. 10). San Francisco, CA: American Society of Mechanical Engineers. doi: 10.1115/OMAE2014-24011

Appendix A

MATLAB® code listings

A.1 Main function for modal structure

```
function [parMod, parStr] = modal_Structure
%% FUNCTIONALITY
% - Assembles beam element mass and stiffness matrices. Euler-Bernoulli and
%   Timoshenko 3D beam elements of 12x12 size are included
% - Assembles global mass and stiffness matrices of support structure
% - Applies point mass and inertia at an arbitrary node of structure
% - Applies boundary conditions and rotates the coordinates of foundation
% - Removes unwanted nodal DOFs from global mass and stiffness matrices
% - Eigenanalysis and modal reduction
% - Plots eigenmodes and frequencies

% AUTHOR
% Wojciech Popko
% Fraunhofer Institute for Wind Energy Systems IWES
% Am Luneort 100, 27572 Bremerhaven, Germany

%% READ STRUCTURAL AND GEOMETRICAL PROPERTIES
Def_structure_final         % Support structure
Def_foundation_final        % Foundation

%% USER INPUTS
% 0 = compliant structure, 1 = rigid structure. In case of a rigid
% structure the structure is fixed in the model and initial conditions
% are automatically set to zero.
parStr.rigid      = 0;

% Select beam element model: 1 = Euler-Bernoulli, 2 = Timoshenko
beamType          = 2;

```

```
% Select boundary conditions: 0 = rigid foundation, 1 = flexible foundation
parStr.boundary = 0;

% Select a number of eigenmodes for the modal analysis and modal reduction
% of the support structure
parMod.nModes    = 9;
modeStart        = 1;

% Vector with nodal DOFs, which can be optionally switched off:
% 1 - x (axial), 2 - y (side-to-side), 3 - z (fore-aft)
% 4 - theta_x (torsion)
% 5 - theta_y (fore-aft rotation)
% 6 - theta_z (side-to-side rotation)
% Example: parMod.DOFs_off = [] means that all local DOFs are included, if
% parMod.DOFs_off = [1,4] means that axial and torsional DOFs are off.
% parMod.DOFs_off = [1,3,4,5];
% parMod.DOFs_off = [1,4];
parMod.DOFs_off = [];

%% DERIVED PARAMETERS
% Number of beam elements in support structure
parMod.Nel      = length(parStr.L);

% Number of nodes in support structure
parMod.Nodes    = parMod.Nel + 1;

% Number of DOFs per single node
parMod.NodeDOFs    =  6;

% Number of global DOFs in support structure
parMod.DOFs = parMod.Nodes*parMod.NodeDOFs;

%% ASSEMBLY OF ELEMENT MASS AND STIFFNESS MATRICES
% Initialization of element matrices
ke = zeros(2*parMod.NodeDOFs,2*parMod.NodeDOFs,parMod.Nel);
me = zeros(2*parMod.NodeDOFs,2*parMod.NodeDOFs,parMod.Nel);

for k = 1:parMod.Nel
    if beamType == 1
        [ke_temp, me_temp] = element_matrix_EulerBernoulli(parStr.E(k),...
            parStr.G(k),parStr.rho(k),parStr.L(k),parStr.A(k),...
            parStr.Ixx(k),parStr.Iyy(k),parStr.Izz(k));
    elseif beamType == 2
```

```
        [ke_temp, me_temp] = element_matrix_Timoshenko(parStr.E(k),...
            parStr.G(k),parStr.rho(k),parStr.L(k),parStr.A(k),...
            parStr.ASy(k),parStr.ASy(k),...
            parStr.Ixx(k),parStr.Iyy(k),parStr.Izz(k));
    end

    ke(:,:,k) = ke_temp;
    me(:,:,k) = me_temp;
end

%% ASSEMBLY OF GLOBAL MASS AND STIFFNESS MATRICES
[K, M] = assemble_global_matrix(ke,me,parMod.Nel);

%% ADD POINT MASSES AND INERTIA AT SPECIFIED STRUCTURAL NODES

% 6900 kg (mass of TP anodes) at node no 8 located at MSL -2.1 m
node_p_Mass = 8;
p_Mass      = 6900;            % [kg]
p_Inertia   = zeros(3);        % [-]
p_Offset    = [0, 0, 0];       % [m]
[M] = include_point_mass(M,p_Mass,p_Inertia,p_Offset,node_p_Mass);

% 18900 kg (mass of MP-TP flange) at node 12 located at MSL +2.5 m
node_p_Mass = 12;
p_Mass      = 18900;           % [kg]
p_Inertia   = zeros(3);        % [-]
p_Offset    = [0, 0, 0];       % [m]
[M] = include_point_mass(M,p_Mass,p_Inertia,p_Offset,node_p_Mass);

% 2500 kg (mass of upper work platform) at node 15 located at MSL +11.3 m
node_p_Mass = 15;
p_Mass      = 2500;            % [kg]
p_Inertia   = zeros(3);        % [-]
p_Offset    = [0, 0, 0];       % [m]
[M] = include_point_mass(M,p_Mass,p_Inertia,p_Offset,node_p_Mass);

% 25000 kg (mass of external platform) at node 16 located at MSL +12.29 m
node_p_Mass = 16;
p_Mass      = 25000;           % [kg]
p_Inertia   = zeros(3);        % [-]
p_Offset    = [0, 0, 0];       % [m]
[M] = include_point_mass(M,p_Mass,p_Inertia,p_Offset,node_p_Mass);

```

```
% 7100 kg (mass of TP-tower flange) at node 17 located at MSL +12.5 m
node_p_Mass = 17;
p_Mass      = 7100;           % [kg]
p_Inertia   = zeros(3);       % [-]
p_Offset    = [0, 0, 0];      % [m]
[M] = include_point_mass(M,p_Mass,p_Inertia,p_Offset,node_p_Mass);

% Rotor-nacelle assembly mass and inertia attached at tower top MSL +98.5 m
node_p_Mass = length(K)/parMod.NodeDOFs;      % The last node (Tower top)
p_Mass      = 536780;         % [kg] Nacelle + Rotor + Generator
p_Inertia   = zeros(3);       % [-]
p_Offset    = [3.05, 0, 0];   % [m] Nacelle CoG
%                                   x- vertical offset from tower top
%                                   y- horizontal offset side-to-side
%                                   z- horizontal offset fore-aft
[M] = include_point_mass(M,p_Mass,p_Inertia,p_Offset,node_p_Mass);

% Global damping matrix
C = 2*parStr.ksi*sqrt(abs(M.*K));

%% BOUNDARY CONDITIONS - FOUNDATION FLEXIBILITY
Rx = rotx(0);                 % [deg] Rotation about x-axis
Ry = roty(90);                % [deg] Rotation about y-axis
Rz = rotz(0);                 % [deg] Rotation about z-axis

T = Rx*Ry*Rz;
M_foundation=T'*M_Ramboll*T;  % Rotation of the foundation mass matrix
C_foundation=T'*C_Ramboll*T;  % Rotation of the foundation damping matrix
K_foundation=T'*K_Ramboll*T;  % Rotation of the foundation stiffness matrix

[M, C, K] = include_boundary_conditions(M, C, K,...
    M_foundation, C_foundation, K_foundation, parStr.boundary);

%% ELIMINATING UNWANTED DOFs FROM GLOBAL MATRICES (OPTIONAL)
M = remove_DOFs(M,parMod.DOFs_off); % Global mass matrix
C = remove_DOFs(C,parMod.DOFs_off); % Global damping matrix
K = remove_DOFs(K,parMod.DOFs_off); % Global stiffness matrix

% Number of global DOFs in support structure after elimination of
% unwanted DOFs
parMod.DOFs          = length(M);

% Number of DOFs in a single node after elimination of unwanted DOFs
```

```
parMod.NodeDOFs    = parMod.NodeDOFs - length(parMod.DOFs_off);

%% GENERALIZED EIGENVALUE PROBLEM
%   Returns diagonal matrix parMod.D of generalized eigenvalues
%   and full matrix parMod.S whose columns are the corresponding right
%   eigenvectors. The displacements are represented in terms of
%   the modeshapes. For this purpose the modeshape vectors are ordered as
%   columns in the DOFs x DOFs matrix parMod.S.

[parMod.S,parMod.D] = eig(K,M);

parMod.S=parMod.S(1:parMod.DOFs,modeStart:parMod.nModes);
parMod.D=parMod.D(modeStart:parMod.nModes,modeStart:parMod.nModes);

parMod.nModes = length(modeStart:parMod.nModes);

% Eigenfrequencies
parMod.omega = sqrt(diag(parMod.D));                    % [rad/s]
parMod.f = parMod.omega./(2*pi);                        % [Hz]

disp('Eigenfrequencies [Hz]')
parMod.f

% Modal mass and stiffness matrix
parMod.mm = parMod.S'*M*parMod.S;
parMod.km = parMod.S'*K*parMod.S;

% Modal damping matrix
parMod.cm = 2*parStr.ksi*sqrt(abs(parMod.mm.*parMod.km));

% Initial modal displacement and velocity
parMod.r0       = zeros(parMod.nModes,1);
parMod.s0       = zeros(parMod.nModes,1);

% Modal loading vector
parMod.f0       = ones(parMod.nModes,1)/parMod.nModes;

if parStr.boundary == 0
% Node at which the ice load will be applied in case of RIGID Foundation
    parMod.pLoad    = parMod.NodeDOFs*9-4;      % at MSL
    % parMod.pLoad    = parMod.NodeDOFs*16-4;   % at MSL+12.5 m
    % parMod.pLoad    = length(K) - 4;          % at Tower top
elseif parStr.boundary ==1
```

```
% Node at which the ice load will be applied in case of FLEXIBLE Foundation
    parMod.pLoad    = parMod.NodeDOFs*10-4;      % at MSL
    % parMod.pLoad   = parMod.NodeDOFs*17-4;     % at MSL+12.5 m
    % parMod.pLoad   = length(K) - 4;            % at Tower top
end

% [m]   Structure width or width of ice-structure contact zone
parStr.d_struc = 7.3;

%% EFFECTIVE MODAL MASS
% The influence matrix, which represents the displacements of the masses
% resulting from static application of unit ground displacements and rotations
    .
rx = zeros(length(M));
ry = zeros(length(M));
rz = zeros(length(M));
for i = 1:6:length(M)
    rx(i,i) = 1;
    ry(i+1,i+1) =1;
    rz(i+2,i+2) =1;
end

for j = 1:parMod.nModes
    L_mx(j) = parMod.S(:,j)'* M * diag(rx);
    L_my(j) = parMod.S(:,j)'* M * diag(ry);
    L_mz(j) = parMod.S(:,j)'* M * diag(rz);
    m_eff_x(j) = L_mx(j)^2 / parMod.mm(j,j);
    m_eff_y(j) = L_my(j)^2 / parMod.mm(j,j);
    m_eff_z(j) = L_mz(j)^2 / parMod.mm(j,j);

    % Modal participation factor is indicative of how a particular mode
    % responds to ground vibration
    gamma_x(j) = L_mx(j) / parMod.mm(j,j);
    gamma_y(j) = L_my(j) / parMod.mm(j,j);
    gamma_z(j) = L_mz(j) / parMod.mm(j,j);
end

%% PLOT EIGENMODES
plot_eigenmodes
end
```

A.2 Structural and geometrical properties of monopile support structure

```
%% DEFINITION OF THE OFFSHORE SUPPORT STRUCTURE
% The monopile offshore support structure was designed by Ramboll GmbH
% within the SeaLOWT project (Impact of Sea Ice Loads on Global Dynamics
% of Offshore Wind Turbines, FKZ 0324022B).
%
% This script was prepared based on the Ramboll design data and consists
% the following:
% - Support structure geometrical and structural properties
% Those properties are part of the IWT-7.5-164 Rev4 report and can be found
% in https://doi.org/10.24406/IWES-N-518562

% COORDINATE SYSTEM
% x - Along the element central axis (pointing verticaly upward in case of
%     the monopile support structure)
% y - Side-to-side (in horizontal plane)
% z - Fore-aft (in horizontal plane)

% AUTHOR
% Wojciech Popko
% Fraunhofer Institute for Wind Energy Systems IWES
% Am Luneort 100, 27572 Bremerhaven, Germany

% [-]   Structural damping as a fraction of critical
parStr.ksi      = 0.0105;

%% Definition of member structutral and geometrical properties
% Member length            [m]
parStr.L = [
2.50 3.11 10.50 7.00 6.00 2.59 1.20 1.60 0.50 2.20 0.30 3.10 3.18 2.52...
0.99 0.21 1.00 1.00 1.00 1.00 1.00 1.00 1.00 1.00 1.00 1.00 1.00 1.00...
1.00 1.00 1.00 1.00 1.00 1.00 1.00 1.00 1.00 1.00 1.00 1.00 1.00 1.00...
1.00 1.00 1.00 1.00 1.00 1.00 1.00 1.00 1.00 1.00 1.00 1.00 1.00 1.00...
1.00 1.00 1.00 1.00 1.00 1.00 1.00 1.00 1.00 1.00 1.00 1.00 1.00 1.00...
1.00 1.00 1.00 1.00 1.00 1.00 1.00 1.00 1.00 1.00 1.00 1.00 1.00 1.00...
1.00 1.00 1.00 1.00 1.00 1.00 1.00 1.00 1.00 1.00 1.00 1.00 1.00 1.00...
1.00 1.00 1.00 1.00];

% Member radius            [m]
```

```
parStr.R = [
7.75 7.75 7.75 7.75 7.49 7.11 7.00 7.00 7.00 7.00 7.00 7.00 7.00 7.00...
7.00 7.00 7.00 7.00 7.00 7.00 7.00 7.00 7.00 7.00 7.00 7.00 7.00 7.00...
7.00 7.00 7.00 7.00 7.00 7.00 7.00 7.00 7.00 7.00 7.00 7.00 7.00 7.00...
6.97 6.90 6.83 6.77 6.70 6.63 6.57 6.50 6.43 6.37 6.30 6.23 6.17 6.10...
6.03 5.97 5.90 5.83 5.77 5.70 5.63 5.57 5.50 5.43 5.37 5.30 5.23 5.17...
5.10 5.03 4.97 4.90 4.83 4.77 4.70 4.63 4.57 4.50 4.43 4.37 4.30 4.23...
4.17 4.10 4.03 3.97 3.90 3.83 3.77 3.70 3.63 3.57 3.50 3.43 3.37 3.30...
3.23 3.17 3.10 3.03]/2;

%Member thickness        [m]
parStr.t = [
90.00 95.00 75.00 70.00 70.00 75.00 75.00 75.00 80.00 80.00 80.00 80.00...
95.00 75.00 75.00 75.00 34.90 34.85 34.75 34.60 34.45 34.35 34.25 34.15...
34.05 33.90 33.75 33.65 33.55 33.45 33.35 33.20 33.05 32.95 32.85 32.75...
32.65 32.50 32.35 32.25 32.15 32.05 31.95 31.80 31.65 31.55 31.45 31.35...
31.25 31.10 30.95 30.85 30.75 30.65 30.55 30.40 30.25 30.15 30.05 29.95...
29.85 29.75 29.60 29.45 29.35 29.25 29.15 29.05 28.90 28.75 28.65 28.55...
28.45 28.35 28.20 28.05 27.95 27.85 27.75 27.65 27.50 27.35 27.25 27.15...
27.05 26.95 26.80 26.65 26.55 26.45 26.35 26.25 26.10 25.95 25.85 25.75...
25.65 25.55 25.40 25.25 25.15 25.05]/1000;

parStr.Length = length(parStr.L);
for i = 1: length(parStr.L)
    parStr.Length(i) = sum(parStr.L(1:i));
end

% Second moment of inertia   [m^4]
parStr.Ixx = pi/2*(parStr.R.^4-(parStr.R-parStr.t).^4);
parStr.Iyy = pi/4*(parStr.R.^4-(parStr.R-parStr.t).^4);
parStr.Izz = pi/4*(parStr.R.^4-(parStr.R-parStr.t).^4);

% Torsional constant         [m^4]
parStr.It = 2/3*pi*parStr.R.*parStr.t.^3;

% Effective area of shear for thin wall circular cross-section
parStr.ASy = pi*(parStr.R-parStr.t/2).*parStr.t;
parStr.ASz = parStr.ASy;

% Member cross-section area  [m^2]
parStr.A   = pi.*(parStr.R.^2-(parStr.R-parStr.t).^2);

% Young's modulus            [N/m^2]
```

```
parStr.E          = ones(1,length(parStr.L));
parStr.E(1:6)     = 2.10E+11;      % MP_a
parStr.E(7)       = 2.10E+11;      % MP_Skirt1
parStr.E(8:10)    = 2.10E+11;      % MP_Skirt2
parStr.E(11:15)   = 2.10E+11;      % TP
parStr.E(16:end)  = 2.10E+11;      % Tower

% Poisson's ratio
nu = 0.3;

% Shear modulus                  [N/m^2]
parStr.G    = ones(1,length(parStr.L))*(2.10E+11/(2*(1+nu)));

% Material density               [kg/m^3]
parStr.rho          = ones(1,length(parStr.L));
parStr.rho(1:6)     = 7890;      % MP_a
parStr.rho(7)       = 11667;     % MP_Skirt1
parStr.rho(8:11)    = 11713;     % MP_Skirt2
parStr.rho(12:16)   = 8092;      % TP
parStr.rho(17:end)= 7850;        % Tower

% Mass of the support structure (excluding point masses which are added
% later)
parStr.M_tot      = sum(parStr.rho.*parStr.A.*parStr.L);
parStr.M_MP       = sum(parStr.rho(1:11).*parStr.A(1:11).*parStr.L(1:11));
parStr.M_TP       = sum(parStr.rho(12:16).*parStr.A(12:16).*parStr.L(12:16));
parStr.M_tower    = sum(parStr.rho(17:end).*parStr.A(17:end).*parStr.L(17:end));
```

A.3 Foundation mass, damping, and stiffness matrices

```
%% DEFINITION OF THE FOUNDATION MATRICES
% The foundation matrices were provided by Ramboll GmbH for the final
% design of the offshore support structure within the SeaLOWT project
% (Impact of Sea Ice Loads on Global Dynamics of Offshore Wind Turbines
% FKZ 0324022B).
% This script was prepared based on the Ramboll design data and consists
% the following:
% - Foundation mass and stiffness matrices 6x6 in ROSAP coordinate system.

% COORDINATE SYSTEM IN ROSA:
% - x - in horizontal plane pointing towards North
% - y - in horizontal plane pointing towards West
```

```
% - z - points vertically upward

% AUTHOR
% Wojciech Popko
% Fraunhofer Institute for Wind Energy Systems IWES
% Am Luneort 100, 27572 Bremerhaven, Germany

%% Mass and stiffness matrices for foundation in the ROSA coordinate system
% It would be necessary to rotate them in order to comply with
% the coordinate system used in the MATLAB script "modal_Structure".

M_Ramboll =[...
1.4439E+05  0           0           0           -5.1785E+05  0;
0           1.4439E+05  0           5.1785E+05  0            0;
0           0           4.3652E+05  0           0            0;
0           5.1785E+05  0           2.7459E+06  0            0;
-5.1785E+05 0           0           0           2.7459E+06   0;
0           0           0           0           0            5.9848E+06];

K_Ramboll =[...
1.61E+09    0           0           0           -1.8234E+10  0;
0           1.61E+09    0           1.8234E+10  0            0;
0           0           7.74E+09        0           0            0;
0           1.8234E+10  0           3.40E+11    0            0;
-1.8234E+10     0           0           0           3.40E+11     0;
0           0           0           0           0            1.34E+10];

C_Ramboll = zeros(6,6);
```

A.4 Mass and stiffness matrices for Euler-Bernoulli beam element

```
function [ke, me] = element_matrix_EulerBernoulli(E,G,rho,L,A,Ixx,Iyy,Izz)
% Euler-Bernoulli mass and stiffness matrices for a 3D beam element with
% 2 nodes and 6 DOFs per each node
%
% INPUTS
% - E   - [N/m^2]   Young's modulus of the element
% - G   - [N/m^2]   Shear modulus of the element
% - rho - [kg/m^3]  Material density of the element
% - L   - [m]       Element length
```

```
% - A   - [m^2]     Element cross-sectional area
% - Ixx - [m^4]     Second moment of area (polar moment of inertia)
% - Iyy - [m^4]     Second moment of area with respect to the y-axis
% - Izz - [m^4]     Second moment of area with respect to the z-axis
% OUTPUTS
% - ke  - [-]       Element stiffness matrix,   size (12x12)
% - me  - [-]       Element mass matrix,        size (12x12)
%
% LOCAL COORDINATE SYSTEM OF THE BEAM ELEMENT
% - x-axis points along the beam element from node 1 to node 2
% - y- and z-axis parallel to the beam element cross-section

% AUTHOR
% Wojciech Popko
% Fraunhofer Institute for Wind Energy Systems IWES
% Am Luneort 100, 27572 Bremerhaven, Germany

a   = L/2;      % [m]
r2  = Ixx/A;    % [m^2]

%% ---------- Element mass and stiffness matrices -------------------------
% Element mass matrix
m = zeros(12);
m(1,1)      = 70;               % [kg]
m(2,2)      = 78;               % [kg]
m(3,3)      = 78;               % [kg]
m(4,4)      = 78*r2;            % [kg m^2]
m(5,5)      = 8*a^2;            % [kg m^2]
m(6,6)      = 8*a^2;            % [kg m^2]
m(7,7)      = 70;               % [kg]
m(8,8)      = 78;               % [kg]
m(9,9)      = 78;               % [kg]
m(10,10)    = 78*r2;            % [kg m^2]
m(11,11)    = 8*a^2;            % [kg m^2]
m(12,12)    = 8*a^2;            % [kg m^2]
m(1,7)      =  35;              % [kg]
m(2,6)      =  22*a;            % [kg m]
m(2,8)      =  27;              % [kg]
m(2,12)     = -13*a;            % [kg m]
m(3,5)      = -22*a;            % [kg m]
m(3,9)      =  27;              % [kg]
m(3,11)     =  13*a;            % [kg m]
m(4,10)     = -35*r2;           % [kg m^2]
```

```
m(5,9)      = -13*a;            % [kg m]
m(5,11)     = -6*a^2;           % [kg m^2]
m(6,8)      =  13*a;            % [kg m]
m(6,12)     = -6*a^2;           % [kg m^2]
m(8,12)     = -22*a;            % [kg m]
m(9,11)     =  22*a;            % [kg m]
m = m.*rho*A*a/105;

% Mirroring mass matrix along the diagonal
me = (m+m') - eye(size(m,1)).*diag(m);

% Element stiffness matrix
k = zeros(12);
k(1,1)      = A*E/(2*a);             % [N/m]     Axial stiffness
k(2,2)      = 3*E*Izz/(2*a^3);       % [N/m]
k(3,3)      = 3*E*Iyy/(2*a^3);       % [N/m]
k(4,4)      = G*Ixx/(2*a);           % [Nm]      Torsional stiffness
k(5,5)      = 2*E*Iyy/a;             % [Nm]
k(6,6)      = 2*E*Izz/a;             % [Nm]
k(7,7)      = A*E/(2*a);             % [N/m]     Axial stiffness
k(8,8)      = 3*E*Izz/(2*a^3);       % [N/m]
k(9,9)      = 3*E*Iyy/(2*a^3);       % [N/m]
k(10,10)    = G*Ixx/(2*a);           % [Nm]      Torsional stiffness
k(11,11)    = 2*E*Iyy/a;             % [Nm]
k(12,12)    = 2*E*Izz/a;             % [Nm]
k(1,7)      = -A*E/(2*a);            % [N/m]     Axial stiffness
k(2,6)      =  3*E*Izz/(2*a^2);      % [N]
k(2,8)      = -3*E*Izz/(2*a^3);      % [N/m]
k(2,12)     =  3*E*Izz/(2*a^2);      % [N]
k(3,5)      = -3*E*Iyy/(2*a^2);      % [N]
k(3,9)      = -3*E*Iyy/(2*a^3);      % [N/m]
k(3,11)     = -3*E*Iyy/(2*a^2);      % [N]
k(4,10)     = -G*Ixx/(2*a);          % [Nm]      Torsional stiffness
k(5,9)      =  3*E*Iyy/(2*a^2);      % [N]
k(5,11)     =  E*Iyy/a;              % [Nm]
k(6,8)      = -3*E*Izz/(2*a^2);      % [N]
k(6,12)     =  E*Izz/a;              % [Nm]
k(8,12)     = -3*E*Izz/(2*a^2);      % [N]
k(9,11)     =  3*E*Iyy/(2*a^2);      % [N]

% Mirroring stiffness matrix along the diagonal
ke = (k+k') - eye(size(k,1)).*diag(k);
end
```

A.5 Mass and stiffness matrices for Timoshenko beam element

```
function [ke, me] = element_matrix_Timoshenko(E,G,rho,L,A,ASy,ASz,Ixx,Iyy,Izz)
% Timoshenko mass and stiffness matrices for a 3D beam element with
% 2 nodes and 6 DOFs per each node
%
% INPUTS
% - E   - [N/m^2]   Young's modulus of the element
% - G   - [N/m^2]   Shear modulus of the element
% - rho - [kg/m^3]  Material density of the element
% - L   - [m]       Element length
% - A   - [m^2]     Member cross-sectional area
% - ASy - [m^2]     Effective area of shear for thin wall circular
%                   cross-section
% - ASz - [m^2]     Effective area of shear for thin wall circular
%                   cross-section
% - Ixx - [m^4]     Second moment of area (polar moment of inertia)
% - Iyy - [m^4]     Second moment of area with respect to the y-axis
% - Izz - [m^4]     Second moment of area with respect to the z-axis
% OUTPUTS
% - ke  - [-]       Element stiffness matrix,   size (12x12)
% - me  - [-]       Element mass matrix,        size (12x12)
%
% LOCAL COORDINATE SYSTEM OF THE BEAM ELEMENT
% - x-axis points along the beam element from node 1 to node 2
% - y- and z-axis parallel to the beam element cross-section

% AUTHOR
% Wojciech Popko
% Fraunhofer Institute for Wind Energy Systems IWES
% Am Luneort 100, 27572 Bremerhaven, Germany

%% ---------- Parameters ------------------------------------------
m = L*A*rho; % [kg]  Element mass

%% ---------- Physical quantities ----------------------------------
Py = 12*E*Izz/(G*ASy*L^2); % [-] Relative importance of the shear
%                                deformations to the bending deformations
Pz = 12*E*Iyy/(G*ASz*L^2); % [-] Relative importance of the shear
%                                deformations to the bending deformations
```

```

%% ---------- Element mass and stiffness matrices ------------------------------
% Element mass matrix
m11 = zeros(6,6);
m11(1,1) = 1/3;                        % [kg]
m11(2,2) = 13/35 + 6*Izz/(5*A*L^2);    % [kg]
m11(3,3) = 13/35 + 6*Iyy/(5*A*L^2);    % [kg]
m11(4,4) = Ixx/(3*A);                  % [kg m^2]
m11(5,5) = L^2/105 + 2*Iyy/(15*A);     % [kg m^2]
m11(6,6) = L^2/105 + 2*Izz/(15*A);     % [kg m^2]
m11(6,2) = 11*L/210 + Izz/(10*A*L);    % [kg m]
m11(2,6) = m11(6,2) ;                  % [kg m]
m11(5,3) = -11*L/210 - Iyy/(10*A*L);   % [kg m]
m11(3,5) = m11(5,3) ;                  % [kg m]
m22 = -m11 + 2*diag(diag(m11));        % [kg]

m21 = zeros(6,6);
m21(1,1) = 1/6;                        % [kg]
m21(2,2) = 9/70 - 6*Izz/(5*A*L^2);     % [kg]
m21(3,3) = 9/70 - 6*Iyy/(5*A*L^2);     % [kg]
m21(4,4) = Ixx/(6*A);                  % [kg m^2]
m21(5,5) = -L^2/140 - Iyy/(30*A);      % [kg m^2]
m21(6,6) = -L^2/140 - Izz/(30*A);      % [kg m^2]
m21(6,2) = -13*L/420 + Izz/(10*A*L);   % [kg m]
m21(2,6) = -m21(6,2);                  % [kg m]
m21(5,3) = 13*L/420 - Iyy/(10*A*L);    % [kg m]
m21(3,5) = -m21(5,3);                  % [kg m]

me = m*[m11, m21'; m21, m22];

% Element stiffness matrix
k11 = zeros(6,6);
k11(1,1) = E*A/L ;                     % [N/m]    Axial stiffness
k11(2,2) = 12*E*Izz/(L^3*(1+Py)) ;     % [N/m]
k11(3,3) = 12*E*Iyy/(L^3*(1+Pz)) ;     % [N/m]
k11(4,4) = G*Ixx/L ;                   % [Nm]     Torsional stiffness
k11(5,5) = (4+Pz)*E*Iyy/(L*(1+Pz)) ;   % [Nm]
k11(6,6) = (4+Py)*E*Izz/(L*(1+Py)) ;   % [Nm]
k11(2,6) = 6*E*Izz/(L^2*(1+Py)) ;      % [N]
k11(6,2) = k11(2,6) ;                  % [N]
k11(3,5) = -6*E*Iyy/(L^2*(1+Pz)) ;     % [N]
k11(5,3) = k11(3,5) ;                  % [N]
k22 = -k11 + 2*diag(diag(k11));
```

```
k21 = k11 - 2*diag(diag(k11));
k21(5,5) = (2-Pz)*E*Iyy/(L*(1+Pz)) ;      % [Nm]
k21(6,6) = (2-Py)*E*Izz/(L*(1+Py)) ;      % [Nm]
k21(2,6) = -k21(6,2);
k21(3,5) = -k21(5,3);

ke = [k11, k21'; k21, k22];
end
```

A.6 Assembly of global mass and stiffness matrices

```
function [K, M] = assemble_global_matrix(ke,me,nel)
% This function assembles global mass and stiffness matrices for a monopile
% support structure created from Euler-Bernoulli or Timoshenko beam elements
%
% INPUTS
% - ke       - [-]   Element stiffness matrix,    size (12,12,nel)
% - me       - [-]   Element mass matrix,         size (12,12,nel)
% - nel      - [-]   Number of elements in the entire support structure
% OUTPUTS
% - K        - [-]   Global stiffness matrix,     size (DOFs,DOFs)
% - M        - [-]   Global mass matrix,          size (DOFs,DOFs)

% AUTHOR
% Wojciech Popko
% Fraunhofer Institute for Wind Energy Systems IWES
% Am Luneort 100, 27572 Bremerhaven, Germany

%% GLOBAL MASS AND STIFFNESS MATRICES ASSEMBLY
% Number of available DOFs per single node in the beam element matrix
ndfpn = length(ke(:,:,1))/2;

% Number of nodes in the support structure consisting of nel elements
nodes = nel + 1;

% Number of global DOFs in the support structure
DOFs  = nodes*ndfpn;

% Global matrices - size allocation
M = zeros(DOFs);
K = zeros(DOFs);

```

```
% Assembly of global mass and stiffness matrices for a monopile support
% structure
for k=1:nel                % going through all elements in the structure
    for i=1:ndfpn*2        % going through all DOFs in 2 nodes of the element
        for j=1:ndfpn*2    % going through all DOFs in 2 nodes of the element
            M((k-1)*ndfpn+i,(k-1)*ndfpn+j) =...
                M((k-1)*ndfpn+i,(k-1)*ndfpn+j) + me(i,j,k);
            K((k-1)*ndfpn+i,(k-1)*ndfpn+j) =...
                K((k-1)*ndfpn+i,(k-1)*ndfpn+j) + ke(i,j,k);
        end
    end
end
end
```

A.7 Contribution from point mass and inertia

```
function [M] = include_point_mass(M, p_Mass, p_Inertia, p_Offset,...
    node_p_Mass)
% This function includes additional point mass and inertia at an arbitrary
% node of the support structure.
%
% INPUTS
% - M          - [-]    Global mass matrix,                size (DOFs,DOFs)
% - p_Mass     - [kg]   Point mass
% - p_Inertia  - [-]    Inertia matrix of the point mass, size (3x3)
% - p_Offset   - [m]    Point mass offset in 3D space, vector with x,y,z
%                       coordinates from the selected node. If x=0, y=0, z=0,
%                       the extra point mass is included directly at the
%                       prescribed node
% - node_p_Mass [-]     Node number in support structure where the point
%                       mass should be applied
% OUTPUTS
% - M          - [-]    Global mass matrix including point mass and inertia,
%                       size (DOFs,DOFs)
%
% COORDINATE SYSTEM FOR POINT MASS ELEMENT
% x-axis points vertically up
% y-axis points to the side (side-to-side)
% z-axis points downwind (fore-aft)

% AUTHOR
% Wojciech Popko
```

```
% Fraunhofer Institute for Wind Energy Systems IWES
% Am Luneort 100, 27572 Bremerhaven, Germany

%% ASSEMBLY OF THE POINT MASS ELEMENT MATRIX
% Initialization of the point mass matrix with 3 translation and
% 3 rotational DOFs
ndfpn = 6;
M_p = zeros(ndfpn);

% [kg] Including translational inertia of the point mass
for i = 1:3
    M_p(i,i) = p_Mass;
end

% [kg m^2] Including rotational inertia of the point mass
M_p(4,4) = p_Inertia(1,1) + p_Mass*p_Offset(2)^2 + p_Mass*p_Offset(3)^2;
M_p(5,5) = p_Inertia(2,2) + p_Mass*p_Offset(1)^2 + p_Mass*p_Offset(3)^2;
M_p(6,6) = p_Inertia(3,3) + p_Mass*p_Offset(1)^2 + p_Mass*p_Offset(2)^2;

% [kg m] Including coupled inertia between translation and rotation due to
% offset of the point mass
M_p(2,4) = -p_Mass*p_Offset(3);
M_p(3,4) =  p_Mass*p_Offset(2);

M_p(1,5) =  p_Mass*p_Offset(3);
M_p(3,5) = -p_Mass*p_Offset(1);

% [kg m^2] Including contributions of the horizontal and vertical offsets
% % of the point mass
M_p(4,5) =  p_Inertia(1,2)- p_Mass*p_Offset(1)*p_Offset(2);

% [kg m] Including coupled inertia between translation and rotation due to
% offset of the point mass
M_p(1,6) = -p_Mass*p_Offset(2);
M_p(2,6) =  p_Mass*p_Offset(1);

% [kg m^2] Including contributions of the horizontal and vertical offsets
% % of the point mass
M_p(4,6) =- p_Inertia(1,3) - p_Mass*p_Offset(1)*p_Offset(3);
M_p(5,6) =- p_Inertia(2,3) - p_Mass*p_Offset(2)*p_Offset(3);

% Mirroring matrix along the diagonal
M_p = (M_p+M_p') - eye(size(M_p,1)).*diag(M_p);
```

```
%% ADDING POINT ELEMENT MASS MATRIX TO ARBITRARY NODE IN GLOBAL MASS MATRIX
% First DOF of the structural node where point mass is applied
 first = node_p_Mass*ndfpn-ndfpn+1;
% Last DOF of the structural node where point mass is applied
 last  = node_p_Mass*ndfpn;

M(first:last,first:last) = M(first:last,first:last) + M_p;
end
```

A.8 Foundation

```
function [M_out, C_out, K_out] = include_boundary_conditions(M, C, K,...
    M_f, C_f, K_f, boundary)
% This function applies boundary conditions (rigid or flexible) for
% a monopile support structure. Flexible foundation can be modeled
% with mass, damping, and stiffness matrices, each of 6x6 size.
%
% INPUTS
% - M        - [-]   Global mass matrix,              size (DOFs,DOFs)
% - C        - [-]   Global damping matrix,           size (DOFs,DOFs)
% - K        - [-]   Global stiffness matrix,         size (DOFs,DOFs)
% - M_f      - [-]   Foundation mass matrix,          size (6,6)
% - C_f      - [-]   Foundation damping matrix,       size (6,6)
% - K_f      - [-]   Foundation stiffness matrix,     size (6,6)
% - boundary- [-]   0 - rigid foundation, 1 - flexible foundation
% OUTPUTS
% - M_out    - [-]   Global mass matrix with applied boundary condition,
%                    size (DOFs-6,DOFs-6) - for rigid foundation
%                    size (DOFs,DOFs)     - for flexible foundation defined
%                                           with (6,6) foundation matrices
% - C_out    - [-]   Global damping matrix with applied boundary condition,
%                    size (DOFs-6,DOFs-6) - for rigid foundation
%                    size (DOFs,DOFs)     - for flexible foundation defined
%                                           with (6,6) foundation matrices
% - K_out    - [-]   Global stiffness matrix with boundary condition,
%                    size (DOFs-6,DOFs-6) - for rigid foundation
%                    size (DOFs,DOFs)     - for flexible foundation defined
%                                           with (6,6) foundation matrices

% AUTHOR
% Wojciech Popko
```

```
% Fraunhofer Institute for Wind Energy Systems IWES
% Am Luneort 100, 27572 Bremerhaven, Germany

%% BOUNDARY CONDITIONS
ndfpn = 6;             % 6 DOFs per node
DOFs = length(K);      % [-]    Total number of DOFs from all elements
                       %        in the support structure

% Rigid foundation - ndfpn columns and ndfpn rows are removed from K and M
if boundary == 0
    M_out = M(ndfpn+1:DOFs,ndfpn+1:DOFs);
    C_out = C(ndfpn+1:DOFs,ndfpn+1:DOFs);
    K_out = K(ndfpn+1:DOFs,ndfpn+1:DOFs);

% Flexible foundation - modeled with K and/or M matrix
elseif boundary == 1
    if ~isempty(M_f)
        % Add foundation mass matrix to the global structure matrix
        M(1:ndfpn,1:ndfpn) = M(1:ndfpn,1:ndfpn) + M_f;
    end
    if ~isempty(C_f)
        % Add foundation damping matrix to the global structure matrix
        C(1:ndfpn,1:ndfpn) = C(1:ndfpn,1:ndfpn) + C_f;
    end
    if ~isempty(K_f)
        % Add foundation stiffness matrix to the global structure matrix
        K(1:ndfpn,1:ndfpn) = K(1:ndfpn,1:ndfpn) + K_f;
    end

% Mass matrix of the entire support structure including foundation mass
    M_out = M;

% Damping matrix of the entire support structure including
% foundation damping
    C_out = C;

% Stiffness matrix of the entire support structure including
% foundation stiffness
    K_out = K;

end
end
```

A.9 Elimination of nodal DOFs

```
function A = remove_DOFs(A,DOF_off)
% Function eliminates nodal DOFs from global matrices (optional feature)
%
% INPUTS
% - A        - [-]   Global matrix, size (DOFs x DOFs)
% - DOF_off - [-]   Vector with DOF numbers, which should be eliminated
%                   from a single node
%                   1 x (axial), 2 y (side-to-side), 3 z (fore-aft)
%                   4 theta_x (torsion)
%                   5 theta_y (fore-aft rotation)
%                   6 theta_z (side-to-side rotation)
% OUTPUTS
% - A        - [-]   Global matrix, with removed DOFs
%                   size (DOFs - DOF_off*nodes, DOFs - DOF_off*nodes)

% AUTHOR
% Wojciech Popko
% Fraunhofer Institute for Wind Energy Systems IWES
% Am Luneort 100, 27572 Bremerhaven, Germany

%% FIND ALL NODAL DOFs, WHICH SHOULD BE REMOVED
allDOFs = [];
for i = 1:length(DOF_off)
    temp = DOF_off(i):6:length(A);
    allDOFs = [allDOFs temp];
end

% Sort DOFs in descending order
allDOFs = sort(allDOFs,'descend');

% Remove DOFs from rows and columns of the global matrix
for i = 1:length(allDOFs)
    try A(allDOFs(i),:)=[]; catch,end
    try A(:,allDOFs(i))=[]; catch,end
end
end
```

A.10 Rotation matrices for 3D beam elements

```
function Rx = rotx(ang)
```

```
% INPUT
% - ang - [deg] - Rotation angle
% OUTPUT
% - Rx  - [-]   - Rotational matrix around x-axis, size (6x6)

% AUTHOR
% Wojciech Popko
% Fraunhofer Institute for Wind Energy Systems IWES
% Am Luneort 100, 27572 Bremerhaven, Germany

Rx = [...
1  0                  0                  0                      0         0;
0  cosd(ang)^2        sind(ang)^2        2*cosd(ang)*sind(ang)  0         0;
0  sind(ang)^2        cosd(ang)^2        -2*cosd(ang)*sind(ang) 0         0;
0  -cosd(ang)*sind(ang) cosd(ang)*sind(ang) (cosd(ang)^2-sind(ang)^2) 0 0;
0  0                  0                  0         cosd(ang)  -sind(ang);
0  0                  0                  0         sind(ang)  cosd(ang)];
end
```

```
function Ry = roty(ang)
% INPUT
% - ang - [deg] - Rotation angle
% OUTPUT
% - Ry  - [-]   - Rotational matrix around y-axis, size (6x6)

% AUTHOR
% Wojciech Popko
% Fraunhofer Institute for Wind Energy Systems IWES
% Am Luneort 100, 27572 Bremerhaven, Germany

Ry = [...
cosd(ang)^2           0  sind(ang)^2          0          2*cosd(ang)*sind(ang)      0;
0                     1  0                    0          0                          0;
sind(ang)^2           0  cosd(ang)^2          0          -2*cosd(ang)*sind(ang)     0;
0                     0  0                    cosd(ang)  0                 -sind(ang);
-cosd(ang)*sind(ang)  0  cosd(ang)*sind(ang)  0          (cosd(ang)^2-sind(ang)^2)  0;
0                     0  0                    sind(ang)  0                  cosd(ang)];
end
```

```
function Rz = rotz(ang)
% INPUT
% - ang - [deg] - Rotation angle
% OUTPUT
% - Rz  - [-]   - Rotational matrix around z-axis, size (6x6)
```

```

% AUTHOR
% Wojciech Popko
% Fraunhofer Institute for Wind Energy Systems IWES
% Am Luneort 100, 27572 Bremerhaven, Germany

Rz = [...
cosd(ang)^2           sind(ang)^2    0   0           0   2*cosd(ang)*sind(ang);
sind(ang)^2           cosd(ang)^2    0   0           0   -2*cosd(ang)*sind(ang);
0                     0              1   0           0          0;
0                     0              0   cosd(ang)   sind(ang)  0;
0                     0              0   -sind(ang)  cosd(ang)  0;
-cosd(ang)*sind(ang)  cosd(ang)*sind(ang)  0  0  0  (cosd(ang)^2-sind(ang)^2)];
end
```

Appendix B

Short-term DELs at different heights of OWT support structure

Short-term DELs at three distinct heights of the support structure — at the seabed (35 m below MSL), at the tower bottom (12.5 m above MSL), and at the tower top (98.5 m above MSL).

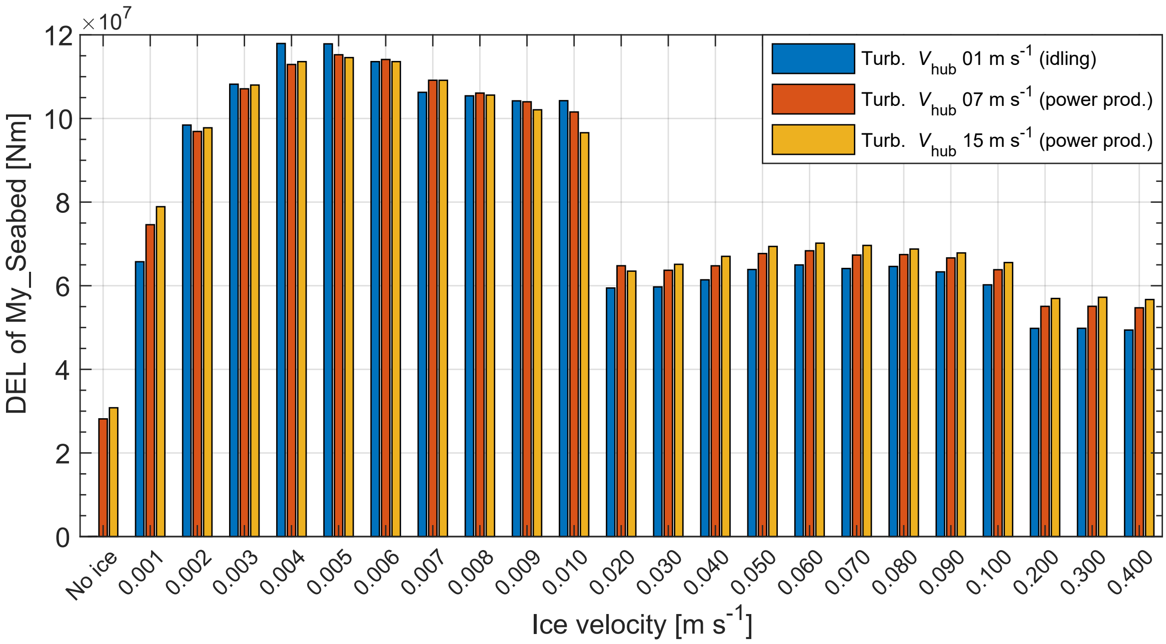

Figure B.1: Short-term DELs of fore-aft bending moment at the seabed (35 m below MSL). Results for LCs with turbulent wind.

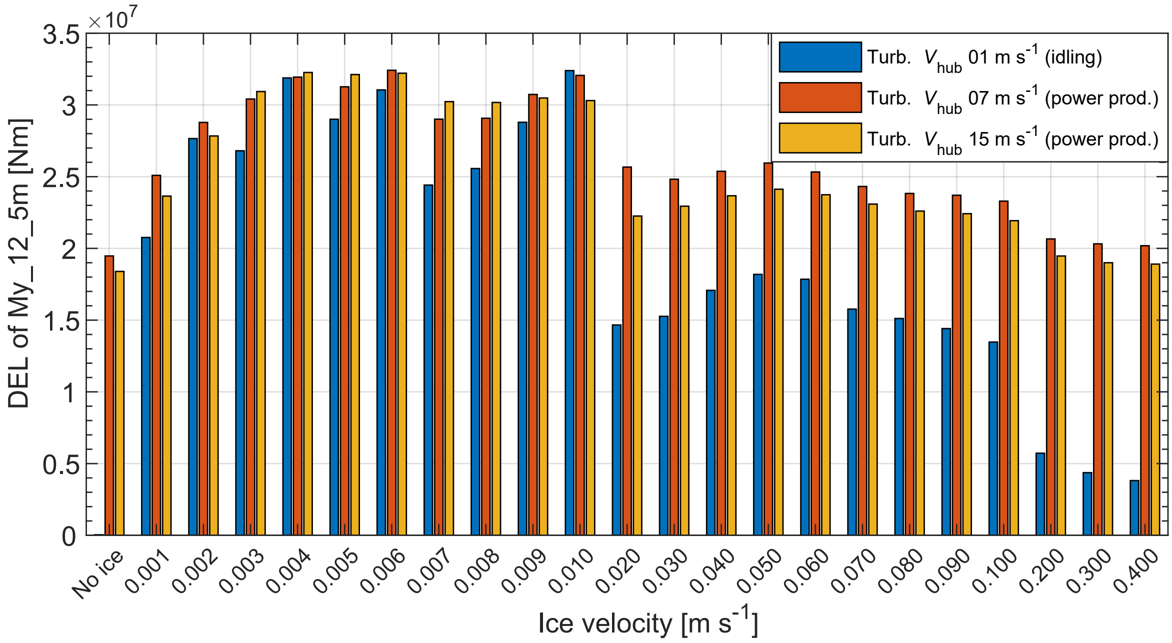

Figure B.2: Short-term DELs of fore-aft bending moment at the tower bottom (12.5 m above MSL). Results for LCs with turbulent wind.

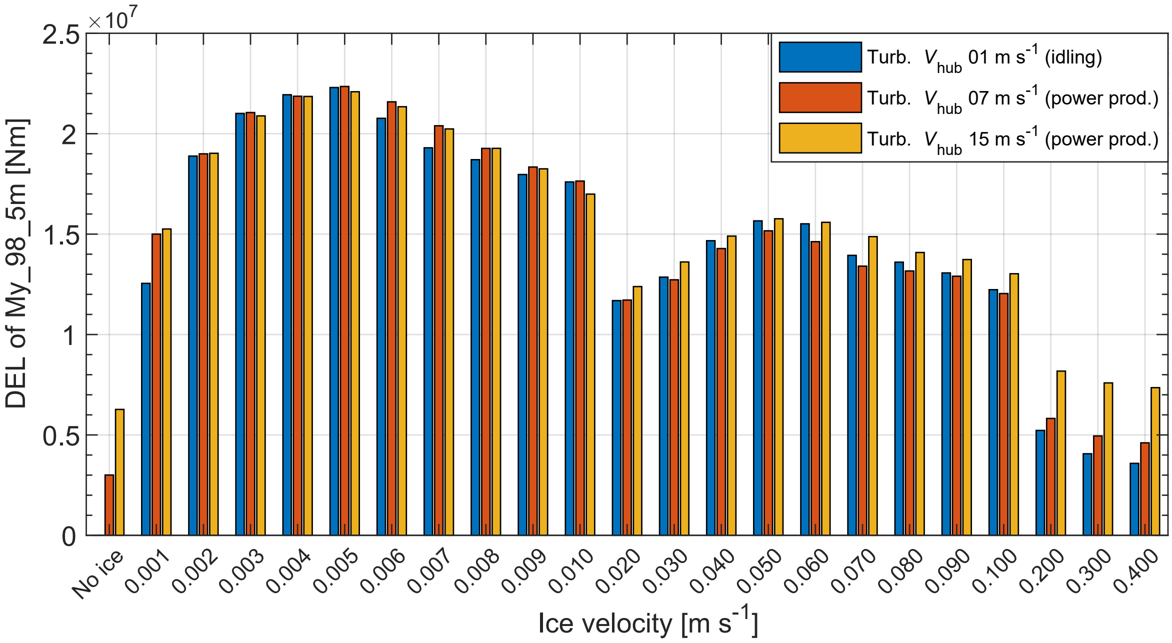

Figure B.3: Short-term DELs of fore-aft bending moment at the tower top (98.5 m above MSL). Results for LCs with turbulent wind.

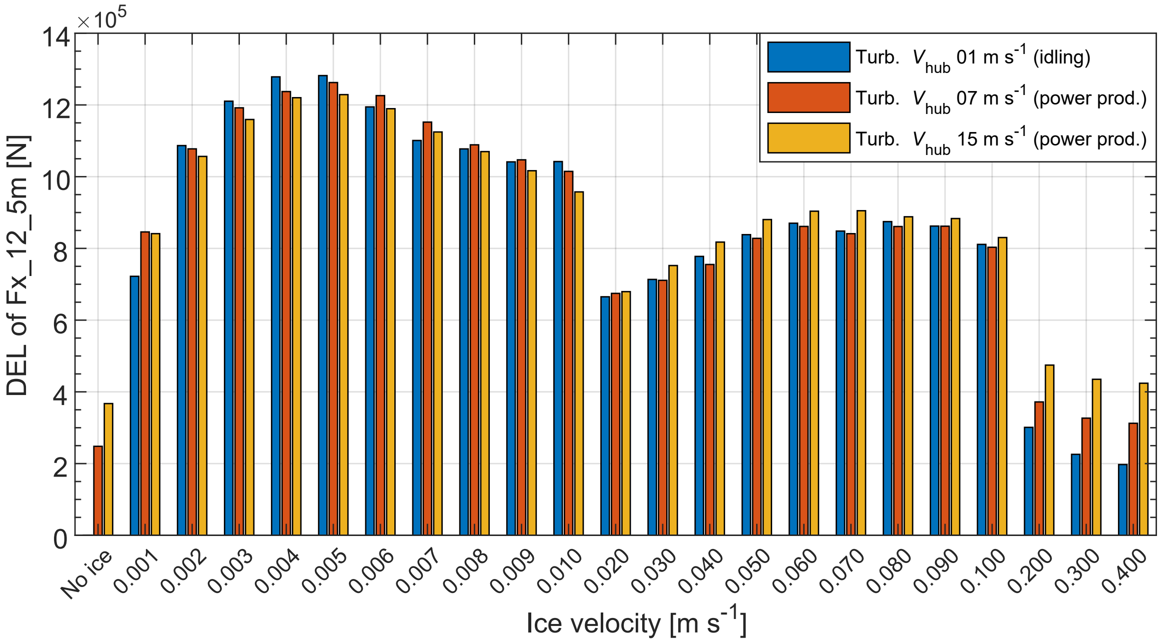

Figure B.4: Short-term DELs of fore-aft shear force at the tower bottom (12.5 m above MSL). Results for LCs with turbulent wind.

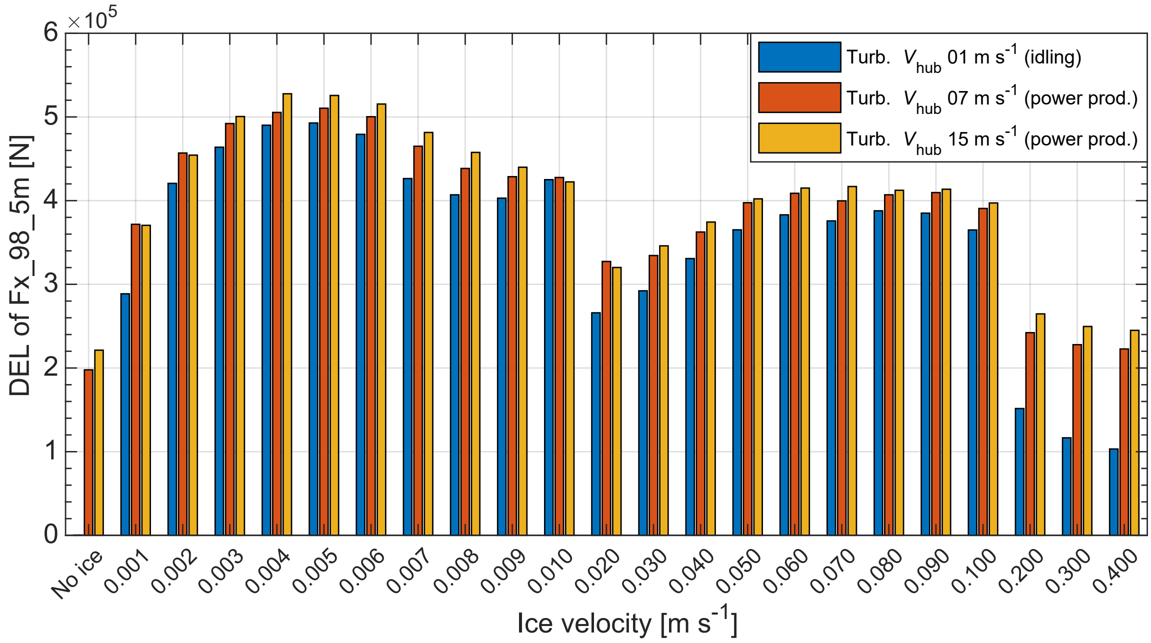

Figure B.5: Short-term DELs of fore-aft shear force at the tower top (12.5 m above MSL). Results for LCs with turbulent wind.

Wojciech Popko — Curriculum Vitae

Summary

Experience in project management, technical execution, and lead of international R&D and industrial projects focused on the global dynamics of OWTs with emphasis on bottom-fixed and floating support structures. Profound knowledge of verification, validation, and development of aero-hydro-servo-elastic tools for coupled simulation of OWTs. Excellent knowledge of fatigue and extreme load analysis for certification of OWTs. An active member of the IEC standardization committee. An author of multiple peer-reviewed articles and conference publications in top international journals and proceedings.

Degrees

Master of Science in Wind Energy, graduated with honors — Jun. 2010

Technical University of Denmark

Bachelor of Engineering in Mechatronics — Jun. 2008

University of Southern Denmark

Experience

Fraunhofer Institute for Wind Energy Systems IWES — Since Oct. 2010
Division System Technology, Group of Global Turbine Dynamics
Bremerhaven, Germany

Research associate/Project manager

Project management, technical execution, and lead of multinational R&D and industrial projects focused on:

- Verification and validation of aero-hydro-servo-elastic codes for coupled/fully-integrated simulation of OWTs with bottom-fixed and floating support structures. Co-leader of the Offshore Code Comparison Collaboration Continuation (OC4) and Correlation (OC5) multinational projects — jointly coordinated with the National Renewable Energy Laboratory (NREL), the USA. 154 participants from 61 organizations in 18 countries participated in the task.

- Simulation and analysis of fatigue and extreme load effects for certification of OWTs according to IEC 61400-3-1, IEC 61400-3-2, DNVGL-ST-0126, DNVGL-ST-0119, and DNVGL-ST-0437 standards.
- Reduction of fatigue and extreme load effects with different control techniques for industrial customers.
- Consultancy concerning a selection of the Design Load Cases for certification of OWTs with bottom-fixed (monopiles, jackets, tripods) and floating (semi-submersibles, tension-leg platforms) support structures for industrial customers.
- Consultancy concerning a selection of metocean conditions and specification of the Design Basis for OWTs for leading industrial customers.
- Impact of sea ice loads on the global dynamics of OWTs — Leader of two R&D projects (executed with Ramboll Deutschland GmbH, Hamburg University of Technology, VTT Research Centre of Finland, and Hamburg Ship Model Basin) and author of expert opinions for leading industrial customers.
- Impact of different stochastic wind field models (Veers, Mann, continuous time random walk, large-eddy simulation) on OWT load effects.
- Local dynamics of jacket support structures influenced by the higher harmonics of the spinning rotor.
- Hybrid models of jacket support structures with beam element representation for legs and braces; and superelement representation for joints.
- Automatic converters for OWT models between different aero-elastic codes.
- Development of generic OWT models and their documentation (IWT-7.5-164 Rev 4) for R&D needs.
- Training for industrial customers focused on global dynamics of OWTs, aero-hydro-servo-elastic codes, Design Load Cases, and postprocessing of fatigue and extreme load effects.

University of Stuttgart Jun. – Aug. 2009
Stuttgart, Germany

Student researcher in the UpWind project, Work Package 4 at Stuttgart Wind Energy at Institute of Aircraft Design — Analysis and reduction of fatigue load effects on a monopile substructure in Bladed by tower feedback control and soft cut-out.

Newtec A/S Aug. 2007 – Aug. 2008
Odense, Denmark

Internship and diploma project — Research and development of a semi-active damper based on the magnetorheological fluid.

Professional memberships

Member of standardization committees:

- The German Commission for Electrical, Electronic & Information Technologies (DKE) of DIN and VDE, two national working groups for IEC 61400-1 and IEC 614003-3 standards
- The International Electrotechnical Commission TC 88: Maintenance Team 3-1
  — One of the revisers of IEC 61400-3 Annex E "Recommendations for design of offshore wind turbine support structures with respect to ice loads"

Member of scientific and technical committees of:

- The Renewable Energy & Environment Symposium, International Society of Offshore & Polar Engineers (ISOPE), Mountain View, CA, USA
- The International Conference on Renewable Energies Offshore, Lisbon, Portugal
- The 8th European Seminar Offshore Wind and other marine renewable Energies in Mediterranean and European Seas (OWEMES) 2015, Rome, Italy

Operating agent of:

- The International Energy Agency (IEA) Wind Task 30: OC4 and OC5 projects in 2010 – 2018

Research stay

Norwegian University of Science and Technology Sep. 2016 – Mar. 2017
Offshore Wind Turbine Technology group at the Department of Civil and Transport Engineering

Awards, scholarships

- **Recognition for outstanding performance** in subsequent years: 2012, 2013, 2014, 2015, and 2017
  – awarded by the Fraunhofer Society for the Advancement of Applied Research
- **IP@Leibniz Scholarship** for the research stay at the Norwegian University of Science and Technology in the time period from January to March 2017
  – awarded by the Leibniz University Hannover
- **Erasmus Scholarship** for the spring semester 2010 at the University of Stuttgart
  – awarded by the Technical University of Denmark
- **Danish Government Scholarship** for the academic year 2009 – 2010
  – awarded by the Danish Centre for International Cooperation and Mobility in Education and Training
- **Erasmus Scholarship** for the academic year 2006 – 2007 at the University of Southern Denmark
  – awarded by the Bialystok University of Technology

Wojciech Popko — List of Publications

Author-level metrics

- Citations: ~320, *h*-index: 8 — Scopus, as of November 2020
- Citations: ~470, *h*-index: 8 — ResearchGate, as of November 2020
- Citations: ~770, *h*-index: 11 — Google Scholar, as of November 2020

Journal articles

- **Popko W.**, Robertson A., Jonkman J., Wendt F., Thomas P., Müller K.,. . . Harries R. (2021, February). Validation of numerical models of the offshore wind turbine from the alpha ventus wind farm against full-scale measurements within OC5 Phase III. *Journal of Offshore Mechanics and Arctic Engineering, 143*(1), 1–18. doi:10.1115/1.4047378
- Huhn, M. L. & **Popko W.** (2020, September). Best practice for verification of wind turbines numerical models. *Journal of Physics: Conference Series, 1618*, 1–10. doi:10.1088/1742-6596/1618/5/052026
- Robertson A. N., Wendt F., Jonkman J. M., **Popko W.**, Dagher H., Gueydon S.,. . . Debruyneu, Y. (2017, October). OC5 Project Phase II: Validation of global loads of the DeepCwind floating semisubmersible wind turbine. *Energy Procedia, 137*, 38–57. doi:10.1016/j.egypro.2017.10.333
- Robertson A. N., Wendt F., Jonkman J. M., **Popko W.**, Borg M., Bredmose H.,. . . Guerinel M. (2016, September). OC5 project Phase Ib: Validation of hydrodynamic loading on a fixed, flexible cylinder for offshore wind applications. *Energy Procedia, 94*, 82–101. doi:10.1016/j.egypro.2016.09.201
- **Popko W.**, Georgiadou S., Loukogeorgaki E., & Vorpahl F. (2016, February). Influence of joint flexibility on local dynamics of a jacket support structure. *Journal of Ocean and Wind Energy, 3*(1) 1–9.
- **Popko W.**, Antonakas P., & Vorpahl F. (2014, May). Investigation of local vibration phenomena of a jacket sub-structure caused by coupling with other components of an offshore wind turbine. *Journal of Ocean and Wind Energy, 1*(2), 111–118.
- **Popko W.**, Vorpahl F., Zuga A., Kohlmeier M., Jonkman J., Robertson A.,. . . von Waaden H. (2014, February). Offshore Code Comparison Collaboration Continuation (OC4), Phase I—Results of coupled simulations of an offshore wind turbine with jacket support structure. *Journal of Ocean and Wind Energy, 1*(1), 1–11.

Peer-reviewed conference papers

- **Popko W.**, Robertson A., Jonkman J., Wendt F., Thomas P., Müller K.,. . . Harries R. (2019, June). Validation of numerical models of the offshore wind turbine from the alpha ventus wind farm against full-scale measurements within OC5 Phase III. In *Proceedings of the 38th International Conference on Ocean, Offshore and Arctic Engineering*, Glasgow, The United Kingdom: American Society of Mechanical Engineers. doi:10.1115/OMAE2019-95429
- **Popko W.**, Huhn M. L., Robertson A., Jonkman J., Wendt F., Müller K.,. . . Cai J. (2018, June). Verification of a numerical model of the offshore wind turbine from the alpha ventus wind farm within OC5 Phase III. In *Proceedings of the 37th International Conference on Ocean, Offshore and Arctic Engineering, 10*, Madrid, Spain: American Society of Mechanical Engineers. doi:10.1115/OMAE2018-77589
- **Popko W.**, Wächter M., & Thomas P. (2016, June). Verification of Continuous Time Random Walk wind model. In *Proceedings of the 26th International Ocean and Polar Engineering Conference, 1*, 471–483, Rhodes, Greece: International Society of Offshore and Polar Engineers.
- **Popko W.**, & Georgiadou S. (2015, June). Validation of Määttänen-Blenkarn ice model for ice-structure interaction against ice tank tests. In *Proceedings of the 25th International Ocean and Polar Engineering Conference, 1*, 1814–1821, Kona, HI, USA: International Society of Offshore and Polar Engineers.
- **Popko W.**, Georgiadou S., Loukogeorgaki E., & Vorpahl F. (2015, June). Influence of joint flexibility on local dynamics of a jacket support structure. In *Proceedings of the 25th International Ocean and Polar Engineering Conference, 1*, 277–284, Kona, HI, USA: International Society of Offshore and Polar Engineers.
- Robertson A. N., Wendt F. F., Jonkman J. M., **Popko W.**, Vorpahl F., Stansberg C. T., . . . Bouy L. (2015, June). OC5 Project Phase I: Validation of hydrodynamic loading on a fixed cylinder. In *Proceedings of the 25th International Ocean and Polar Engineering Conference, 1*, 471–480, Kona, HI, USA: International Society of Offshore and Polar Engineers.
- Robertson A., Jonkman J., Vorpahl F., **Popko W.**, Qvist J., Frøyd L., . . . Kofoed-Hansen H. (2014, June). Offshore Code Comparison Collaboration, Continuation: Phase II results of a floating semisubmersible wind system. In *Proceedings of the 33rd International Conference on Ocean, Offshore and Arctic Engineering, 9B*, San Francisco, CA, USA: American Society of Mechanical Engineers. doi:10.1115/OMAE2014-24040
- **Popko W.** (2014, June). Comparison of full-scale and numerical model dynamic responses of Norströmsgrund lighthouse. In *Proceedings of the 33rd International Conference on Ocean, Offshore and Arctic Engineering, 10*, San Francisco, CA, USA: American Society of Mechanical Engineers. doi:10.1115/OMAE2014-23562
- **Popko W.**, Antonakas P., & Vorpahl F. (2013, July). Investigation of local vibration phenomena of a jacket sub-structure caused by coupling with other components of an offshore wind turbine. In *Proceedings of the 23rd International Offshore and Polar Engineering Conference, 1*, 336–344, Anchorage, AK, USA: International Society of Offshore and Polar Engineers.

- Jussila V., **Popko W.**, & Heinonen J. (2013, June). Interfacing of ice load simulation tools for cylindrical and conical structure with OneWind simulation tool for offshore wind turbines. In *Proceedings of the 22nd International Conference on Port and Ocean Engineering under Arctic Conditions*, Espoo, Finland
- **Popko W.**, Heinonen J., Hetmanczyk S., & Vorpahl F. (2012, June). State-of-the-art comparison of standards in terms of dominant sea ice loads for offshore wind turbine support structures in the Baltic Sea. In *Proceedings of the 22nd International Offshore and Polar Engineering Conference, 1*, 426–435, Rhodes, Greece: International Society of Offshore and Polar Engineers.
- **Popko W.**, Vorpahl F., Zuga A., Kohlmeier M., Jonkman J., Robertson A., . . . von Waaden H. (2012, June). Offshore Code Comparison Collaboration Continuation (OC4), Phase I — Results of coupled simulations of an offshore wind turbine with jacket support structure. In *Proceedings of the 22nd International Offshore and Polar Engineering Conference, 1*, 337–346, Rhodes, Greece: International Society of Offshore and Polar Engineers.
- Fischer T., **Popko W.**, Sørensen J.D., & Kühn M. (2010, November). Load analysis of the UpWind jacket reference support structure. In *Proceedings of the 10. Deutsche Windenergie-Konferenz DEWEK*, Bremen, Germany: Deutsches Windenergie-Institut GmbH
- Kaufer D., Fischer T., Vorpahl F., & **Popko W.** (2010, November). Different approaches to modelling jacket support structures and their impact on overall wind turbine dynamics. In *Proceedings of the 10. Deutsche Windenergie-Konferenz DEWEK*, Bremen, Germany: Deutsches Windenergie-Institut GmbH

Other conference papers

- Vorpahl F., & **Popko W.** (2014, October). An overview of current aeroelastic design tools — Benefits and limitations. *Presentation at Windpower Monthly: Future Offshore Foundations Forum 2014*, Hamburg, Germany
- Robertson A., Jonkman J., Musial, W., Vorpahl F., & **Popko W.** (2013, November). Offshore Code Comparison Collaboration, Continuation: Phase II results of a floating semisubmersible wind system. In *Proceedings of European Wind Energy Association EWEA Offshore 2013*, Frankfurt, Germany
- Schwarze H., Vorpahl F., & **Popko W.** (2013, February). Simulation von Windenergieanlagen als schwingende Systeme. In *4. VDI-Fachtagung Schwingungen von Windenergieanlagen*, 187–199, Bremen, Germany
- **Popko W.**, Vorpahl F., Jonkman J., & Robertson A. (2012, September). OC3 and OC4 projects — Verification benchmark exercises of the state-of-the-art coupled simulation tools for offshore wind turbines. In *Proceedings of the 7th European Seminar Offshore Wind and other Marine Renewable Energy in Mediterranean and European Seas*, 499–503, Rome, Italy
- **Popko W.** (2011, July). Breaking the Ice project (BRICE) — Dynamic investigation of offshore wind energy converters influenced by ice loads. *Poster at the PhD summer school Role of Sea Ice in Climate System*, University Centre in Svalbard, Longyearbyen, Norway

Significant technical reports

- **Popko W.**, Thomas P., Sevinc A., Rosemeier M., Bätge M., Braun R.,... Reuter A. (2018, December). IWES Wind Turbine IWT-7.5-164 Rev 4. Fraunhofer Institute for Wind Energy Systems IWES, Bremerhaven, Germany. doi:10.24406/IWES-N-518562
- **Popko W.** (2017, December). OC5 Phase III — RNA and tower definition for verification and validation of OWT models. Fraunhofer Institute for Wind Energy Systems IWES, Bremerhaven, Germany
- **Popko W.** (2017, December). OC5 Phase III — Verification procedure for OWT models. Fraunhofer Institute for Wind Energy Systems IWES, Bremerhaven, Germany
- **Popko W.**, Ziemer G., & Evers K.-U. (2015, July). Schlussbericht — BReaking the ICE (BRICE) — Dynamische Untersuchungen von Offshore-Windenergieanlagen unter dem Einfluss von Meer-Eis. Fraunhofer Institute for Wind Energy and Energy System Technology IWES and Hamburg Ship Model Basin, Bremerhaven and Hamburg, Germany. doi:10.2314/GBV:859611647
- Vorpahl F., & **Popko W.** (2013, July). Description of the load cases and output sensors to be simulated in the OC4 project under IEA Wind Annex 30. Fraunhofer Institute for Wind Energy and Energy System Technology IWES, Bremerhaven, Germany
- Vorpahl F., **Popko W.**, & Kaufer D. (2013, July). Description of a basic model of the 'UpWind reference jacket' for code comparison in the OC4 project under IEA Wind Annex 30. Fraunhofer Institute for Wind Energy and Energy System Technology IWES, Bremerhaven, Germany

Invited talks

- *IEA Tasks 23 & 30 Verification and validation of simulation tools for wind turbines*. The keynote speech at the 3rd International Conference on Renewable Energies (RENEW), October 8, 2018, Lisbon, Portugal
- *Dynamics of offshore wind turbines in context of coupled load simulation in aero-hydro-servo-elastic tools*. Forschungsverbund Windenergie (FVWE) Kolloquium, October 8, 2013, Bremen, Germany
- *Sea ice load provisions in IEC 61400-3 Ed. 1.0 — Suggestions and recommendations for revision*. The International Electrotechnical Commission TC 88 meeting — IEC 61400-3 and 61400-3-2 standards for offshore wind turbines, ALSTOM, August 30, 2013, Barcelona, Spain
- *OC3 and OC4 projects — Verification benchmark exercises of the state-of-the-art coupled simulation tools for offshore wind turbines*. The 7th European Seminar Offshore Wind and other Marine Renewable Energy in Mediterranean and European Seas (OWEMES 2012), September 7, 2012, Rome, Italy
- *IEA Wind Annex 30 — OC4 project*. A Seminar: Offshore Wind Energy — The New Green Energy Opportunity, Engineers Ireland, May 26, 2011, Dublin, Ireland

Conferences — participation and role

The 38th International Conference on Ocean, Offshore and Arctic Engineering (OMAE 2019)
in Glasgow, The United Kingdom Jun. 9–14, 2019

- Paper presentation
- Session chair and organizer
- Chair and main presenter at the biannual IEA Wind Task 30 all-day meeting

EERA DeepWind'2019, 16th Deep Sea Offshore Wind R&D Conference
in Trondheim, Norway Jan. 16–18, 2019

- Chair and main presenter at the biannual IEA Wind Task 30 all-day meeting

The 3rd International Conference on Renewable Energies (RENEW 2018)
in Lisbon, Portugal Oct. 8–10, 2018

- Keynote presentation at the conference opening
- Session chair

The 37th International Conference on Ocean, Offshore and Arctic Engineering (OMAE 2018)
in Madrid, Spain Jun. 17–22, 2018

- Paper presentation
- Session chair and organizer
- Chair and main presenter at the biannual IEA Wind Task 30 all-day meeting

EERA DeepWind'2018, 15th Deep Sea Offshore Wind R&D Conference
in Trondheim, Norway Jan. 17–19, 2018

- Chair and main presenter at the biannual IEA Wind Task 30 all-day meeting

The 27th International Ocean and Polar Engineering Conference (ISOPE 2017)
in San Francisco, CA, USA Jun. 25–30, 2017

- Session chair and organizer
- Chair and main presenter at the biannual IEA Wind Task 30 all-day meeting

EERA DeepWind'2017, 14th Deep Sea Offshore Wind R&D Conference
in Trondheim, Norway Jan. 18–20, 2017

- Chair and main presenter at the biannual IEA Wind Task 30 all-day meeting

The 26th International Ocean and Polar Engineering Conference (ISOPE 2016)
in Rhodes, Greece Jun. 26 –Jul. 1, 2016

- Paper presentation
- Session chair and organizer

- Presenter at the biannual IEA Wind Task 30 all-day meeting

The 25th International Ocean and Polar Engineering Conference (ISOPE 2015)
in Kona, HI, USA Jun. 22–26, 2015

- Papers presentation
- Session chair and organizer
- Chair and main presenter at the biannual IEA Wind Task 30 all-day meeting

The 33rd International Conference on Ocean Offshore and Arctic Engineering (OMAE 2014)
in San Francisco, CA, USA Jun. 8–13, 2014

- Paper presentation

Europe's Premier Wind Energy Event (EWEA Offshore 2013)
in Frankfurt, Germany Nov. 19–21, 2013

The 23rd International Offshore and Polar Engineering Conference (ISOPE 2013)
in Anchorage, AK, USA Jun. 30–Jul. 5, 2013

- Paper presentation

The 22nd International Conference on Port and Ocean Engineering under Arctic Conditions
in Espoo, Finland Jun. 9–13, 2013

Europe's Premier Wind Energy Event (EWEA 2013)
in Vienna, Austria Feb. 4–7, 2013

The 7th European Seminar Offshore Wind and other marine renewable Energy in Mediterranean and European Seas (OWEMES 2012)
in Rome, Italy Sep. 5–7, 2012

- Paper presentation
- Session chair

The 22nd International Offshore and Polar Engineering Conference (ISOPE 2012)
in Rhodes, Greece Jun. 17–22, 2012

- Papers presentation
- Main presenter at the biannual IEA Wind Task 30 all-day meeting

The 7th PhD Seminar on Wind Energy in Europe
in Delft, The Netherlands Oct. 27–28, 2011

Offshore Wind Energy — The New Green Energy Opportunity, Engineers Ireland
in Dublin, Ireland May 26, 2011

- Invited speech and presentation

The European Wind Energy Conference and Exhibition (EWEC 2010)
in Warsaw, Poland Apr. 20–23, 2010

The 2009 European Offshore Wind Conference and Exhibition
in Stockholm, Sweden Sep. 14–16, 2009

Support structures for offshore wind turbines (OWTs) are designed and certified site-specific based on the calculated load effects. These load effects originate from static, cyclic, stochastic, and transient loads from the met-ocean environment and rotating components of the wind turbine. The met-ocean environment of the Baltic Sea accounts for variable wind and marine conditions. Sea ice is part of marine conditions which – among others – should be included in the design process of OWT support structures. The load analysis and design of OWTs, including its components, rely on the time-domain based, coupled aero-hydro-servo-elastic simulation tools. Only this approach can provide an accurate prediction of the OWT dynamic response. Dynamic interaction between an OWT and external loads – including ice loads – cannot be disregarded as it may result in considerable loss of accuracy. A proper understanding of sea ice impact on the global dynamics of OWTs – involving the fully-integrated simulation approach – is necessary within the offshore wind research community, industry, and certification authorities.

ISBN 978-3-8396-1684-0